FAULT DAMAGE ZONES – OBSERVATIONS, DYNAMIC MODELING, AND IMPLICATIONS ON FLUID FLOW

SRB Volume 131

A DISSERTATION
SUBMITTED TO THE DEPARTMENT OF GEOPHYSICS
AND THE COMMITTEE ON GRADUATE STUDIES
OF STANFORD UNIVERSITY
IN PARTIAL FULFILLMENT OF THE REQUIREMENTS
FOR THE DEGREE OF
DOCTOR OF PHILOSOPHY

Madhur Johri

October 2012

I certify that I have read this dissertation and that in my opinion it is fully adequate, in scope and quality, as a dissertation for the degree of Doctor of Philosophy.

_____

Mark D. Zoback (Principal Advisor)

I certify that I have read this dissertation and that in my opinion it is fully adequate, in scope and quality, as a dissertation for the degree of Doctor of Philosophy.

_____

Eric M. Dunham

I certify that I have read this dissertation and that in my opinion it is fully adequate, in scope and quality, as a dissertation for the degree of Doctor of Philosophy.

_____

Norm Sleep

I certify that I have read this dissertation and that in my opinion it is fully adequate, in scope and quality, as a dissertation for the degree of Doctor of Philosophy.

_____

Peter Hennings

Approved for the University Committee on Graduate Studies.

ABSTRACT

This thesis describes a methodology for characterizing fault damage zones, modeling and quantifying damage zone attributes to facilitate integration with reservoir models, and developing a technique for incorporating damage zones in reservoir models for modeling flow and production. This study can help address some of the fundamental questions pertaining to estimating reserves, production performance, improving recovery rates, water production during recovery operations and strategic reservoir development of fractured and faulted reservoirs, all of which are relevant and applicable to a number of current endeavors in industries such as the oil and gas, and geothermal industry.

The first part of this thesis uses image and other geophysical logs to analyze sub-surface damage zones in two distinct geologic environments – granitic rocks in the ConocoPhillips example (CPE) gas field and arkosic sandstone and conglomerates adjacent the San Andres Fault. The analysis indicates that despite the geologic differences of the two study areas, damage zones in both the areas are similar in terms of damage zone width, peak fracture/fault density and rate of fracture/fault decay with distance from the main fault. Damage zones in both, the CPE gas field and the arkosic section are ~ 50-80 meters wide. The decrease of fracture/fault density with distance from the main fault can approximately be described by a power law $F = F_0 r^{-n}$. Fault constant F_0 is the fracture density at unit distance (1 meter) from the fault. It ranges from 10-30 fractures/m in damage zones in the CPE gas field, and from 6-17 fractures/m in damage zones in the arkosic section. The decay rate n ranges from 0.68-1.06 in the damage zones in the CPE gas

field, and from 0.4-0.75 in the damage zones in the arkosic section. Such a quantification of damage zone attributes facilitates their assimilation in reservoir models.

The second part of this thesis uses dynamic rupture propagation models with strongly rate-weakening friction and off-fault plasticity to model damage zones associated with second-order thrust faults observed in the CPE gas field in Indonesia. The region deforming inelastically due to stress perturbations generated by the propagating rupture is assumed to be the damage zone associated with the fault. A single slip event model suggests a spatially heterogeneous width of damage zones (since width scales with propagation distance). The cumulative effect of multiple slip events of various sizes (consistent with the Gutenberg Richter scaling relationship) is considered by superimposing the plastic strain field from individual slip events. Considering multiple slip events homogenizes the spatial heterogeneity in the damage zone widths. Results show that the decay of fracture density with distance from the fault can be described by a power law $F = F_0 r^{-n}$. The rate of decay *n* is approximately 0.85 close to the fault and increases to ~ 1.4 at larger distances (> 10 m). Modeled damage zones are 60-100 meters wide. These attributes are similar to those observed in the CPE gas field, and those reported in various outcrop studies.

The third part provides a methodology for incorporating damage zones in reservoir models. Information derived from fracture characterization (image logs) and modeled damage zones (from dynamic rupture modeling) is used to generate a discrete fracture network (DFN) model of a region of the CPE reservoir. DFN models are more representative of fractured, low matrix permeability reservoirs which demonstrate phenomenon such as channeling and preferential flow. Fractures are assigned flow properties using Willis-Richard's and Barton's relations. Simulating flow through discrete fractures in a fracture network is computationally expensive, especially when the fracture density is high (like in damage zones). Therefore, the DFN model is upscaled to an equivalent grid (Oda's method), where individual grid blocks have a unique permeability tensor representative of the fracture properties inside that grid block. Flow simulations are then conducted in a dual porosity framework. Use of dual porosity models is appropriate in highly fractured, low matrix permeability reservoirs (e.g. CPE). Flow simulations are performed on two models, one containing both the background fractures and damage zones, while the other containing only background fractures. The objective is to show the signature of

damage zones on the reservoir flow properties. The reservoir models are produced a constant rate of 30 MMSCF/day for 300 days. A distinct difference in the pressure drawdown between the two models is observed, the difference in pressure decay being almost 600 psi after 300 days. This clearly highlights the importance of incorporating fault damage zones in reservoir models for modeling flow correctly, and how ignoring their presence can lead to erroneous results. This study also investigates the effect of various drilling strategies in fractured reservoirs. Simulations suggest that higher flow rates can be achieved by coursing the well through damage zones, increasing the reservoir-wellbore contact length and providing a larger projection of the well in the direction of maximum flow.

The last portion of this thesis does not focus on damage zones. This study applies rupture propagation (similar to second part) on a smaller scale to model damage caused due to slip induced on small natural fractures and faults in the vicinity of hydraulic fractures during slick-water hydraulic fracturing operations. The objective is to investigate whether co-seismic slip on natural fractures induced by increase in pore pressure is a dominant deformation mechanism in stimulating the reservoir. Results suggest that this co-seismic slip does not significantly affect the bulk porosity and permeability of the surrounding host rock. However, strain localization features that develop at the tips of poorly-oriented faults as a consequence of slip suggest the formation of new fractures. This increases the percolation zone by not only increasing the total area of fractures hydraulically connected to the well (percolation zone) but also the interconnectivity between the pre-existing fracture network. The pre-existing fracture network, therefore, appears to be critical in determining the stimulation potential of the reservoir. This could, therefore, be a potential mechanism in stimulating the reservoir.

ACKNOWLEDGEMENTS

The years spent in Stanford have been immensely enriching, both on an academic and personal level, and I feel greatly indebted to several people who have made my stay here so fruitful and rewarding…and they are absolutely worth stacking this thesis up just a little more. I must begin with my advisor, Mark Zoback for providing me the incredible opportunity of studying Geophysics in Stanford. Being a civil engineering graduate, my transition into Geophysics could have been extremely challenging, but for the immense amount of support, guidance, and patience from Mark. Thanks Mark for being patient with me, and allowing me ample time to find my groove. Thanks for teaching me that 'it's all a gradual process' at times when I've been frustrated with slow progress and trying to do too much too soon. I have always been in awe of Mark's work ethic, and how he fits in so much each day. Mark says '60 is the new 40'…I strongly suspect he's going to make 65 the new 25!…the curious case of Mark Zoback! Mark, I'll always strive to imbibe your work ethic and discipline in life. Thank you, Mark, for being more than just a Ph.D. advisor - a friend and a huge support (on both professional and personal issues).

I would like to thank Eric Dunham for patiently guiding me through a sizeable chunk of my thesis. Thanks Eric for being so approachable, and available for lengthy discussions (usually at short notice), and for accommodating my 'last-minute' deadlines into your schedule. Eric's been more of a friendly mentor, but what impresses me most is his uncompromising attitude

towards scientific rigor, something that I'll try to imbibe in my future endeavors. And of course I feel hugely indebted to you, Eric, for allowing me to use your numerical code on dynamic rupture simulations.

I also thank the other members of my reading committee - Norm Sleep and Peter Hennings. Thanks Norm, for being a tremendous resource and providing several insights and recommendations. Thanks Peter for providing me a great internship with ConocoPhillips. Your guidance and the field trip (my first elaborate rendezvous with field work) will always be cherished. I owe a lot of gratitude to Tapan Mukerji, not only for serving as my committee chair, but being an invaluable resource when it comes to new research ideas, various research tools, courses or any form of guidance. You can be rest assured that regardless of the topic, you walk into his office with a problem, and you come out with a solution (at times multiple, which is another problem … and more work!). Tapan, I shall always cherish the peripatetic discussions on several evenings on our way towards Stanford Avenue.

I wish to acknowledge Neal Josephson, Thomas Doe, Zijun Fang and Priscila Ribeiro who have been of great assistance at various stages of my research. A special note of thanks to Amit Suman for accommodating several hours of help between his wedding preparations, an uncompromising workout regimen and research deadlines! I also thank Pijush Paul, Dave Amendt, Uday Tare and Shailesh Ekbote for the excellent mentorship during my internships, where I got a flavor of working on industry-oriented problems.

I thank the Stanford Rock Physics and Borehole Geophysics (SRB) consortium for financial support during my studies, as well as ConocoPhillips for providing datasets I worked on. I also thank the Stanford CEES for computational support. Dennis Michael has been a great help with support on the CEES cluster. Thanks Dennis for keeping things in check, and for the several times when you've provided me access to idle queues owned by other groups!

If there is one reason why we grad students avoid administrative idiosyncrasies so prevalent in most establishments, it is the excellent staff of the Geophysics Department, most notably Susan Phillips-Moskowitz, Tara Illich (now Arenas) and Lauren Nelson who have made my stay so much smoother. I wish to thank Tara for ensuring all departmental deadlines were

duly met, and more importantly, improvising, when they were not (which was more often the case)! Susan's care has extended much beyond the usual group-related activities, right from my first week in the US when she took on the AT&T salesperson for refusing to provide me a phone connection because I didn't have a credit history (of course, knowing AT&T that didn't help) to ensuring I have everything checked in the graduation check-list. Given their obsession with Indian culture, several hours have been spent with Tara and Susan discussing Indian philosophy, classical music, tourism and cuisine to name a few. These discussions will definitely be missed.

I will fondly remember the times spent in office, and I owe that to my fellow research group members and colleagues – Katie Boyle, Marco Bohnhoff, Jeremy Brown, Chandong Chang, Laura Chiaramonte, Indrajit Das, Pratik Dutta, Paul Hagin, Rob Heller, Owen Hurd, Sander Hol, Arjun Kohli, Amie Lucier, Pijush Paul, Hiroki Sone, John Vermylen, Rall Walsh, Randi Walters, Ali Yaghoubi, Alec 'baby-face' Yang, Ramil Ahmadov, Sabrina Aliyeva, Kaushik Bandopadhyay and Tanima Dutta. Thanks for your humor, friendship and encouragement. Special thanks to Hiroki for lots of help over the years, insightful scientific discussions, and providing several by-lanes from apparent research cul-de-sacs.

Many friends, who I have been fortunate to have in close vicinity, have prevented me from becoming socially awkward! Ratna (my supposed mentor) has been my go-to guy right from day one. I still cherish our photography 'field' trips when you were around. Cheers to my lunch and workout mates - gogo master Kushagra, Indrajit, Suman and Nishank for making lunch the most-looked-out-for part of the day. Lunch will never be the same joy, and workout the same torture without you guys! I also want to acknowledge my very special friends Pattu and Roopa (you made Friday evenings the best part of the week), Khushboo and Sid (thanks for not delaying my graduation by preventing my addiction towards play stations), the shadows, Sudhish Baku, Palagumi, Ninja, Rajshekhar and Momo. Thanks for providing just the right amount of distractions for surviving grad life!

I am sincerely thankful to my uncle Suresh and aunt Veena for support, encouragement and love over the years. My cousin Vardan and I have almost grown up together right from our days in boarding school (Sherwood College), and have shared most of our formative years. It's been great fun growing up together! I also wish to acknowledge my aunt Meena bua, my cousin

Arun and Hitu bhabhi for providing a home away from home. Thanks for your warmth, affection and concern. Seeing my nephews Adi and Aryaman grow over these five years has been a delight! I also wish to thank my cousin Anita and brother in law Sanjay for their help and care during my internships in Houston. Time spent with them and my nephew Abhishek has been a lot of fun.

Lastly, I must reserve my most heartfelt acknowledgements for my family – my grandparents Brijraj Bahadur Johri and Gargi, my parents Indu Mohan and Sushma, and my soon-to-be wife Juhi. My parents have been most particular about providing me the best possible education, often times at the expense of their own interests. In many ways, my graduation is the culmination of their efforts and endeavors. Thanks Papa Mumma for your unwavering love, faith and support over all these years. I feel privileged and honored to be your son. Juhi has been a pillar of strength right since we've known each other, a great inspiration and fierce critic. She'll testify, with a wry smile, to being the 'sink' to several frustrating moments during grad life, but thanks, Juhi, for holding up in spite of all my weirdness!

I dedicate this thesis to Baba, Dadi, Papa, Mumma and Juhi.

Mark feels I am verbose in my writing. I may have lived up to it… and not just in the acknowledgements.

TABLE OF CONTENTS

LIST OF TABLES

LIST OF FIGURES

Chapter 1

INTRODUCTION

1.1 Overview

This thesis focuses on developing a quantitative understanding of damage zones associated with relatively smaller second-order reservoir-scale faults and incorporating them in flow simulators to model flow through fractured reservoirs. Second-order faults represent relatively isolated faults with small slips having relatively simpler damage zones with less overprinting due to successive stages of deformation. However, these play an important role in governing fluid flow at reservoir scales. Modeling flow through fractured reservoirs is significantly more challenging than it is for conventional clastic reservoirs since fractures introduce strong permeability anisotropy due to large permeability along the fracture plane. Spatially variable fracture density introduces permeability heterogeneity. Field and laboratory experiments have demonstrated strong evidence of channeling and preferential flow paths in fractured networks (Neretnieks el al. 1982, 1993). Fault damage zones are regions of high fracture density around faults. Presence of damage zones in reservoirs further adds to the complexity of the flow characteristics of reservoirs. The impact of damage zones on fluid flow through fractured reservoirs has been clearly demonstrated by Paul et al. (2009) and Hennings et al (2012). The primary impediment, however, that disables the incorporation of damage zones in flow simulators is a lack of adequate data (bulk of the subsurface information comes from seismic images, image logs and core data, none of which comprehensively characterize damage zones)

and a lack of a quantitative understanding of damage zone characteristics. Currently, fracture and damage zone characterization in reservoirs is usually performed using qualitative analysis whereas predictions of production and reserves involve quantitative modeling and numerical simulations. Therefore, it is critical to develop a methodology to predict damage zones and a workflow by which fault damage zones can be numerically incorporated into flow simulators.

In order to develop such a methodology, I adopt a three-pronged approach. First, I aim to identify and characterize damage zones associated with second-order reservoir scale faults located at reservoir depths using field data (borehole image logs and other geophysical logs). Damage zone attributes characterized include the width of damage zones (spatial extent of damage zones around the faults), the peak fracture density and the spatial variability of fracture density inside damage zones. Second, I model damage zones using principles of dynamic rupture propagation incorporating extremely rate weakening friction and off-fault plasticity. The modeled damage zone attributes are compared with those identified from field observations. Finally, I use damage zone attributes identified from field observations and dynamic rupture simulations to generate a discrete fracture network model of a part of the reservoir that includes both, the background fractures and damage zones associated with second-order reservoir-scale faults. This part of the research essentially presents a technique for modeling permeability heterogeneity and anisotropy introduced by the fracture population and damage zones associated with faults. Flow simulations are then performed to predict flow through the portion of reservoir under consideration.

The main contributions of this research are:

1. Observation and characterization of damage zones associated with second-order faults at reservoir depths using field data;

2. Prediction of fault damage zones using dynamic rupture propagation models;

3. Generation of a discrete fracture network reservoir model incorporating fault damage zones;

4. Modeling fluid flow through the upscaled reservoir fracture model.

In addition, I devote one chapter to modeling the effect of co-seismic slip across small natural fractures and faults during hydraulic fracture operations. The objective of this part of the research is to investigate if the effect of co-seismic slip across natural fractures on the surrounding rock matrix is substantial enough to warrant the steep increase in production witnessed post hydraulic fracturing.

1.2 Motivation

A substantial amount of global oil and gas reserves are trapped in fractured reservoirs. Several low matrix permeability reservoirs (like those in carbonates and basement rocks) almost completely rely on natural fractures for production. The projected production from unconventional, fractured reservoirs is expected to cap 20 MMBO/day (million barrels of oil per day) and contribute 17% of global daily production by year 2030. An equal or larger contribution is foreseen for gas, especially with the advent of new technologies that are making production from unconventional systems such as tight gas reservoirs and shale-gas plays increasingly economical. Despite the extensive resource, production from these reservoirs is inhibited by our inability to predict the location, orientation and flow properties of fractures in the reservoir. As such, recovery rates from such reservoirs are significantly low (~5-25%). Poor understanding of the reservoir fracture characteristics also present difficulties in estimating reserves and production performance. A weak handle on fracture characteristics also makes it more difficult to manage water production during recovery operations. A report by Produced Water Management, Asia claims that approximately 90 % of the water produced during oil and gas production comes from fractured reservoirs. Since this water is usually contaminated with oil and heavy metals, it must either be recycled or treated prior to discharge overboard. Cost of handling this water is ~ $30 -$40 billion/year. Other problems associated with production from fractured reservoirs include steep reservoir pressure decline, well underperformance etc. Most of these problems are associated with permeability heterogeneity and anisotropy introduced by a spatially variable fracture distribution inside reservoirs. Therefore, any improvement in geomodeling technology that assists in characterizing the fracture distribution and fracture flow properties can help address the above mentioned problems. Improved recovery rates can have a significant impact on the world's oil and gas supplies. Moreover, such methods also find application in the development of geothermal reservoirs that are usually dominated by fracture systems for

extracting heat geothermal energy from the earth. Further, safe sequestration of CO_2 during CO_2 sequestration operations relies heavily on the sealing properties of the cap rock. Since natural fractures provide an escape route for the sequestered CO_2, it is critical that the natural fracture system is thoroughly characterized before injection to minimize the possibility of leakage. As part of this effort of characterizing sub-surface natural fracture systems, I present a methodology for predicting fault damage zones (which are regions around faults of anomalously large fracture density) and incorporating them in generating more geologically informed reservoir models to constrain fluid flow modeling and production in the CPE gas fiel.

1.3 Thesis outline

This dissertation covers three main topics: damage zone observations from field data, modeling fault damage zones and incorporating damage zones in building a reservoir model to simulate fluid flow. In addition, there is also a section on modeling the effect of co-seismic slip across natural fractures on the matrix surrounding the fracture during hydraulic fracture operations to assess if this co-seismic slip creates the extra permeability manifested in the form of increased flow rates post hydraulic fracturing operations.

Chapter 2 - A Scaling Law to Characterize Fault Damage Zones at Reservoir Depths: Observations from the CPE Gas Field and SAFOD, Parkfield, California

Chapter 2 discusses sub-surface fault damage zones associated with second-order faults that are identified in image logs. There are several studies of exposed damage zones, but we concentrate on damage zones located at reservoir depths. Damage zones are studied in two different regions, the arkosic section adjacent the San Andreas Fault and the CPE gas field. Sub-seismic resolution, second-order faults are identified by changes in bedding plane orientations seen in image logs. A statistical correction is applied to the fracture population (obtained from image log analysis) to correct for the sampling bias that is introduced due to the inability of the borehole to intersect fractures sub-parallel to the borehole. Damage zones around the second-order faults identified are then analyzed to obtain damage zone attributes such as the width of damage zones, fault constant (fracture density at unit distance from the fault) and trends of spatial variation in fracture density inside damage zones.

Chapter 3 – Predicting Fault Damage Zones by Modeling Dynamic Rupture Propagation and Comparisons with Field Observations

Chapter 3 discusses a methodology for modeling damage zones around second-order faults using dynamic rupture propagation models. Damage zones are probably a result of a combination of quasi-static processes over geologic time scales and dynamic slip over co-seismic time scales. This study assumes formation of damage zones only due to dynamic slip across faults during earthquakes. The model assumes extremely rate weakening friction law and off-fault Drucker-Prager plasticity. Specifically, damage zones are modeled around the second-order thrust faults present in the CPE gas field. As the slip pulse propagates on the fault plane, stress perturbations around the propagating rupture tip lead to the formation of plastic strains if the stresses exceed yield stresses. Since fault damage zones represent a cumulative effect of several slip events over geologic time scales, we consider the effect of numerous slip events of various magnitudes (scaling between the event magnitude and frequency being consistent with the Gutenberg Richter scaling law) by superimposing the plastic strain field created due to each individual event. The strain field produced by the slip event is converted into a fracture population by assuming that the volume created due to dilatant plastic strains is manifested completely in the form of fractures. Due to uncertainties involved with regards to fracture dimensions and number of slip events that the fault has hosted, the model is calibrated using a fault constant value (which is either obtained from image log analysis or from a scaling relationship between fault constant and fault displacement). The damage zones obtained following the above workflow are analyzed to obtain damage zone attributes. Spatial heterogeneity of damage zones is analyzed by studying their width, fault constant (fracture density 1 m from the fault) and decay of fracture density with distance from the fault along several transects across the fault. Finally, I compare the modeled damage zone attributes with those identified from observations (chapter 2).

Chapter 4 – Modeling Fluid Flow through Damage Zones – A Case Study from the CPE Gas Field.

Chapter 4 discusses a methodology for incorporating damage zones into reservoir models and flow simulations that show the effect of damage zones on fluid flow and production. The reservoir model is generated using information derived from damage zones observations (in

chapter 2) and those modeled (in chapter 3) in the form of a discrete fracture network (DFN). The DFN comprises of both the background fracture population and damage zones. Background fractures are stochastically generated using fracture density and orientation information derived from image logs while damage zone fractures are deterministically introduced using damage zone modeling results (chapter 3). Flow properties such as effective aperture and permeability are then assigned to the fracture population. Well test simulations are performed to calibrate the permeability of large-scale fractures. The DFN model is then upscaled to obtain the effective porosity and permeability tensor in the grid blocks. Finally, flow simulations are performed on the upscaled grid to show the signature of damage zones on pressure drawdown during production.

Chapter 5 – Slip-induced Damage around Small Natural Fractures and Faults during Hydraulic Stimulation Opearions

Chapter 5 discusses the effect of coseismic slip across natural fractures on the surrounding matrix during hydraulic fracture operations in gas shale reservoirs. As the hydraulic fracture penetrates into the formation, water seeps into the surrounding natural fractures and increases the pore pressure. This decreases the effective normal stress on the fracture and causes co-seismic slip (of ~10s of microns) leading to a low magnitude event. Such low magnitude events are manifested in the form of microseismicity. Slip across small fractures is modeled using dynamic rupture propagation models. This modeling is similar to that performed in chapter 3, but on a smaller scale. The objective is to investigate if such these small magnitude slip events (~ -2 to -3) are a dominant deformation mechanism that stimulated the reservoir.

1.4 References

Hennings, P., Allwardt, P., Paul, P., Zahm, C., Reid, R., Alley, H., Kirschner, R., et al. (2012). Relationship between fractures, fault zones, stress, and reservoir productivity in the Suban gas field, Sumatra, Indonesia. *AAPG Bulletin*, *96*(4), 753-772. doi:10.1306/08161109084

Neretnieks I., T. Eriksen, and P. Tahtinen. 1982. Traces movement in a single fissure ingranitic rock: some experimental results and their interpretation. *Water Resources Research*, 18(4): 849-58

Neretnieks I. 1993. Solute transport in fracture rock – Applications to radionuclide waste repositories. Flow and contaminant transport in fractured rock. San Diego: Academic Press Inc., 39-127

Paul, P., Zoback, M., & Hennings, P. (2009). Fluid Flow in a Fractured Reservoir Using a Geomechanically Constrained Fault-Zone-Damage Model for Reservoir Simulation. *SPE Reservoir Evaluation & Engineering*, *12*(4). doi:10.2118/110542-PA

Chapter 2

A SCALING LAW TO CHARACTERIZE FAULT DAMAGE ZONES AT RESERVOIR DEPTHS: OBSERVATIONS FROM CPE GAS FIELD AND SAFOD, PARKFIELD, CALIFORNIA

2.1 Abstract

In this study, we analyze sub-surface damage zones found in two distinct geologic environments – damage zones adjacent to faults in granitic rock in the CPE gas field and damage zones adjacent to faults in arkosic sandstones and conglomerates near the San Andreas Fault in central California. Despite the geologic differences of the two study areas, damage zones in both are similar in terms of damage zone width, peak fracture/fault density and the rate of fracture/fault density decay with distance from the main fault. In this study, we consider macroscopic scale fractures observed in electric image logs. Seismic images from the CPE gas field show a large basement master fault associated with twenty-seven seismically-resolvable second-order faults. A maximum of five to six fractures/faults per meter are seen in four wells in 50-80m wide damage zones of the ‘second-order’ faults. Damage zones associated with similar

second-order faults immediately southwest of the San Andreas Fault were analyzed in the SAFOD research borehole. These damage zones are also typically 50-80 meters wide with the peak fracture/fault density ranging from 2.5-6 fractures per meter. The density of the fractures and faults in damage zones observed in both the areas of study is found to decrease with distance according to a power law $F = F_0 r^{-n}$. Fault constant F_0 is the fracture density at unit distance (1 meter) from the fault. It ranges from 10-30 fractures/m in damage zones in the CPE gas field, and from 6-17 fractures/m in damage zones in the arkosic section. The decay rate *n* ranges from 0.68-1.06 in the damage zones in the CPE gas field, and from 0.4-0.75 in the damage zones in the arkosic section. Wells drilled through damage zones in the CPE gas field are significantly more productive than those that do not intercept damage zones; therefore we characterize these damage zones at reservoir depths and quantify damage zone attributes so that they can conveniently be incorporated in reservoir models for modeling flow and production.

2.2 Introduction and Motivation

Field observations of relatively large-scale faults and damage zones frequently show a fault core surrounded by damaged rock. The fault core, where most of the displacement is accommodated, occurs as a narrow, localized slip zone containing high strain products (Figure 2.1) such as breccias, cataclasites and gouge (Aydin, 1978; Caine et al., 1996; Chester et al., 1993). Damage zones which are mechanically related to the growth of the fault zone show a network of subsidiary structures surrounding the fault cores (Chester and Logan, 1986; Smith et al., 1990; Scholz and Anders, 1994; Goddard and Evans, 1995). These fault-related subsidiary structures in damage zones include smaller faults, fractures, veins, cleavage and folds. Wide damage zones may represent multiple fault slip events and the over printing of successive stages of deformation (Caine et al., 1996). The damage zones are, in turn, surrounded by relatively undeformed host rock devoid of any faulting-associated features. Understanding the components of fault structure is critical to understanding the mechanical, seismological and fluid flow properties of the fault system.

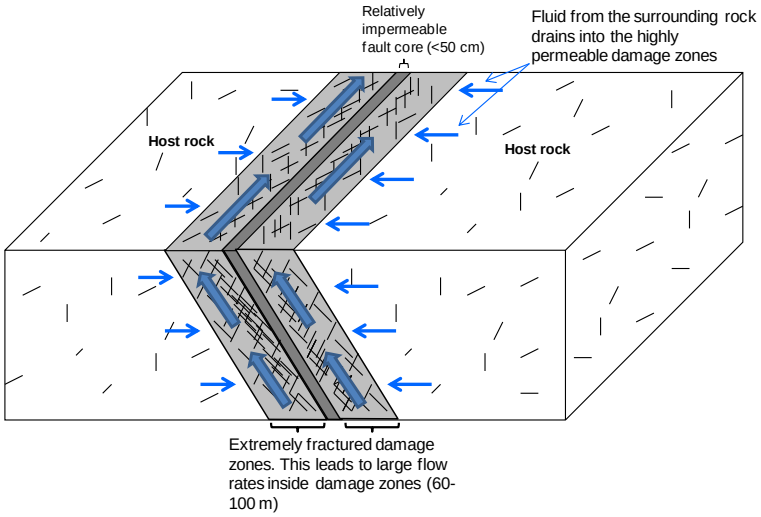

Figure 2.1: A schematic of a fault zone showing the relatively impermeable fault core surrounded by the highly fractured damage zone. In a fractured, low matrix permeability reservoir, fluid from the fractures in the surrounding rock mass drains into the highly permeable damage zones where large flow rates can be maintained when a reservoir is produced from damage zones.

Fault cores and damage zones are distinct hydrogeological units that reflect the material properties and deformation conditions within a fault zone (Caine et al., 1996). Typically, the fault core, which is composed of high strain products, has low permeability and porosity and acts as a barrier to fluid flow. However, damage zone permeability is high (Lockner et al., 1999) and produces bulk permeability anisotropy by increasing the permeability along the fault plane and enhances fluid flow (Paul et al., 2009). Lockner et al. (1999) and Wibberley and Shimamoto (2002) report experimentally measured permeabilities of samples obtained from the Nojima fault zone and the Median Tectonic Line (MTL) respectively. The permeability of core samples from the damage zone is several orders higher than that of samples taken from the fault core. Besides, their experiments also show that the permeability decreases with distance from the fault core. This is suggestive of decreasing microfractures density (assuming microfractures present in cores and created due to slip on the fault enhance permeability) with distance from the fault core. Although these results are more representative of the microfracture characteristics and their spatial heterogeneity inside the damage zones, we would expect a similar observation for macrofractures. In fact, the impact of macrofractures in the damage zones would be more dramatic assuming their large-scale impact on the bulk flow properties. Since the degree of brittle deformation is significantly larger in the fault core (Chester et al., 1993; Andersson et al., 1991), the low fault core permeability is governed by grain scale (or smaller) matrix deformation

of the fault rock (lowered further by clay gouge development) while the damage zone permeability is governed by the hydraulic properties of a larger scale fracture network. The relative importance of fractures in controlling rock hydraulic properties depends on the fracture density and orientation, along with the hydraulic and mechanical characteristics of fractures themselves. However, the primary difficulty in predicting or modeling the movement of hydrocarbons through damage zones arises because the permeability enhancement varies significantly as a function of distance from the fault core as a result of the change in fracture density with distance. Therefore, understanding the spatial variability of fracture density inside damage zones is one of the key aspects in evaluating their impact on flow.

Several studies have documented the influence of damage zones on hydrocarbon production. Paul et al. (2009) studied a gas field in the Timor Sea where it was only possible to explain large gas production rates by introducing spatially variable permeability anisotropy representative of damage zones adjacent to faults in the reservoir. Hennings et al. (2012) carried out a study of the Suban gas field (a fractured gas reservoir with very low matrix permeability) in SE Asia where wells that intersect damage zones, especially those with a large population of critically-stressed fractures are most productive. In their study, two wells with trajectories designed to intersect the most number of fractures and faults in the damage zones of larger faults showed an increase in productivity by factors of 3 and 7 compared to wells not designed to intersect damage zones.

The occurrence of permeable fractures and faults in damage zones are usually not incorporated into reservoir simulation models because the quantitative understanding of damage zones is poor. There is uncertainty regarding the spatial location, clustering, size, geometry, and flow properties of the fractures and faults in damage zones making it difficult to model fluid flow and predict their effect on reservoir performance.

Paul et al. (2009) modeled the impact on damage zones on fluid flow by characterizing damage zones and incorporating them in fluid simulation models. In terms of fluid flow, damage zones create spatial permeability anisotropy due to increased flow paths (greater fracture density) and preferential flow directions (along the fracture plane). In a fractured, low matrix permeability reservoir, fluid drains from the fractures present in the surrounding rock mass into

the highly permeable damage zones where large flow rates can be maintained when the well perforation interval lies within the damage zone (Figure 2.1). Flow simulation models incorporating damage zones are usually generated by assigning effective permeability tensors to reservoir grid blocks that feature fractures and damage zones. The permeability tensor of each grid block depends on the characteristics of fractures inside the grid block, such as fracture density, orientation and fracture permeability. The outstanding question, therefore, is how can we estimate the spatial extent and heterogeneity of permeability anisotropy at reservoir scale using the available subsurface data? This issue can be addressed by studying properties of damage zones such as the spatial extent of damage zones and variation of fracture density with distance from the fault surface in damage zones using subsurface data such as image logs. Paul et al. (2009) adopted this methodology to study the decay of fracture density inside damage zones. However, since all the wells in that study were outside the fault damage zones, they had to guess these damage zone characteristics and their spatial variability (of fracture density with distance from the fault).

The importance of damage zones motivates the need to develop a better understanding of damage zone attributes such as damage zone width and density, and the distribution and orientation of fractures within it. These attributes are functions of a wide range of factors such as slip across the fault, size of the fault (Mitchell and Faulkner, 2009), lithology, rupture processes, movement history (Caine et al., 1996) etc. Various outcrop studies in the past have shown that fracture density decreases with distance from a fault inside damage zones (Savage and Brodsky, 2011; Vermilye and Scholz, 1998; Mitchell and Faulkner, 2009). Savage and Brodsky (2011) have suggested that the fracture density decays with distance from isolated faults according to a power law $F = F_0 r^{-n}$ where F_0 is the fault constant (the fracture density at 1 meter distance from the fault), r is the distance from the fault and *n* is an exponent describing the decay (Figure 2.2 a). Using various published fracture density profiles, they find the decay rate (*n*) is ~0.8 for smaller faults (with slip less than ~100 m), and ~0.4 for larger faults with slip larger than 100 m. They also report that the fault constant F_0 is fault specific and seems to depend on lithology and fault displacement. However, an alternate study by Mitchell and Faulkner (2009) suggests that this fracture density at unit distance is constant and independent of the size of the fault (~100 fractures/m) and represents a critical level of fracturing before fracture damage is so intense that brecciation and cataclysis begin. Previous studies have also reported that fracture density decay

can be expressed by exponential and logarithmic laws (Chester et al., 2005; Faulkner et al, 2008). However, power law decay with distance seems more reasonable since stress perturbations decay with the inverse of distance from a propagating crack tip during dynamic rupture propagation that eventually leads to damage (Freund, 1976). Savage and Brodsky (2011) also compiled data from several published studies and reported that the fault zone width scales with fault displacement up to a threshold value of approximately 150 meters, beyond which the scaling breaks down and the fault zone width stabilizes at approximately 150-200 meters (Figure 2.2b).

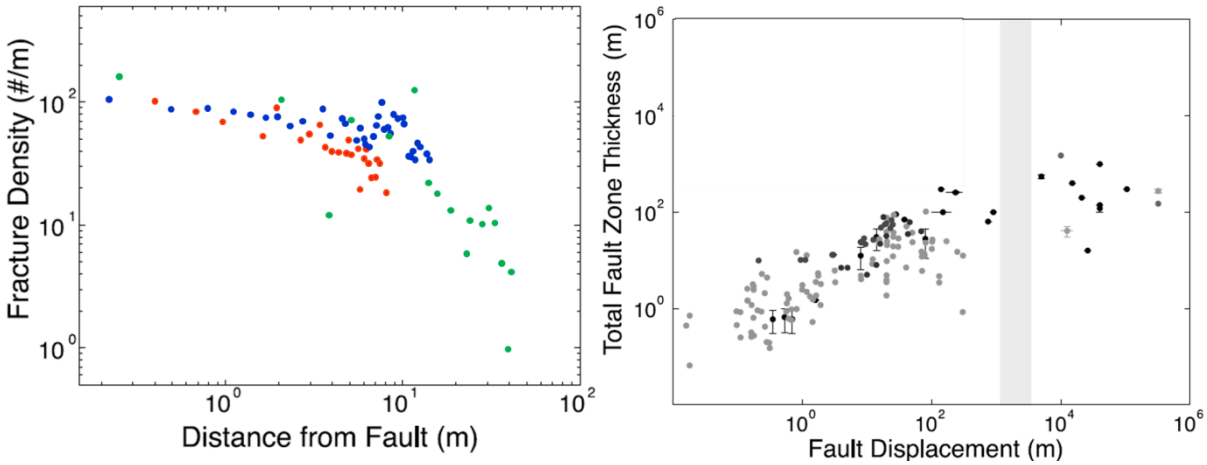

(a) (b)

Figure 2.2: (a) Decay of fracture density with distance from the main fault. The colors represent three transects along which damage zones around the Punchbowl fault are studied. Although there is considerable scatter, the decay of fracture density with distance from the fault seems to follow a power law or varying decay rates. (b) Thickness of the fault zone seems to scale with fault displacement up to a displacement of ~150 meters, after which it saturates. (modified from Savage and Brodsky, 2011).

The previously published studies of damage zones are principally outcrop studies. Thus, there is an absence of subsurface data characterizing damage zones at depth. The presence and attributes of damage zones at depth can be studied with the help of image logs, and sonic, resistivity and porosity logs which show changes in physical properties due to the presence of fractures. Such attributes directly affect fluid flow through damage zones and hence are of much interest for efficiently modeling fluid flow through damage zones and fractured reservoirs.

In this study, sub-surface damage zones associated with what we term second-order faults at depth are characterized using fault and fracture information derived from image logs, and then compared with those reported from outcrop studies. Only the macroscopic scale fractures visible

in the image logs are considered. For reference, the very large faults such as the San Andreas Fault are refered to as first-order faults, the relatively smaller faults (which are usually seismically resolvable) as second-order faults and the subsidiary fractures and faults seen in image logs as third-order faults. The first-order faults are associated with well-developed fault systems with complex and mature damage zones, and several generations of splaying faults and fault core strands formed by over printing of successive stages of slip and deformation. In the case of mature first order faults, a fault core may occur as a wider zone containing multiple strands of fault cores (Faulkner et al., 2003; Faulkner et al., 2008; Mitchell and Faulkner, 2009; Zoback et al., 2011). Second-order faults represent relatively isolated faults with small slips having relatively simpler damage zones with less overprinting due to successive stages of deformation, and perhaps without as many generations of splaying faults. In this work, we specifically investigate damage zones associated with these second-order faults. Observations from two different regions are reported. The first area of study is the faulted CPE gas field where damage zones encountered in 5 wells drilled in the reservoir are characterized. Following Hennings et al. (2012), optimal drilling orientations for superior well performance are discussed. Then we discuss damage zones associated with second-order faults embedded in the well-cemented arkosic sandstone section adjacent to the San Andreas Fault in central California. These sub-surface damage zones are then compared with those identified in outcrop studies in terms of damage zone widths, fracture density inside damage zones and the decay-rate of fracture density with distance from the fault. In the next chapter, damage zone attributes observed are compared with those modeled theoretically using dynamic rupture propagation models. In that study, it is shown that damage zones evolve with multiple episodes of dynamic slip over time.

2.3 Damage Zones associated with Faults in the CPE Gas Field

2.3.1 Location and background

The CPE gas field produces wet gas principally from compressionally-uplifted, fractured, crystalline and metamorphic basement rocks and overlying clastic and reefal carbonate rocks. Figure 2.3 presents a perspective view of the field showing the master fault, seismically-mappable second order faults and well trajectories. All second order faults have a reverse

separation. They strike sub-parallel to the master fault and are concentrated in a 1x8 km area along the crest of the anticline. The region of interest is in the hanging-wall of a large master thrust fault which is characterized by a strike slip stress regime.

Figure 2.3 shows the 5 wells studied here, A, B, C, E, and I. Wells A, E, and I are near vertical wells while wells B and C are deviated wells. Well tests were performed after drilling the vertical wells (A, E and I). These tests suggested that there is poor correlation between wellbore-reservoir contact length and well performance. In fact there is also a very weak correlation between well performance (AOF) and the total number of fractures that they intersect. However, there is a strong correlation between the total number of critically stressed fractures transected by the wellbore and well performance (pc, ConocoPhillips).

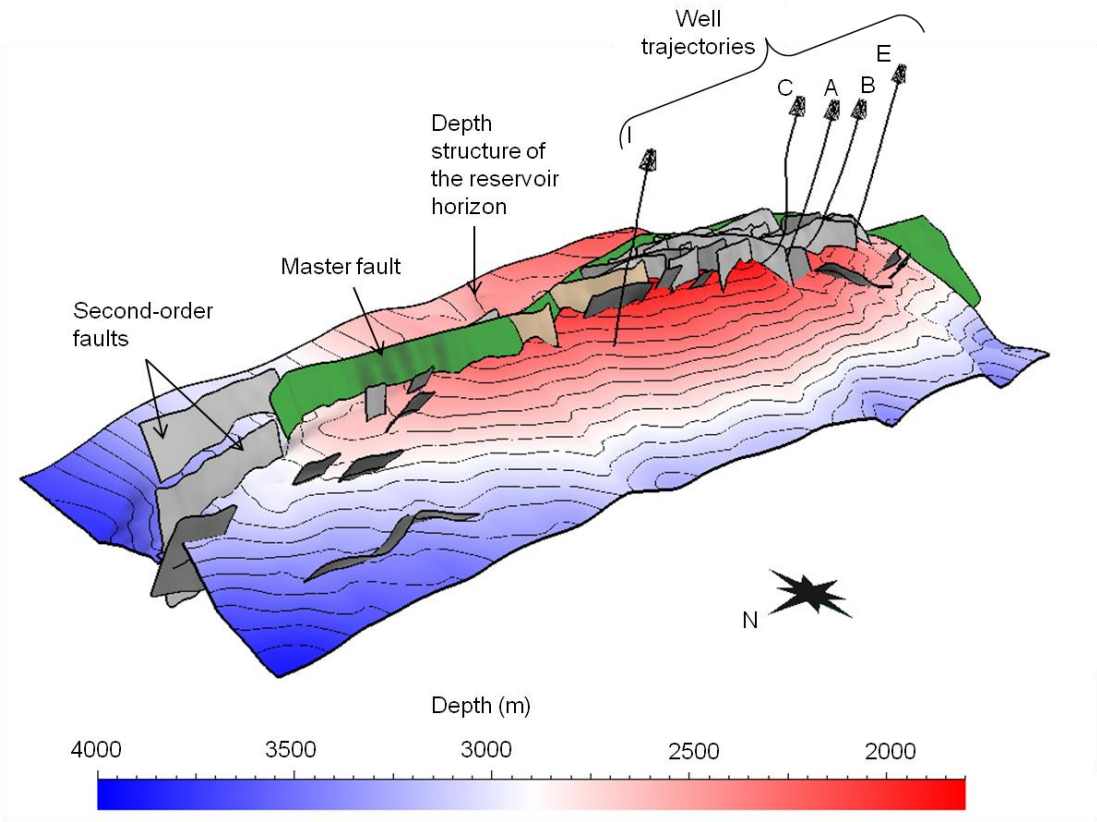

Figure 2.3: Three dimensional structural model of CPE gas field. The model shows the master fault (first order fault), second order faults, well bore trajectories and the depth structure of the reservoir horizon.

According to the critically stressed fault hypothesis, fractures or faults that are mechanically alive are hydraulically alive and those that are mechanically dead are hydraulically dead (Barton et al., 1995; Zoback, 2007). This means that faults with a ratio of resolved shear to

normal traction is greater than the coefficient of sliding friction (normally 0.6 (Byerlee, 1978)) would be mechanically active and slip. This slip leads to dilatancy and brecciation which in turn imparts enhanced permeability to the fracture. However, it is important to note that while the critically-stressed-fault hypothesis may help us identify which fractures and faults are likely to be permeable, other geologic factors, such as degree of alteration and cementation of the brecciated rock within the fracture and its diagenetic history (Fisher and Knipe, 1998; Fisher et al., 2003), determine the actual permeability.

Characterization of fractures identified in image logs reveals that critically stressed fractures are steeply dipping. Since there is strong evidence that well performance correlates strongly with the number of critically stressed fractures that the well intersects, two wells, B and C were planned to intersect a large number of critically stressed fractures by deviating them through the damage zones of the second-order faults (Figure 2.3). Coursing the well through fault damage zones increases the fracture population that the well intersects while deviating them increases the probability of wells intersecting a larger population of steeply dipping critically stressed fractures. Wells B and C are extremely productive, with production rates as large as 1 bcf/day while the other vertical wells produce between 0.1 and 0.3 bcf/day.

2.3.2 Characterization of damage zones identified along boreholes

Figure 2.4 shows the histograms of fractures identified in wells A, E, I and B as a function of measured depth along the well path. The red color represents all fractures while the blue color represents critically stressed fractures. Relevant calculations for identifying the critically stressed fractures are provided in Appendix 2E.

The depth intervals over which the wells run through carbonate and granitic rock are also illustrated in the plots. The green lines indicate the presence of seismically resolvable faults that the borehole intersects (shown in Figure 2.3) while the small black arrows represent the boundaries between various structural blocks which we identified by abrupt changes in bedding plane orientations. We interpret these as representing sub-seismic second order faults surrounded by their damage zones. Dotted blue arrows represent faults inferred from concentrations of faults in the image logs, but for which there is no other evidence since the lithology at most of these depths is granite which does not host bedding planes. In these cases, there is high fracture density

that decays sharply with distance on either side. The peak fracture density and peak critically-stressed fracture density in most damage zones identified in these wells is approximately 1.5-3 fractures per meter and 0.25-0.5 fractures per meter, respectively. Many apparent damage zones seem to overlap making it difficult to identify their width. However, most damage zones appear to be approximately 50-80 m wide. Fracture density is larger in the deviated well (well B) as compared to the vertical wells. Most of the wells do not intersect the seismically identified second order faults. Well A intersects only one of those faults (at 2490 m). However, we observe well-defined concentrations of faults and fractures that resemble damage zones in image logs around positions marked by arrows in Figure 2.4. Well E does not intersect any seismically-identified second-order faults, but it grazes one between, 2700 m and 3100 m. Thus, although it does not intersect the fault, it does sample the damage zone over an extended length. Several other well-defined damage zone-like features are seen around positions marked by dotted blue arrows in well E (Figure 2.4), but there is no direct evidence suggesting the presence of a fault. Well I is also not interpreted to intersect any second order fault, yet the fracture histogram reveals well-defined damage zones and fracture peaks around positions marked by dotted blue arrows (Figure 2.4), again suggesting the presence of seismically irresolvable faults. This well terminates very close to the master fault, which may be the reason for an elevated fracture density at the bottom of the well. Well B is one of the wells that was drilled with the intention of intersecting a large number of natural fractures and damage zones, and is also the well with the highest production. It intersects 3 seismically identified second order faults. While the regions where the well intersects the first two faults are marked by increase in fracture density, a high fracture density is not observed around the third fault as a result of poor data quality in an area of extremely large fracture density which prevents identification of individual fractures. Since well B also terminates close to the first-order master fault, there is elevated fracture density at the bottom of this well.

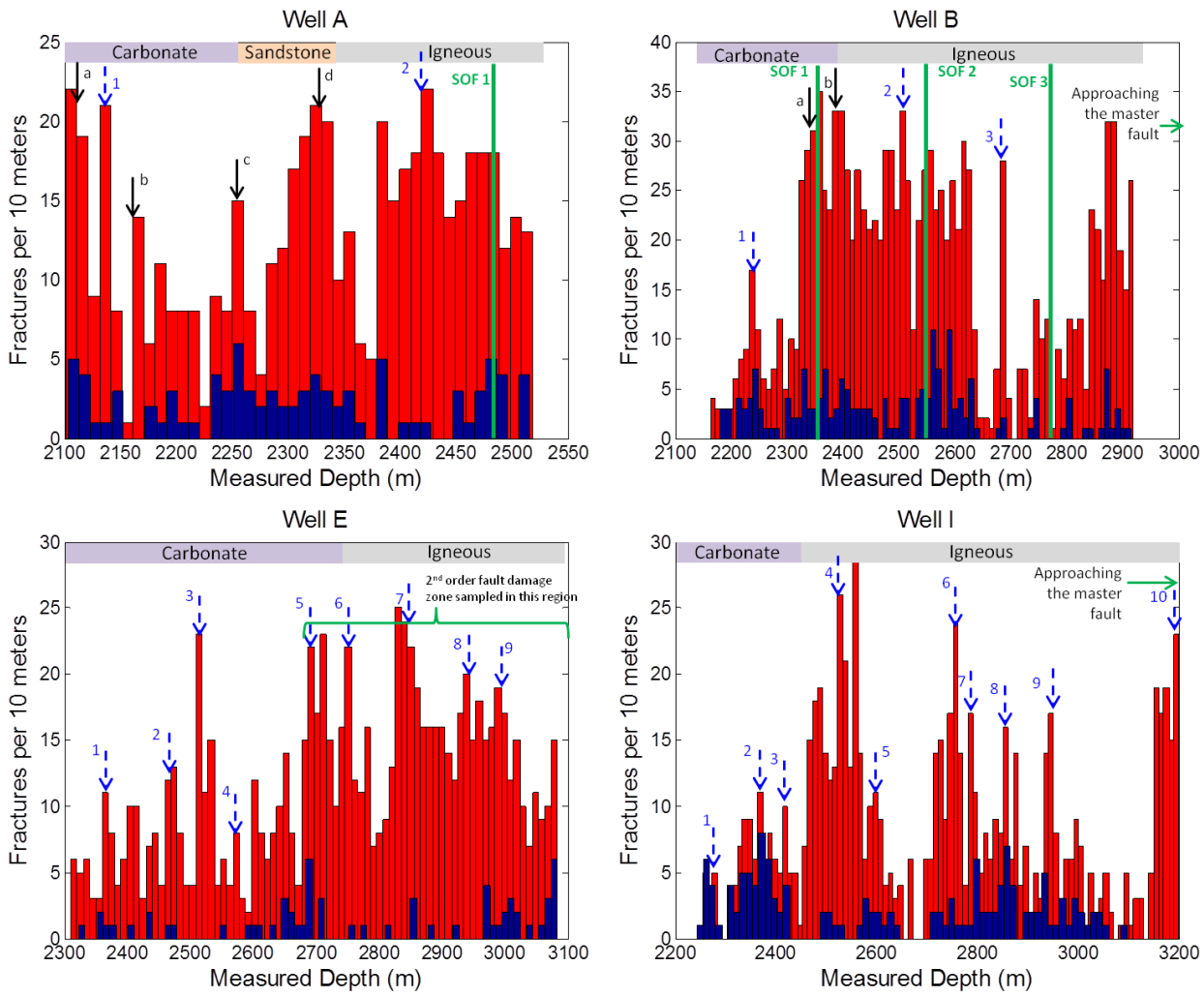

Figure 2.4: Histograms of natural fractures identified in wells A, E, I and B. The red color represents all the fractures while the blue color represents critically stressed fractures. Purple, orange and grey bars on the top on individual histograms represent the lithology (carbonates, sandstone or igneous rocks comprising granite, dacite and rhyolite). The green lines represent the seismically identified second order faults (SOFs), the solid black arrows represent the inferred location of sub-seismic second order faults inferred by changes in the orientation of bedding planes, while dotted blue arrows represent suspected faults for which there is no evidence but are surrounded by regions where the regional fracture population has a strong damage zone character.

2.3.3 Removal of sampling bias from the well fracture data

In order to characterize the number of sub-surface fractures and faults at depth using image logs, it is necessary to correct for the sampling bias resulting from the inability of the boreholes to sample fractures oriented sub-parallel to the boreholes. The statistical correction of fracture populations for fracture dip has been discussed by several authors (Terzaghi, 1965; Einstein and Baecher, 1983; Barton and Zoback, 1994). A discussion on removing sampling bias is provided in Appendix 2A. As wells A, E and I are vertical wells, they seriously under sample steeply

dipping fractures. Figure 2.5 shows two histograms of the dipping angles of the fracture population in well A before and after the correction is applied. As expected, there is a significant increase in the number of fractures dipping steeply after the correction is applied. For example, there are only four fractures dipping between 85º and 90º in the original fracture population. However, this number increases to 160 in the corrected fracture population. This clearly demonstrates that under-sampling of fractures sub-parallel to the well is an important concern and needs to be addressed in order to obtain a more appropriate and representative fracture characterization within the reservoirs.

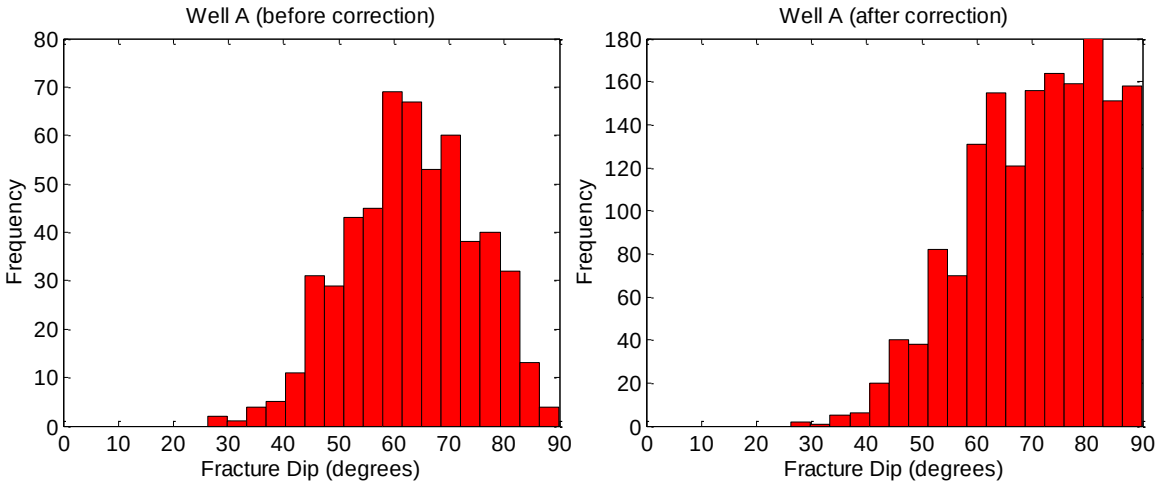

Figure 2.5: Histograms of fracture dips before and after the correction of sampling bias for well A.

Figure 2.6 shows the histograms of the corrected fracture population in various wells. There is a significant increase in the total and critically-stressed fracture population. The peak fracture density in most damage zones in wells A, E and I is approximately 5-6 fractures per meter where the original peak fracture intensities were approximately 2-3 fractures per meter. The percentage increase in the critically-stressed fracture population (from ~ 0.25-0.5 to 1-3 fractures per meter) is greater since the critically stressed fractures in a strike-slip stress regime are steeply dipping, the orientations which are most strongly biased against by the vertical wells. The peak critically stressed fracture density is approximately 1-2.5 fractures per meter in wells A, E and I. The peak fracture density in damage zones in well B increases from approximately 2.5-3.5 fractures per meter to approximately 6-7 fractures per meter. The difference in the fracture population between the vertical and deviated wells before the correction was significant; however, that difference is only modest after the correction is applied. This is expected since the

regional fracture population is likely to be consistent to first order. A table listing the number of fractures intersected by the wells before and after correcting for the sampling bias is provided in Appendix 2B.

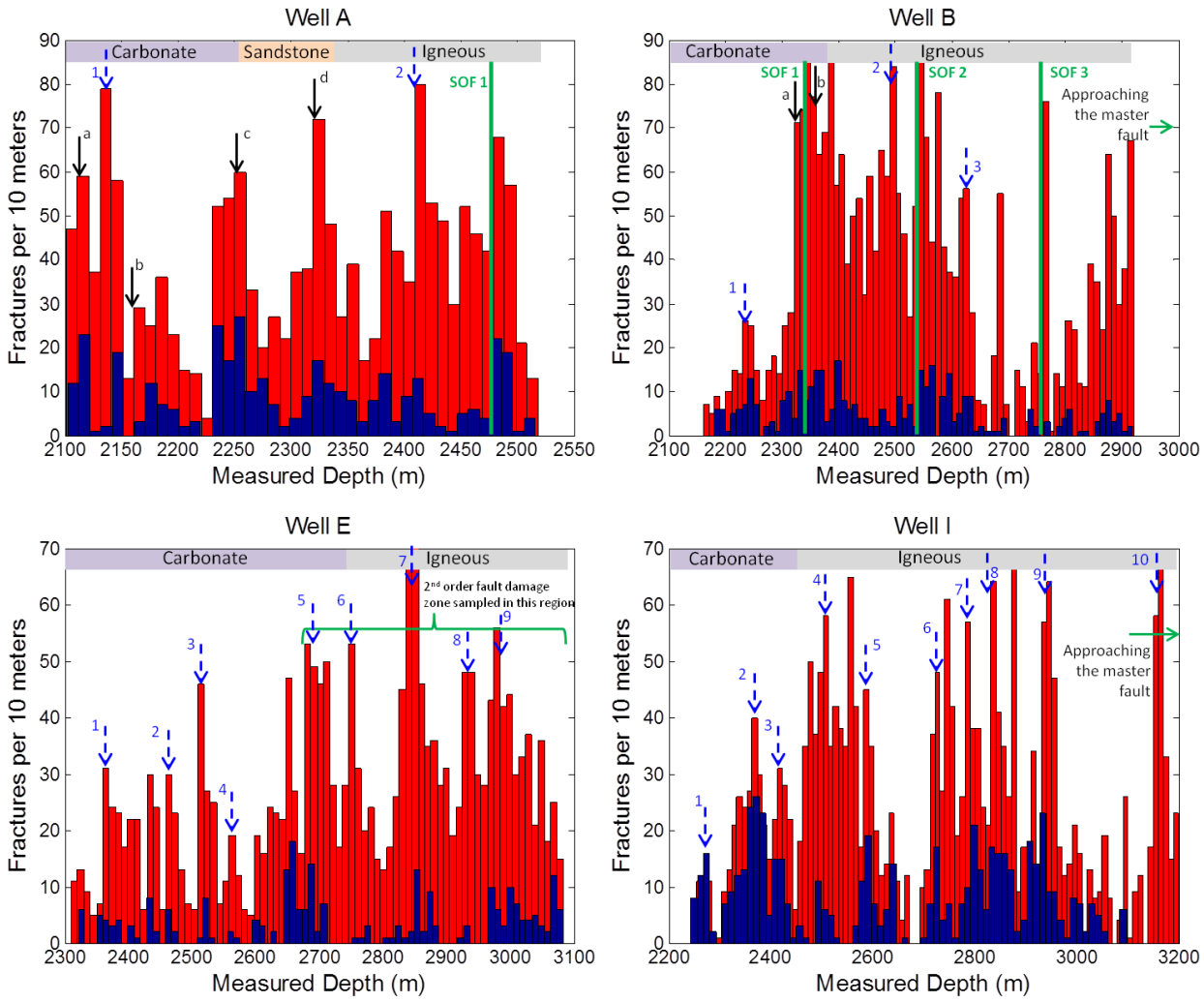

Figure 2.6: Same as Figure 2.4, but for a fracture population corrected for sampling bias.

The corrected fracture population represents the actual number of fractures that are expected to be present in the rock mass as opposed to the number observed in the image logs due to spatial sampling along a one-dimensional linear borehole. The purpose of this statistical correction is to extrapolate a three-dimensional perspective of the regional fracture population from one-dimensional data acquisition, and hence obtain a more meaningful fracture characterization of the reservoir. A well-constrained reservoir fracture characterization, along with knowledge of prominent fracture sets, locations of second-order faults, their damage-zone

characteristics and critically-stressed fracture orientations can help us design borehole trajectories which could exploit damage zones and the more productive critically-stressed fractures by orienting wells perpendicular to them, in the process sampling most of those fractures and hence optimizing production. As previously mentioned, it can also assist us in making more geologically informed reservoir models for simulating fluid flow, and hence predicting production rates and reservoir performance with greater accuracy.

2.4 Arkosic Section Adjacent to the San Andreas Fault, Parkfield, California

2.4.1 Location of the San Andreas Fault and SAFOD

The San Andreas Fault is a continental transform fault with a strike of approximately 810 miles along California. The motion of the fault is right-lateral strike-slip. It is the principal zone of deformation that accommodates relative motion between the Pacific and North American plates. The Pacific plate moves approximately 48 mm/year northwest with respect to the North American plate. The San Andreas Fault Observatory at Depth (SAFOD) is a scientific drilling project aimed at studying physical and chemical processes occurring within the San Andreas Fault at seismogenic depths. These processes are understood to control faulting and earthquake generation along the fault. SAFOD is located near Parkfield, California (Figure 2.7), almost mid-way between San Francisco and Los Angeles. It penetrates a section of the fault that moves due to a combination of aseismic creep and microseismic earthquakes. The slip rate at the vicinity of SAFOD is approximately only half that of the plate, the remainder of the plate location if accommodated by slip along other faults.

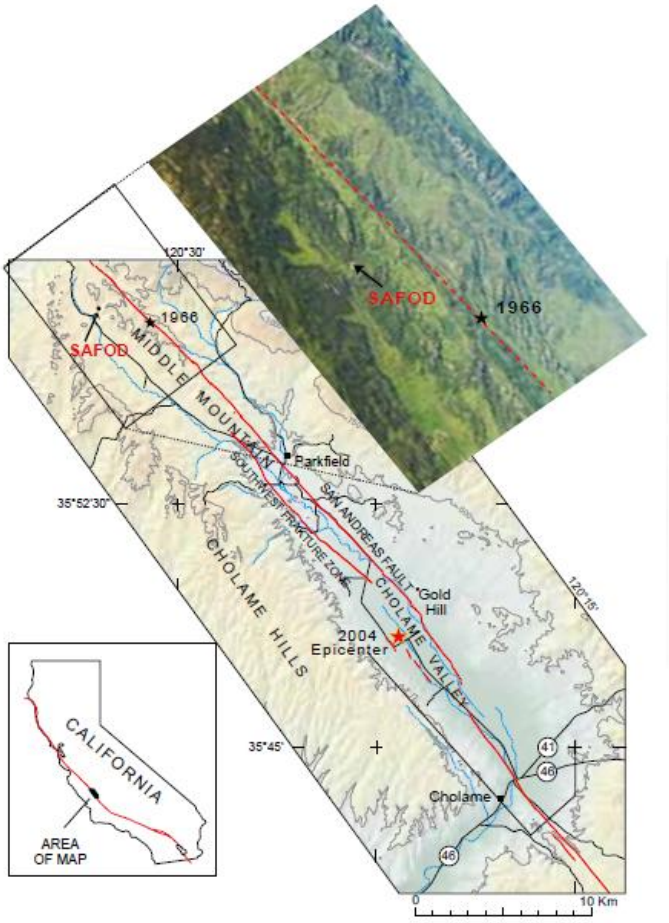

Figure 2.7: Map of the segment of the San Andreas Fault at Parkfield showing epicenters of the 1966 and 2004 Parkfield earthquakes and the SAFOD drillsite (Rymer et al., 2006). The air photo shows the terrain in the area of the SAFOD drill site and the epicenter of the 1966 Parkfield earthquake (Zoback et al., 2011).

2.4.2 Arkosic section adjacent the San Andreas Fault

A detailed study of damage zones that are encountered in well-cemented arkosic sandstones and conglomerates immediately southwest of the San Andreas Fault Zone at the SAFOD site (Figure 2.8) is performed. The previously unknown arkosic sandstones and conglomerates, with some interbedded shales (Boness and Zoback, 2006; Solum et al., 2007) are juxtaposed against granitic rocks of the Salinian block to the southwest and against fine-grained Great Valley Group and Jurassic Franciscan rocks to the northeast (Figure 2.8). These rocks are strongly cemented and their seismic velocities and resistivity are similar to the fractured Salinian granites and granodiorites from which they are likely derived. The Buzzard Canyon is sub-parallel to the San Andreas Fault (Rhymer et al., 2003; Thayer and Arrowsmith, 2005). In the main SAFOD borehole, it separates the granodiorite from the arkosic rocks (Bradbury et al.,

2007). This section of arkose is present from 1920 to 3157 m (measured depth) along the main hole drilled at SAFOD. The San Andreas Fault and the Buzzard Canyon Fault are the first-order faults in this region.

The arkosic section is divided into several structural blocks. Springer et al. (2009) have identified three main lithologic units within the arkosic section, which have further been subdivided into eleven structural domains based on bedding orientations determined from the analysis of the electric image log data. Our first objective is to constrain the position of second order faults which divide the arkosic section into several structural domains. This is achieved by identifying sudden changes in bedding-plane orientations observed in the image logs. The second objective is to study the damage zones associated with these second-order faults.

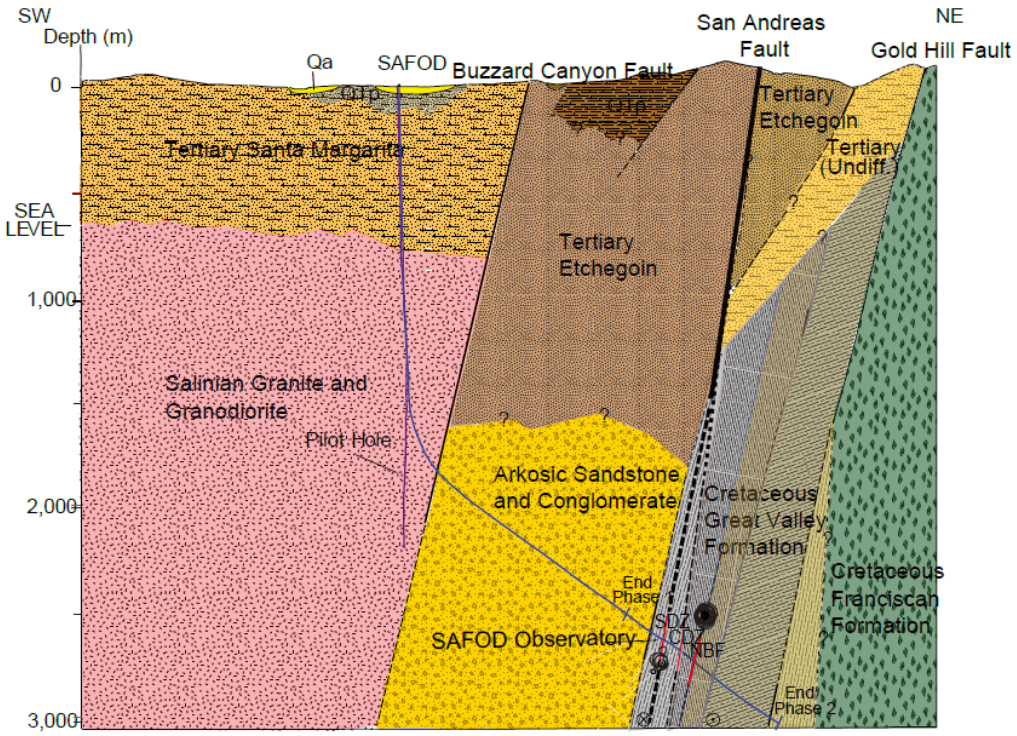

Figure 2.8: Simplified geologic cross-section parallel to the trajectory of the San Andreas Fault Observatory at Depth (SAFOD) borehole. The geologic units are constrained by surface mapping and the rock units encountered along both the main borehole and the pilot hole (Zoback et al., 2011)

Dynamically normalized electrical image logs were collected in the arkosic section. The software used to analyze these electrical image logs and identify third order features and bedding planes, and evaluate their orientations was GMI-Imager. A set of geophysical logs was also

collected at the SAFOD site during all phases of drilling. The logs used for this study are P wave velocity logs derived from sonic monopole velocity logs, dipole S wave velocity logs, resistivity logs and neutron porosity logs. These logs were used to observe the signature of damage zones since highly fractured depth intervals would have a low velocity, low resistivity and high porosity response. Fourteen blocks (referred to as blocks a - n) have been identified on the basis of changes in orientation of bedding planes (see Appendix 2C). I suspect that these blocks are separated by sub-seismic second order faults since many of these block boundaries have well defined damage zones around them marked by an increase in observed fracture density. Besides, several of these boundaries are marked by decrease in sonic velocities, resistivity and increase in porosity. Figure 2.9 shows P and S wave velocity, resistivity and gamma ray logs in the arkosic section. The geology encountered along the borehole is also shown. Blocks a - i make up the upper arkose as defined by Springer et al. (2009). These rocks are quartz and feldspar rich, and are relatively homogeneous. A clay rich region with a marked increase in gamma ray and porosity log and a decrease in sonic velocities (Boness and Zoback, 2006) extends from 2530 m to 2680 m measured along the borehole. Two blocks (j and k) are identified in this region. Blocks l, m, and n lie in the lower arkosic region (as defined by Springer et al. (2009)). The average porosity in this region is less than that in upper arkose. It is also seen that the amount of quartz in the lower arkose is less, and most of the quartz that is present is plastically deformed, which may be indicative of more faulting. Of the fourteen block boundaries we identified, nine are the same as those identified by Draper et al. (2009). The depths of bedding block interfaces identified by Draper Springer et al are 1920 m, 2145 m, 2225 m, 2250 m, 2290 m, 2530 m, 2565 m, 2680 m, 2880 m, 3010 m and 3157 m.

On the right of Figure 2.9 is the histogram of third order features identified in the arkosic section. The bars in the histogram represent the number of third order features identified every 10m. The orange horizontal lines represent the constrained positions of sub-seismic, second-order faults surrounded by their respective damage zones with anomalously high fracture density. These second-order faults are numbered 1-14, where fault number 1 separates block a from block b and so on. The widths of damage zones associated with the second-order faults are typically on the order of 50 to 80 meters. For reference, the damage zone associated with the San Andreas Fault is approximately 250m in width. The Buzzard Canyon Fault, the major, near-vertical fault striking sub-parallel to the San Andreas Fault at the western boundary of the

arkosic section has a damage zone about 120 m in width. The width of the damage zones of faults 1, 9, 12 and 14 is approximately 60-80 m. The damage zones of faults 12 and 13 seem to overlap each other. The peak fracture density around these faults is approximately 3-4 fractures per meter. The damage zones of faults 3-8 overlap each other. This may, perhaps, be a fault with multiple strands. The peak fracture density in their damage zone is approximately 2 fractures per meter. The damage zones around faults 2, 10 and 11 are fairly well defined, but they have a relatively lesser peak fracture density. Poor image quality (probably due to very intense damage) could be a reason. Damage zones around these faults are approximately 40-50 meters wide and their peak fracture density is approximately 1.5-2 fractures per meter. It is also seen that the density of third order features (fractures) decays rapidly with distance. Since damage zone widths and fracture density inside these damage zones scale with slip (Mitchell and Faulkner, 2009), faults 1, 9, 12, 13 and 14 may have greater slip as compared to the others.

The P and S wave velocities, as expected are usually low in the vicinity of most suspected second order faults (Figure 2.9). There is a marked decrease in velocities and resistivity around second order faults numbered 1 and 10. However, damage zone signatures around most of the other second-order faults on the geophysical logs are only subtle, marked by a subtle local decrease in velocities and resistivity. Fracture mineralization could be a possible reason. Sealed fractures would not reduce sonic velocities and increase neutron porosity significantly. Since sealed fractures are, perhaps, not active in the current stress regime, it would be interesting to investigate whether inactive and active damage zones (depending on whether or not the fractures in the damage zone are active or not in the present day stress field) have distinct seismic signatures on geophysical logs. However, this issue has not been addressed in the present study.

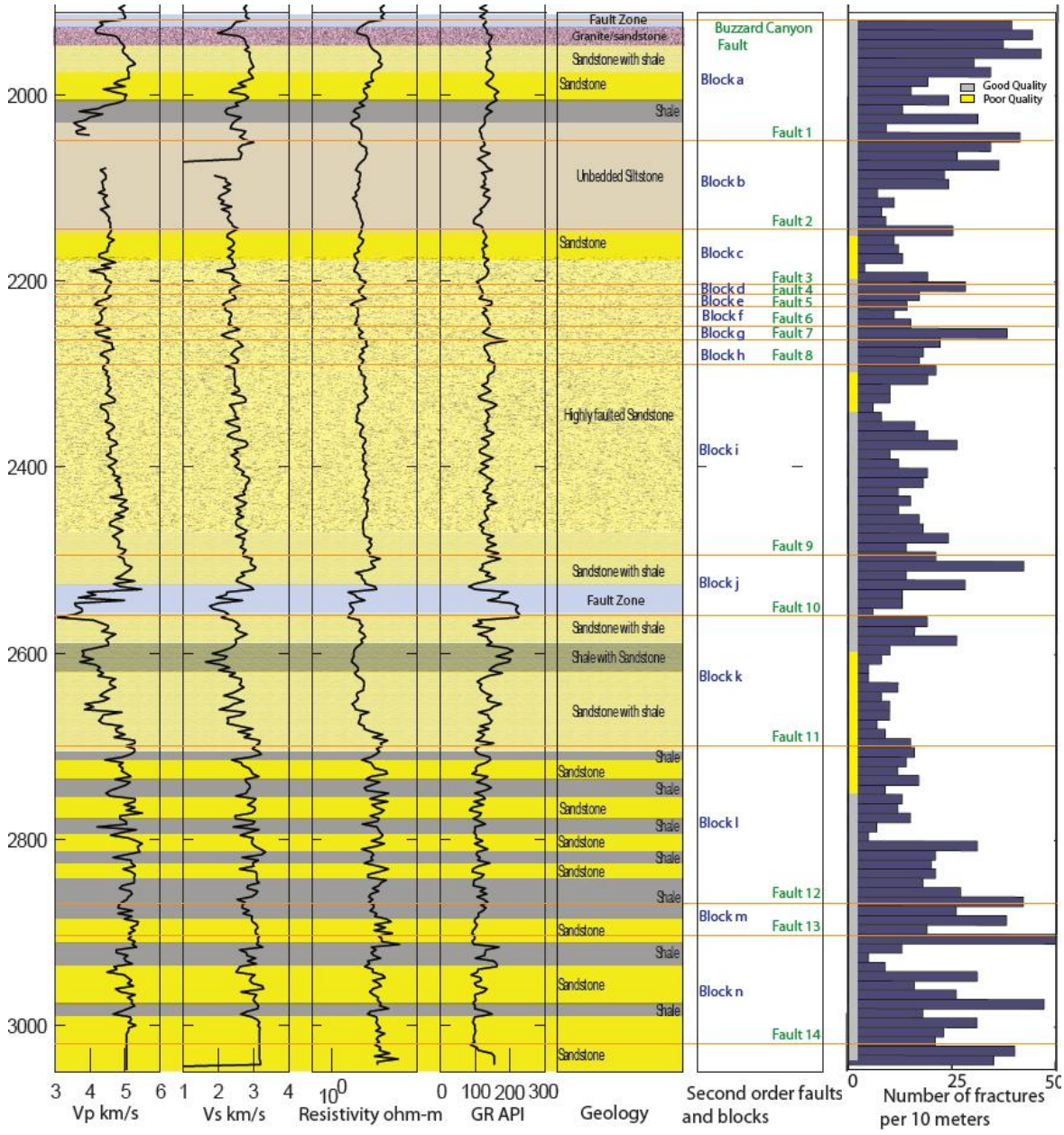

Figure 2.9: The figure above shows the P wave, S wave, resistivity and gamma ray logs and geology in the arkosic section encountered by the borehole at SAFOD. The histogram on the far right represents the third order features identified in the FMI logs. The orange horizontal lines (numbered 1-14) indicate the block boundaries that may represent second order, sub-seismic faults. Grey and yellow bars in the histogram represent good and poor quality of the image log. Well-developed damage zones (evidenced by the histogram peaks) around most of the block interfaces strengthens our conviction that these are second order faults.

2.4.3 Removal of sampling bias from well fracture data

A statistical correction to correct the fracture data for sampling bias is applied using the technique explained in the Appendix 2A. Figure 2.10 shows the histogram of the third order features before and after the third-order-feature population is corrected for a sampling bias.

The peak fracture density in damage zones after correcting for sampling bias is approximately 2.5-6 fractures per meter. The minimal increase in the fracture population could be due to two reasons. First, the fracture population oriented sub-parallel to the wellbore may actually be sparse. Second, the way the sampling-bias-removal algorithm works, it upscales the number of fractures with a certain orientation identified in the image logs by an upscaling factor. If there are no fractures identified within a certain orientation range, there will be no upscaling and increase in fracture population associated with that range of orientations (Figure 2A3). Fracture orientations sub-parallel to the well identified in the image logs are completely absent, hence the minimal increase in fracture population.

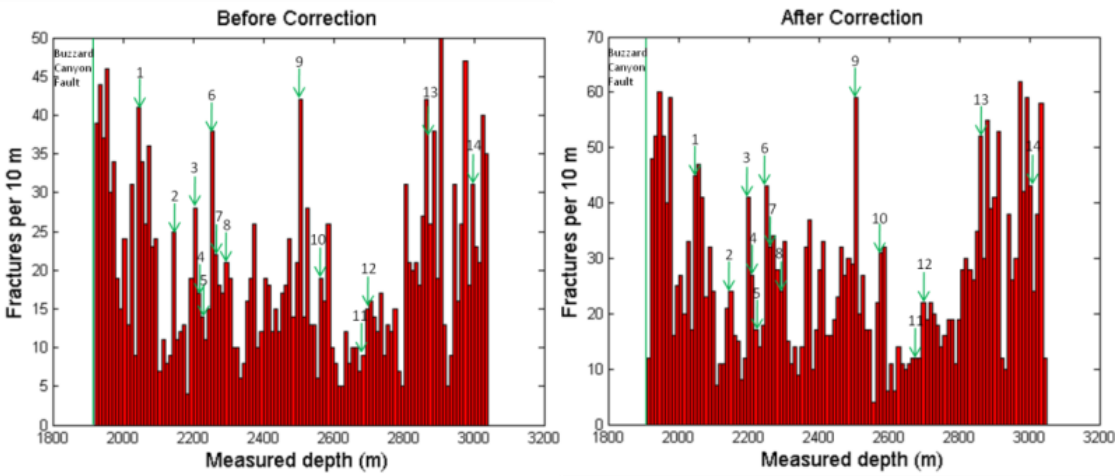

Figure 2.10: Histograms showing the third order features identified in the arkosic section before and after correction for removing the sampling bias is applied. The green arrows represent the inferred location of second order faults.

2.5 Variation of Fracture Density with Distance from Faults in Damage Zones

In this section, I investigate the trend of decreasing macrofracture density with distance from second-order faults (a trend that is observed in outcrop studies). However, there are certain inherent difficulties in performing this analysis using image logs. Firstly, the well in SAFOD and most wells in the CPE gas field do not intersect seismically resolvable or confirmed second-order faults. The presence of faults is inferred indirectly by changes in bedding planes. Secondly, the orientation of constrained second-order faults is unknown, so calculating the perpendicular distance of fractures from the second-order fault plane is difficult. Thirdly, most damage zones

observed in the image logs overlap, so it is difficult to associate certain fractures with a fault uniquely. Lastly, varying image log quality at various intervals greatly affects the identifiable fractures, and hence the damage zone characteristics. These caveats should be kept in mind while drawing conclusions.

In order to investigate relationships of macrofracture density with distance from a fault, only well-defined and isolated damage zones are selected. Figure 2.11 shows fracture density plotted against distance from the fault in isolated, well-defined damage zones identified in various wells in the CPE gas field while Figure 2.12 shows such a plot for damage zones observed in the arkosic section adjacent the San Andreas Fault. The fracture densities reported at various distances is the average in a 10 meter interval (from the 10 meter binning performed to obtain histograms in Figures 2.4, 2.6 and 2.10). From Figures 2.11 and 2.12, we see that the decay of fracture density with distance can be described by a power law $F(r) = F_0 r^{-n}$. This is consistent with observations reported by Savage and Brodsky (2011) from outcrop studies. However, the fracture density seems to fall dramatically to background levels across the damage zone, suggesting that damage zones are of limited extent. The sections below discuss various damage zone attributes.

2.5.1 Rate of decay

The decay exponent n is approximated by fitting a power law curve to the fracture density decay profile. The values of n for each of the damage zones shown in Figures 2.11 and 2.12 are reported in Appendix 2D. Damage zones in the CPE gas field are characterized by decay rates ranging from 0.68-1.06 (with an average of ~0.8) while those in the arkosic section show slightly gradual decay rates lying between 0.4 and 0.75 (an average of ~0.56). These values are consistent with those reported in surface outcrop studies (Savage and Brodsky, 2011). Studies also suggest more gradual decay rates (~0.5) in damage zones around mature faults with fault displacements greater than ~100 m (Savage and Brodsky, 2011). This might suggest that second-order faults in the arkosic section have larger fault displacement than across those in the CPE gas field.

2.5.2 Fault constant

Fault constant is the fracture density at unit distance (1 meter) from the fault plane. Since the fracture population has been binned into intervals of 10 meters, fault constant cannot be read directly from histograms. Besides, since the region 1 meter from the fault is severely damaged, most fractures in this region cannot be identified in image logs. Therefore, the fault constant F_0 is calculated by extrapolating the power law fit to unit distance from the fault plane. Most damage zones in the CPE gas field exhibit F_0 values from 10-30 fractures/m while those in the arkosic section are characterized by F_0 values of 6-17 fractures/m. ranges. Mitchell and Faulkner (2009) report F_0 values of ~100 fractures/m in damage zones around the Atacama fault system, which is considerably larger than our observations. This inconsistency arises due to detection threshold that prevents smaller fractures from being seen in image logs, unlike outcrops that expose fractures on all scales.

Savage and Brodsky (2011) suggest that the fault constant appears to be fault-specific. They report no clear relationship between fault constant and fault slip, but for siliclastic rocks, it appears that fault constant scales with slip up to a fault displacement of 150 meters, after which it becomes almost constant at ~ 80 fractures per meter. For F_0 ~ 6-30 fractures/m (this study), this scaling relationship suggests fault displacements of 3-30 m. Since the value of F_0 for faults in the arkosic section is less than those in the CPE gas field, this scaling may suggest a lesser fault displacement across faults in the arkosic section, antithetic to our inference of larger fault displacement across these faults due to gradual decay rate (section 2.6.1). However, the fracture population in the arkosic section may be under-predicted due to intense fracturing (which makes it difficult to identify individual fractures) and poor image data quality.

2.5.3 Damage zone width

Damage zone width is identified as the region around the fault where the fracture density is greater than the background fracture density. Since there is considerable overlap in damage zones identified in this work, it is difficult to identify a specific background fracture density. The background fracture density (i.e. fracture density away from the damage zones) in the wells in the CPE gas field is ~0.5-1 fractures/m while that in the arkosic section adjacent the San Andreas Fault is ~0.4 fractures/m. The damage zones are approximately 50-80 meters wide in both the arkosic section and the CPE gas field. The hyperbolic model suggested by Mitchell and Faulkner

(2009) predicts that there is a finite limit to the damage zone width and the rate of damage zone growth decreases with fault displacement. Savage and Brodsky (2011) have compiled data from several published studies and reported that the fault zone width scales with fault displacement up to a threshold value of approximately 150 meters, beyond which the scaling breaks down and the fault zone width stabilizes at approximately 150-200 meters (Figure 2.2(b)). Figure 2.2(b) suggests a slip of ~ 30-60 meters across faults whose damage zones are 50-80 meters wide (observations from this study). The slip observed across the second-order faults in the CPE gas field (from seismic images) is 8-180 meters, which supports our estimate from the scaling relationship.

The damage zone attributes identified are not only consistent with those reported from field studies but also with those predicted using principles of dynamic rupture propagation (chapter 3). This modeling suggests power law decay in fracture density with a decay rate of ~0.85 inside damage zones around faults with a fault constant of 20 fractures/m. Damage zones modeled are 60-100 m wide.

2.5.4 Incorporating damage zones into reservoir simulators

The three main attributes for characterizing damage zones associated with second-order faults, namely, the damage zone width, fault constant and rate of fracture density decay with distance from the fault have been quantified. This information can be used to populate reservoir flow simulator models with damage zones. Seismic images provide information on the position of reservoir scale faults. These images also provide information on the slip across the fault. The scaling between fault constant F_0 and fault slip (Savage and Brodsky, 2011) can then be used to obtain the appropriate F_0 values for those faults. F_0 can also be obtained from image logs (as in the present study), if available. F_0 obtained from the two sources may not be the same due to detection threshold (inability to identify small fractures in image logs). However, a reasonable range of F_0 values can be used. Once these faults are introduced in the model, and F_0 known, fractures constituting the 50-80 meter wide damage zones can be introduced around faults (perhaps as a discrete fracture network) such that the spatial decay of fracture density with distance from the faults is consistent with the power law decay

$$F(r) = F_0 r^{-n} \tag{2.1}$$

Rate of decay n can be approximated as ~0.8 across faults with displacement less than 100 m and ~0.6 across faults with displacements greater than 100m. Although using average values of fault constant F_0, decay rate 'n' and damage zone width all along the fault may be an approximation since these attributes are not constant, it does not make a large difference for fluid flow modeling purposes since small scale heterogeneities, anyway, get homogenized while upscaling rock flow properties to simulate flow. A range of reasonable fault constant and decay rates (Appendix 2D) can also be considered to obtain several realizations of damage zones. Once the fracture network comprising fault damage zones is modeled, fluid flow can be simulated by either upscaling fractures using effective media methods or directly using finite element methods (software packages such as FracMan). Since simulating flow through discrete fractures using finite element methods is computationally expensive (especially in a dense fracture network typical of damage zones), the fracture population is usually upscaled to obtain effective continuum grid flow properties using methods such as Oda's method etc. Commercial simulators such as Eclipse can then be used for modeling flow. A methodology for including damage zones in building geologically representative reservoir discrete fracture network (DFN) models and modeling flow through them is described in chapter 4. Considering several realizations of damage zones using a range of values of fault constant and decay rates can help perform uncertainty analysis in flow predictions.

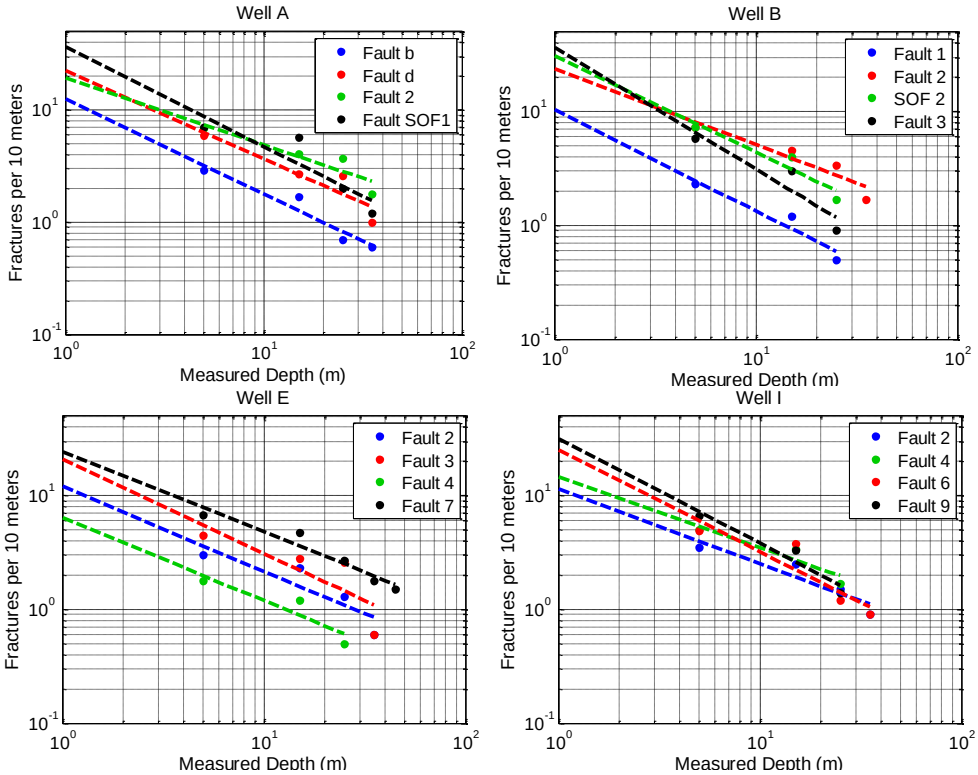

Figure 2.11: The plots above show the decay of fracture density with distance from the fault inside various damage zones encountered in the 4 wells in the CPE gas field.

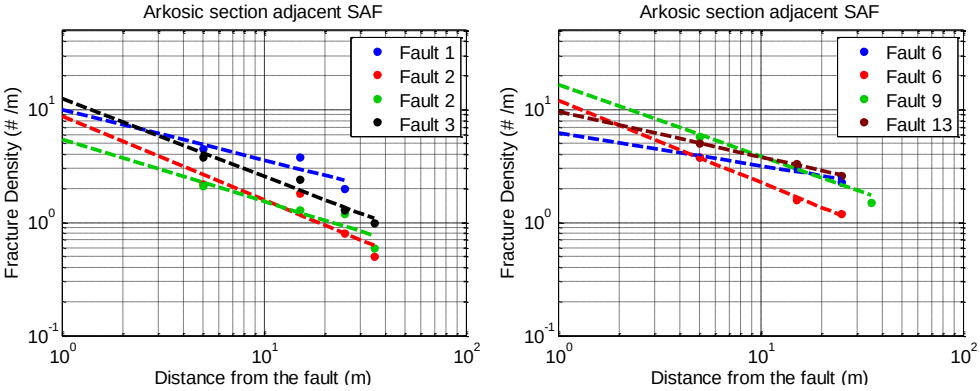

Figure 2.12: Decay of fracture density with distance from the fault inside various damage zones encountered in the arkosic section adjacent the San Andreas Fault. Faults 2 and 6 appear twice in the legend since fracture density decay in damage zones on both sides of faults 2 and 6 have been shown in the above plots.

2.6 Discussion

With the importance of fractures and damage zones in influencing fluid flow in low permeability reservoirs firmly established, it is critical to incorporate these damage zones appropriately for fluid flow simulation purposes. As discussed previously, the challenge

associated with this task was the difficulty in estimating the spatial extent and variability of permeability anisotropy introduced by damage zones in quantitative terms. In the current study, characteristics and spatial heterogeneity of sub-surface damage zones associated with second-order faults have been quantified using image logs. These characteristics can help incorporate damage zones in flow simulation models by assigning appropriate effective permeability tensor values to various reservoir grid blocks depending on fracture density in those grid blocks, and the flow properties of those fractures. For example, since the fracture density decay with distance from the fault can be described by a power law, the reservoir grid blocks close to the fault would have larger permeability, and this value would decrease in grid blocks away from the fault surface in accordance with the power law decay relationship. Since the damage zone attributes in both, the CPE gas field and arkosic sandstones are very similar despite the difference in lithology, we believe these damage zone attributes in other lithologies would be very similar, at least to first order. This can be useful at times when data available is scarce. At times when image logs are not available and we only have information of the spatial location of second-order faults derived from seismic images, we can make reasonable estimates of damage zones associated with those faults assuming they would be very similar to those identified in the current study, and work towards generating appropriate reservoir models to simulate fluid flow.

2.7 Conclusions

Attributes of fault damage zones associated with second-order faults at reservoir depths have been identified in two regions, the arkosic section adjacent to the San Andreas Fault and the CPE gas field. Second-order faults and their damage zones are characterized using image logs and other geophysical logs. The positions of sub-seismic resolution second-order faults at depth are constrained by noting changes in the orientation of bedding planes and anomalous changes in geophysical properties. Damage zones observed in both the regions are similar in terms of damage zone widths and fault constant F_0 despite the geologic differences. These damage zone characteristics are also very similar to those observed in outcrop studies. The decay of fracture density with distance from faults can be described by a power law $F = F_0 r^{-n}$. Such a decay rate has been reported from outcrop field studies (Savage and Brodsky, 2011); this study extends this understanding to damage zones at reservoir depths. The decay rate n from 0.68-1.06 (average ~0.8) is observed in damage zones in the CPE gas field while n from 0.4-0.75 (average ~0.56) is

observed in damage zones in the arkosic sandstone section. Damage zones in both the regions are typically 50-80 m wide. The extrapolated value of the fault constant ranges from10-30 fractures/m for damage zones in the CPE gas field and from 6-17 fractures/m in those in the arkosic section. F_0 for damage zones in the arkosic section may be under-estimated due to poor data quality and intense fracturing. Scaling between fault displacement and fault zone width (from data compiled by Savage and Brodsky (2011) using various published studies) suggests a fault displacement of 30-60 m across faults whose damage zones are 50-80 m wide. This expected slip is within the range of fault displacements observed in seismic images (8-180 m). A number of these damage zones have a signature of reduced sonic velocities and resistivity, and increased porosities in the geophysical logs. Others that do not have a distinct signature could represent damage zones comprised of sealed fractures that would not significantly reduce sonic velocities and formation resistivity.

This study also demonstrates the importance of correcting the fracture population, obtained from image logs, for the sampling bias introduced due to the under-sampling of fractures sub-parallel to the well for more appropriate fracture characterization of the reservoir. There is significant increase in the fracture population, especially in the CPE gas field when the fracture dataset obtained from image logs is statistically corrected to remove the sampling bias.

2.8 References

Andersson, J. E., L. Ekman, R. Nordqvist, and A. Winberg. 1991. Hydraulic testing and modeling of a low angle fracture zone at Finnsjon, Sweden. Journal of Hydrology, 126, 45-77. doi: 10.1016/0022-1694(91)90200-2

Aydin, A. 1978. Small faults formed as deformation bands in sandstone. Pure and Applied Geophysics, 116, 913-930. doi: 10.1007/BF00876546

Barton, C. A., and M. D. Zoback. 1994. Self-similar distribution and properties of macroscopic fractures at depth in crystalline rock in the Cajon pass scientific drill hole. Journal of Geophysical Research, 97, 5181-5200. doi:10.1029/91JB01674

Barton C. A., M. D. Zoback, and D. Moos. 1995. Fluid flow along potentially active faults in crystalline rock. Geology, 23, 683-686. doi: 10.1130/0091-7613(1995)023<0683:FFAPAF>2.3.CO;2

Boness, N. and M. D. Zoback. 2006. A multiscale study of the mechanisms controlling shear velocity anisotropy in the San Andreas Fault observatory at depth. Geophysics, 71 (5): F131–F146. doi: 10.1190/1.2231107

Bradbury, K. K., D. C. Barton, S. D. Draper, J. G. Solum, and J. P. Evans. 2007. Mineralogic and textural analyses of drill cuttings from the San Andreas Fault Observatory at Depth (SAFOD) boreholes: Initial interpretations of fault zone composition and constraints on geological models. Geosphere 3: 299-318. doi:10.1130/GES00076.1

Byerlee, J. D. 1978. Friction of rock. Pure and Applied Geophysics, 116: 615-626. doi: 10.1007/BF00876528

Caine, J. S., J. P. Evans, and C. B. Foster. 1996. Fault zone architecture and permeability structure. Geology, 24: 1025-1028. doi: 10.1130/0091-7613(1996)024<1025:FZAAPS>2.3.CO;2

Chester, F. M., and J. M. Logan. 1986. Composite planar fabric of gouge from the Punchbowl Fault, California. Journal of Structural Geology, 9: 621–634. doi: 10.1016/0191-8141(87)90147-7

Chester, F. M., J. P. Evans, and R. L. Biegel. 1993. Internal structure and weakening mechanisms of the San Andreas Fault. Journal of Geophysical Research-Solid Earth 98(B1): 771-786.

Chester, J. S., F. M. Chester, and A. K. Kronenberg. 2005. Fracture surface energy of the Punchbowl fault, San Andreas system. Nature, 437(7005), 133-136, doi: 10.1038/nature03942

Dholakia, S. K., A. Aydin, D. D. Pollard, and M. D. Zoback. 1998. Fault-controlled hydrocarbon Pathways in the Monterey formation, California. American Association of Petroleum Geologists Bulletin 82: 1551-1574.

Einstein H. H., and G. B. Baecher. 1983. Probabilistic and statistical methods in engineering geology specific methods and examples, part 1. Exploration, Rock Mechanics and Rock Engineering, 16: 39-72. doi:10.1007/BF01030217

Faulkner, D. R., A. C. Lewis, and E. H. Rutter. 2003. On the internal structure and mechanics of large strike slip fault zones: field observations of the Carboneras fault in southeastern Spain. Tectonophysics, 367 (3-4): 235-251. doi: 10.1016/S0040-1951(03)00134-3

Faulkner, D. R., T. M. Mitchell, E. H. Rutter, and J. Cembrano. 2008. On the structure and mechanical properties of large strike slip faults. Geological Society, London. Special Publications 299: 139-150. doi: 10.1144/SP299.9

Fisher, Q. J., and R. J. Knipe. 1998. Fault sealing processes in siliciclastic sediments. Geological Society, London, Special publications, 147, 117-134. doi: 10.1144/GSL.SP.1998.147.01.08

Fisher, Q. J., M. Casey, S. D. Haris, and R. J. Knipe. 2003. Fluid-flow properties in sandstone: The importance of temperature history. Geology, 3(11), 965-068. doi: 10.1130/G19823.1

Goddard. J. V., and J. P. Evans. 1995. Chemical changes and fluid-rock interaction in faults of crystalline thrust sheets, northwestern Wyoming, U.S.A. Journal of Structural Geology, 17: 533-547. doi:10.1016/0191-8141(94)00068-B

Hennings, P., P. Allwardt, P. Paul, C. Zahm, and R. Reid. 2012. Relationship between fractures, fault zones, stress and reservoir productivity in the Suban gas field, Sumatra, Indonesia. AAPG Bulletin, 96(4), 753-772. doi: 10.1306/08161109084

Johri, M., E. M. Dunham, M. D. Zoback and Z. Fang. 2012. Predicting fault zone damage zones by modeling dynamic rupture propagation and comparison with field observations.

Johri, M., M. D. Zoback, and E. M. Dunham. Modeling fluid flow through damage zones.

Lockner, D., H. Naka, H. Tanaka, H. Ito, and R. Ikeda. 1999. Permeability and strength of core samples from the Nojima fault of the 1995 Kobe Earthquake, Proceedings of the International Workshop on the Nojima fault core and borehole data analysis, preliminary report: 147-152.

Mitchell, T. M., and D. R. Faulkner. 2009. The nature and origin of off-fault damage surrounding strike-slip fault zones with a wide range of displacements: A field study from the Atacama fault system, northern Chile. Journal of Structural Geology, 31(8), 802-816. doi: 10.1016/j.jsg.2009.05.002

Paul. P, M. D. Zoback, and P. Hennings. 2009. Fluid flow in a fractured reservoir using a geomechanically constrained fault zone damage model for reservoir simulation. Society of Petroleum Engineers, 12(4), 562-575. doi: 10.2118/110542-PA

Rymer, M. J., R. D. Catchings, and M. R. Goldman. 2003. Structure of the San Andreas fault zone as revealed by surface geologic mapping and high-resolution seismic profiling near Parkfield, California. Geophysical Research Abstracts 5: 13523.

Savage, H. M, and E. E. Brodsky. 2011. Collateral Damage: Evolution with displacement of fracture distribution and secondary fault strands in fault damage zones. Journal of Geophysical Research, 116, 14. doi:10.1029/2010JB007665

Scholz, C. H., and M. H. Anders. 1994. The permeability of faults, and the mechanical environment of fluids in faulting. U.S. Geological Survey Open-File Report 94-228: 247-253.

Smith, L., C. B. Forster, and J. P. Evans. 1990. Interaction of fault zones, fluid flow, and heat transfer at the basin scale. Hydrogeology of permeability environments, (S. P. Newman and I. Neretnieks, eds.), International Association of Hydrogeological Sciences selected papers in Hydrogeology, 2, 41-67.

Solum, J. G., S. Hickman, D. A. Lockner, S. Tembe, J. P. Evans, S. D. Draper, D. C. Barton, D. L. Kirschner, J. S. Chester, F. M. Chester, B. A. Van Der Pluijm, A. M. Schleicher, D. E. Moore, C. Moore, K. Bradbury, W. M. Calvin, and T. Wong. 2007. San Andreas fault zone mineralogy, geochemistry and physical properties from SAFOD cuttings and core. Scientific Drilling Special Issue 1:64-67.

Springer, D. S., J. Evans, J. I. Garver, D. Kirschner, and S. U. Janecke. 2009. Arkosic rocks from the San Andreas Fault observatory at depth (SAFOD) borehole, central California: Implications for the structure and tectonics of the San Andreas Fault zone. Lithosphere, 1(4), 206- 226. doi: 10.1130/L13.1

Terzaghi, R. D. 1965. Sources of error in joint surveys. Geotechnique, 15: 287-304.

Thayer, M., and R. Arrowsmith. 2005. Fault zone structure of Middle Mountain, central California. American Geophysical Union, fall meeting, abstract T21A0458.

Vermilye, J. M., and C. H. Scholz. 1998. The process zone: a microstructural view of fault growth. Journal of Geophysical Research, 103 (B6), 12223–12237. doi: 10.1029/98JB00957

Wibberley, A. J. C., and T. Shimamoto. 2002. Internal structure and permeability of major strike-slip fault zones: the Median Tectonic Line in Mie Prefecture, Southwest Japan.Journal of Structural Geology, 25, 59-78. doi:

Zoback M. D. 2007. Reservoir Geomechanics. Cambridge University Press, Cambridge, 341

Zoback, M. D., S. Hickman, W. Ellsworth, and the SAFOD Science Team. 2011. Scientific drilling into the San Andreas Fault Zone – An overview of SAFOD's first five years. Scientific Drilling, 11, 14-28. doi:10.2204/iodp.sd.11.02.2011

Appendix 2A: Removal of sampling bias

In order to characterize sub-surface natural fractures and damage zones using geophysical logs such as image logs, it is necessary to make necessary corrections, the foremost being correction for the sampling bias introduced by the inability of boreholes to sample fractures oriented sub-parallel them. The statistical correction to correct for the sampling bias has been discussed by several authors (Terzaghi, 1965; Einstein and Baecher, 1983; Barton and Zoback, 1994). Terzaghi (1965) was the first to propose a method for removing this sampling bias in a vertical well. If we consider a set of fractures intersecting a vertical well dipping at angle θ, and d is the actual average spacing between two fractures, the apparent fracture spacing as seen in the image log would be $d/\cos\theta$ (Figure 2A1). Consequently, if N is the number of fractures intersecting this vertical borehole per unit length along the borehole, the actual fracture density of this fracture set would be $N\sec\theta$ per unit length measured along the normal to this fracture set. This approach can be extended to non-vertical wells (Figure 2A1). If we consider a set of fractures striking α_1 and dipping ϕ_1, the trend and plunge of the normal to this fracture set would be $(\alpha_1 - 90)°$ and $(90 - \phi_1)°$ respectively. If the trend and plunge of the borehole are α_2 and ϕ_2, then the unit vectors along the normal to the fracture set $\vec{u}$ and along the borehole $\vec{v}$ would be

$$\vec{u} = \sin(\alpha_1 - 90)\cos(90 - \phi_1)\,\overrightarrow{e_x} + \cos(\alpha_1 - 90)\cos(90 - \phi_1)\,\overrightarrow{e_y} - \sin(90 - \phi_1)\,\overrightarrow{e_z} \quad (2.2)$$

$$\vec{v} = \sin(\alpha_2)\cos(\phi_2)\,\overrightarrow{e_x} + \cos(\alpha_2)\cos(\phi_2)\,\overrightarrow{e_y} - \sin(\phi_2)\overrightarrow{e_z} \quad (2.3)$$

If the average distance between the fractures in this fracture set is d, the apparent distance between these fractures seen along the borehole would be $d\sec\theta$. I define 'bias factor' as the projection of the normal to a fracture of a certain orientation along the borehole ($\cos\theta$). Larger values of the bias factor represent lesser bias while lower values represent a larger bias.

$$\text{Bias Factor} = \cos\theta = \left(\frac{\vec{u}.\vec{v}}{|\vec{u}||\vec{v}|}\right) \quad (2.4)$$

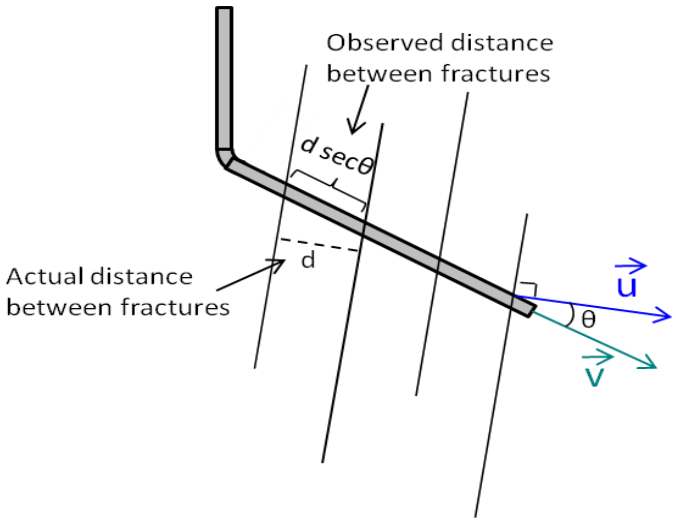

Figure 2A1: Geometry of correction for the systematic under sampling of steeply dipping fractures in vertical boreholes (modified from Barton and Zoback (1994))

Using this concept, the following approach is adopted to remove the sampling bias. Continuous intervals of a certain length along the borehole are selected. For each interval, the fractures striking and dipping within a certain interval are identified, and their number is upscaled by a factor of $\sec\theta$. The new fractures introduced, are distributed along that depth interval, and assigned strike and dip values according to the distribution of the spatial location and orientation of fractures present in the original fracture population in that depth-strike-dip window. The depth interval considered in this study is 10 meters, while the strike and dip intervals used are 10°. The corrected population predicts the actual fracture population present.

The orientation of the borehole in the arkosic section is variable but the plunge lies largely between 35° and 37° while the plunge direction lies largely between 36° and 39°. The apparent fracture density of a certain fracture set measured along a borehole when divided by the bias factor gives the actual fracture density. Figure 2A2 shows the bias factors introduced by the borehole for all possible orientations of fractures. Such a plot would be valid for a certain orientation of the borehole. Since the borehole orientation changes continuously, different plots are obtained at different depths. The plot in Figure 2A2 represents the bias factors at a depth of 2270m along the borehole where the plunge and plunge direction of the borehole are 35° and 36° respectively. The warmer colors represent higher values of the bias factor. These occur for fractures approximately striking 125° and dipping 55°. This is expected since such a fracture set would be perpendicular to the borehole and present maximum probability of being sampled or

intersected. On the other hand, the cooler colors represent the lowest values of the bias factor. Fracture sets with such orientations are sub-parallel to the borehole and will present minimum probability of being intersected by the borehole.

Figure 2A3 (a) shows the distribution of fracture (third order feature) orientations identified in the arkosic section while Figure 2A3 (b) shows the distribution of orientations of the corrected fracture population. We notice that the number of fractures striking approximately 125° and dipping 35° (sub-parallel to the well bore – a red spot in Figure 2A3 (a)) almost remains the same after a correction is applied, but for fractures approximately striking 320° and dipping 55°, their number increases from 6 before correction to 70 after correction. The dark blue regions in Figure 2A3 (a) representing fracture orientations which are completely missing in the original fracture set remain missing in the updated fracture set as well (Figure 2A3 (b)) since there is no fracture population to upscale.

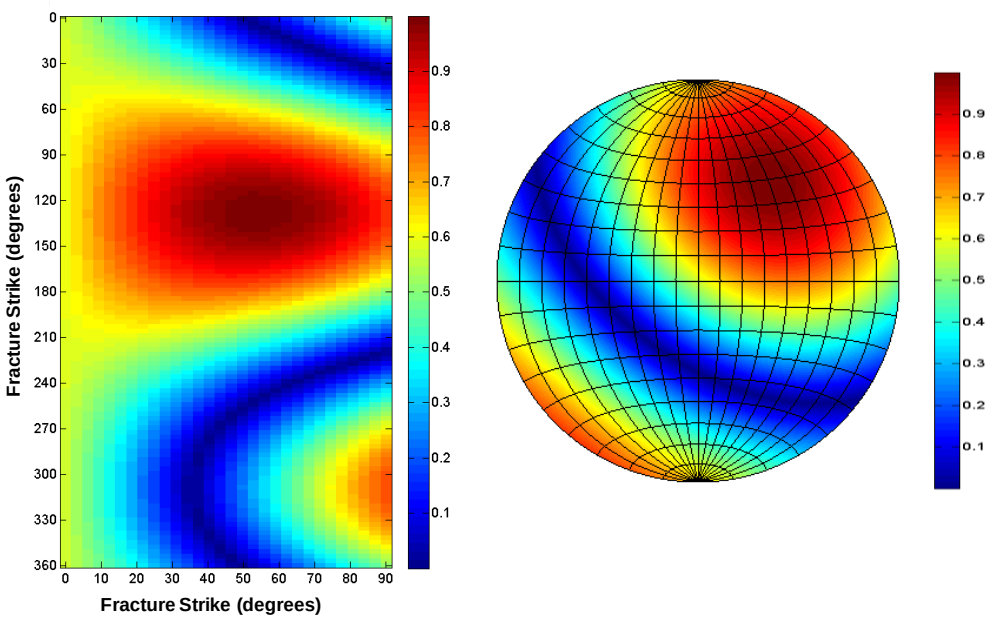

Figure 2A2: Values of the bias factor for fractures with various orientations with respect to a borehole whose plunge and plunge direction are 35° and 36°. These values are shown in a planer plot (left) and a stereonet (to the right). Warmer colors represent larger values of BF (lesser bias) while the cooler colors represent lower values of BF (greater bias).

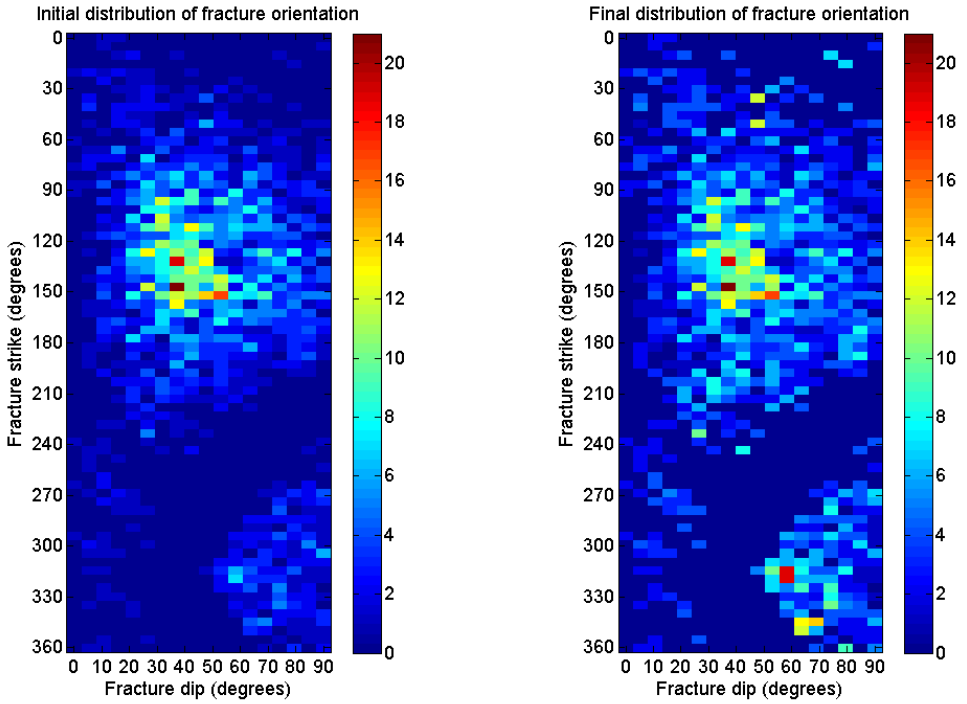

Figure 2A3: The above figure represents the number of fractures of various orientations present in (a) original fracture dataset (b) updated fracture dataset (after correcting for sampling bias) from the arkosic section, SAFOD

Appendix 2B: Fracture statistics before and after statistically correcting the fracture population for the sampling bias

Table 2B1 shows the fracture population in various wells in the CPE gas field before and after the correction to remove sampling bias is applied. The fracture population obtained after the correction is applied represents the regional fracture characteristics. Since there is a strong correlation between well performance and number of critically stressed fractures that the well intersects, wells drilled in the region with the largest density of critically stressed fractures with the appropriate orientation should be most productive. From the corrected fracture population, we notice that the regional density of critically stressed fractures around well A is 1.58 fractures per meter which is larger than that around other wells (0.36, 0.59 and 0.52 critically stressed fractures per meter around wells E, I and B respectively). We can, perhaps, argue that if an appropriately deviated well was drilled in the region around well A, it could potentially have been even more productive than the prolific well B.

Well (Suban)	Reservoir wellbore contact length (m)	Before Correction		After Correction	
		All fractures	Critically stressed fractures	All fractures	Critically stressed fractures
Well A	234	547	91	1646	370
Well B	758	1261	194	2906	396
Well E	772	903	63	2113	282
Well I	957	800	140	2420	561

Table 2B-1: The table lists the contact length of wells A, B, E and I with the reservoir along with the number of all fractures and critically stressed fractures that the well intersects prior to and after the fracture population has been corrected for the sampling bias

Appendix 2C: Identifying the location of second-order faults

The arkosic section is divided into fourteen structural blocks (blocks a – n) such that the orientation of bedding planes in each block is significantly different from the orientation of bedding planes in the adjacent blocks (Figure 2C1). Block a comprises of widely oriented bedding planes dipping towards southwest, but their orientation is distinctly different from the orientations of bedding planes in block b which dip steeply towards the N-NNE. Block c comprises of very shallow dipping bedding planes while block d comprises of bedding planes dipping steeply towards the southeast. Bedding planes in block e dip with intermediate angles towards the south. In block f the bedding planes dip with intermediate angles towards the southwest while in block g, bedding planes dip towards the west with shallow to intermediate angles. Bedding planes in block h dip at angles between 10 and 20° towards the north while those in block i dip steeply towards the northeast. Blocks a-i make up the upper arkose as defined by Draper Springer et al. (2009). These rocks are quartz and feldspar rich, and are relatively homogeneous for most part. A clay rich region marked with a marked increase in gamma ray and porosity log and a decrease in sonic velocities (Boness and Zoback, 2006) extends from 2530m to 2680m measured along the borehole. Two blocks are identified in this region. Block j comprises of bedding planes dipping with intermediate angles towards the southeast while block k comprises bedding planes dipping towards the southwest. Blocks l, m, and n lie in the lower arkosic region (as defined by Springer et al., 2009). The average porosity in this region is less than that in upper arkose. It is also seen that the amount of quartz in lower arkose is less, and most of the quartz present is plastically deformed, which may be indicative of more faulting.

There is not a very significant difference in the bedding plane orientations of beds in blocks k, l, and m, but subtle differences do exist. The bedding planes in these blocks have shallow dipping angles and dip towards the southwest, south of southwest and south respectively. Finally, the beds in block n dip steeply towards the northeast.

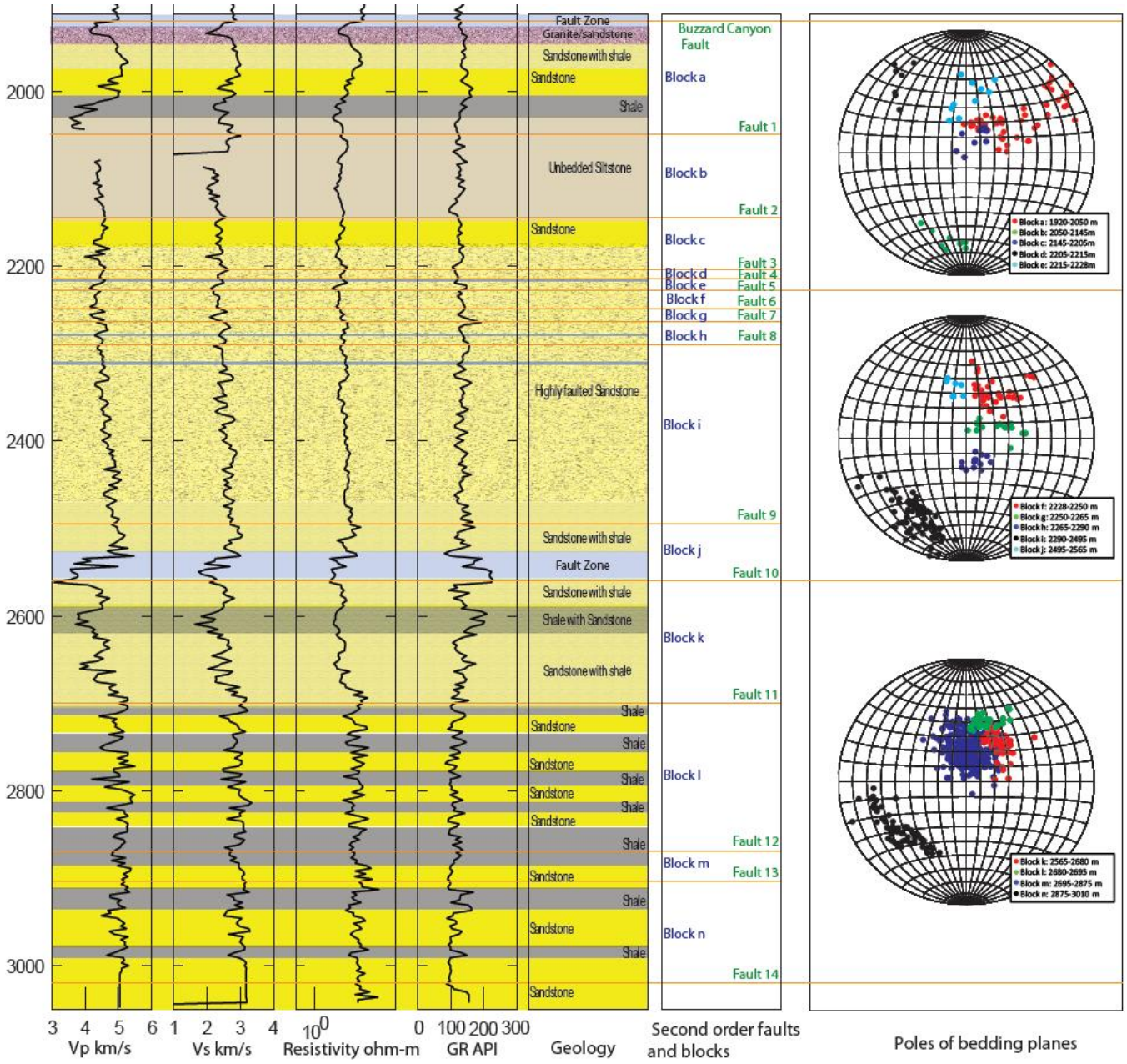

Figure 2C1: The figure above shows the P wave, S wave, resistivity and gamma ray logs and geology in the arkosic section encountered by the borehole at SAFOD. The stereonets on the far right represent the orientations of bedding planes in various structural blocks (numbered a-n).

Appendix 2D: Fault constant and decay rates observed in various damage zones

Suban Gas Field								
Well A					Well E			
Fault	n	F_0	r^2		Fault	n	F_0	r^2
Fault b	-0.84	12.5	0.93		Fault 2	-0.75	12	0.79
Fault d	-0.79	22	0.85		Fault 3	-0.82	21	0.65
Fault 2	-0.6	19.4	0.84		Fault 4	-0.73	6.4	0.84
SOF1	-0.89	37	0.8		Fault 7	-0.71	24.4	0.93
Well B					Well I			
Fault	n	F_0	r^2		Fault	n	F_0	r^2
Fault 1	-0.89	10.5	0.92		Fault 1	-0.65	11.4	0.88
Fault 2	-0.67	23.9	0.87		Fault 3	-0.61	14.6	0.87
SOF2	-0.85	31	0.91		Fault 5	-0.89	25.2	0.82
Fault 3	-1.06	37	0.87		Fault 7	-0.92	31.7	0.93
Arkosic section adjacent SAF								
Fault	n	F_0	r^2		Fault	n	F_0	r^2
1	-0.44	10	0.75		6	-0.3	6.3	0.9
2	-0.74	8.64	0.82		6	-0.73	12	0.99
2	-0.55	5.48	0.83		9	-0.63	16.6	0.94
3	-0.69	12.5	0.94		13	-0.4	9.6	1

Table 2D-1: The table lists the fault constant F0 and decay rate n obtained by fitting a power law curve to describe the decay of fracture density with distance from the fault. The coefficient of determination r2 (for the linear fit between the logarithms of fracture density and distance from the fault) are also listed.

Appendix 2E: Identification of critically stressed fractures

According to the critically stressed fault hypothesis, fractures or faults that are mechanically alive are hydraulically alive and those that are mechanically dead are hydraulically dead (Barton et al., 1995; Zoback, 2007). This means that the faults and fractures on which the ratio of resolved shear (τ) to normal traction (σ_n) is greater than the coefficient of sliding friction (normally 0.6-1.0 (Byerlee, 1978)) would be mechanically active and slip. τ and σ_n are found by resolving the in-situ stress along and perpendicular to the fracture planes. The in-situ stress state (principal stress magnitudes and directions) is constrained using wellbore image data and additional information (pc, ConocoPhillips). The minimum principal stress S_{hmin} is constrained from XLOTs, vertical stress S_v is estimated from integration of density logs from shallow levels through to the reservoir interval, and pore pressure P_p is interpreted from drillstem test data. The direction of maximum horizontal stress S_{hmax} is interpreted from the azimuth of drilling induced

tensile fractures seen in image logs. Drilling induced tensile fractures and borehole breakouts occur where the circumferential hoop stress exceeds the tensile strength and UCS of the rock respectively. Since the circumferential hoop stress scales with differential stress (difference between the maximum and minimum principal stress), the presence or absence of DITFs and borehole breakouts help constrain the differential stress, which in turn helps constrain the magnitude of the maximum principal stress (which in this case is S_{hmax}). The azimuth of S_{hmax} along the well is ~128º except from 2400-2500 m (along the borehole) where it abruptly changes to 164º. The gradient of S_{hmin} is approximately 17 MPa/km while that of S_v is 22 MPa/km. Pore pressure is interpreted to be ~12MPa/km. The gradient of S_{hmax} is constrained to be 34 MPa/km along the entire borehole except from 2400-2500 m measured depth, when it is 30 MPa/km.

In order to compute the shear and normal tractions acting on fracture plane, the in-situ stress tensor S (expressed in the coordinate system along the principal stress directions) is first rotated to obtain the tensor S_G along the geographic coordinate system (where X axis is along the East, Y axis is along the north and Z axis points vertically downwards into the Earth).

$$S_G = R_1' S R_1 \tag{2.5}$$

where

$$S = \begin{bmatrix} S_1 & 0 & 0 \\ 0 & S_2 & 0 \\ 0 & 0 & S_3 \end{bmatrix} \tag{2.6}$$

S_1, S_2 and S_3 are the maximum, intermediate and minimum effective principal stresses, which in this case are $S_{hmax} - P_p$, $S_v - P_p$, and $S_{hmin} - P_p$ respectively.

$$R_1 = \begin{bmatrix} \cos a \cos b & \sin a \cos b & -\sin b \\ \cos a \sin b \sin c - \sin a \cos c & \sin a \sin b \sin c + \cos a \cos c & \cos b \sin c \\ \cos a \sin b \cos c + \sin a \sin c & \sin a \sin b \cos c - \cos a \sin c & \cos b \cos c \end{bmatrix} \tag{2.7}$$

Angle a is the trend of S_1 (which in this case is either 128º or 164º depending on the depth along the borehole), b is the negative of the plunge of S_1 (which in this case is 0), and c is rake of S_2

(which is 90º). Stress tensor S_G is then rotated into the fault coordinate system (where one direction is normal to the fault plane, while the other two are in the plane of the fault).

$$S_f = R_2 S_G R_2' \tag{2.8}$$

where

$$R_2 = \begin{bmatrix} \cos(\text{strike}) & \sin(\text{strike}) & 0 \\ \sin(\text{strike})\cos(\text{dip}) & -\cos(\text{strike})\cos(\text{dip}) & -\sin(\text{dip}) \\ -\sin(\text{strike})\sin(\text{dip}) & \cos(\text{strike})\sin(\text{dip}) & -\cos(\text{dip}) \end{bmatrix} \tag{2.9}$$

Strike, dip and rake refer to the orientation of the fracture plane. Finally,

$$S_r = R_3 S_f R_3' \tag{2.10}$$

where

$$R_3 = \begin{bmatrix} \cos(\text{rake}) & \sin(\text{rake}) & 0 \\ -\sin(\text{rake}) & \cos(\text{rake}) & 0 \\ 0 & 0 & 1 \end{bmatrix} \tag{2.11}$$

Effective normal stress $S_n = S_f(3,3)$

Shear stress $\tau = S_r(3,1)$.

Coulomb Failure Function $CFF = \tau - \mu\sigma_n$ (2.12)

where μ is the coefficient of sliding friction (~0.6). A fracture is critically stressed in the current stress state if CFF > 0.

Chapter 3

PREDICTING FAULT DAMAGE ZONES BY MODELING DYNAMIC RUPTURE PROPAGATION AND COMPARISON WITH FIELD OBSERVATIONS

3.1 Abstract

This study uses a two-dimensional plane-strain dynamic rupture model with strongly rate-weakening friction and off-fault Drucker-Prager plasticity to model damage zones associated with buried second-order thrust faults (approximately 3 km long) observed in the CPE gas field. The modeling of ruptures propagating as self-sustaining pulses is performed in the framework of continuum plasticity where the plasticity formulation includes both deviatoric and volumetric plastic strains. The material deforming inelastically due to stress perturbations generated by the propagating rupture is assumed to be the damage zone associated with the fault. Modeling a single rupture suggests a spatially heterogeneous damage zone width since the damage zone width scales linearly with propagation distance (distance from the point of nucleation). Dilatant plastic strains are converted into a fracture population using volume balancing assuming that the entire dilatant plastic strain is manifested in the form of fractures and small faults. The cumulative effect of multiple slip events (i.e., earthquakes) is considered by superposition of the

plastic strain field obtained from individual slip events. The relative number of various magnitude slip events is chosen so as to honor the Gutenberg-Richter law. The nucleation points of these slip events are uniformly distributed on the fault plane.

Results show that the decay of fracture density (number of fractures per unit length) with distance from the fault can be described by a power law $F = F_o r^{-n}$. The rate of decay (n) in the modeled damage zones is approximately 0.85 close to the fault and increases to ~ 1.4 at larger distances (>10 meters) from the fault. Modeled damage zones are approximately 60-100 meters wide. The spatial variability in the widths of damage zones modeled due to a single rupture gets relatively homogenized on considering multiple slip events. These modeled damage zone attributes are very similar to those observed in the CPE field using wellbore image logs and those reported in outcrop studies. Considering fault roughness affects local damage zone characteristics, but these characteristics are similar to those modeled around planar faults at a scale (~10 m) that affects bulk pore fluid flow properties and can be assimilated in flow simulators.

3.2 Introduction and Motivation

Damage zones are regions of anomalously high fault and fracture density surrounding larger-scale faults. Fractures in damage zones present both problems and opportunities during production from hydrocarbon reservoirs, especially those that have low matrix permeability. The heterogeneity and complexity of fluid-flow paths in fractured reservoirs makes it difficult to predict their behavior. A few field studies have documented the influence of damage zones on production. For example, Paul et al. (2009) report a study from the CS gas field where it is only possible to explain large gas production rates by introducing spatially variable permeability anisotropy (in flow simulators) representative of damage zones present in the reservoir. Hennings et al. (2012) report a case from the Suban gas field in SE Asia where the production from wells that sample damage zones is several times greater than those which do not traverse through damage zones.

Since damage zones strongly influence fluid flow in fractured reservoirs, it is important to have sufficient data to characterize and incorporate them in fluid flow simulators to model flow accurately. Direct observations of fractures and faults at depth in reservoirs typically come from

3-D seismic reflection data, image logs in wellbores, and studies of exhumed core. Of course, 3-D seismic data identifies only larger scale faults and fails to resolve smaller fractures that can strongly influence fluid flow. As core is rarely available over significant ranges of depth, wellbore image data are the best available source of sub-surface fracture information. However, these data are one-dimensional, and sample only limited parts of a reservoir. Thus, it is difficult to build geologically representative models of reservoirs having damage zones. Our goal is to help develop a methodology for modeling and predicting damage zones associated with reservoir scale faults (whose position is constrained from seismic images); the damage zone modeling results can be used in conjunction with information on major fracture sets (fracture intensity and orientation) derived from borehole image logs to build geologically consistent and seismologically constrained fracture networks to inform fluid flow modeling through fractured reservoirs.

Fault damage zones may be created by various cumulative processes during or after fault formation, including Andersonian fracturing (Anderson, 1942; Scholz, 2002), early fault-tip migration, fault-tip linkage, cumulative fault wear with increasing displacement, (which are all quasi-static processes), and damage caused by dynamic rupture events (Rudnicki, 1980; Wilson et al., 2003; Paul et al., 2009). These models are discussed by Mitchell and Faulkner (2009). In most applications to oil and gas reservoirs, damage zones are modeled as a result of slip on fault planes using static dislocations in elastic media (Shipton and Cowie, 2003). Such models only consider static stress changes. Time dependence of slip is not included. In these models, stress concentrations are limited to fault tips and geometrical irregularities. Regions over which the stresses exceed the rock yield stress are considered to comprise the damage zone of the fault. Since stress concentrations occur only near the ends of fault segments or with other structural discontinuities such sharp bends or offsets in the fault surface, these static-dislocation models do not produce damage all along the length of the fault, in contrast to what is observed in outcrop studies. Damage all along the fault length, however, can be replicated by considering multiple slip events along various patches of the fault plane and summing up the damage due to quasi-static dislocation of each slipping fault patch. Nevertheless, the quasi-static models neglect inertial effects, which may be significant.

Dynamic rupture models are fundamentally different from static models. These models consider stress perturbations around the fault tip at each stage of propagation and hence can account for damage all along the length of the rupture (Madariaga, 1976; Kostrov, 1964; Andrews, 1976). These models also account for dynamic and inertial effects, which are neglected in the static models. Previously, Paul and Zoback (2007) used principles of dynamic rupture propagation to model damage zones associated with reservoir scale faults. They used Freund's asymptotic solution of stress perturbations around a propagating rupture tip (Freund, 1979) coupled with Kostrov's solution for a circular crack (Kostrov, 1974) to calculate stresses induced by slip in regions close to a propagating rupture tip. The induced stresses were then used to calculate the extent of the damage zone by identifying the region around the fault where the induced stress exceeded the rock strength. A shortcoming of this methodology is that the solution of stress concentrations around a propagating crack tip implies a $1/\sqrt{r}$ stress singularity at the tip and exceptionally high stresses very close to the tip. This singularity is a consequence of an instantaneous stress drop on the fault surface leading to an elliptical distribution of displacement on the fault which produces infinite strains at fault tips. The issue of stress singularity can be resolved by tapering the slip towards the fault tips which can be obtained by transitioning the fault strength over a displacement known as the weakening distance. This forms the basis for the slip-weakening model (Ida, 1972; Andrews, 1976b; Rice et al., 2005). Another shortcoming of the above methodology is that the modeling is limited to an elastic domain. Stresses produced around a propagating fault tip in an elastic model are unreasonably large, which is clearly not possible since the material starts deforming inelastically once the stresses exceed the yield stress. This inelastic deformation leads to stress relaxation and limits stresses to reasonable values.

3.3 Current Study

In this study, principles of dynamic rupture propagation are used to numerically model damage zones formed as a result of off-fault damage created due to slip on a fault plane. As the rupture propagates, stress perturbations are induced around the rupture tip, leading to failure. Rupture propagation is studied using two-dimensional plain-strain models. The off-fault material is described by a Drucker-Prager elastic-plastic rheology. A similar assumption has also been made in other published studies on dynamic rupture propagation (Andrews, 2005; Ben-Zion and Shi, 2005; Duan and Day, 2008; Ma, 2009; Templeton and Rice, 2008; Viesca et al., 2008). We

neglect cohesion since the deformation processes prior to and during fault formation would have intrinsically damaged the surrounding rock leading to near-negligible cohesion values. The fault coefficient of friction obeys a rate-and-state law that features the direct effect and evolution towards a strongly velocity-weakening steady state friction coefficient. The amount of slip required for the friction to evolve completely (completely weaken) is L. This weakening occurs over a spatial distance of R_0 at the rupture tip. The plasticity formulation, failure law and yield criterion, and the friction law are discussed in greater detail in section 3.4. The model parameters chosen to describe the friction law and the off-fault material rheology are mentioned in Appendix 3A

Most dynamic models that simulate rupture propagation with rate-weakening friction have been limited to ruptures in an elastic domain. As a result, extremely high stresses and slip velocities are predicted near the rupture front. Noda et al. (2009) predict maximum slip velocity exceeding 100 m/s and strains of order 0.1. These stresses are far greater than yield stresses, which is inconsistent. Once the yield stress is exceeded, the region around the fault deforms inelastically, leading to stress relaxation, dissipation of energy and formation of the associated damage zone. Accounting for plasticity prevents unreasonably large stresses and limits the slip velocities to ~10 m/s (Dunham et al., 2011a), consistent with the estimates of Sleep (2010).

Experimental evidence suggests that frictional resistance decreases very significantly (up to one order of magnitude) at coseismic slip rates (~1 m/s) during earthquakes (Tsutsumi and Shimamoto, 1997; Tullis and Goldby, 2003 a, b; Prakash and Yuan, 2004; Hirose and Shimamoto, 2005; Beeler et al., 2008; Toro et al. 2011; Goldsby and Tullis, 2011). This is known as dynamic weakening. Two weakening mechanisms, flash heating and thermal pressurization are discussed in Appendix 3C. A consequence of dynamic weakening is that for a certain range of initial stress conditions, ruptures propagate as self-healing slip pulses instead of as cracks (Cochard and Madariaga, 1994; Zheng and Rice, 1998; Noda et al. 2009; Dunham et al., 2011a). The understressing theory developed by Zheng and Rice (1998) shows that for ruptures in elastic solids, a critical background shear stress level (τ^{pulse}) exists below which ruptures cannot propagate as cracks. The mode of rupture propagation is uncertain above this critical stress level, but numerical simulations suggest that there is a narrow range of background stress levels around the critical stress level at which ruptures propagate as self-sustaining slip

pulses (Cochard and Madariaga, 1994; Zheng and Rice, 1998; Noda et al., 2009). This phenomenon is also observed for shear ruptures in laboratory experiments (Lykotrafitis et al., 2006). Substantial evidence supports the idea that ruptures propagate as self-sustaining slip pulses instead of cracks. The duration of slip at a point on a fault calculated from seismic inversions is much shorter than expected from crack-like propagation models (Heaton et al., 1990). Simulation results show that only pulse-like propagation honors the scaling between slip and rupture length, and that the slip for crack-like propagation is an order larger (Noda et al., 2009). It is expected that natural faults are most likely to host ruptures soon after the stresses build up to the minimum level that would support pulse-like propagation provided nucleation events are sufficiently frequent. Although crack-like propagation is certainly possible at higher stress levels, yet the likelihood decreases as stresses keep building. Potentially, it may be possible to quantify the probability of the propagation mode as a function of background shear stress levels under given constraints on the rate of nucleation events from sources such as background seismicity, or earthquake cycle simulations that produce a realistic distribution of event sizes. In this study, we assume that ruptures propagate as self-sustaining pulses.

We use this approach to model damage zones formed due to slip on reservoir-scale second-order, buried, thrust faults observed in the CPE gas field. Since the modeling in performed in a continuum framework, results obtained are in terms of plastic strains. In order to facilitate comparisons with field observations of fracture density (number of fractures per unit length), plastic strains are converted into a fracture population by assuming the volume created by plastic strains to be expressed in the form of fractures, and considering appropriate fracture dimensions. Since the observed damage zones are a result of several slip events of various magnitudes that the fault may have hosted, we account for them in the modeling workflow by superposing the plastic strain field due to several slip events of various sizes, such that the magnitude of those slip events and their frequency are consistent with the Gutenberg Richter scaling law. We then compare the modeled damage zones with field observations (chapter 2) which report 50-80 meter wide damage zones in which the decay of fracture intensity with distance from the fault can be described by a power law, the rate of decay between 0.4 and 1.

Information derived from modeling can then be used to constrain the magnitude and extent of damage in the material off of the fault. This information, used in conjunction with knowledge

of fracture intensity and orientations (from borehole image data) can facilitate us in building more geologically constrained and seismologically consistent fracture network models which, in turn, can help constrain fluid flow modeling through damage zones and fractured reservoirs.

3.4 Model Description

3.4.1 Model setup

In this study, rupture propagation is studied using two-dimensional plain-strain models. The fault obeys a strongly rate-weakening friction law in a rate and state framework. The inelastic deformation of the material surrounding the fault is accounted for by using Drucker-Prager plasticity. The medium is assumed to be homogeneous and semi-infinite half space in extent, and is governed by the momentum conservation equation and constitutive response given by equations 3.1 and 3.2.

$$\rho \frac{\partial v_i}{\partial t} = \frac{\partial \sigma_{ij}}{\partial x_j} \tag{3.1}$$

$$\frac{\partial \sigma_{ij}}{\partial x_j} = C_{ijkl}\left(\dot{\varepsilon}_{kl} - \dot{\varepsilon}^{p}_{kl}\right) \tag{3.2}$$

where ρ is the density, v_i is the particle velocity, σ_{ij} is the stress component, $\dot{\varepsilon}_{kl}$ and $\dot{\varepsilon}^{p}_{kl}$ are the total and plastic strain rates (the difference between the two is the elastic strain rate) and C_{ijkl} is the elastic modulus tensor. The total strain rate is given by:

$$\dot{\varepsilon}_{ij} = \frac{1}{2}\left(\frac{\partial v_i}{\partial x_j} + \frac{\partial v_j}{\partial x_i}\right) \tag{3.3}$$

Assuming isotropic elastic properties we get:

$$C_{ijkl}\dot{\varepsilon}_{kl} = K\dot{\varepsilon}_{kk}\delta_{ij} + 2G\left(\dot{\varepsilon}_{ij} - \delta_{ij}\dot{\varepsilon_{kk}}/3\right) \tag{3.4}$$

where K and G are the bulk and shear moduli. The S wave speed is $c_s = \sqrt{G/\rho}$ and Poisson's ratio υ is 0.25.

3.4.2 Drucker Prager yield criteria

We idealize the material surrounding the fault as a Drucker-Prager elastic-plastic solid. A similar assumption has also been made in other published studies on dynamic rupture propagation (Andrews, 2005; Ben-Zion and Shi, 2005; Duan and Day, 2008; Ma, 2009; Templeton and Rice, 2008; Viesca et al., 2008). The Drucker-Prager yield criterion (Drucker and Prager, 1952) is a pressure-dependent modification of the Huber-von Mises yield criterion and is given by

$$\bar{\tau} + \mu(\sigma_{kk}/3) = b \tag{3.5}$$

where $\bar{\tau}$ is the second invariant of the deviatoric stress tensor S_{ij} ($\bar{\tau} = \sqrt{S_{ij}S_{ij}/2}$, $S_{ij} = \sigma_{ij} - (\sigma_{kk}/3)\delta_{ij}$), $\sigma_{kk}/3$ is the mean stress, μ is the Drucker-Prager (DP) friction coefficient while b is the DP cohesion or shear strength at zero mean stress. The pressure-dependent elastic plastic formulation described by Rudnicki and Rice (1975) reduces to it when μ is assumed to be independent of the stress level. The yield surface defining the shear strength, therefore, is a function of the mean normal stress. In plane strain models, the DP criterion approximates the Mohr Coulomb (MC) criterion which is given by

$$\tau + (\tan\phi)\sigma_n = c \tag{3.6}$$

where τ and σ_n are shear and normal traction acting on the fault plane, ϕ is the coefficient of internal friction and c is the cohesion. For a two-dimensional stress state where the out of plane principal stress is approximated as $\sigma_{zz} = (\sigma_{xx} + \sigma_{yy})/2$, the DP and MC criteria exactly coincide. In such cases, the DP cohesion and friction coefficient are related to the MC coefficients as $b = c\cos\phi$ and $\mu = \sin\phi$. Both, the MC and DP criteria idealize the behavior of brittle materials to compressive stresses, but neither fully describes the inelastic behavior of rocks (Davis and Selvadurai, 2002; Colmenares and Zoback, 2002). However, we use the DP criterion since it is easier to implement numerically due to a smooth yield surface. We neglect cohesion since the deformation processes prior to and during fault formation would have intrinsically damaged the surrounding rock leading to near-negligible cohesion values.

3.4.3 Velocity weakening fault friction

The steady-state friction coefficient used is extremely velocity-weakening. This is supported by experimental evidence (Tsutsumi and Shimamoto, 1997; Tullis and Goldby, 2003 a, b; Prakash and Yuan, 2004; Hirose and Shimamoto, 2005; Beeler et al., 2008). This friction law is provided by the flash heating model by Rice (1999, 2006), Beeler and Tullis (2003), Tullis and Goldsby (2003a, 2003b), and Beeler et al., (2008). This theory provides us with a model for the steady state friction (which is a function of slip velocity and temperature) coefficient $f_{ss}(V, T)$ of the fault. If we assume asperities of a mean length D sliding with a constant velocity V, the life time of the asperities is $\theta_{max} = D/T$. The average contact shear strength τ_c is approximately $0.1\mu = 3\text{GPa}$ (Rice (2006)). The one-dimensional heat conduction equation is solved to evaluate the increase in temperature due to heat generated at the asperity contact.

$$T_c = T + \frac{\tau_c V\sqrt{\theta}}{\rho c\sqrt{\pi\alpha_{th}}} \tag{3.7}$$

T_c is the asperity contact temperature, T is the initial temperature (assumed to be the background temperature), θ is the contact time, ρ is the density and c is the specific heat capacity. Since the actual area of contact of the asperities is much smaller than the actual macroscopic area, the change in contact temperature and hence the local rate of heat production per unit surface area at the contacts ($\tau_c V$) is larger than the average macroscopic rate of heat production (τV). However, the total rate of heat production is same at the micro and macro scales ($\tau VA = \tau_c VA_c$).

If we now assume that the asperities completely weaken at the weakening temperature T_w, the time required for them to weaken (from (2.7)) is

$$\theta_w = \frac{\pi\alpha_{th}}{V^2}\left(\frac{T_w - T}{\frac{\tau_c}{\rho c}}\right)^2 \tag{3.8}$$

In order for the asperities to weaken completely within their lifetime, the time required for weakening θ_w should be less than the asperity life-time θ_{max}. Solving for the weakening velocity V_w assuming an equality between θ_w and θ_{max}, we get

$$V_w(t) = \frac{\pi\alpha_{th}}{D}\left(\frac{T_w - T}{\frac{\tau_c}{\rho c}}\right)^2 \tag{3.9}$$

Using values $D = 5\mu m, T_W = 500℃, \tau_c = 3GPa, \alpha_{th} = 0.7mm2/s, \rho c = 2.7MPa/K$ and initial background temperature $T_0 = 210℃$, we obtain an slip weakening velocity of 0.17 m/s.

We assume that the asperity contact loses shear strength abruptly at the onset of flash heating when the temperature reaches T_w from τ_c to completely weakened constant contact strength τ_{cw}. The coefficients f_{LV}(friction coefficient at low velocity $V < V_W$) and f_w (fully-weakened friction coefficient) are obtained by dividing $\tau_c$and τ_w by the effective normal stress acting on the fault. So far, we have considered the contact shear strength before weakening τ_c a constant, which implies that the low-velocity friction coefficient f_{LV} is a constant (assuming no change in the contact area). However, if we consider sliding as a process that thermally activates defect motion at asperity contacts, the low-velocity friction coefficient would be a function of sliding velocity V (Rice et al., 2001). Thus, a conventional logarithmic velocity-weakening friction law employed for f_{LV} is (Noda et al., 2009).

$$f_{LV}(V) = f_0 + (a - b)\ln(V/V_0) \tag{3.10}$$

$f_0 = 0.7, V_0 = 1\mu m/s$ and $(b - a)$ =0.004 (Noda et al., 2009). a is the direct effect parameter and b is the state evolution parameter. The value of a that we use is 0.016. It is obtained by a linear extrapolation with absolute temperature, a being 0.01 at room temperature. f_0 and V_0 are the reference slip and velocity values.

The value of fully-weakened friction f_w that we use is 0.13. This is obtained by fitting to experimental data (Beeler and Tullis, (2003); Tullis and Goldsby (2003 a, 2003 b); Beeler et al., (2008)). The steady state friction coefficient in the flash heating model is obtained by averaging the strength over the existing set of asperities. Consequently, if a single contact gets instantaneously weakened upon the temperature reaching weakening temperature, the macroscopic large-scale strength is not significantly affected. Therefore, in steady state, the average shear strength of the entire asperity population is equal to the average strength of a contact over its life time. This procedure provides us with the following relations (Rice, 1999, 2006).

$$f_{ss}(V,T) = \begin{cases} f_{LV}(V) & \text{if } V \le V_w \\ f_w + [f_{LV}(V) - f_w]\left[\frac{V_w(t)}{V}\right] & \text{if } V \ge V_w \end{cases} \tag{3.11}$$

The expression in 3.11 is non-differentiable at V=Vw. In order to make the transition smoother, we use $f_{ss}(V,T) = f_w + \frac{f_{LV}(V) - f_w}{[1+(V/V_w)^n]^{1/n}}$ when$V \geq V_w$. Finite values of *n* smooth the onset of strongly rate-weakening behavior. This expression approaches 3.11 in the limit $n \to \infty$. In this study, we choose *n* = 8.

The use of purely rate-weakening law as described above leads to mathematically ill-posed problems (Rice et al., 2001). Hence, the steady state frictional response is encapsulated in a rate and state friction framework.

$$f(V,\Theta) = a\ln\left(\frac{V}{V_0}\right) + \Theta \tag{3.12}$$

$$\frac{d\Theta}{dt} = -\frac{V}{L}[f(V,\Theta) - f_{ss}(V,T)] \tag{3.13}$$

The fault strength τ, which is always equal to the shear stress acting on the fault is

$$\tau = f(V,\Theta)\sigma \tag{3.14}$$

The value of state evolution distance L that is used is comparable to the asperity diameter D assuming a slip of D refreshes all contacts. Value of L used in these simulations is 0.00397 m. If we assume that all asperity contacts are refreshed after slipping a distance D, it means that the state evolution distance should be a fraction of D. Such values of L are too small to be used in rupture propagation simulations.

The initial value of the state variable is obtained as following:

From (3.12), the initial value of steady state friction at initial stress conditions is

$$f(V_i,\Theta_i) = a\ln(V_i/V_0) + \Theta_i \tag{3.15}$$

where V_i and Θ_i are the initial velocity and initial state variable.

$$\text{Also, } f(V_i,\Theta_i) = \tau_i/\sigma_i \tag{3.16}$$

where τ_i and σ_i are the initial shear stress and effective normal stress acting on the fault.

Suppose the velocity suddenly changes to the peak slip velocity V_p at which the friction acting on the fault achieves its maximum value f_s. As long as the slip velocity increases suddenly, the value of state variable remains unchanged. Therefore,

$$f_s = a\ln(V_p/V_0) + \Theta_i \tag{3.17}$$

Substituting (3.16) in (3.15) and subtracting (3.15) from (3.17) gives us

$$f_s - \tau_i/\sigma_i = a\ln(V_p/V_i) \tag{3.18}$$

Therefore, $V_i = V_p \exp\left(-\frac{1}{a}(f_s - \tau_i/\sigma_i)\right)$ (3.19)

Substituting (3.19) and (3.18) in (3.17) and solving for Θ_i we get

$$\Theta_i = f_s - a\ln(V_p/V_0) \tag{3.20}$$

For $f_s = 0.7$, $a = 0.016$, $V_p \sim 1$m/s and $V_0 = 1\mu m/s$, we get $\Theta_i = 0.4790$

3.4.4 Off-fault inelastic response

In this model, the stresses are allowed to exceed the yield surface, but the stresses in excess of the yield surface relax back towards the yield surface in the absence of additional loading. Viscous effects are neglected in this study (we consider rate-independent plasticity). The material behaves elastically as long as $F(\sigma_{ij}) = \bar{\tau} + \mu\left(\frac{\sigma_{kk}}{3}\right) < 0$. The way the numerical code works is that at any time step, equation (2) is solved assuming zero plastic strain rate ($\dot{\varepsilon}^p_{kl} = 0$). If the updated stresses calculated for the next time step are such that the stress state lies below the yield surface (i.e. $F(\sigma_{ij}) < 0$), we move on to the next time step. However, if the stress state lies above the yield surface (i.e. $F(\sigma_{ij}) < 0$), a non-zero value of the plastic strain rate $\dot{\varepsilon}^p_{kl}$ is introduced such that the stress state relaxes back to the yield surface. The path of relaxation is governed by the flow rule given by:

$$\dot{\varepsilon}^p_{kl} = \lambda P_{ij}(\sigma_{ij}) \tag{3.21}$$

λ is the equivalent plastic strain rate, which essentially is a scalar measure or magnitude of the shear plastic strain rate. During rate-independent plastic flow, λ is evaluated such that stresses lie exactly on the yield surface. $P_{ij}(\sigma_{ij})$ defines how the plastic strain rate is partitioned between various components of the plastic strain rate tensor. λ and $P_{ij}(\sigma_{ij})$ are defined as:

$$\lambda = \sqrt{2\dot{e}_{ij}^{p}\dot{e}_{ij}^{p}} \tag{3.22}$$

where $\dot{e}_{ij}^{p} = \dot{\varepsilon}_{ij}^{p} - (\dot{\varepsilon}_{kk}^{p}/3)\delta_{ij}$

$$P_{ij}(\sigma_{ij}) = S_{ij}/(2\bar{\tau}) + (\beta/3)\delta_{ij} \tag{3.23}$$

β is the plastic dilatancy which is the ratio of volumetric to shear plastic strain. The total shear plastic strains are calculated by integrating the plastic strain rate over time.

$$\gamma^{p} = \int \lambda dt \tag{3.24}$$

Corresponding volumetric strains are calculated as a product of dilatancy and total shear plastic strain.

$$\varepsilon^{p} = \beta\gamma^{p} \tag{3.25}$$

On substituting the flow rule (21) into Hooke's law (2), we obtain

$$\frac{\partial\sigma_{ij}}{\partial x_j} = C_{ijkl}[\dot{\varepsilon}_{kl} - \lambda P_{kl}(\sigma_{kl})] \tag{3.26}$$

In this work which considers rate-independent plasticity, stresses are not allowed to exceed the yield surface. Mathematically, the yield condition is written as

$$F(\sigma_{ij}) = 0 \tag{3.27}$$

3.5 Area of Study – CPE Gas Field

Damage zones associated with second-order thrust faults (~3 kilometer long) in the CPE gas field are modeled. This field produces wet gas from compressionally uplifted, fractured,

crystalline and metamorphic basement and overlying sedimentary rocks. Active deformation has partitioned the reservoir into distinct structural and stress domains. Figure 3.1 presents a perspective view of the field prepared on GOCAD showing the master fault and second-order faults identified in seismic images. The map lengths of the second-order faults vary from 50 m to 3 km. All seismically resolvable faults have reverse slip. They strike sub-parallel to the master fault and are concentrated in a 1x8 km area along the crest of the anticline. The fault dips lie between 55° and 80°. The maximum throw across these faults ranges from 8 to 180 m. There is uncertainty regarding the downdip extent and trajectory of most faults due to poor seismic reflectivity at depth; therefore, a conservative approach is adopted and only the fault surfaces with direct seismic evidence are interpreted.

Figure 3.1 also shows the 5 wells studied here - A, B, C, E, and I. Wells A, E, and I are near vertical wells while wells B and C are deviated wells. Well tests were performed after drilling the vertical wells (A, E and I). These tests suggested that there is poor correlation between wellbore-reservoir contact length and well performance. In fact there is also a very weak correlation between well performance and the total number of fractures that they intersect. However, there is a strong correlation between the total number of critically stressed fractures transected by the wellbore and well performance (pc, ConocoPhillips). This inference was used to design the trajectory of wells B and C with the intention of maximizing the borehole intersection with reservoir-scale second-order faults and their respective damage zones containing a rich population of critically stressed faults. As expected, wells B and C were extremely productive, with production rates as large as 1 billion cubic feet per day (bcf/day) while the other vertical wells produced between 0.1 and 0.3 bcf/day (pc, ConocoPhillips). With the critical role of damage zones in influencing flow and production clearly evident, the objective is to model these damage zones associated with second-order faults so that they can eventually be incorporate in flow simulation models.

In order to determine whether the second-order faults slipped in the present-day stress state or in the geologic past under a different stress state, we study the present-day stress regime, orientation of second-order faults, and the nature of faulting. The present-day strike-slip stress field and the steeply dipping fault orientations cannot explain the reverse slip across faults observed in 3D seismic images. Therefore, it is concluded that these second-order faults must

have slipped in the geologic past under a reverse-faulting stress regime and a rotated configuration (so that the faults have shallow dipping angles (~30°)) that promotes thrust faulting. Stratigraphic studies suggest that changes in the depth of faults from the free surface may not be significant, so I do not depth-shift the faults for modeling purposes.

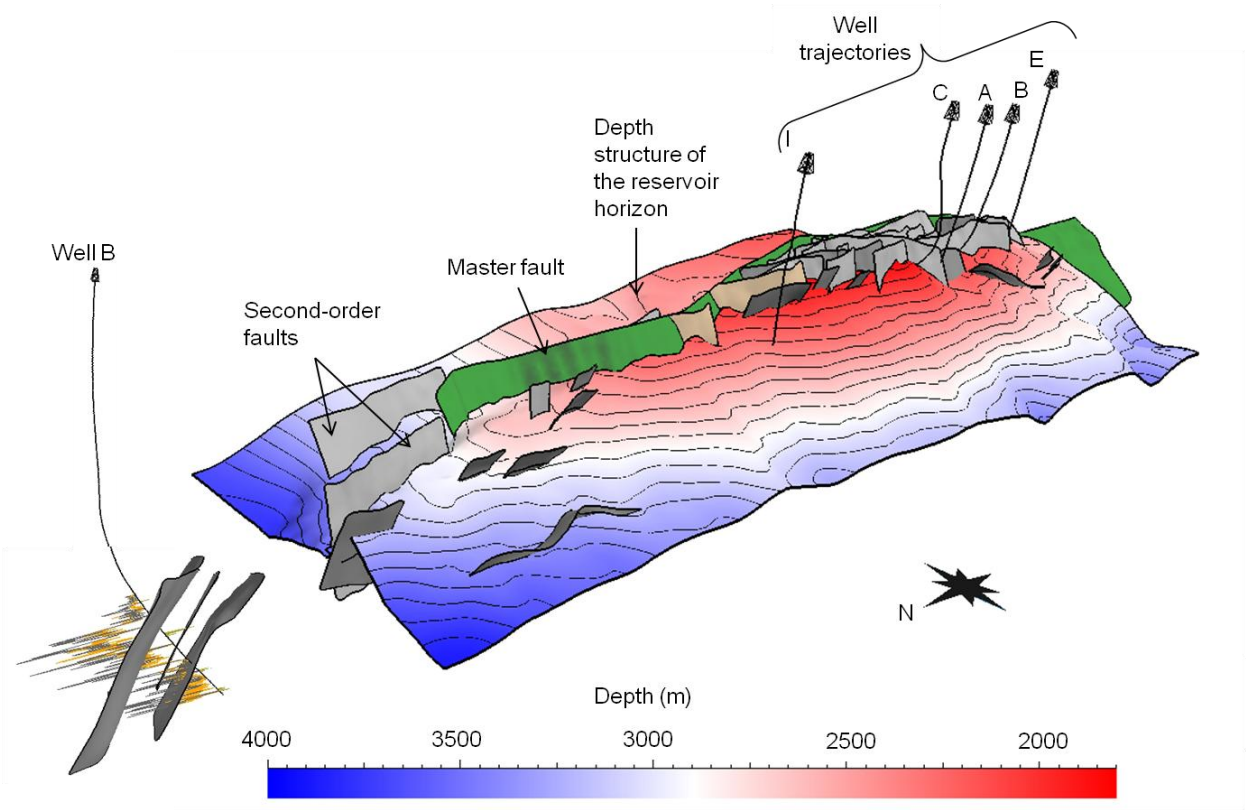

Figure 3.1: Three dimensional structural model of CPE gas field. The model shows the master fault (first order fault), second order faults, well bore trajectories and the depth structure of the reservoir horizon. Histogram of fractures identified along with the 3 second-order faults intersected by well B are also shown.

3.6 Model Development and Initial Conditions

3.6.1 Model set-up

A 30° dipping reverse fault in a homogeneous half space representing an optimally oriented fault is considered (Figure 3.2). The fault is 3 km long. Since there is uncertainty regarding the downward extent of the seismic-scale faults due to poor seismic image quality, I assume the dip length of the fault to be equal to the strike length (which is easier to identify in seismic images). The top of the model represents the free surface. The fault does not break the surface. An absorbing boundary condition is applied to the bottom and sides of the blocks, and a

traction free boundary condition is applied to the surface. The origin is placed at the center of the fault located at a depth of 2.2 km. Ruptures may propagate bilaterally or unilaterally along the fault surface. To begin with, I will show an example of a rupture that nucleates at the center of the fault (origin) and propagates bilaterally in both directions, and another example of a rupture that nucleates close to the lower extent of the fault and propagates unilaterally along the up-dip direction.

3.6.2 Fault profile

Both planar and nonplanar faults are considered in this study. Previous studies suggest that natural fault surfaces exhibit deviations from planarity at all scales (Brown and Scholz, 1985; Power et al., 1988; Power and Tullis, 1991; Lee & Bruhn, 1996; Renard et al. 2006; Sagy et al., 2007; Candela et al., 2009; Candela and Renard, 2012). Observations demonstrate that faults are self-similar fractal surfaces (Power and Tullis, 1991). The amplitude to wavelength ratio α of these surfaces lies between 10-3 and 10-2, the lower limit being more representative of mature faults (Power and Tullis, 1991), and this is independent of scale. Sagy and Brodsky, (2009) suggest that α decreases as faults mature due to wear processes. In this study, we generate a fault having α 0.005 and minimum roughness wavelength of 60 m. A mathematical description for generating rough fault profiles is provided in Appendix 3B. Stress perturbations caused by the roughness impact the rupture propagation by introducing heterogeneities in the slip distribution and cause rapid accelerations and decelerations at the rupture front (Dieterich and Smith, 2009).

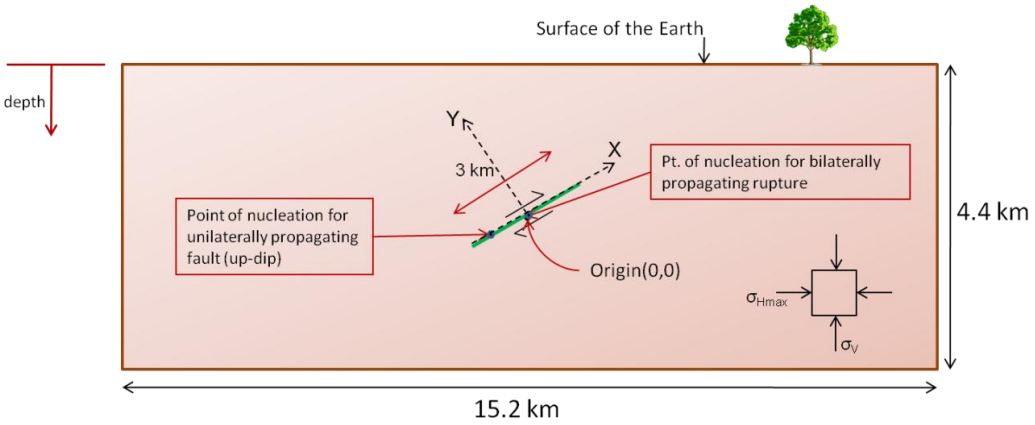

Figure 3.2: Two-dimensional idealization to model slip on a buried thrust fault dipping at 30^0. The green line represents the fault surface. X axis is aligned along the fault in the up-dip direction.

3.6.3 Background stresses

Next, the model described above is loaded with a reverse-faulting stress state. The maximum horizontal stress and the vertical stress are assumed to be the maximum and minimum principal stresses, while the minimum horizontal stress lies in the plane of the fault. The stress field applied is depth dependent. The total vertical stress gradient is 23 MPa/km (obtained from density logs) while the pore pressure is 12 MPa/km (interpreted from drillstem test data).

In this study, ruptures are assumed to propagate as self-sustaining pulses. Since pulses propagate only at a very narrow range of background shear stresses (or a narrow range of the ratio between shear to normal stresses resolved on the fault plane), it is possible to constrain the maximum horizontal principal stress at which slip nucleates given the vertical stress. The magnitude of the maximum horizontal stress is assumed to be the minimum stress at which the resolved shear to effective normal stress ratio (τ/σ_n) on the fault is barely sufficient to cause a rupture to propagate as a self-healing pulse. For the parameters used to define the strongly rate-weakening friction law chosen in this study, the value of τ/σ_n is 0.336 for a planar fault and 0.3476 for a nonplanar fault. These values are far less than the levels conventionally assumed in rupture modeling (e.g., Harris et al., 2009). This might suggest that the stresses in Earth's crust should not build up to larger levels. However, fault roughness on nonplanar faults introduces an additional resistance to slip (roughness drag) due to which larger values of τ^{pulse}/σ_n (depending on the amplitude to wavelength ratio α and the local slope of the fault at the nucleation point) would be required to propagate the rupture as a pulse (Fang and Dunham, pc). A discussion on the stress state on faults and weakening mechanisms is provided in Appendix 3C.

In the present study, for a vertical stress gradient of 23 MPa/km, the maximum principle stress gradient calculated from the appropriate τ/σ_n is 33.6 MPa/km for a planar fault and 34.04 MPa/km for a nonplanar fault. The initial out-of-plane normal stress (minimum horizontal stress) is taken to be the average of the two in-plane normal stresses (following Templeton and Rice, 2008). This stress component is only relevant during plastic flow. For this assumption, the Drucker-Prager yield function coincides with the Mohr-Coulomb condition. However, this correspondence ceases once plastic flow commences.

3.6.4 Simulation details and input parameters

A 2D finite-difference method is used to model the dynamic rupture propagation. This is done in the framework of continuum plasticity. The governing equations (3.1, 3.26 and 3.27) are written as a system of first-order partial differential equations with an algebraic constraint. The structured mesh discretizes the medium keeping the grid spacing approximately 1 m in both directions. All components of velocity and stress are defined at each grid point. Spatial derivatives are approximated using a summation-by-parts finite difference method (Kreiss and Scherer, 1974, 1977; Strand, 1994; Mattsson and Nordström, 2004). The boundary conditions are weakly enforced using the simultaneous approximation term technique (Carpenter et al., 1994). This scheme is high-order accurate (Kozdon et al., 2012). A complete description of the numerical method and simulation process is provided in Dunham et al. (2011a) and Kozdon et al. (2011, 2012). Table 3A-1 in Appendix 3A lists the values of various model parameters used in the simulations. The parameters of the friction law are similar to those used by Noda et al. (2009) who selected them from a compilation of laboratory studies. The time step in the flat fault and rough fault simulations is 40 μs and 20 μs respectively.

3.6.5 Arresting a propagating rupture

Ruptures propagating on a fault may arrest due to several reasons such as end of a fault surface, fault intersection, or unfavorable fault geometry. Arresting the rupture abruptly generates large plastic strains. This is an artifact of the sudden stoppage of the rupture that creates large stress perturbations. Evidence from seismic inversions suggests that the rupture arrest process is gradual. A gradual rupture arrest process is mimicked in these simulations by ramping up the value of the direct effect parameter a to values larger than the evolution effect parameter b gradually over a spatial distance of 80 meters. Ramping up the a value gradually transforms the friction law from rate weakening to rate strengthening. This arrests the rupture gradually over a relatively large distance, and prevents the generation of unreasonably large stress perturbations and plastic strains.

3.7 Results

Please note that although most results shown below and the distinctions made in terms of differences in damage zone attributes in the hanging wall and footwall are general, others may be specific to thrust faults that we have modeled in this study.

3.7.1 Slip-induced inelastic deformations

As a rupture propagates, it deforms the rock around the propagating rupture front inelastically. A discussion on the mode of rupture propagation and fault slip profiles is provided in Appendix 3D. Here, I will only focus on inelastic deformations due to rupture propagation. Figures 3.3(a) and (b) show the equivalent plastic shear strain field generated due to shear ruptures on planar and nonplanar faults that nucleate at the center of the fault and propagate bilaterally, while Figures 3.3(c) and (d) represent the plastic strain field generated due to unilaterally propagating ruptures on planar and nonplanar faults that propagate in the up-dip direction. The fault dips at 30º, but the plot has been rotated by 30º in the clockwise direction so that the fault surface is aligned with the X-axis (Figure 3.2). The region undergoing inelastic deformations is considered the damage zone formed due to slip on the fault.

The plastic strains are mostly limited to the extensional stress quadrants with respect to the slip mode on the fault. This is in accordance with Templeton and Rice (2008), who have shown that the region undergoing inelastic deformation around a propagating crack tip depends on the angle ψ between the fault plane and the direction of maximum principal stress. For ψ less than 20º, the inelastic deformation occurs primarily in the compressional quadrants while for ψ larger than 45º, the inelastic deformation occurs exclusively in the extensional quadrants. For angle ψ of 30º as used in this study, the inelastic deformation occurs primarily in the extensional quadrants. We also notice that the equivalent plastic strain field is relatively uniform for a planar fault as compared to a nonplanar fault where the plastic strain field is strongly modulated by the fault nonplanarity (Dunham et al., 2011b). Figure 3.3 also shows transects perpendicular to the fault surface along which we study the variation of plastic strains and fracture density. These transects are located at 300 m, 600 m, 900 m, 1200 m and 1500 m from the point of nucleation for bilaterally propagating ruptures and at 500 m, 1000 m, 1500 m, 2000 m and 2500 m for the unilaterally propagating ruptures.

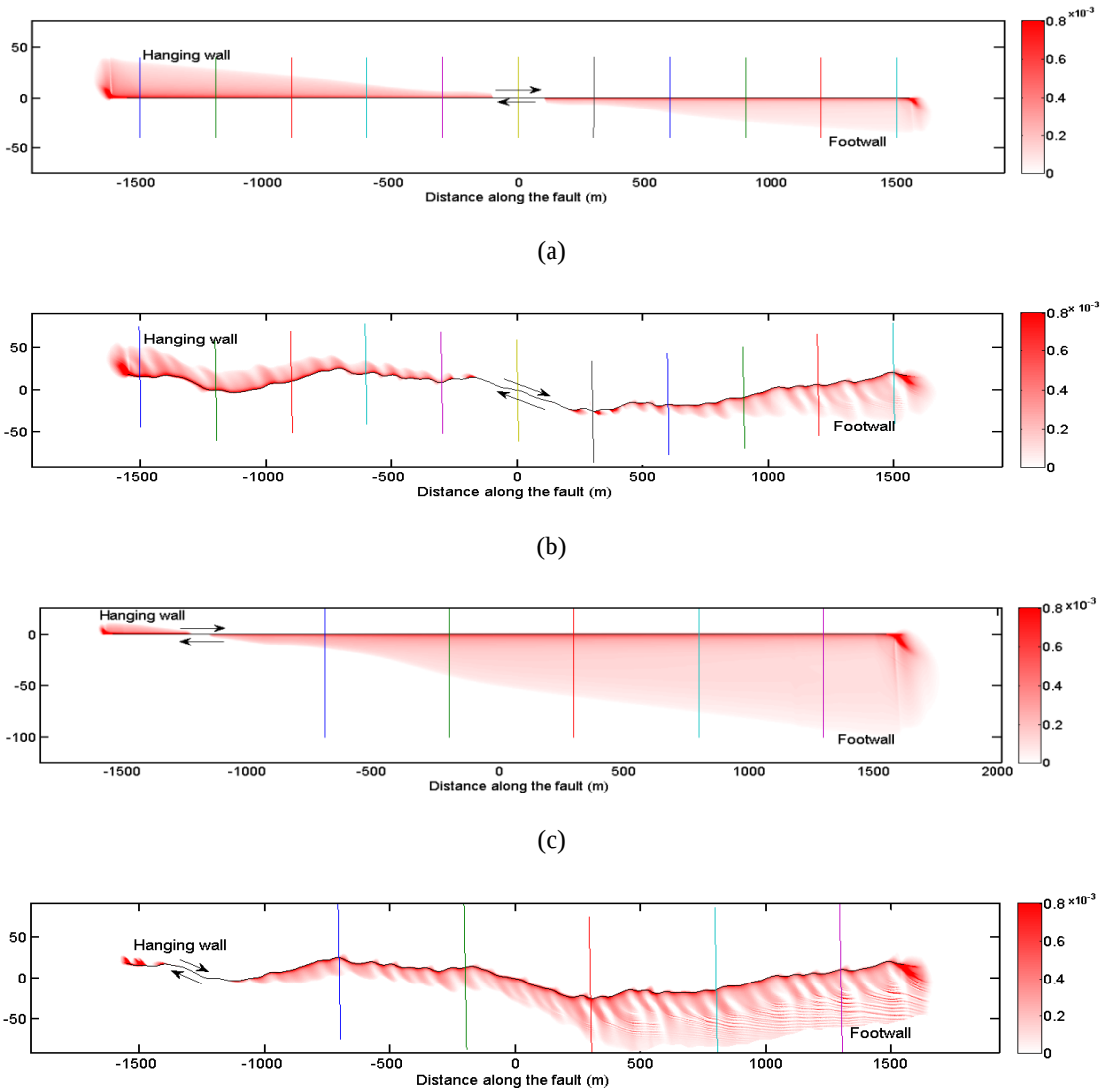

Figure 3.3: Equivalent plastic strain field generated during dynamic shear rupture. (a) and (b) Ruptures that nucleate at the fault center (origin) and propagate bilaterally on a planar and nonplanar fault, respectively. (c) and (d) Ruptures that nucleate close to the lower end of a planar and nonplanar fault and propagate unilaterally. These 30^{o} dipping planes have been rotated clockwise to lie along the X-direction. The vertical lines represent transects along which we study plastic strain and fracture density variation. (All dimensions are in meters) Volumetric plastic strains are obtained as a product of dilatancy and shear plastic strains. Vertical exaggeration in scale of 2.7

Figure 3.4 shows the spatial extent of plastic strains generated from the surface of faults. The X-axis represents the distance along the fault with positive values indicating the fault surface above the center of the fault. The Y-axis represents the perpendicular distance from the fault up to which finite plastic strains (damage) are generated. Figure 3.4(a) represents the extent of finite plastic strains (inelastic deformations) for bilaterally propagating ruptures that nucleate at the

origin, while Figure 3.4(b) represents the extent of plastic strains around ruptures that nucleate close to the lower extreme of the fault and propagate unilaterally, primarily in the up-dip direction. Blue lines represent the extent of plastic strains from the fault due to rupture propagation on a planar fault while the red lines represent those due to propagation on a nonplanar fault.

From both the plots, we notice that the extent of inelastic deformations increases with propagation distance (distance from the point of nucleation) for both planar and nonplanar faults. A similar phenomenon has also been reported by Andrews (2005); Yamashita (2000); Dalguer et al. (2003a, b); Templeton and Rice, (2008), but for cracks. The reason emerges out of self-similarity of the propagating rupture. The crack length or the size of the slip pulse increases linearly with propagation distance. This results in a linear increase of the energy release rate with propagation distance. The energy release rate is balanced by the fracture energy, which has two contributors, frictional weakening on the fault and energy dissipated due to plastic deformation. In the simulations performed in this study, contribution from plastic deformation dominates; therefore, the amount of net plastic strains adjacent a particular section of the fault increases linearly with propagation distance. However, since the magnitude of plastic strain almost remains constant, the extent of inelastic deformation from the fault increases linearly with propagation distance. Details of energy balance during rupture propagation showing increase in extent of off-fault plastic strains with propagation distance are provided in Appendix 3E. (Please note that in Figure 3.4, the extent of damage at values of X to the right of the nucleation point represent the damage in the footwall while those on the left represent damage in the hanging wall of the modeled thrust fault.) Consequently, for a fault of a certain size, unilateral ruptures can achieve larger propagation distances resulting in a larger region deforming inelastically. Therefore, damage zones modeled due to a single rupture are spatially heterogeneous, their widths increasing linearly with distance from the nucleation point. However, we will see later that this variability gets homogenized when we consider the effect of multiple slip events uniformly distributed on the fault plane.

For ruptures propagating on nonplanar faults, stress perturbations caused by fault roughness impact the rupture propagation by introducing heterogeneities in the slip distribution, stress heterogeneities that affect the occurrence of plastic strain, and rapid accelerations and

decelerations of the rupture front. From the red lines in Figure 3.4, we see that the local fault roughness modulates the extent of inelastic deformations from the fault. This leads to short wavelength variations in the extent of the inelastically deforming region. However, the overall trend of increasing off-fault extent of plastic strains with propagation distance holds.

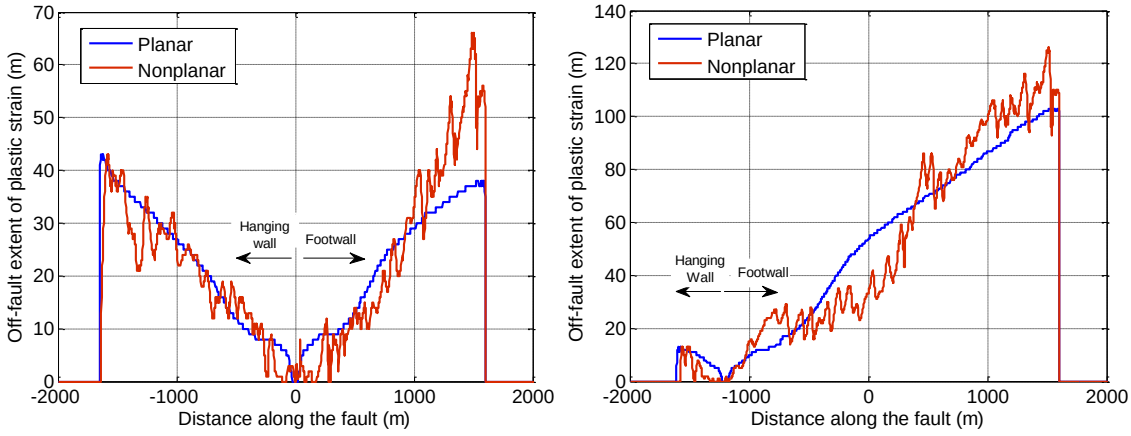

(a) (b)

Figure 3.4: Extent of damage from the surface of a planar fault vs. a nonplanar fault. The damage zone at points above the nucleation point (points to the right of the nucleation point in the plots above) is present in the footwall while that below the nucleation point is in the hanging wall.

3.7.2 Converting plastic strains to fractures

So far, we have obtained continuum plastic shear and volumetric strains generated in the material surrounding the fault on which the rupture propagates. However, the objective is to compare model results (obtained in continuum) with damage zones observed around faults (chapter 2) which are quantified in terms of fracture density (number of fractures per unit length). Therefore, it is required to convert dilatant plastic strains to fractures. With that objective, it is assumed that the entire volume created by dilatant plastic strains is manifested completely in the form of macro-fractures. As mentioned earlier, the structured mesh discretizes the medium keeping a grid spacing of about 1 m x 1 m. I consider a cubic volume element of dimension h around each grid point and assume the plastic strain present at that grid point to be representative of the plastic strain in this unit volume (Figure 3.5).

Total volume created by plastic strains in this cubic volume = $\beta\gamma^{p}h^{3}$ where β is the dilatancy and γ^{p} is the shear plastic strain.

Assuming the average fracture dimension inside this cubic volume to be h^2 , the average volume of a fracture inside the cubic volume = $\text{aperture} \times h^2$

Therefore, number of fractures in the cubic volume = $(\beta\gamma^p h^3)/(\text{aperture} \times h^2) = \beta\gamma^p h/\text{aperture}$

Hence, fracture density = $(\beta\gamma^p/\text{aperture})$ fractures per meter. The result is thus independent of the spatial discretization h.

Dilatancy is defined as the change in volume resulting from the shear distortion of material element. Dilatancy can mathematically be expressed as $\sin(\varphi)$ where φ is the dilatancy angle. Assuming a dilatancy angle of 15º (Alejano and Alonso, 2005), we obtain a dilatancy of 0.26.

Several studies report experimentally observed values of average fracture apertures (Esaki et al. 1999; Chen et al. 2000; Lee and Cho, 2002). Morphological analyses of fracture surfaces show prominent surface undulations (Giacomini, 2008). This leads to a spatially heterogeneous aperture distribution over the fracture surface. Studies also suggest that the fracture surface aperture distribution could be approximated by a normal distribution (Hakami, (1995) for the case of natural fractures, Esaki et al. (1999) for artificially created tensile fractures, and Lee and Cho, (2002) for tensile fractures in granite). Therefore, in the absence of a unique fracture aperture value, an equivalent mechanical aperture is measured by various methods such as using gas to measure fracture volume (Chen et al. 2000). These studies also show that the mechanical aperture of fractures is sensitive to shear displacement across fractures and the confining pressure. For confining stresses between 6.9 MPa and 34.5 MPa (which includes the range of normal stresses acting on fractures in our region of study) and shear displacement of 0.5 mm across fractures (we assume a modest shear slip assuming fractures formed are shear fractures with a finite shear displacement), the average mechanical aperture experimentally reported is approximately 0.1 mm (Chen et al., 2000).

Following this methodology helps to compute the spatial distribution of fracture intensity created by slip on the fault. Although the magnitude of fracture density is dependent on the assumption of mean fracture aperture, the relative fracture density at various points around the fault is independent of this assumption. We will see later in this chapter that since the model

anyway is calibrated by matching the absolute magnitude of fracture density observed in the CPE data set, the assumption on the mean fracture aperture is inconsequential.

Ideally, the partitioning of dilatant plastic strains into both microfractures (characteristic length scale in millimeters) and macrofractures (characteristic length scale in meters) should be considered, but since the ultimate objective is to study the large-scale permeability anisotropy introduced by damage zones, I limit my analysis to macro fractures.

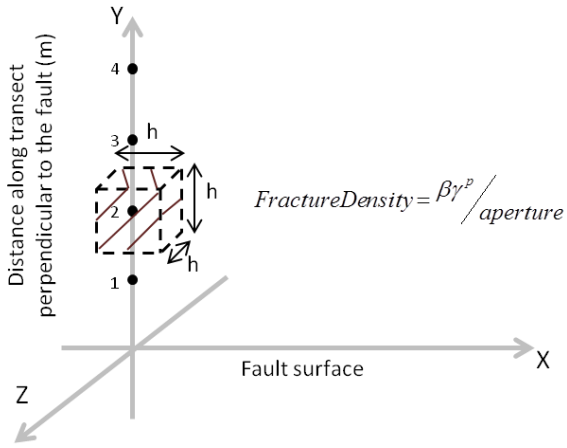

Figure 3.5: Conversion of plastic strains to fracture intensity. Volume created by dilatant plastic strain inside the cubic volume is assumed to be manifested completely in the form of fractures. By making reasonable assumptions of fracture dimensions, the fracture density at various points can be calculated.

3.7.3 Decay of fracture density with distance from the fault

Adopting the above methodology, the fracture density along various transects perpendicular to the fault is calculated and its variation with distance from the fault studied. Figure 3.6 shows this variation in the damage zone resulting from a bilaterally propagating rupture that nucleates at the center of a planar fault. The transects are selected at distances 300 m, 600 m, 900 m, 1200 m and 1500 m from the point of nucleation (Figure 3.3(a)). As mentioned previously, the peak fracture density and damage zone width increase with propagation distance. However, there is also a subtle dependence of damage zone widths on depth (since depth-dependent stresses are considered, greater stress drops are produced at larger depths leading to larger energy dissipation and width of damage zones). These two variables compete against each other in the footwall since propagation distance increases with decreasing depth. As a result, the fracture decay profiles significantly overlap in the footwall, as opposed to

those in the hanging wall which are pretty distinct. Both the propagation distance and depth co-increase in the hanging wall leading to explicitly larger fracture density and damage zone widths at larger distances from the point of nucleation.

The width of the damage zone ranges from 6 – 40 meters in both the hanging wall and the footwall, damage zone being wider farther away from the point of nucleation. These are considerably narrower than 50-80 meter wide damage zones reported in chapter 2 using image log observations.

The fracture decay rate can be described by a power law. The rate of decay (value of n in the power law described by $F = F_O r^{-n}$ where F is the fracture density at r meters from the fault, F_O, also known as the fault constant, is the fracture density at 1 meter from the fault) ranges from 0.51 to 1.06, larger decay rates being closer to the point of nucleation. This range of decay rates is similar to that reported from field observations in chapter 2 and outcrop studies (Savage and Brodsky, 2011).

Although the actual number of fractures computed is dependent on our assumption of the mean fracture aperture, the width of damage zones and the fracture density decay profiles are independent of that assumption. Fracture density in this study is computed assuming a mean fracture aperture of 100 μm. A different assumption would only change the fracture density, but not the decay rate and extent of damage from the fault. The fault constant computed assuming an average aperture of 100 μm is approximately 1-2 fractures/m. This is lower than that reported in chapter 2 (approximately 8-20 fractures/m). Outcrop studies suggest that the fault constant may have a wide range of values depending on the lithology and the amount of slip across the fault (Savage and Brodsky, 2011), but in general they are larger than what our single-event model predicts. The above results also suggest a spatial variability in the width of damage zones which is inconsistent with field observations. There are two possible explanations for such discrepancies, first the assumption of a single event (damage zones are a result of the cumulative effect of several slip events) and second, our assumption of fracture aperture. Accounting for several slip events in order to reconcile with the above discrepancies is discussed in section 3.7.4.

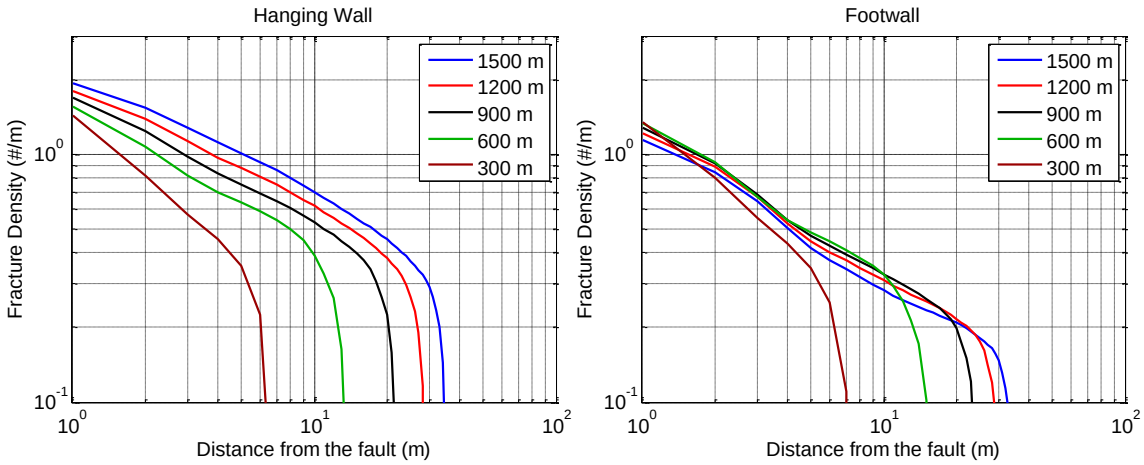

Figure 3.6: Fracture decay profiles in the damage zone in the hanging wall and footwall. The damage zone modeled is due to a bilaterally propagating rupture which nucleates at the center of a planar fault. Various colors represent transects at various distances from the nucleation point.

Figure 3.7 shows the fracture decay profiles in the damage zones of the hanging wall and the footwall formed due to a rupture propagating bilaterally on a nonplanar fault. The fault constant in both the hanging wall and the footwall is approximately 1-3 fractures/m. Although the trend of increasing damage zone width and fracture density with depth and propagation distance still holds in general, fault roughness disturbs the trend. From Figure 3.7(a) we notice that unlike in the case of planar faults, the decay rate in the damage zones in the hanging wall is not constant, especially at larger distances from the nucleation point as seen for the transect at 1500 meters. Damage zone in the footwall (Figure 3.7(b)) is even more complex where the fracture decay rate is not even monotonic at larger distances (transects at 1200 and 1500 meters) from the nucleation point. The fracture density first monotonically decreases with distance from the fault, then increases again before plummeting. This is the result of severe strain heterogeneity and variability. Figure 3.3(b) shows the transects at 1200 and 1500 meters from the nucleation point in the footwall to be traversing across a very heterogeneous strain field which produces a fracture density decay profile as seen in Figure 3.7(b). The fracture decay profile at 300 meters in Figure 3.7(b) is not shown as there is no plastic strain produced along the entire transect (Figure 3.3(b)). The fracture density decay rate in regions where it decreases monotonically continues to lie between 0.5 and 1 (similar to that for planar faults). Overall, fracture density decay for a nonplanar fault can no longer be explained accurately by a power law or any other mathematical law due to a strong heterogeneity arising from local fault roughness.

Damage zones modeled around nonplanar faults are approximately 10-60 m wide and include regions with a non-monotonic fracture decay and build-up. Although the damage zone attributes such as width, fault constant, and fracture decay rates are sensitive to the local fault roughness, on average these attributes are of the same order of magnitude as those derived from modeling damage zones around planar faults.

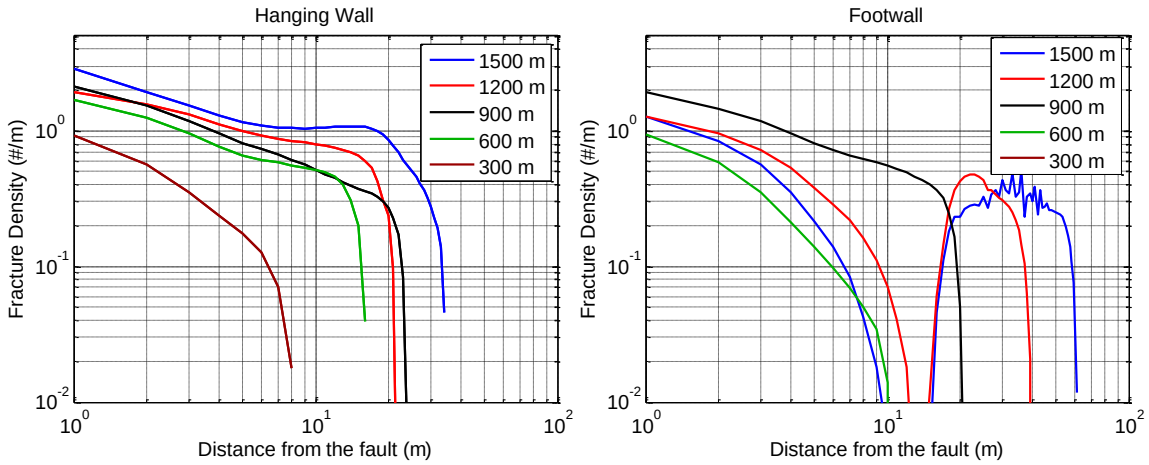

Figure 3.7: Same as Figure 3.6 but for a nonplanar fault.

Figure 3.8 shows the fracture decay profiles in the damage zones modeled due to an upwards unilaterally propagating rupture. Damage due to such a rupture is restricted primarily to the footwall of the thrust fault. Figure 3.8(a) represents transects in the rupture induced damage zone around a planar fault while Figure 3.8(b) represents those around a nonplanar fault. In case of a planar fault (Figure 3.8(a)), the fault constant is approximately 1-2 fractures/m (similar to that obtained in damage zones modeled around bilaterally propagating ruptures). Damage zone becomes wider with increasing propagation distance and are as large as 60-100 m. This happens because larger propagation distances can be achieved for ruptures propagating unilaterally on a fault of a certain length. The above argument may imply a direct scaling between damage zone width and fault length. Field observations suggest that such a scaling between damage zone width and fault size does exist up to a certain threshold fault size of approximately 2400 m, beyond which the width of damage zone saturates (Mitchell and Faulkner, 2009; Savage and Brodsky, 2011). However, since we are only dealing with relatively smaller, reservoir-scale, second-order faults, such a scaling should hold. The fracture density decay can again be explained by a power law with the decay rate approximately between 0.5 and 1.

The fracture density decay profiles in the damage zone around a unilaterally upwards propagating nonplanar fault are, as expected, not monotonically decreasing (Figure 3.8(b)). From Figure 3.3(d) which represents the equivalent plastic strain field produced due to such a rupture, we notice very fine strain localizations especially after 1500 m of propagation (X>500 m). This produces extremely short wavelength variations in fracture density as seen in Figure 3.8(b), especially at larger distances (transects at 2200 and 2700 m) from the nucleation point. Essentially, these variations become more pronounced in those parts of the damage zone which are adjacent to sections of the fault at larger distances from the nucleation point, as these regions have a greater population of strain localization features (Figure 3.3(d)). The fault constant is approximately 1-2 fractures per meter in damage zones that are 20-100 m wide - very similar to those around planar fault. So, although it is difficult to explain fracture density decay profiles and damage zone widths around nonplanar faults mathematically, we can still obtain an idea of effective or approximate damage zone attributes.

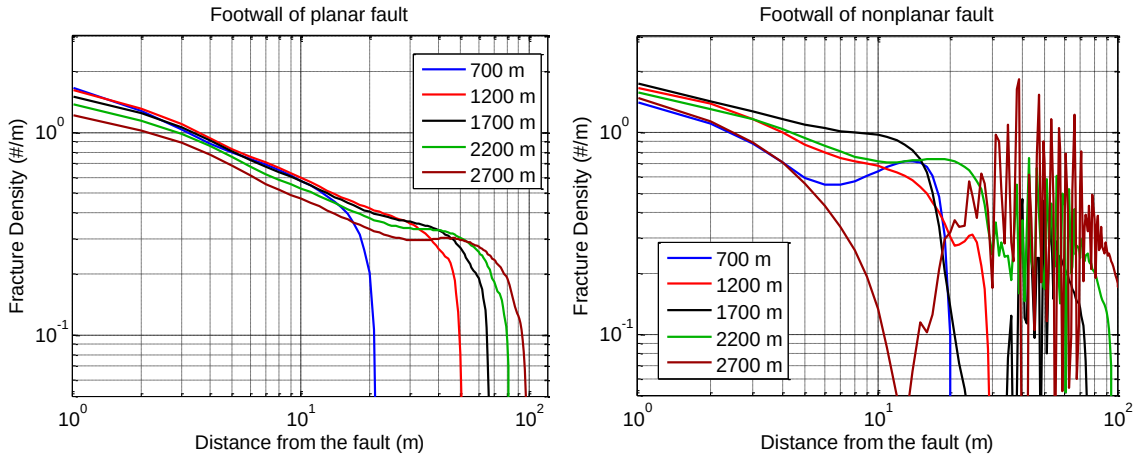

Figure 3.8: Fracture decay profiles in the damage zone modeled formed by to a unilaterally propagating rupture which nucleates close to the lower tip of a (a) planar and (b) nonplanar fault. Various colors represent transects at various distances from the nucleation point. Damage zone in a unilaterally upwards propagating thrust fault are primarily restricted to the footwall

3.7.4 Mathematical calibration and consideration of multiple slip events

Fault damage zones observed in nature are the cumulative product of multiple slip events that the faults have hosted over geologic times. So far we have only considered a single slip event. Results from such modeling (previous section) suggest that the width of damage zones and rate of fracture density decay inside damage zones are consistent with those observed in image logs (chapter 2) and those reported from field studies (Mitchell and Faulkner, 2009;

Savage and Brodsky, 2011). The prominent difference, however, is in the values of fracture density, where fracture density in the modeled damage zones is significantly lower. The uncertainty in fracture density arises out of uncertainty in mean fracture aperture (which is an inherent problem in transforming from continuum to discrete space) and the cumulative effect of multiple slip events in shaping fault damage zones. Besides, there is also a systematic spatial heterogeneity in the width of damage zones which is inconsistent with field observations.

The issue of considering the cumulative effect of multiple slip events adds complexity. While it may be possible to model the cumulative effect of multiple earthquakes more accurately by quantifying the probability of various potential nucleation sites hosting a rupture, using data on background seismicity and earthquake cycles to estimate the frequency of rupture events, and modifying surrounding rock material properties after each slip event, a simplified approach has been adopted in this study. In order to reconcile with the uncertainty pertaining to multiple slip events, plastic strains generated due to multiple slip events are superimposed assuming that the residual stress field left by one rupture has negligible influence on the occurrence of plastic strain in subsequent events. The number of these slip events is obtained by calibrating the model as explained below.

Faults in nature have hosted many slip events of various magnitudes in the geologic past. It is reasonable to assume that the number of earthquakes of certain magnitudes that a fault has hosted scales with the magnitude in accordance with the Gutenberg-Richter law. The law expresses the relationship between the magnitude and total number of earthquakes in any given region and time period of at least that magnitude as $\log_{10}N = a - bM$ where N is the number of events having a magnitude $\geq$ M, and a and b are constants (constants a and b are distinct from the constants used to describe the rate and state friction). The constant b is approximately equal to 1.0 in seismically active regions. We consider earthquakes ranging from magnitude 1 to magnitude 5.2 to have been hosted on the fault. The upper limit (M=5.2) is constrained by the largest magnitude earthquake that a 3 km long fault can host (scalar seismic moment $M_0 \approx \Delta\sigma \times l^3$ where l is the fault length and $\Delta\sigma$ is the stress drop, a reasonable assumption of the stress drop is ~ 2 MPa (Allmann and Shearer, 2009); magnitude $M_W = 2/3\ \log M_0 - 6.03$ in SI units) while the lower limit (M=1) is constrained by our choice of earthquake size that would create a damage zone whose width is the lower limit of damage zone widths we wish to consider in this study. Let

us suppose we are interested in those slip events which at least create a 1 m damage zone. Since rupture propagation and the plastic strain field they create are self-similar, we can argue that if a 3000 meter long rupture creates a damage zone that has a maximum width of 110 m (Figure 3.9), slip on a 3000/110 = 27.27 m long fault patch would create a damage zone that has a maximum width of 1 m. An earthquake on a fault segment 27.27 m long would approximately be a magnitude 1 earthquake.

The unconstrained parameter a in the above formulation is used to calibrate the model. For any value of a, we get a distribution of slip events of various magnitudes from the Gutenberg-Richter law. Magnitudes of plastic strains generated around the fault are independent of propagation distance while the extent of plastic strains from the fault scales with propagation distance. Therefore, the plastic strain field created due to a small event is obtained by downscaling the spatial distribution of the plastic strain field (but not the magnitudes) obtained around a 3 km long rupture to that around a small fault segment. For example (Figure 3.9), the plastic strain field ε_l^p around a fault of length *l* can be computed from the plastic strain field ε_L^p produced around a fault of length *L*. The plastic strain at a distance x from the point of nucleation and a perpendicular distance y from the surface of a fault of length *l* [i.e. $(\varepsilon_l^p(x, y)]$ would be equal to the plastic strain at a distance *Lx/l* from the point of nucleation and a perpendicular distance *Ly/l* from the surface of the fault of length *L* $[\varepsilon_L^p(xL/l, yL/l)]$, i.e. $\varepsilon_l^p(x, y) = \varepsilon_L^p(xL/l, yL/l)$. Damage zone attributes are obtained by superimposing the plastic strain field due to all the events and converting the net plastic strains into a fracture population.

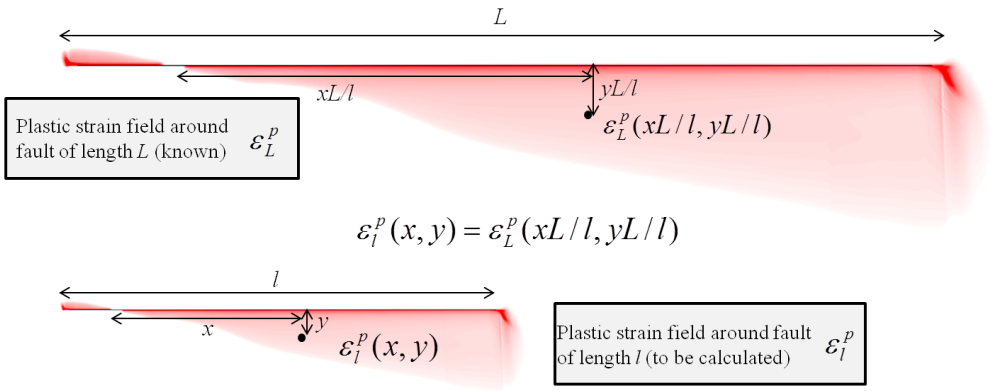

Figure 3.9: Calculating the plastic strain field around a fault of length *l* from the known plastic strain field around a fault of length *L*.

The model is calibrated by placing the constraint that the fault constant predicted by the model should be equal to that suggested by field observations. Savage and Brodsky (2011) have compiled data from various published studies and reported that although in general there exists no clear relationship between displacement across the fault and fault constant, there seems to be a trend between the two parameters for siliciclastic sedimentary host rocks. In this lithology, the fault constant increases with displacement until approximately 150 m and then remains constant. This is expected since there is an upper limit for fracturing beyond which there is complete damage and cataclysis. Although the rocks in the CPE gas field are igneous, I use this relationship since the scaling between fault constant and fault displacement in other lithologies is expected to be of the same order of magnitude. A good estimate of displacement across reservoir scale faults can be obtained from seismic images. For model calibration purposes, I choose that value of a which gives an earthquake magnitude-number distribution such that the plastic strain field obtained by the superposition of the individual event plastic strains produces a fault constant that matches the one given by this trend from field observations.

Seismic images from the CPE gas field show that the displacement across various reservoir-scale faults lies between 8 and 180 m. For example, if we consider a specific fault with a displacement of 20 m, the scaling relationship (Savage and Brodsky, 2011) suggests that the fault constant should be approximately 20 fractures/m. Model calibration involves choosing an a value such that the net plastic strain field translates into an approximate fault constant of 20 fractures per meter. The estimated value of a in this case is ~ 6.6. If we consider a fault with a different displacement, the scaling relationship would point towards choosing a different a value.

The a value is representative of the regional seismicity. In the context of modeling, it may be representative of the frequency of occurrence of ruptures on the fault, and the size and age of the fault. More mature faults have probably hosted more earthquakes than the new ones. Faults found in regions of higher seismicity rates probably host more earthquakes. Therefore, the a value may be representative of all the factors that influence the total number of slip events to have occurred on the fault.

Please note that if the Gutenberg-Richter law suggests n number of earthquakes within a certain magnitude window, we can assume the events to be uniformly distributed on the fault plane. However, since we are using a two-dimensional model in which a fault is modeled as one-dimensional, the number of earthquakes within that magnitude window occurring on the 1-D fault would be $\sqrt{n}$.

3.7.5 Nucleation points for various slip events

The nucleation points for various slip events obtained from the previous step are required to be constrained. Nucleation points are points on the fault surface where ruptures start, and are thought to be localized regions where conditions are most favorable to slip. Various factors that create a conducive nucleation environment include locally elevated pore pressures, fault geometry effects that locally increase the shear to normal stress ratio, localized geochemical and lithology effects that locally decrease fault friction, etc. In the present study, we adopt a simpler approach. The number of slip events of various magnitudes, and hence the number of events occurring on fault segments of various lengths, is obtained from the previous step. We choose both the fault segment on the main fault and the nucleation point on that fault segment randomly assuming a uniform distribution.

3.7.6 Damage zones resulting from the cumulative effect of multiple slip events

The equivalent plastic strain field obtained after superimposing plastic strains due to multiple events as described in the previous section is shown in Figure 3.10. It is clear that the variability in the widths of damage zones modeled due to a single rupture gets homogenized. Besides, considering a power law event size distribution (Gutenberg-Richter law) enhances the plastic strain concentration near the fault due to a very large number of relatively small magnitude events that produce small damage zones.

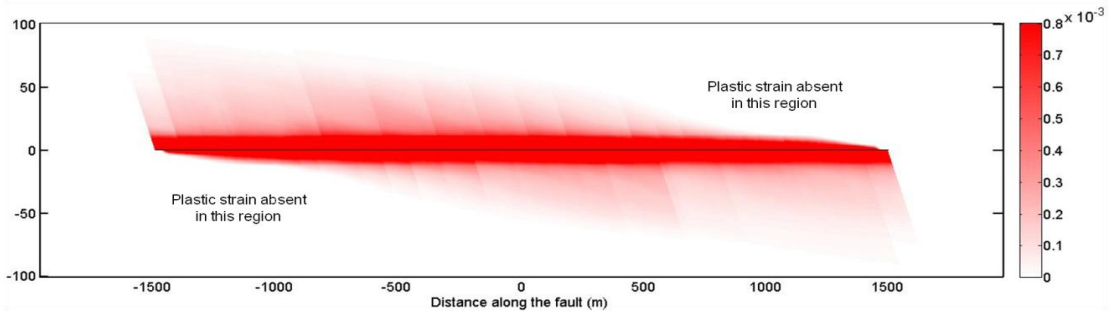

Figure 3.10: Equivalent plastic shear strain field obtained by superposition of the plastic strain fields caused by multiple slip events on a planar fault. All dimensions are in meters) Volumetric strains are obtained as a product of dilatancy and shear plastic strains. Vertical exaggeration=4.7. The width of damage zone relatively gets homogenized. Plastic strain concentration near the fault gets enhanced.

Figure 3.11 shows the width of the damage zone at various positions along the fault. The X axis represents the fault surface. The spatial variability in the width of damage zones modeled due to a single slip event gets homogenized by considering the cumulative effect of several events uniformly distributed along the fault. The damage zones modeled are approximately 60-100 m wide in most regions.

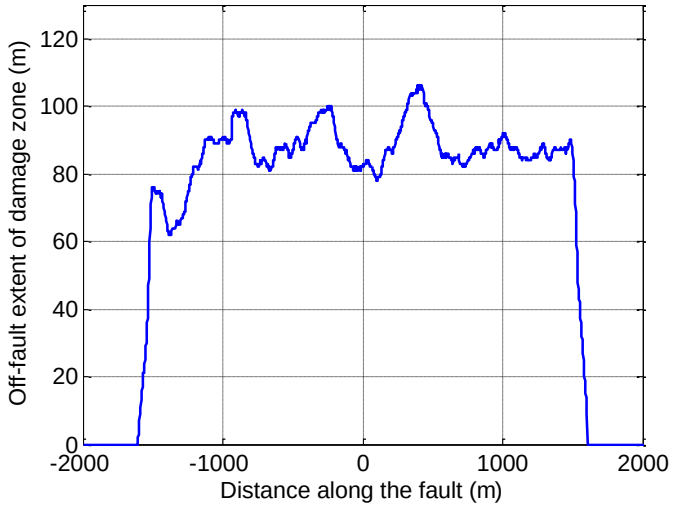

Figure 3.11: Damage zone modeled around a planar fault as a cumulative effect of multiple slip events. The X axis represents the fault surface. The effect of superpositioning is the homogenization of the spatial variability in the width of damage zones. The damage zone is approximately 60-100 meters wide.

Figure 3.12 shows the fracture decay profiles along various transects in the modeled damage zones. The decay of fracture density in both the hanging wall and footwall seems to follow power law decay. For reference, the red dotted line represents a power law decaying at a

rate of 0.8. The modeled fracture density inside damage zones appears to be decaying at this rate up to 10 m from the fault, after which the decay rate increases. This happens due to the concentration of plastic strains close to the fault resulting from a relatively large number of small magnitude slip events.

Damage zone attributes modeled are very similar to those reported from field observations using image logs (chapter 2) which report 50-80 m wide damage zones. From observations discussed in chapter 2, damage zones in the CPE gas field are characterized by decay rates ranging from 0.68-1.06 (with an average of ~0.8) while those in the arkosic section show slightly gradual decay rates lying between 0.4 and 0.75 (an average of ~0.56). Based on compilation of results from several outcrop studies, Savage and Brodsky (2011) suggest fault zones 50-80 m wide around faults with a fault displacement between 30 and 60 meters (which is the displacement across the faults in the CPE gas field that we are modeling). They also suggest that the fracture density decay inside damage zones can be described by a power -law with an average decay rate of approximately 0.8. These observations are consistent with the 60-100 meter wide damage zones modeled in which the decay rate is approximately 0.85 up to a distance of 10 meters after which it increases at a greater rate. The 60-100 meter wide damage zones modeled around a 3000 m long fault are also consistent with the fault size-damage zone width scaling suggested in Mitchell and Faulkner (2009).

The damage zones modeled in this study are around a 3000 m long fault. Invoking self-similarity of rupture propagation for second-order faults, we can say that the modeled width of damage zones scales with fault size. The maximum width of the damage zone scales with propagation distance of the largest ruptures, which is, in fact, a measure of the fault size. Therefore, it is important to note that the width of damage zones modeled depends on the fault size and can be estimated if the fault size (which can be constrained from seismic images) is known. The scaling of damage zone widths with fault size, however, does not hold for large first-order faults since damage zone widths saturate beyond a certain fault size (due to the limited thickness of the seismogenic zone). The results presented here account for multiple slip events on a planar fault. We have omitted results for a nonplanar fault since introducing fault roughness does not significantly affect the modeled damage zone attributes (except introducing small scale local heterogeneities).

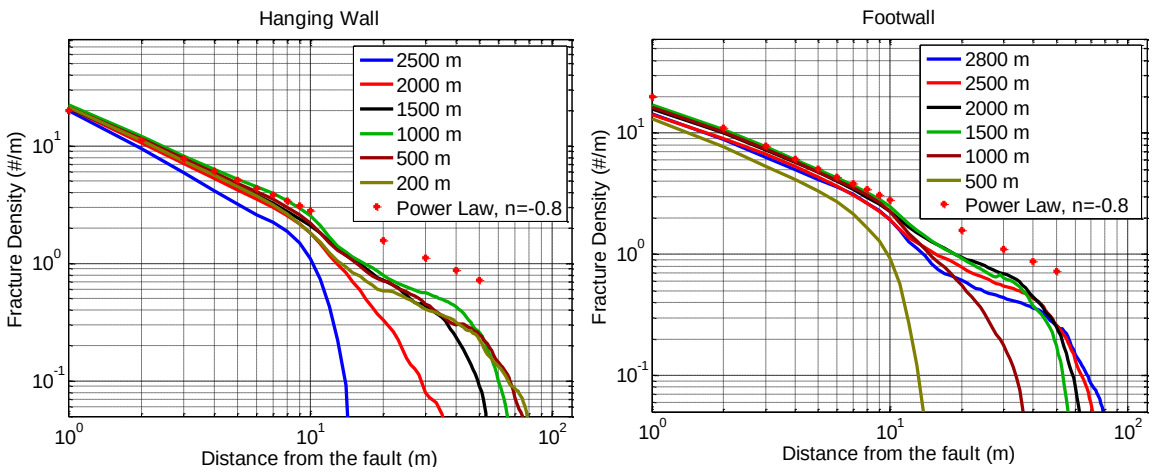

Figure 3.12: Fracture decay profiles in the (a) hanging wall and (b) footwall of the damage zone modeled. Various lines represent fracture density decay profiles across transects at the mentioned distances from the base of the fault. Dots represent a power law decay (decay rate of 0.8) reported for damage zones identified in the CPE gas field using image logs (chapter 2).

3.8 Summary

A methodology for modeling damage zones associated with buried thrust faults using principles of dynamic rupture propagation has been developed. A rupture propagating on a fault surface produces plastic strains in the regions around the fault that deform inelastically. These regions are considered to be damage zones associated with the fault. The plastic strains are converted into a fracture population by volume-balancing assuming the volume created by the dilatant plastic strains are manifested completely in the form of macro fractures. Modeling a single rupture on a planar fault suggests systematic spatial variability of damage zone attributes along the fault length. The width of damage zones scales directly with propagation distance, therefore damage zones are wider adjacent to the sections of the fault which are farther away from patches on the fault where ruptures frequently nucleate. Damage zones modeled due to a bilaterally propagating rupture nucleating at the fault center are 6-40 m wide, while those modeled as a consequence of a unilaterally propagating rupture nucleating at the lower tip of the fault are 20-100 m wide. Unilaterally propagating ruptures create wider damage zones since they get a larger fault length to propagate. The decay of fracture density in the modeled damage zones around planar faults seems to fit a power law, the rate of decay lying between 0.5 and 1.

Accounting for fault roughness impacts the damage zone attributes. The trend of increasing damage zone width with propagation distance does not strictly hold at fine scale since the width of damage zone is strongly modulated by the local surface roughness. This leads to a short wavelength spatial variation in damage zone widths, although the trend of increasing average damage zone width with propagation distance continues to hold. On average, the width of damage zones modeled around a nonplanar fault is of the same order as that around a planar fault (provided the size of the slip event is held constant).

Roughness also causes the fracture density decay with distance from the fault to become nonmonotonic (due to the strongly heterogeneous plastic strain field created), making it extremely difficult to be described by any mathematical law. However, despite the aberrations introduced by fault roughness, damage zone attributes modeled around nonplanar faults, on average, are similar to those modeled around planar faults on a scale (of tens of meters) at which they impact bulk flow properties of damage zones and can be incorporated in flow simulators.

Although the fracture density decay rate and damage zone widths obtained due to a single rupture are consistent with field observations, there is a strong systematic spatial heterogeneity in damage zone attributes which is not observed in nature. The fracture density predicted is also not consistent with values reported from field studies. These inconsistencies arise due to uncertainty in the chosen value of the average aperture and disregard for considering the cumulative effect of multiple slip events in shaping the damage zone. The cumulative effect of multiple earthquakes is accounted for by considering multiple slip events of various magnitudes (consistent with the Gutenberg-Richter law) uniformly distributed along the fault and superimposing the plastic strain field obtained from each individual slip event. The a parameter in the Gutenberg-Richter law which determines the number of slip events of various magnitudes is used to calibrate the model. The a parameter is chosen such that the value of fault constant obtained by superimposing plastic strains due to events of various magnitudes determined by a is equal to the fault constant obtained for field studies (direct observations or scaling relationship between fault constant and fault offset). Model calibration removes the uncertainty introduced by choosing an average fracture aperture, since different aperture values would only change the chosen a value which we are anyway using for calibration. Adopting this methodology homogenizes the spatial variability in the widths of damage zones; these modeled damage zones are almost uniformly 60-100 m

wide along the fault. This range of damage zone width is specific to a 3000 m long fault. By invoking self-similarity of rupture propagation, we can claim that the modeled damage zone width scales linearly with the fault size. The fracture density decays with distance from the fault inside damage zones according to a power law. A large number of small magnitude events (consistent with the Gutenberg-Richter law) leads to large strain concentrations close to the fault. This leads to a gradual fracture density decay rate close to the fault (~ 0.85) and a greater decay rate (~1.4) further away from the fault. These model results are consistent with damage zones observed in this region from image logs (chapter 2) and those reported from other field studies (Savage and Brodsky, 2011).

There are few field experiments that have been performed to investigate the structure of fault damage zones associated with dipping thrust faults that do not break the surface. Since the present study suggests an interesting change in the decay rate of fracture intensity some distance away from the fault, it could provide theoretical insights into future field studies and experiments to investigate such a change.

The above methodology, therefore, requires a model calibration step to fix the a value in the Gutenberg-Richter law. The chosen a value depends on the target fault constant. Therefore, if we can obtain the value of the fault constant of the fault (either from image logs or scaling relationships between fault constant and fault displacement), we can constrain and predict the remaining attributes of damage zones, namely the damage zone widths and the spatial variability of fracture density with distance from the fault.

3.9 Discussion

Various assumptions have been made in modeling damage zones and comparing these results with observations from field studies. Plastic strains obtained from modeling performed in a framework of continuum plasticity are converted into a fracture population after assuming fracture dimensions, followed by volume balancing. This is a necessary step in translating from a continuum space into a discrete space. The cumulative effect of multiple earthquakes is accounted for by calibrating the model and superimposing plastic strains from multiple slip events such that the fault constant matches that observed from field studies. The nucleation points for multiple slip events are randomly distributed using a uniform distribution, disregarding

the fact that certain locations on the fault could be more likely to nucleate ruptures. Besides, subsequent slip events deform the material and alter the rock properties. This may affect rupture dynamics. Technically, we should update the material properties and keep track of accumulated deformation after each slip event. However, we assume a Drucker-Prager yield criterion. This is a shear failure criterion which assumes that fracture surfaces of all orientations are already present in the rock, and yielding results in slip of well oriented planes. In the light of this assumption which considers pre-damaged rock, it may not be required to keep track of material deformation after each slip event (since it is already damaged). However, the outstanding assumption of the surrounding material being pre-damaged with all fracture orientations needs to be reconciled with. This may be true if we consider the damage due to deformation processes prior to and during the fault formation stage. Prior to the stage when faults become capable of hosting earthquakes, various deformation processes could inherently damage the rock. Perhaps, larger fractures form later when faults become capable of hosting earthquakes leading to the formation of the observed character of damage zones.

In this study, we have assumed a pre-existing fault on which dynamic rupture simulations have been performed. In order to account for the effect of multiple slip events, ruptures of various magnitudes are uniformly distributed on the fault and their individual plastic strain fields are superimposed. However, in doing so we ignore the stages that involve fault formation. Large scale faults perhaps form as a result of interaction between multiple small faults. In the initial stages of fault formation, the small faults slip giving rise to small magnitude events and the associated damage zone (in the extensional quadrant). Fractures formed at the tips of small faults (commonly referred to as wing cracks) may link the relatively close fault segments (for example, the adjacent faults in case there is an en echelon pattern of small faults) leading to fault growth. Size of events hosted by faults is constrained by fault size. As the fault size increases, they become capable of hosting larger magnitude events. In our model, we are superimposing plastic strains due to multiple slip events of various sizes. Contribution from the smaller magnitude events probably comes in the earlier phases of fault growth when the fault comprised of smaller fault segments, while contribution from larger magnitude events comes from progressively greater magnitude events which occur during the latter stages of fault growth. Superimposing plastic strain fields due to multiple slip events would, perhaps, result in damage

very similar to the cumulative damage around faults during fault evolution over geologic ages, the primary difference being the sequence of incremental damage accumulation.

In the process of superimposing plastic strain fields due to multiple slip events, the residual stresses are essentially ignored. The inherent assumption is that the stresses relax after a slip event, and gradually begin building up in geologic time. The next rupture occurs when the stresses have built up sufficiently to create conditions conducive for slip to occur. However, it may be important to consider residual stresses because usually, only certain patches of a fault slip during an earthquake. The residual stresses may not favor slip on the same fault patch, but could favor slip on another fault patch which is more favorably oriented to slip under the residual stress state. Such scenarios considerably complicate the analysis and can potentially be considered in 3 dimensional modeling. However, they have not been included in this study.

In the present study, only damage zones associated with relatively small, second-order, localized and isolated faults have been modeled. Damage zones associated with mature faults are broader and more complex due to the presence of secondary strands that have their own loci of fracturing (Chester et al., 2004). These damage zones can potentially be modeled by stochastically allowing a few fractures in the damage zone of the parent fault to become secondary strands, and superimposing their respective damage zones on the parent damage zone (Savage and Brodsky, 2011).

This study has been limited to a homogeneous, isotropic material. It is well known that often times, a geologic fault is likely to occur on a bimaterial interface. If the material on either side of a geometrically symmetric fault is the same, with identical elastic properties and density, the change in normal stress is zero. However, if the materials across the fault have different elastic properties and density, there is a finite change in normal stress. Since the fault strength is dependent on the normal stress acting on the fault, the slip dynamics gets more complex by the coupling between slip and normal stress (Yamashita, 2009).

The current study also does not consider poroelastic effects. The undrained response of fluid-saturated material surrounding the fault to rapid stressing caused by rupture propagation may be strengthened or weakened against inelastic deformation. For nondilatant undrained response on the compressional side of the fault, large increase in pore pressure decreases the

mean effective normal stress and weakens the material. However, positive dilatant material response on the extensional side of the fault reduces the pore pressure, increases the mean effective normal stress and strengthens the material (Viesca et al., 2008). Other than impacting the rock strength, changes in effective normal stress can also affect the rupture dynamics (Yamashita, 2009).

In entirety, although the present study uses a relatively simple model in comparison with the complex processes involved in rupture propagation and slip dynamics, the damage zones associated with relatively smaller, isolated second-order faults modeled closely match field observations from outcrop data and image logs. For hydrocarbon production purposes, the position of reservoir scale faults can be constrained from seismic images and the modeling from the present study can be used to constrain the damage zone characteristics associated with these faults. This information used in conjunction with information on major fracture sets derived from image logs can assist us in building more geologically informed damage zone and fracture network models and help constrain fluid flow.

3.10 Conclusions

This study finds that damage zones associated with relatively smaller second-order buried thrust faults (~ 3000 m) can be modeled by simulating earthquake rupture events using principles of dynamic rupture propagation. Damage zones modeled as a result of a single rupture show a spatially heterogeneous character of damage zone widths along the fault length. This is a consequence of a linear scaling of damage zone width with propagation distance. The inconsistencies are resolved by considering the cumulative effect of multiple slip events of various magnitudes consistent with the Gutenberg Richter law. Such a formulation homogenizes the spatial variability in the thickness of the modeled damage zone. The modeled damage zones are 60-100 m wide. This width scales linearly with fault size. The decay of fracture intensity with distance from the fault follows power law decay. These attributes are similar to those reported in outcrop studies for similar sized faults. The modeled rate of decay is 0.85 up to a distance of approximately 10 m from the fault. The decay rate becomes sharper (~1.4) at larger distances from the fault. Such a change in decay rate can be explained by a large concentration of plastic strains close to the fault as a result of a very large number of small magnitude events

(consequence of considering a power law scaling between earthquake size and frequency). These rates are similar to those reported from field studies, although field studies do not report a break in decay rate of fracture intensity with distance from the fault.

Fault roughness strongly modulates the local damage zone attributes, but on average, these attributes are of the same order of magnitude as those obtained for planar faults. Damage zones modeled around nonplanar faults do not strictly show a monotonic fracture density power law decay and uniform increase in damage zone width with propagation distance. Since real faults are nonplanar, it is only reasonable that we consider nonplanar faults for modeling damage zones. However, in spite of the short wavelength spatial variations introduced by fault roughness, damage zone attributes modeled around nonplanar faults, on average, are similar to those modeled around planar faults at a scale (tens of meters) at which they impact bulk flow properties of damage zones and can be incorporated in flow simulators.

3.11 References

Alejano, L. R., and E. Alonso (2005). Considerations of the dilatancy angle in rocks and rock masses. International Journal of Rock Mechanics and Mining Sciences, 42(4), 481-507. doi:10.1016/j.ijrmms.2005.01.003

Allmann B. P., and P. M. Shearer (2009). Global variations of stress drop for moderate to large earthquakes. Journal of Geophysical Research, 114, B01310. doi: 10.1029/2008JB005821

Andrews, D J. (1976a). Rupture Propagation With Finite Stress in Antiplane Strain. Journal of Geophysical Research, 81(20), 3575-3582. doi: 10.1029/JB081i020p03575

Andrews, D J. (1976b). Rupture Velocity of Plane Strain Shear Cracks. Journal of Geophysical Research, 81(32), 5679-5687. doi: 10.1029/JB081i032p05679

Andrews, D. J. (2005). Rupture dynamics with energy loss outside the slip zone. Journal of Geophysical Research, 110(B1), 1-14. doi:10.1029/2004JB003191

Beeler, N. M., T. E. Tullis, and D. L.Goldsby (2008). Constitutive relationships and physical basis of fault strength due to flash heating. Journal of Geophysical Research, 113(B1), 1-12. doi:10.1029/2007JB004988

Ben-Zion, Y., and Z. Shi (2005). Dynamic rupture on a material interface with spontaneous generation of plastic strain in the bulk. Earth and Planetary Science Letters, 236(1-2), 486-496. doi:10.1016/j.epsl.2005.03.025

Brown, S. R., and C. H. Scholz (1985). Broad Bandwidth Study of the Topography of Natural Rock Surfaces. Journal of Geophysical Research, 90(B14), 12575. doi:10.1029/JB090iB14p12575

Candela T., F. Renard, M. Bouchon, A. Brouste, D. Marsan, J. Schmittbuhl, and C. Voisin (2009). Characterization of fault roughness at various scales: Implications of three-dimensional high resolution topography measurements. Pure and Applied Geophysics, 166, 1817-1851. doi: 10.1007/s00024-009-0521-2

Candela T., and F. Renard (2012). Segment linkage process at the origin of slip surface roughness: Evidence from the Dixie Valley fault. Journal of Structural Geology, in press. doi: 10.1016/j.jsg.2012.06.003

Carpenter, M. H., D. Gottlieb, and S. Abarbanel (1994). Time-Stable Boundary Conditions for Finite-Difference Schemes Solving Hyperbolic Systems: Methodology and Application to High-Order Compact Schemes. Journal of Computational Physics, 111(2), 220-236. doi:10.1006/jcph.1994.1057

Chen, Z., S. P. Narayan, Z. Yang, and S. S. Rahman (2000). An experimental investigation of hydraulic behaviour of fractures and joints in granitic rock. International Journal of Rock Mechanics and Mining Sciences, 37(7), 1061-1071. doi:10.1016/S1365-1609(00)00039-3

Chester, F. M., J. S. Chester, D. L. Kirschner, S. E. Schulz, and J. P. Evans (2004). Structure of large-displacement , strike-slip fault zones in the brittle continental crust. Rheology and Deformation of the Lithosphere at Continental Margins, 223-260, Columbia University Press

Cochard, A., and R. Madariaga (1994). Dynamic faulting under rate-dependent friction. Pure and Applied Geophysics, 142(3-4), 419-445. doi:10.1007/BF00876049

Colmenares, L. B., and M. D. Zoback (2002). A statistical evaluation of intact rock failure criteria constrained by polyaxial test data for five different rocks. International Journal of Rock Mechanics and Mining Sciences, 39 (6), 695-729

Dalguer, L A, K. Irikura, and J. D. Riera (2003). Generation of New Cracks Accompanied by the Dynamic Shear Rupture Propagation of the 2000 Tottori (Japan) Earthquake, 93(5), 2236-2252. doi: 10.1785/0120020171

Dalguer, L. A., K. Irikura, and J. D. Riera (2003). Simulation of tensile crack generation by three-dimensional dynamic shear rupture propagation during an earthquake. Journal of Geophysical Research, 108(B3), 2144. doi:10.1029/2001JB001738

Davis, R. O., and A. P. S. Selvadurai (2002). Plasticity and Geomechanics. Cambridge Univ. Press, Cambridge, N. Y.

Dieterich J.H., and D. E. Smith (2009). Nonplanar faults: Mechanics of slip and off-fault damage. Pure and Applied Geophysics, 166, 1799-1815. doi: 10.1007/s00024-009-0517-y

Di Toro G., R. Han, T. Hirose, N. De Paola, S. Nielsen, K. Mizoguchi, F. Ferri, M. Cocco, and T. Shimamoto (2011). Fault lubrication during earthquakes. Nature 471, 494-498. doi: 10.1038/nature09838

Duan, B., and S. M. Day (2008). Inelastic strain distribution and seismic radiation from rupture of a fault kink. Journal of Geophysical Research, 113(B12), 1-19. doi:10.1029/2008JB005847

Dunham, E. M., D. Belanger, L. Cong, and J. E. Kozdon (2011a). Earthquake Ruptures with Strongly Rate-Weakening Friction and Off-Fault Plasticity, Part 1: Planar Faults. Bulletin of the Seismological Society of America, 101(5), 2296-2307. doi:10.1785/0120100075

Dunham, E. M., D. Belanger, L. Cong, and J. E. Kozdon (2011b). Earthquake Ruptures with Strongly Rate-Weakening Friction and Off-Fault Plasticity, Part 2: Nonplanar Faults. Bulletin of the Seismological Society of America, 101(5), 2308-2322. doi:10.1785/0120100076

Esaki, T., S. Du, Y. Mitani, K. Ikusada, and L. Jing (1999). Development of a shear-flow test apparatus and determination of coupled properties for a single rock joint. International Journal of Rock Mechanics and Mining Sciences, 36(5), 641-650. doi:10.1016/S0148-9062(99)00044-3

Freund, L. B. (1979). The Mechanics of Dynamic Shear Crack Propagation. Journal of Geophysical Research, 84(8), 2199-2209. doi: 10.1029/JB084iB05p02199

Giacomini, A., O. Buzzi, A. Ferrero, M. Migliazza, and G. Giani (2007). Numerical study of flow anisotropy within a single natural rock joint. International Journal of Rock Mechanics and Mining Sciences, 45(1), 47-58. doi:10.1016/j.ijrmms.2007.04.007

Hakami, E. (1995). Aperture distribution of rock apertures. Ph.D. dissertation, Royal Institute of Technology, Stockholm, Sweden.

Harris, R. A., M. Barall, R. Archuleta, E. Dunham, B. Aagard, J. P. Ampuero, H. Bhat, V. Cruz-Atienza, L. Dalguer, P. Dawson, S. Day, B. Duan, G. Ely, Y. Kaneko, Y. Kase, N. Lapusta, Y. Liu, S. Ma, D. Oglesby, K. Olsen, A. Pitarka, S. Song, and E. Templeton (2009). The SCEC/ USGS dynamic earthquake rupture code verification exercise, Seismological Research Letters, 80, no. 1, 119–126, doi 10.1785/gssrl.80.1.119.

Heaton, T. H. (1990). Evidence for and implications of self-healing pulses of slip in earthquake rupture, Physics of the Earth and Planetary Interiors, 64, 1-20. doi: 10.1016/0031-9201(90)90002-F

Hennings, P., P. Allwardt, P. Paul, C. Zahm, R. Reid, H. Alley, and R. Kirschner (2012). Relationship between fractures, fault zones, stress, and reservoir productivity in the Suban gas field, Sumatra, Indonesia. AAPG Bulletin, 96(4), 753-772. doi:10.1306/08161109084

Hirose, T., and T. Shimamoto (2005). Growth of molten zone as a mechanism of slip weakening of simulated faults in gabbro during frictional melting. Journal of Geophysical Research, 110(B5), 1-18. doi:10.1029/2004JB003207

Ida, Y. (1972). Cohesive Force across the Tip of a Longitudinal-Shear Crack and Griffith's Specific Surface Energy, Journal of Geophysical Research, 77(20), 3796-3805. doi: 10.1029/JB077i020p03796

Johri, M., M. D. Zoback, and P. Hennings. (2012). A Scaling Law to Characterize Fault Damage Zones at Reservoir Depths, SRB Bulletin, 2012.

Kostrov, B. V. (1964). Selfsimilar problems of propagation of shear cracks, Journal of Applied Mathematics, Mech., 28, pp 1077-1087.

Kozdon, J. E., E. M. Dunham, and J. Nordström (2011). Interaction of Waves with Frictional Interfaces Using Summation-by-Parts Difference Operators: Weak Enforcement of Nonlinear Boundary Conditions. Journal of Scientific Computing, 50(2), 341-367. doi:10.1007/s10915-011-9485-3

Kozdon, J. E., E. M. Dunham, and J. Nordström (2012). Simulation of Dynamic Earthquake Ruptures in Complex Geometries Using High-Order Finite Difference Methods, Journal of Scientific Computing. doi: 10.1007/s10915-012-9624-5

Kreiss, H.O., and G. Scherer (1974). Mathematical Aspects of Finite Elements in Partial Differential Equations, edited by C. de Boor, Academic Press, New York, 195–212.

Kreiss, H.O., and G. Scherer (1977). On the existence of energy estimates for difference approximations for hyperbolic systems, Tech. Rep.,Dept. of Scientific Computing, Uppsala University, Uppsala, Sweden.

Lee, H. S., and T. F. Cho (2002). Hydraulic Characteristics of Rough Fractures in Linear Flow under Normal and Shear Load. Rock Mechanics and Rock Engineering, 35(4), 299-318. doi:10.1007/s00603-002-0028-y

Lee, J.J., and R. L. Bruhn (1996). Structural anisotropy of normal fault surfaces. Journal of Structural Geology, 18(8), 1043-1059. doi:10.1016/0191-8141(96)00022-3

Lykotrafitis, G., A. J. Rosakis, and G. Ravichandran (2006). Self-healing pulse-like shear ruptures in the laboratory. Science, 313(5794), 1765-8. doi:10.1126/science.1128359

Ma, S. (2009). Distinct asymmetry in rupture-induced inelastic strain across dipping faults: An off-fault yielding model. Geophysical Research Letters, 36(20), 1-5. doi:10.1029/2009GL040666

Madariaga, B. Y. R. (1976). Dynamics of Expanding Circular Fault. Bulletin of the Seismological Society of America, 66(3).

Mattsson, K., and J. Nordström (2004). Summation by parts operators for finite difference approximations of second derivatives. Journal of Computational Physics, 199(2), 503-540. doi:10.1016/j.jcp.2004.03.001

Mitchell, T. M., and D. R. Faulkner (2009). The nature and origin of off-fault damage surrounding strike-slip fault zones with a wide range of displacements: A field study from the Atacama fault system, northern Chile. Journal of Structural Geology, 31(8), 802-816. doi:10.1016/j.jsg.2009.05.002

Noda, H., E. M. Dunham, and J. R. Rice (2009). Earthquake ruptures with thermal weakening and the operation of major faults at low overall stress levels. Journal of Geophysical Research, 114(B7). doi:10.1029/2008JB006143

Paul, P., M. D. Zoback, and P. Hennings (2009). Fluid Flow in a Fractured Reservoir Using a Geomechanically Constrained Fault-Zone-Damage Model for Reservoir Simulation. SPE Reservoir Evaluation & Engineering, 12(4). doi:10.2118/110542-PA

Power, L., T. E. Tullis, and J. D. Weeks (1988). Roughness and Wear During Brittle Faulting. Journal of Geophysical Research, 93(88), 268-278. doi: 10.1029/JB093iB12p15268

Power, W.L. and T. E. Tullis (1991). Euclidean and Fractal Models for the Description of Rock Surface Roughness Self-similar profile. Journal of Geophysical Research, 96(90), 415-424. doi:10.1029/90JB02107

Power, W. L., and T. E. Tullis (1995). Review of the fractal character of natural fault surfaces with implications for friction and the evolution of fault zones, in Fractals in the Earth Sciences, edited by C. C. Barton and P. R. L. Pointe, chap. 5, pp. 89–105, Plenum Press.

Prakash, V. and F. Yuan (2004). Results of a pilot study to investigate the feasibility of using new experimental techniques to measure sliding resistance at seismic slip rates, AGU Fall Meeting, abstract T21D-02

Renard F., C. Voisin, D. Marsan, and J. Schmittbuhl (2006). High resolution 3D laser scanner measurements of a strike-slip fault quantify its morphological anisotropy at all scales. Geophysical Research Letters, 33, L04305. DOI: 10.1029/2005GL025038

Rice, J. R. (1983). Constitutive relations for fault slip and earthquake instabilities. Pure and Applied Geophysics 121(3), 443-475. doi:10.1007/BF02590151

Rice, J. R., N. Lapusta, and K. Ranjith (2001). Rate and state dependent friction and the stability of sliding between elastically deformable solids. Journal of the Mechanics and Physics of Solids, 49(9), 1865-1898. doi:10.1016/S0022-5096(01)00042-4

Rice, J. R., C. G. Sammis, R. Parsons (2005). Off-Fault Secondary Failure Induced by a Dynamic Slip Pulse. Bulletin of the Seismological Society of America, 95(1), 109-134. doi:10.1785/0120030166

Rudnicki J.W. (1980). Fracture mechanics applied to the Earth's crust, Annual Review of Earth and Planetary Sciences, Volume 8, pp. 489-525.

Sagy A., E. E. Brodsky, and G. J. Axen (2007). Evolution of fault-surface roughness with slip. Geology, v. 35, no. 3, 283-286. doi: 10.1130/G23235A.1

Sagy, A., and E. E. Brodsky (2009). Geometric and rheological asperities in an exposed fault zone. Journal of Geophysical Research, 114(B2), 1-15. doi:10.1029/2008JB005701

Savage, H. M., and E. E. Brodsky (2011). Collateral damage: Evolution with displacement of fracture distribution and secondary fault strands in fault damage zones. Journal of Geophysical Research, 116(B3). doi:10.1029/2010JB007665

Scholz, C. H. (2002). The Mechanics of Earthquakes and Faulting (Second.). Cambridge University Press.

Shipton, Z. K., and P. A. Cowie (2003). A conceptual model for the origin of fault damage zone structures in high-porosity sandstone. Journal of Structural Geology, 25(8), 1343-1345. doi:10.1016/S0191-8141(03)00060-9

Sleep, N. H. (2010). Application of rate and state friction formalism and flash melting to thin permanent slip zones of major faults. Geochemistry Geophysics Geosystems, 11(5). doi:10.1029/2009GC002997

Strand, B. (1994). Summation by Parts for Finite Difference Approximations for d/dx. Journal of Computational Physics, 110 no. 1, 47-67. doi: 10.1006/jcph.1994.1005

Templeton, E. L., and J. R. Rice (2008). Off-fault plasticity and earthquake rupture dynamics: 1. Dry materials or neglect of fluid pressure changes. Journal of Geophysical Research, 113(B9), 1-19. doi:10.1029/2007JB005529

Tsutsumi, A., and T. Shimamoto (1997). High Velocity Frictional Properties of Gabbro, Geophysical Research Letters 24 no. 6, 699-702.

Tullis, T. E. and D. L. Goldsby (2003a). Flash melting of crustal rocks at almost seismic slip rates, Eos Trans. AGU, 84 (46), Fall Meet. Suppl., Abstract S51B-05.

Tullis, T. E. and D. L. Goldsby (2003b). Laboratory experiments on fault shear resistance relevant to coseismic earthquake slip, SCEC Ann. Prog. Rep., Southern California Earthquake Center.

Viesca, R. C., E. L. Templeton, and J. R. Rice (2008). Off-fault plasticity and earthquake rupture dynamics: 2. Effects of fluid saturation. Journal of Geophysical Research, 113(B9), 1-13. doi:10.1029/2007JB005530

Wilson, J., J. Chester, and F. Chester (2003). Microfracture analysis of fault growth and wear processes, Punchbowl Fault, San Andreas system, California. Journal of Structural Geology, 25(11), 1855-1873. doi:10.1016/S0191-8141(03)00036-1

Yamashita, T. (2000). Generation of microcracks by dynamic shear rupture and its effects on rupture growth and elastic wave radiation. Geophysical Journal International, 143(2), 395-406. doi:10.1046/j.1365-246X.2000.01238.x

Yamashita, T. (2009). Rupture Dynamics on Bimaterial Faults and Nonlinear Off-Fault Damage. International Geophysics, 94, 187-215. Elsevier Inc. doi:10.1016/S0074-6142(08)00008-9

Zheng, G., and J. R. Rice (1998). Conditions under which Velocity-Weakening Friction Allows a Self-healing versus a Cracklike Mode of Rupture. Bulletin of the Seismological Society of America, 88(6), 1466-1483.

Appendix 3A – Model Parameters Used in Dynamic Rupture Simulations

Material Properties		
Shear Modulus	G	32.04 GPa
Shear Wave Speed	Cs	3.464 km/s
Poisson's Ratio	υ	0.25
Drucker-Prager internal friction parameter	μ	0.5735
Drucker-Prager plastic dilatancy parameter	β	0.26
Friction Law Parameter		
Direct effect parameter	a	0.016
Evolution effect parameter	b	0.02
Reference slip velocity	v_o	1 μm/s
Steady state friction coefficient at Vo	f_o	0.6
State evolution distance	L	0.00397 m
Weakening slip velocity	V_w	0.17 m/s
Fully weakened friction coefficient	f_w	0.13
Initial Conditions		
Vertical (min principal) stress	S_v	23 MPa/km
Maximum horizontal stress	S_{hmax}	21.59 MPa/km (planar fault)
		22.04 MPa/km (nonplanar fault)
Pore Pressure	P_p	12 MPa/km
Initial state variable	Θ	0.4783
Other		
Characteristic extent of state-evolution distance	R_o	20 m

Table 3A-1: Model parameters used in dynamic rupture simulations

Appendix 3B - Mathematical representation of rough faults

The following description is obtained from Dunham et al. (2011). Consider a one-dimensional profile y(x) of a fault with infinite length. Assume $y = h(x)$ for $x \in [-\frac{L}{2}, \frac{L}{2}]$. Here, $h(x)$ is a stationary Gaussian random function with a mean or expectation value of zero (i.e. $E[h] = 0$) where E[.] represents the expectation value such that

$$E[h] = \int_{-\infty}^{\infty} hp(h)dx \tag{3.28}$$

where $p(h)$ is a Gaussian probability density function. This essentially means that y=0 is the mean fault profile about which we will be creating perturbations. $p(h)$is assumed to be Gaussian since one point statistics of natural fault surfaces have not been reported so far. Therefore, the root mean square (rms) roughness of the fault profile is

$$h_{rms}(\lambda < L) = \sqrt{\frac{1}{L}\int_{-L/2}^{L/2} h^2(x)dx} \tag{3.29}$$

If the autocorrelation function only depends on the distance between the two points, and if we assume ergodicity of the profile (so that the expectation value is replaced by an arbitrary realization of the profile), the autocorrelation function can be defined as

$$R_h(x) = E[h(\xi)h(x+\xi)] = \lim_{L\to\infty} \frac{1}{L}\int_{-L/2}^{L/2} h(\xi)h(\xi+x)d\xi \tag{3.30}$$

The Fourier transform of the autocorrelation function gives the power spectral density (PSD) of the fault profile defined as

$$P_h(k) = \int_{-\infty}^{\infty} R_h(x)e^{-ikx}dx \tag{3.31}$$

$P_h(k)$ is defined for both positive and negative wave numbers (k) making it a two-sided PSD. Studies comprising both field and laboratory measurements suggest that the PSD of fault roughness follows a power law distribution

$$P_h(k) = C_h|k|^{-\beta} \tag{3.32}$$

where $1 < \beta \leq 3$.

For a profile with zero mean value (E[h] =0), the standard deviation σ_h is equal to the rms value.

$$h_{rms} = \sigma_h = \sqrt{E[h^2]} \tag{3.33}$$

$$E[h^2] = R_h(0) = \frac{1}{2\pi}\int_{-\infty}^{\infty} P_h(k)dk \tag{3.34}$$

Since $E[h^2]$ is not bounded, a band-limited fault roughness is defined between wave numbers k_{min} and k_{max} Hence,

$$h_{rms}(k_{min}, k_{max}) = \sqrt{\frac{1}{\pi}\int_{k_{min}}^{k_{max}} P_h(k)dk} \tag{3.35}$$

Since P_h is an even function, contributions from negative wave numbers are accounted for by doubling the contributions from their respective positive wave numbers. The rms roughness of the fault whose is PSD defined by the power law in (32) is

$$h_{rms}(k_{min}, k_{max}) = \sqrt{\frac{C_h}{\pi(\beta-1)}(k_{min}^{-\beta+1} - k_{max}^{-\beta+1})} \tag{3.36}$$

The expression (3.36) suggests that h_{rms} is dominated by the smallest wave number (or the longest wave length). Longest wavelength is limited by the fault size, so if we assume the longest wavelength $\lambda_{max} = L$, and minimum wavelength $\lambda_{min} \to 0$, then $k_{min} = 2\pi/L$ and $k_{max} \to \infty$.

Therefore, $h_{rms}(2\pi/L, \infty) = \sqrt{\frac{C_h}{\pi(\beta-1)}(\frac{L}{2\pi})^{\beta-1}}$ (3.37)

The value of β is 3 for a self-similar fault.

$$h_{rms}(2\pi/L, \infty) = \sqrt{\frac{C_h}{(2\pi)^3}}L = \alpha L \tag{3.38}$$

The rms roughness, therefore, is proportional to the profile length L and α $(= \sqrt{\frac{C_h}{(2\pi)^3}})$ is the roughness to wavelength ratio, so $C_h = (2\pi)^3\alpha^2|k|^{-1}$. The PSD for this profile is

$$P_h = (2\pi)^3\alpha^2|k|^{-3} \tag{3.39}$$

In order to draw comparisons with field and laboratory measurements, we define a one-sided PSD $S_h(\kappa)$ in terms of the inverse wavelength (spatial frequency) $\kappa = 1/\lambda = k/2\pi$. Correspondingly, the rms roughness between κ_{min} and κ_{max} can be evaluated by:

$$h_{rms}(\kappa_{min}, \kappa_{max}) = \sqrt{\int_{\kappa_{min}}^{\kappa_{max}} S_h(\kappa)dk} \tag{3.40}$$

For the PSD given by (30), the one-sided PSD becomes

$$S_h(\kappa) = 2P_h(k) = 2C_h(2\pi k)^{-\beta} = 2(2\pi)^{-\beta}C_h k^{-\beta} \tag{3.41}$$

For self-similar faults, $\beta = 3$ and $C_h = (2\pi)^3\alpha^2$. Therefore, we have $S_h(\kappa) = 2\alpha^2\kappa^{-3}$ for $\kappa > 0$ and the corresponding two-sided PSD in terms of spatial frequency is $Q_h(\kappa) = \alpha^2|\kappa|^{-3}$

If we now consider the fluctuation of the fault slope, $m(x) = dh/dx$, whose autocorrelation function is $R_m(x) = -d^2R(x)/dx^2$ and PSD $P_m(k) = k^2P_h(k)$. Therefore, for a self-similar fault we have:

$$P_m(k) = (2\pi)^3\alpha^2|\kappa|^{-1} \tag{3.42}$$

The band limited rms fault slope, therefore, is

$$m_{rms}(\kappa_{min}, \kappa_{max}) = 2\pi\alpha\sqrt{2\ln(k_{max}/k_{min})} \tag{3.43}$$

Here, the shortest and longest wavelengths do not dominate the rms slope. Divergence of the rms slope can occur both by decreasing the minimum wavelength to zero and by increasing the maximum wavelength to infinity.

Appendix 3B.1 Numerical Method for Generating Rough Faults

In this study, a fractal fault profile $y = h(x; L)$ is generated by filtering Gaussian random white noise $y = g(x; L)$in the Fourier domain. Noise is sampled at N evenly spaced sampling points over the fault length L. Gaussian noise is generated with zero mean and unit standard deviation. The standard deviation is equal to the rms value of the fault profile if the mean value of the noise is zero. Therefore, $g_{rms}(L) = 1$.

For N sample points over a distance L, sampling interval is $\Delta x = \frac{L}{N}$. Let the sample points be $x_n = (n-1)\Delta x$ for n=1, 2, …, N. The sampling points in the Fourier domain corresponding to the sampling points in time domain are $\kappa_j = \frac{j}{L}$ where $j = -\frac{N}{2}, -\frac{N}{2}+1, \ldots, \frac{N}{2}-1$. $\Delta\kappa = 1/L$ is the fundamental frequency.

Fourier transform of the vector $h(x_n)$ is

$$H(\kappa_j) = \Delta x \sum_{n=1}^{N} h(x_n)\, e^{-2\pi i(n-1)(j-1)/N} \tag{3.44}$$

We then generate the fractal fault profile by filtering the Gaussian white noise generated with the desired power spectral distribution. In order to generate a self-similar fault profile with a 2-sided power spectral density $P_h(\kappa) = \alpha^2|\kappa|^{-3}$, we let

$$H(\kappa_j) = \alpha|\kappa|^{-\frac{3}{2}} G(\kappa_j) \tag{3.45}$$

In the above expression, $G(\kappa_j)$is the Fourier transform of the noise $g(x; L)$. From the filtering relationship, we get

$$Q_h(\kappa_j) = \left|H(\kappa_j)\right|^2/L = \alpha^2|\kappa|^{-3}\left|G(\kappa_j)\right|^2/L = \alpha^2|\kappa|^{-3} Q_g(\kappa_j) \tag{3.46}$$

For $Q_h(\kappa)$ to equal $\alpha^2|\kappa|^{-3}$, the Gaussian white noise should have unit power spectral density. ($Q_g(\kappa_j) = 1$). For $Q_g(\kappa) = 1$, the rms value of noise is

$$g_{rms}(L) = \sqrt{2(\kappa_{max} - \kappa_{min})} \tag{3.47}$$

where $\kappa_{max} = N/2L$ and $\kappa_{min} = 0$. Therefore, $g_{rms}(L) = \sqrt{N/L}$. This function can be generated in MATLAB using $\text{randn}(N).* \sqrt{N/L}$

Numerically filtering the Gaussian white noise requires calculating Fourier Transform of discretely sampled noise. Discrete Fourier Transform of a vector $h(x)$ of length N is

$$Y(x_j) = \sum_{n=1}^{N} h(x_n) e^{-2\pi i(n-1)(j-1)/N} \tag{3.48}$$

Therefore, $H(\kappa_j) = \Delta x Y(x_j) = (\frac{L}{N}) Y(x_j)$ (3.49)

Appendix 3B.2 Algorithm for generating the profile of a rough fault

1. Generate Gaussian white noise with two-sided PSD. Matlab command is $g = \text{randn}(N).* \sqrt{N/L}$

2. Take the Fourier transform of the noise and multiply by factor (L/N). Matlab command – $G = \text{fft}(g).*(\frac{L}{N})$. G is a vector containing information for frequencies $-\frac{N}{2L}$ to $(N-1)/2L$

3. Filter the noise to the desired spectrum: $H = \alpha\kappa^{-3/2}G$

4. Eliminate the factor L/N and take the inverse Fourier transform. Matlab command: $h = \text{ifft}(H/(\frac{L}{N}))$

Appendix 3C: Stress state on faults and weakening mechanisms

The stress levels at which faults slip still remains an outstanding question in earthquake mechanics. Laboratory experiments performed at low slip rates (~ 1m/s – far lower than co-seismic slip rates) almost universally suggest coefficient of sliding friction to lie between 0.6 and 0.9 (in accordance with the Byerlee's law). This means that faults should slip when stresses build up to levels such that shear to effective normal stress ratio (τ/σ_n) resolved on the faults lies between 0.6 and 0.9. However, several lines of evidence suggest that major faults are actually capable of hosting self-sustaining ruptures at lower τ/σ_n values, provided locally high τ/σ_n is present at spatially small nucleation sites to set off the rupture.

An important line of evidence supporting rupture propagation at low stress levels are lack of temperature anomalies. Frictional sliding of faults at large shear stresses should produce a heat signature that should manifest itself as temperature anomalies at fault traces. Such a temperature anomaly is absent at the San Andres Fault (SAF). Another constraint on the stress state around faults is from in-situ stress measurements. The stress state adjacent to the SAF near Parkfield is consistent with the critically-stressed state of stress in the Earth's crust (with the friction coefficient between 0.6-0.9, consistent with Byerlee's law), but the ratio of τ/σ_n resolved on the fault plane is low (Zoback et al., 1987). Measurements at 2 km depth in the pilot hole drilled at the SAFOD (San Andreas Fault Observatory at Depth) located at ~1.8 km from the surface trace of the SAF indicate that the orientation of the maximum compressive stress is $69 \pm 14°$ with respect to the local strike of the SAF (Hickman and Zoback, 2004). These measurements are consistent with the orientation of the regional stress state reported by Townend and Zoback,

(2004). This high angle between the fault strike and maximum principal stress directions leads to a low τ/σ_n resolved on the fault plane (0.2-0.4).

Another inconsistency with co-seismic slip at high friction values (0.6-0.9) is that the temperature rise due to shear heating would be sufficient to induce melting (McKenzie and Brune, 1972), provided slip is accommodated across a very narrow shear zone (Cardwell et al., 1978). There is substantial evidence suggesting a high degree of shear localization from fieldwork on exhumed faults (eg. Punchbowl fault (Chester and Chester, 1998), Median Tectonic Line fault (Wibebrlet and Shimamoto, 2003). Further, core analysis using core retrieved from a borehole drilled across the Chelungpu fault that hosted the 1999 magntiude 7.6 Chi-Chi earthquake indicates that the entire slip was accommodated 50-300μm thick clay-rich zone (Heermence et al., 2003). Calculations show that if sliding occurs at constant shear stress and hydrostatic pore pressure with coefficient of sliding friction held at 0.6, the thickness of the fault layer across which slip is accommodated should be greater than ~ 35 mm at 7km depth to prevent the onset of melting (Rice 2006; Rempel and Rice, 2006). Evidence of melting is seen in the form of pseudotachylytes in the fault zone. Although pseudotachylytes have been observed along a few natural faults, they are usually associated with deeper faulting within the seismogenic zone (Sibson 1975) and are not commonly seen. This scarcity of pseudotachylytes despite the thinness of the slip zone seems to suggest that co-seismic slip occurs at stress levels lower those predicted by the Byerlee's law.

Certain mechanisms explain dynamic weakening and how faults slip at low stress levels by claiming that the fault strength, due to several reasons is dramatically reduced at co-seismic slip rates. These are known as weakening mechanisms. Two popular weakening mechanisms are thermal weakening due to flash heating (Bowden and Thomas, 1954; Archard 1958/59; Ettles, 1986; Lim and Ashby, 1987; Lim et al., 1989; Molinari et al., 1999; Rice, 1999, 2006; Beeler and Tullis, 2003; Beeler et al., 2008)) and thermal pressurization of fluids (Sibson, 1973; Lachenbruch, 1980; Mase and Amith, 1985, 1987; Lee and Delaney, 1987; Andrews, 2002, 2005; Wibberley, 2002; Noda, 2004; Cocco and Bizzarri, 2004; Noda and Shimamoto, 2005; Sulem et al., 2005; Bizzarri and Coco, 2006a, 2006b; Suzuki and Yamashita, 2006; Rice, 2006; Rempel and Rice, 2006). These mechanisms have been implemented into a spectral boundary equation code for simulating elastodynamic rupture propagation (Noda et al., 2009).

The flash-heating model appeals to friction at the microscopic scale where rough surfaces, when brought together make actual contact only at a finite number of asperities. The net contact area (sum of contact areas of all the asperities) is only a small fraction of the total apparent macroscopic area. As such, the stress supported by the asperities is far greater than the average macroscopic stress acting on the fault surface. When sliding occurs, these asperities slide a small distance before leaving contact, resulting in the renewal of the asperity population. Since the stress supported by the asperities is considerably larger than the average macroscopic stress acting on the fault plane, the local rate of heat production at the asperities is proportionally larger. Consequently, if the temperature at the asperities reaches the melting point (or a level sufficient to thermally mobilize the asperity), the contact weakens. As a result, the fault strength decreases since the fault strength is the sum of all existing contacts. Onset of weakening occurs when the slip rate (known as weakening velocity V_w) reaches a critical level at which the asperities just begin to weaken before they slide out of existence. Experimentally observed value of $V_w$is approximately 0.1 m/s. At higher slip rates, the asperity contacts spend their life time only in the weakened state resulting in weakened fault strength.

The thermal pressurization weakening mechanism involves fluids in the fault zone. Assuming that the fault zone is fully saturated with pore fluids (valid assumption since majority of co-seismic slip occurs below the water table), then shear sliding heats up both the rock matrix and the pore fluids. Since the coefficient of thermal expansion of water is greater than that of rock, fluids have a tendency to expand more than the rock matrix. If the fault material is relatively impermeable (which is usually the case), the stiffness of the rock matrix would prevent the expansion of fluids. Hence, the pressurized fluid would be trapped over the duration of co-seismic slip. This increase in pore pressure decreases the effective normal stress and leads to fault strength weakening.

Fault weakening and the idea of faults operating at low shear stress levels may, however, only hold on major mature faults (eg. SAF). Stress measurements by Townend and Zoback (2000) clearly illustrate that τ/σ_n on optimally oriented faults in the crust reach typical static friction levels (0.6-0.9), consistent with Byerlee's law. This means that faults, especially relatively smaller faults that are not plate boundaries do operate at stress levels $\frac{\tau}{\sigma_n} \in (0.6,0.9)$. It is not clear why these faults operate at higher stress levels, but we can speculate that some of the

requirements critical for weakening to occur are not met. Weakening requires shear localization, so if slip is not accommodated within a very narrow fault zone, faults will not slip at low stress levels. Immature faults comprise of several small fault segments (Segall and Pollard, 1983). Sagy et al., (2007) show that faults become progressively smoother with increase in slip. These factors could prevent shear slip from being accommodated into a narrow shear zone and hence prevent weakening from occurring.

A consequence of slip weakening is that ruptures propagate as self-sustaining pulses. Pulse-like propagation occurs in a very narrow range of shear stresses around τ^{pulse}, the critical background shear stress level for self-sustaining rupture propagation (Zheng and Rice, 1998). Crack-like propagation in the form of expanding cracks (the hypocenter continues to slip until arrest waves emitted on the rupture reaching the fault edges arrives) occurs at larger stresses. Substantial evidence supports the idea that ruptures propagate as self-sustaining slip pulses instead of cracks. The duration of slip at a point on a fault calculated from seismic inversions is much shorter than expected from crack-like propagation models (Heaton et al., 1990). Simulation results show that only pulse-like propagation honors the scaling between slip and rupture length, and that the slip for crack-like propagation is an order larger (Noda et al., 2009).

The faults in this study are approximately 3km long. These are immature, intra-plate faults. That would suggest that these faults slip at stress levels $\frac{\tau}{\sigma_n} \in (0.6,0.9)$. However, these values are much larger than levels at which ruptures propagate as pulses. This issue of considering higher levels of stress ($\frac{\tau}{\sigma_n} \in (0.6,0.9)$) and at the same time being able to obtain pulse-like rupture propagation is an unresolved, outstanding question in earthquake mechanics. A possible explanation to reconcile with the above dichotomy is to consider fault roughness. Fault roughness on nonplanar faults introduces an additional resistance to slip (roughness drag) due to which larger values of τ^{pulse}/σ_n (depending on the amplitude to wavelength ratio α and the local slope of the fault at the nucleation point) ranging from 0.28 to 0.42 would be required to propagate the rupture as a pulse (Fang and Dunham, pc). There could be other factors which explain pulse-like propagation at higher stress levels, but that is beyond the scope of this work. For the purpose of modeling damage zones in this study, we constrain the stress state such that ruptures propagate as pulses so that we at least honor the slip-length scaling (Noda et al., 2009).

Appendix 3D: Rupture propagation - Fault slip on planar and nonplanar faults

We perform dynamic rupture simulations with initial conditions chosen such that ruptures propagate as self-sustaining slip pulses. Figure 3D-1 shows the slip profile on the surface of a flat fault. The X-axis represents the fault surface. The origin represents the point of nucleation of a bilaterally propagating rupture, and the negative and positive values represent distances (in kilometers) along the fault down-dip and up-dip respectively. Various lines represent slip on the fault surface at various instants of time. The shear-to-normal stress ratio required for a pulse-like rupture to propagate on a flat fault dipping at 30° is 0.336. At lower values, the rupture fails to propagate, whereas for values larger than ~0.34, the rupture propagates as a crack. As noted earlier, it is only in a very narrow range of shear-to-normal stress ratios that the rupture travels as a self-healing pulse. It can be seen from Figure 3D-1 that the amount of slip on the fault is greater down-dip (~0.03-0.05 m) than up-dip (~0.023 m). The slip peak at the origin should be disregarded, since the increased slip is an artifact of the nucleation process.

Figure 3D-2 shows a space-time plot of the slip velocity for the rupture on a planar fault. We notice that the center of the fault starts to slip in the beginning, but at approximately 0.05 s, it stops slipping and a finite slip velocity exists only very close to both of the rupture tips. Furthermore, the particle velocity close to the rupture tip down-dip (negative values on the X axis) is slightly greater than up-dip, which could be responsible for greater stress perturbations. This also explains larger slip across the fault in the down-dip direction (as seen from Figure 3D-1).

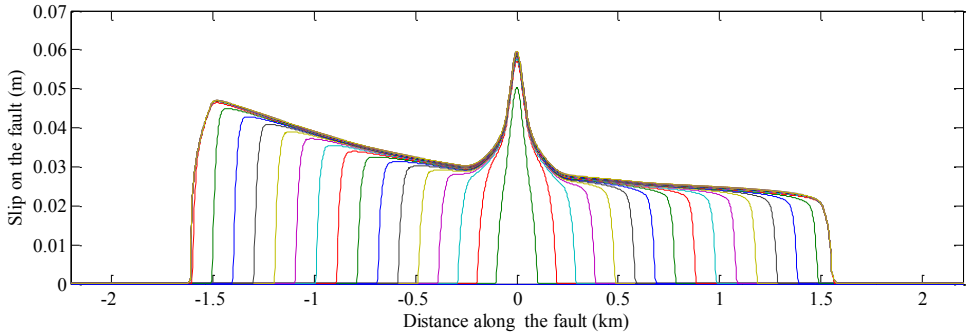

Figure 3D-1: Plot showing the slip profile on a planar fault. Various lines represent slip profile at every 0.0347 s of rupture propagation on the fault. The origin represents the point of nucleation (depth of 2.2 km), negative X values represent distances down-dip while positive X values represent distances up-dip from the point of nucleation.

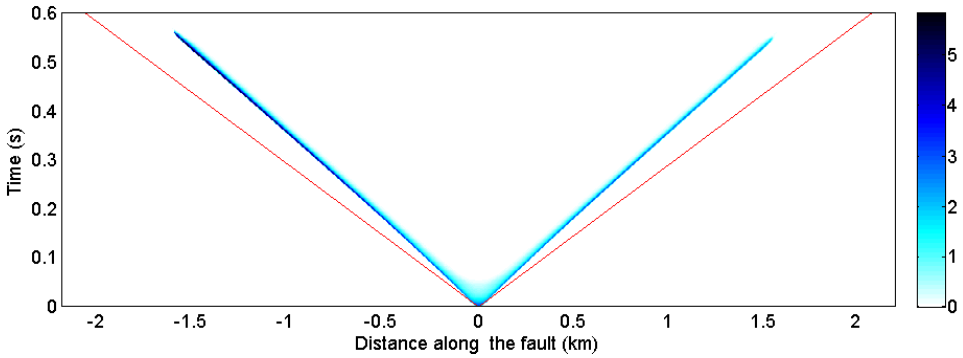

Figure 3D-2: Plot showing the particle slip velocity (m/s) on a planar fault plane at various times. The self-healing nature of the pulse propagation is clearly seen. The red lines represent the shear wave velocity, so the above is a subshear self-healing pulse-like rupture.

The slip profile and space-time plot for a pulse-like rupture propagating on a rough fault are shown in Figures 3D-3 and 3D-4. The fault roughness (amplitude to wavelength ratio α) is 0.005 and minimum roughness wavelength is 60 m. Roughness increases the fault's resistance to slip; therefore, larger shear stresses are required to rupture the fault. The shear-to-normal stress ratio required for a pulse-like rupture to propagate on the rough fault dipping at 30° is 0.3476. However, this value is very sensitive to the ratio of amplitude to wavelength chosen to generate the rough fault (Fang and Dunham, pc). As seen in case of a flat fault, the slip down-dip is greater than up-dip (Figure 3D-3). The magnitude of slip (~0.06 m down-dip and ~ 0.04-0.05 m up-dip) is also very similar to that observed for a flat fault.

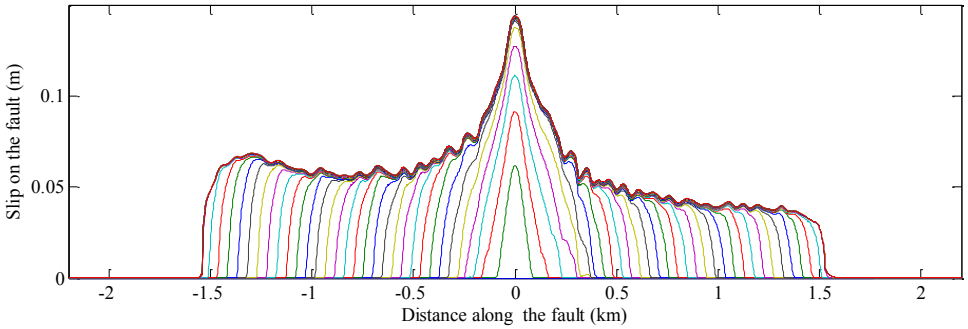

Figure 3D-3: Plot showing the slip profile on a nonplanar fault dipping at 30°. Various lines represent slip profile at every 0.0154 s of rupture propagation on the fault. The origin represents the point of nucleation (depth of 2.2 km), negative X values represent distances down-dip while positive X values represent distances up-dip from the point of nucleation.

Similar to our observations for a flat fault, the center of the rough fault starts to slip during nucleation, but at around 0.1 s it stops slipping, and a finite slip velocity exists only very close to both the rupture tips (Figure 3D-4). The particle velocity close to the rupture tip down-dip (negative values on the X axis) is greater than up-dip. This leads to greater net slip across the fault in the down-dip direction (as seen in Figure 3D-3).

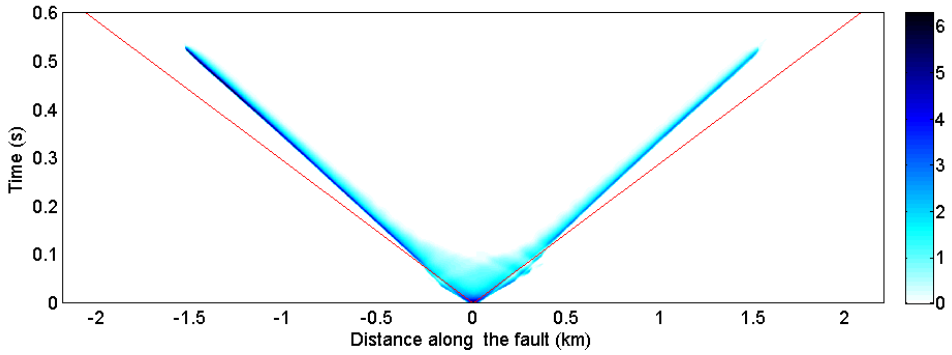

Figure 3D-4: Plot showing the particle slip velocity (m/s) on the nonplanar plane at various times. The self-healing nature of the pulse propagation is clearly seen. The red lines represent the shear wave velocity, so the above is a subshear self-healing pulse-like rupture

Appendix 3E: Rupture Propagation: Energy Balance

The description below shows how the extent of inelastic deformation increases with propagation distance. This description is valid for mode III, but results are nearly identical in mode II. The rate of energy release during the propagation of the rupture is:

$$G = \frac{K^2}{2\mu\sqrt{1-(\frac{V_r^2}{C_s^2})}} \tag{3.50}$$

where K is the dynamic stress intensity factor, μ is the shear modulus, $V_r$is the rupture velocity and $C_s$is the shear wave velocity. The dynamic stress intensity factor is defined as

$$K = \kappa(V_r)\Delta\tau\sqrt{\pi a} \tag{3.51}$$

$\Delta\tau\sqrt{\pi a}$ is the static stress intensity factor, and $\kappa(V_r)$ decreases from 1 (at $V_r = 0$) to 0 as $V_r \to C_s$

On combining (3.50) and (3.51), we get

$$G = \frac{\kappa(V_r)^2}{\sqrt{1-(V_r^2/C_s^2)}}\frac{\pi\Delta\tau^2 a}{2\mu} \tag{3.52}$$

$\sqrt{1-(V_r^2/C_s^2)} \sim [1-\left(\frac{V_r}{C_s}\right)]$ and $\frac{\pi\Delta\tau^2 a}{2\mu} = G_0 =$ quasi-static energy release rate

The rate of release of energy due to advance of the rupture G = fracture energy Γ

Therefore, $\Gamma = \left(1-\frac{V_r}{C_s}\right)\frac{\pi\Delta\tau^2 a}{2\mu}$ (3.53)

Equation (3.53) implies that if the stress drop $\Delta\tau$ and rupture velocity V_r are held constant (which is approximately the case), then fracture energy Γ scales linearly with the source dimension a. An estimate of fracture energy assuming $\Delta\tau = 3$MPa, $V_r/C_s \sim 0.7$and $\mu = 30$ GPa, the fracture energy

$$\Gamma \sim 1\frac{MJ}{m^2}\left(\frac{a}{10\text{ km}}\right) \tag{3.54}$$

The above expression represents the energy release rate for unit area advance of the rupture front of length a. This estimate is consistent with estimates of fracture energy for large strike-slip earthquakes. In order to write (3.54) in terms of the slip, using $\Delta u \sim \frac{\Delta\tau}{\mu}a$, we get $\Gamma = \left(1-\frac{V_r}{C_s}\right)\Delta\tau\Delta u$, which means

$$\Gamma \sim 1\frac{MJ}{m^2}\left(\frac{\Delta u}{10\text{ km}}\right) \tag{3.55}$$

However, if we consider the often used slip weakening law where the fault strength decays from peak shear strength τ_p to residual shear strength $\tau_r$over a slip evolution distance D_c the fracture energy is

$$\Gamma = 0.5(\tau_p - \tau_r)D_c \tag{3.56}$$

The scaling between rupture nucleation length and state evolution distance is

$$l \sim \frac{\mu D_c}{\tau_p - \tau_r} \tag{3.57}$$

For fracture energy to be of the order of magnitude as suggested by (3.55), (3.57) implies that the nucleation lengths would have to be enormous, which is not the case. Therefore, the fracture energy does not fully account for the energy released due to rupture propagation. One of the possibilities could be that the entire energy dissipates within the fault core during frictional sliding (as a continual weakening process).

Another possibility, and what happens in our simulations is that the dominant contribution to fracture energy is provided by the off-fault inelastic deformations. The on-fault frictional weakening provides only a negligible contribution to the fracture energy since slip evolution distance D_c is small. In the simulations shown in this study, the extent of off-fault plastic strains increases with increase in propagation distance, while the magnitude of plastic strain almost remains constant. Plastic work is

$$W \sim \alpha a^3 \tau_y \gamma^p \tag{3.58}$$

where αa^3 is the volume experiencing plastic strain, $\tau_y$is the yield stress at which the plastic flow occurs, and γ^p is the plastic strain.

Therefore, the fracture energy consumed per unit area advance of the rupture when length is a is

$$\Gamma \sim \alpha a \tau_y \gamma^p \tag{3.59}$$

A reasonable estimate of the fracture energy contributed by inelastic deformation can be obtained by assuming $\tau_y \sim 100$ MPa, $\alpha = 0.01$, $\gamma^p \sim 0.001$. Therefore, $\Gamma \sim 1 \frac{\text{MJ}}{\text{m}^2}\left(\frac{a}{10\text{ km}}\right)$

Chapter 4

MODELING FLUID FLOW THROUGH DAMAGE ZONES: CASE STUDY FROM THE CPE GAS FIELD

4.1 Abstract

This study presents a methodology for incorporating damage zones in reservoir models in order to illustrate their impact on the flow characteristics of the reservoir. Modeling fluid flow through fractured reservoirs containing damage zones is extremely challenging, primarily due to two reasons – geomodeling i.e. challenges associated with building a representative reservoir model due to lack of adequate data characterizing damage zones (due to poor quantitative understanding), and challenges associated with modeling flow through a system of fractures without over-simplifying issues of connectivity and scale-dependent heterogeneity. This study addresses both the issues of reservoir characterization and geomodeling, along with flow simulations. A case study from the CPE gas field is presented. A discrete fracture network (DFN) modeling approach in adopted for modeling the reservoir since the CPE gas field is a fractured, low matrix permeability basement reservoir with natural fractures and damage zones governing its flow and production behavior. Reservoir fracture characteristics observed (chapter 2) along with damage zone attributes modeled (chapter 3) are used to build a geologically consistent reservoir model. The DFN model is then upscaled to obtain equivalent grid properties

using Oda's method. Flow simulations are performed on the upscaled model in a dual-porosity (DP) framework. DP models address the dual porosity nature of the system by accounting for both, matrix and fracture porosity. Although DP flow simulation models over-simplify connectivity issues, they provide advantages of speed. Besides, these models have been shown to work well in severely fractured formations where reservoir connectivity issues are not paramount. Model properties are calibrated using a flow after flow well test. Flow simulations are performed on two models, one containing both the background fractures and damage zones, while the other containing only background fractures. The objective is to show the signature of damage zones on the reservoir flow properties. The reservoir models are produced a constant rate of 30 MMSCF/day for 300 days. A distinct difference in the pressure drawdown between the two models is observed, the difference in pressure decay being almost 600 psi after 300 days. This clearly highlights the importance of incorporating fault damage zones in reservoir models for modeling flow correctly. This study also investigates the effect of various drilling strategies in fractured reservoirs. Simulations suggest that higher flow rates can be achieved by coursing the well through damage zones, increasing the reservoir-wellbore contact length and providing a larger projection of the well in the direction of maximum flow (due to permeability anisotropy introduced by major fracture sets along their planes).

4.2 Introduction and Motivation

Natural fractures and faults affect the flow characteristics of a reservoir significantly, especially those with low matrix permeability. The heterogeneity and anisotropy introduced by fractures makes it difficult to predict flow through the reservoir and strategize optimal production. Heterogeneity is introduced by a spatially varying fracture density while anisotropy is introduced due to preferential flow along the fracture plane which is determined by the fracture orientation. Usually, it is difficult to characterize fractures appropriately in terms of their location, geometry, size and orientation due inadequate data. Bulk of the subsurface information is derived from 3D seismic images or borehole image logs. Seismic images provide no information on fracture characteristics while image logs only provide information on major fracture sets present along the borehole. Besides, these sources of information are on markedly different scales making their integration into reservoir-scale models difficult.

Damage zones are regions of anomalously high fracture density surrounding large-scale faults. Several studies have shown the impact of damage zones of reservoir flow properties and production. Hennings et al. (2012) show that wells that traverse through damage zones containing a large population of critically stressed fractures are significantly more productive than wells that do not. Paul et al. (2009) show that the large production rates from the CS gas field can only be accounted for by enhancing permeability close to the faults in order to account for damage zones. From these studies, it is clear that damage zones dominate flow in faulted reservoirs and should be incorporated in reservoir models for modeling flow correctly, in an effort to optimize production and assist in strategic reservoir management.

A strong evidence of channeling and preferential flow in individual fractures has been clearly demonstrated in several field and laboratory experiments (Neretnieks et al. 1982, 1993). Cacas et al. (1990 a, b) have reported a four-order difference in the magnitude of maximum and minimum injection rates, despite good fracture connectivity in the granite uranium mine at Fanay-Augeres, France. This has been attributed to the high degree of channeling and heterogeneity due to a wide distribution of fracture conductivity and is a direct consequence of fracture conductivity distribution and degree of fracture connectivity (Margolin et al. 1998). We suspect damage zones to cause similar channeling of flow in case wells traverse through damage zones. Therefore, it is critical that we account for damage zones while modeling flow.

A number of studies have dealt with modeling fractured reservoirs (Martel and Peterson, 1991; Lee et al. 2001; Long and Billaux, 1987; Gringarten 1996; Matthai et al. 2007). Several methodologies, both deterministic and stochastic, have been developed to model the effect of reservoir heterogeneity on hydrocarbon flow and production. Impact of stress on flow properties of fractured reservoirs have been studied by Oda (1985, 1986), Brown and Bruhn (1998), Bourne and Willemse (2001), and Smart et al. (2001). Several studies also emphasize the importance of coupling geomechanics with fluid flow (Bourne et al., 2000; Chen and Teufel, 2000; Couples et al. 2003). Berkowitz (2002) provides a review on conceptual pictures and mathematical models of flow and transport phenomena in fractured rock systems. However, none of the mentioned studies include fault damage zones in their reservoir models. In this study, the emphasis is on including damage zones in building reservoir models to simulate flow. The primary impediment in accounting for damage zones is the lack of quantitative characterization of damage zones. In

this study, results from the study of modeling damage zone attributes (chapter 3) are used to introduce damage zones in reservoir models.

Fractures, both inside the damage zone and the regional population (background fractures) can either be introduced in the form of a fine scale geologic model (e.g. discrete fracture network model – Dershowitz et al. (2000)), or a coarse scale flow simulation model (e.g. dual porosity (DP) models). Dual porosity models used for simulating flow through fractured reservoirs add a second interacting continuum to reflect storage and permeability characteristics. However, DP models only address the dual porosity nature of fractured reservoirs and in the process simplify issues of connectivity and scale dependent heterogeneity. These issues play a critical role in governing flow in fractured reservoirs and are usually better addressed by discrete fracture network (DFN) models. Besides, DFN models are usually formulated in a stochastic framework, therefore, multiple realizations help in quantizing uncertainty. However, DFN models are computationally expensive since they usually employ continuum finite element analysis to treat flow within each fracture. Naturally fractured and faulted reservoirs containing several damage zones may comprise of millions of fractures. Including each one of them as a discrete feature in the simulation model is limited by the computational power and time (Durlofsky, 2003). On the other hand, despite the simplifying assumptions made by DP models regarding fracture geometry, they do offer significant advantages of model size and speed. Therefore, problems of fluid flow through fractured reservoirs usually best incorporate the use of 'hybrid' models that integrate DFN and DP models in order to take maximum advantage of each approach. This study uses techniques that can help develop DP models that more accurately reflect anisotropy, heterogeneity and scale-dependent connectivity structure of fractured reservoirs.

4.3 Background - Fracture Network Models

A number of modeling approaches have been developed in order to deal with flow problems of interest in fractured media. (In the framework of fractured media, it is important to distinguish between fractured rocks and fractured porous rocks. Fractured rocks emphasize fractures while fractured porous rocks include the role of porous host rock). These models can be formulated in deterministic as well as stochastic frameworks, and can account for a range of fracture properties such as fracture distributions, density and flow properties. Flow simulation

models can broadly be divided into two classes, continuum models and discrete fracture network models.

4.3.1 Continuum models

Continuum models are based on the concept of representative element volume (REV). The REV approach works particularly well if the formation contains a large density of interconnected natural fractures. However, this approach is not appropriate in case of poorly connected fracture networks (Dagan and Neuman, 1997) or if the REV can only be defined at the scale of the problem of interest (in which case all the underlying heterogeneity will be homogenized). Continuum models comprise of single continuum, double continuum and multiple continuum models. Single continuum models are essentially equivalent porous medium models. These are applicable when the fracture network is dense and well-connected, and the interaction between the fracture network and the porous host rock occurs over a time scale that is sufficient to establish a local equilibrium. Double continuum models account for two interacting systems (porous medium and fractures) where each is conceptualized as a continuum occupying the entire space. An exchange parameter is used to define the mass transfer between the two continua (Barenblatt et al. 1960 a, b). Similarly, multiple continuum models account for multiple continua where several continua may represent fracture sets with different properties (eg. permeability) (Narasimhan and Pruess, 1987; Kazemi and Gilman, 1993). Dual porosity and dual permeability models are two popular double continua models used extensively in the petroleum and hydrological community. In dual porosity models, the porous host rock acts as storage for fluids so that fluids drain into the fractures adjacent to the matrix block. Flow does not occur through the porous matrix in dual porosity models. In contrast, dual permeability models permit storage and flow in both the fractures and the porous host rock.

4.3.2 Discrete Fracture Network (DFN) Models

The discrete fracture network modeling approach accounts for flow through individual fractures explicitly and hence provides a better framework for modeling phenomenon such as channeling and preferential flow paths through individual fractures which are observed in fractured reservoirs (Neretnieks et al. 1982, 1993). Since fractures are modeled individually, their geometrical and flow properties can also be individually assigned. As such, it is possible to couple these properties geomechanically, for example assign fracture permeability depending on

the normal stress acting on the fracture and whether or not it is critically stressed. These models, however, suffer from two drawbacks – they are computationally expensive and they usually require detailed field data for calibration. These models are computationally expensive because they use finite element techniques to obtain the flow solution. Fracture meshing becomes extremely challenging, especially in a dense network of fractures of various sizes (which increases the number of intersections and nodes). DFN models are therefore integrated with dual porosity models in an effort to take advantage of both methods, i.e. reduce the computational expense and at the same time maintain capabilities of modeling channeling and preferential flow paths. DFN models are usually treated in a stochastic framework; fractures are stochastically introduced into the model using distributions whose parameters are isolated from field data. Stochastic frameworks are considered of greater utility than deterministic frameworks since they allow quantification of uncertainty and variability.

4.4 Current Study

In this study, a DFN reservoir model is generated using data from various sources. 3D seismic images are used to constrain the positions of reservoir scale faults. Results of damage zone attributes modeled (chapter 3) are used to constrain the extent and spatial variability of fracture density inside damage zones. Background fractures that populate the rest of the model domain are stochastically generated, their density in various intervals constrained from fracture density variability observed in image logs (chapter 2). Fractures are assigned orientations using distributions of major fracture set orientations derived from image logs. Background fracture sizes are assumed to follow a power-law distribution. Fractures are assigned mean aperture values (which are representative of fracture volume) using the formulation provided by Willis-Richards et al. (1996). Hydraulic aperture (representative of the fracture flow properties) is computed from the mechanical aperture using Barton's model (Barton et al., 1977). Fracture permeability is calculated from the hydraulic aperture using a parallel plate model. Following this method, mean fracture apertures and permeability are functions of the effective normal stress acting on the fault plane and whether or not the fracture is active (critically stressed) in the current stress state. The DFN model is then upscaled to derive grid cell parameters (porosity and permeability tensor) using Oda's method. Fluid flow is simulated on this upscaled model in the DP framework. This methodology enables DP models to take advantage of some of the features

of the DFN approach (Dershowitz et al., 2000), particularly those related to fracture induced anisotropy, heterogeneity and scale-dependent reservoir connectivity. Model is calibrated using the first stage of a three-stage flow after flow well test while the next two stages are used to validate the model. Flow simulations are then performed on two models, one containing both the background fractures and damage zones, while the other containing only background fractures. The objective is to show the effect of damage zones on reservoir flow characteristics.Three different drilling strategies are also evaluated, the first trajectory represents a deviated well that intersects three fault damage zones, the second trajectory represents a deviated well that does not intersect any damage zones while the third represents a vertical well that does not intersect any damage zones.The objective of this part of the study is to evaluate the impact of various drilling strategies on well performance.

4.4.1 Upscaling to obtain grid properties (permeability, porosity, shape factor) – Oda's method

Fracture network properties can be upscaled to grid properties using a number of techniques. One of those involves the use of simulations. In this approach, fractures in a grid block are discretized into a finite element mesh, appropriate boundary conditions on the sides of the grid block are applied and the steady state flow solution is calculated and used to invert for the equivalent permeability tensor based on Darcy's law. This method offers advantages of incorporating the exact fracture network connectivity and solving for the flow at the grid block scale. However, this method is extremely time consuming and computationally expensive. Another method of obtaining grid block properties is Oda's method. This offers advantage of speed as it can be calculated without requiring flow simulations. However, Oda's method does not take into account the fracture connectivity and size, therefore, its application is limited to densely fractured, well-connected networks (Dershowitz et al, 1998). Since well tests suggest that the CPE gas reservoir is well connected by fractures (pc, ConocoPhillips), it is acceptable to use Oda's method for computing effective grid block properties (porosity and permeability tensor).

Oda's method works by projecting the fracture area inside the grid block onto a plane parallel to the direction of flow. It considers orientations of all fractures in a grid block expressed

as unit normals *n*. The mass moment of inertia of fracture normals distributed over a unit sphere is given by:

$$N = \int_{\Omega/2} n_i n_j E(n) d\Omega \quad (4.1)$$

where N is the number of fractures in Ω, $n_i n_j$ are components of a unit normal to the fracture *n*, $E(n)$ is the probability density function that describes the number of fractures whose unit normal vectors are oriented within the differential solid angle $d\Omega$ and Ω is the entire solid angle corresponding to the surface of unit sphere (from Dershowitz et al. 1998). For a particular grid cell with known fracture areas A_k, and transmissivities T_k, the empirical fracture tensor is calculated by summing up individual fractures weighted by their area and transmissivity.

$$F_{ij} = \frac{1}{V} \sum_{k=1}^{N} A_k \; T_k n_{ik} n_{jk} \quad (4.2)$$

F_{ij} is the fracture tensor, V is the volume of the grid block, N is the total number of fractures in the grid block, A_k and T_k are the area and transmissivity of fracture k, and n_{ik}, n_{jk} are the components of the unit normal of fracture k. Oda's permeability tensor is finally obtained from the fracture tensor by assuming that the fracture tensor expresses flow as a vector along the unit normal. Further, if we assume the fracture to be impermeable parallel to the fracture normal, the fracture tensor F_{ij} must be rotated into the plane of permeability. Therefore,

$$k_{ij} = \frac{1}{12} (F_{kk} \delta_{ij} - F_{ij}) \quad (4.3)$$

In this study, FracMan modeling package is used to compute equivalent grid properties. The 3 X 3 symmetric permeability tensor of a fracture is computed by projecting the fracture isotropic permeability (k) onto the grid plane and scaling it by the ratio between the fracture volume and volume of the grid cell (FracMan 7 workshop, 2009). Equivalent upscaled grid block permeability tensor of a single fracture is given by

$$k_{ij} = k \frac{eA}{V} (\delta_{ij} - n_i n_j) \quad (4.4)$$

where k is the isotropic permeability of the fracture, e is the fracture aperture, A is the fracture area, and V is the grid cell volume to which the fracture properties in the grid cell are being

upscaled, $n_i n_j$ are components of a unit normal to the fracture *n*. Following the assumption that the flux through each fracture is additive, the permeability tensors obtained from each fracture present inside the grid block are summed up to obtain a net permeability tensor K in that grid block. The principal permeabilities and flow directions within the grid block are given by the Eigen values and Eigen vectors of K.

4.4.2 Dual Porosity model

The idea of treating naturally fractured reservoirs as a dual porosity medium was first introduced by Barenblatt et al. (1960) and later developed by Warren and Root (1963). Analytical solution for a single-phase, unsteady-state flow in a homogeneous fractured reservoir has been derived by several authors (Kazemi et al., 1969; Yamamoto et al., 1971). This model assumes that the porous medium comprises of two interacting regions (or continua), one associated with the fracture system while the other associated with the rock matrix. Mass transfer occurs between rock matrix blocks and fractures, but flow occurs only through the fracture system and not between adjacent matrix blocks. Thus, intra-aggregate pores represent immobile pockets that exchange, retain and store fluid but do not permit convective flow. In the formulation provided by Barenblatt et al. (1960), the two interacting regions – fracture network and matrix blocks were assumed to be overlapping continua in which flow and material properties are provided at each grid point in the continuum. Dual porosity type flow partitions fluid into a mobile (inter-aggregate) and immobile (intra-aggregate) phase (Phillip, 1968; van Genuchten and Wierenge, 1976; Simunek et al., 2002). Essentially, the matrix block continuum contributes to the porosity and storage, and feeds fluid into the fracture continuum that contributes to fluid flow. The physics is governed by the equations of motion and conservation of mass which are written independently for each continuum (media). Fluid transfer between the two media is accounted for by a sink/source term in the mass conservation equation.

Transfer per unit bulk volume between the matrix and the fracture is usually assumed to occur under pseudo steady state conditions (Barenblatt et al., 1960; Warren and Root, 1963). The transfer rate per unit bulk volume from matrix to fracture system has the form

$$q = \sigma \frac{\rho k}{\mu} (P_m - P_f) \tag{4.5}$$

where P_m and P_f are the pressures in the matrix and the fracture, k is the matrix permeability, ρ is the fluid density, μ is fluid viscosity. σ is known as the shape factor and defined as a parameter characteristic of fractured rock. Its dimension is the reciprocal of area. The shape factor has remained controversial and subject of much debate, primarily because of a lack of a theoretical framework. Several studies have proposed various expressions for the shape factor. Warren and Root (1963) idealized fractured media as identical parallelepiped matrix blocks limited by uniform orthogonal fractures (Figure 4.1). The value of the sigma factor that they proposed was

$$\sigma = \frac{4N(N+2)}{L^2} \tag{4.6}$$

where N is the number of sets of fractures (1, 2, or 3). For cubic matrix blocks having a fracture spacing L, the value of σ is $12/L^2$, $32/L^2$, and $60/L^2$ for 1, 2, and 3 sets of fractures respectively.

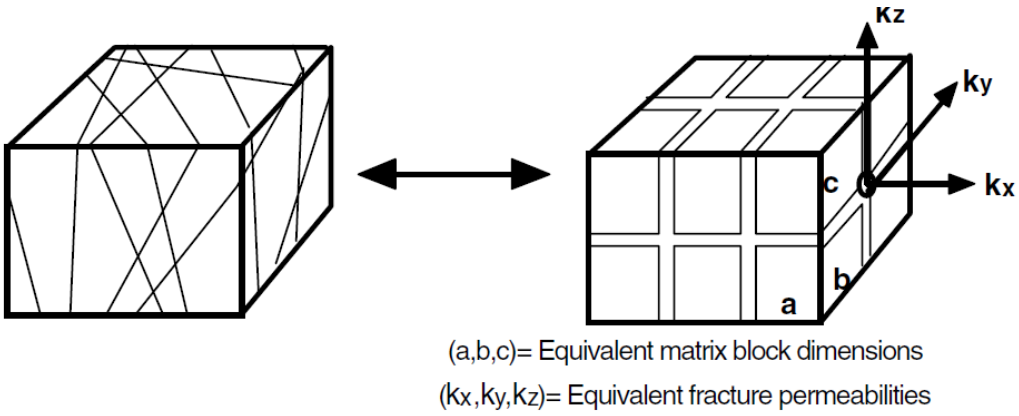

Figure 4.1: Conventional Warren and Root representation (Warren and Root, 1963) of a fractured reservoir (gridblock scale). From Bourbiaux et al., 1999.

Kazemi et al. (1976) first introduced the idea of using shape factor in numerical simulations. They used a finite-difference formulation for flow between the matrix and the fracture to derive the following value of the shape factor.

$$\sigma = 4\left[\frac{1}{L_x^2} + \frac{1}{L_y^2} + \frac{1}{L_z^2}\right] \tag{4.7}$$

where Lx, Ly, and Lz are the fracture spacing in the X, Y, and Z directions. For Lx=Ly=Lz=L, the value of σ is $12/L^2$, $8/L^2$, and $4/L^2$ for three, two and one fracture sets respectively. This expression of the shape factor is used in a number of commercially available simulators

(Firoozabadi and Thomas, 1990). Expression 4.7 is also used in this study to compute the shape factor in each grid block during upscaling the DFN model. Mean fracture spacing along an imaginary borehole in the X, Y, and Z directions in each grid block is calculated to obtain Lx, Ly, and Lz. σ in each grid block is calculated using (4.7). Sigma values are large either when the cells are too thin or the mean fracture spacing is too small. Physically, high sigma values mean that the fracture density in the rock is large and fluid would flow quickly from the matrix into the fractures. However, large sigma values often cause numerical problems as they can lead to highly ill-conditioned problems for which flow simulators fail to converge. To alleviate such problems, sigma values are first computed on a coarse grid, and then mapped to a finer simulation grid. This technique leads to larger mean fracture spacing, and hence lower sigma values. Other than Warren and Root, and Kazemi, there are several other studies that have proposed improvements on Kazemi's shape factors [eg. Coats (1989), Thomas et al. (1983), Ueda et al. (1989), Lim and Aziz (1995), Bourbiaux et al. (1999)]. However, these models are not investigated since it is not the focus of this study).

4.5 Field Study – CPE Gas Field

CPE field is located along the southwestern edge of the South Sumatra Basin in south-central Sumatra. It was discovered in 1998 while production began in 2003. Original gas in place (OGIP) was estimated to exceed 6 TCF while the gas column is approximately 1400 meters. The gas column is supported by a normally pressured aquifer. Well tests suggest that an extensive network of fractures and faults provide widespread pressure communication across all reservoir layers and most structural domains (pc, ConocoPhillips).

The CPE basin formed as rift systems in the early Cenozoic in a terrain comprising of granitic, metasedimentary and volcanic rocks. CPE gas field produces gas from compressionally uplifted, fractured, crystalline and metamorphic basement and overlying clastic and reefal carbonate rocks. These essentially comprise stratigraphic units CPE1, CPE2, and CPE3. Stratigraphic unit CPE1 which represents the main phase of basin development occurred in the late Eocene to early Oligocene. Sedimentation occurred as infilling of structural depressions by clastic debris eroded from the exposed basement rocks which comprise stratigraphic unit SU2. Rifting was then followed by thermal subsidence in late Oligocene to early Niocene. This

allowed a marine inclusion that introduced fine-grained marine sequences and reefal build-ups. These blocks constitute the unit CPE4. Further subsidence immersed this reefal carbonate system under water resulting in organic-rich deep-water shale and marl deposits. Later, these formed the gas containing hydrocarbon source rocks and top seals of the block CPE4. The pre Cenozoic basement has no primary porosity, and all of its permeability comes from fractures at all scales. Stratigraphic unit CPE2 has primary porosity ranging from 8 - 14% and permeability from 0 - 8 md. Stratigraphic unit CPE3 has primary porosity ranging from 4 - 8%, and permeability ranging from 0.5 - 5 md (pc, ConocoPhillips).

Figure 4.2 presents a perspective view of the field showing the master fault and 27 second-order faults identified in seismic images. There are several varied estimates of the displacement across the master (first-order) fault, but a widely cited value is ~150 km (pc, ConocoPhillips). The map lengths of the second-order faults vary from 50 m to 3 km. All seismically-resolvable faults have reverse slip. They strike sub-parallel to the master fault and are concentrated in a 1x8 km area along the crest of the anticline. The fault dips lie between 55° and 80°. The maximum throw across these faults ranges from 8 to 180 m.

Figure 4.2 also shows the 5 wells studied here - A, B, C, E, and I. Wells A, E, and I are near-vertical wells while wells B and C are deviated wells. Well tests were performed after drilling the vertical wells (A, E and I). These tests suggested poor correlation between wellbore-reservoir contact length and well performance. In fact there is also a very weak correlation between well performance and the total number of fractures that they intersect. However, there is a strong correlation between the total number of critically stressed fractures transected by the wellbore and well performance (pc, ConocoPhillips). This inference was used to design the trajectory of wells B and C with the intention of maximizing the borehole intersection with reservoir-scale second-order faults and their respective damage zones containing a large population of critically stressed faults. As expected, wells B and C were extremely productive, with production rates as high as 1 billion cubic feet per day (bcf/day) while the other vertical wells produced between 0.1 and 0.3 bcf/day (pc, ConocoPhillips). With the critical role of damage zones in influencing flow and production clearly evident, the objective of this research is to develop a methodology for incorporating these damage zones associated with second-order faults in reservoir models in order to model fluid flow.

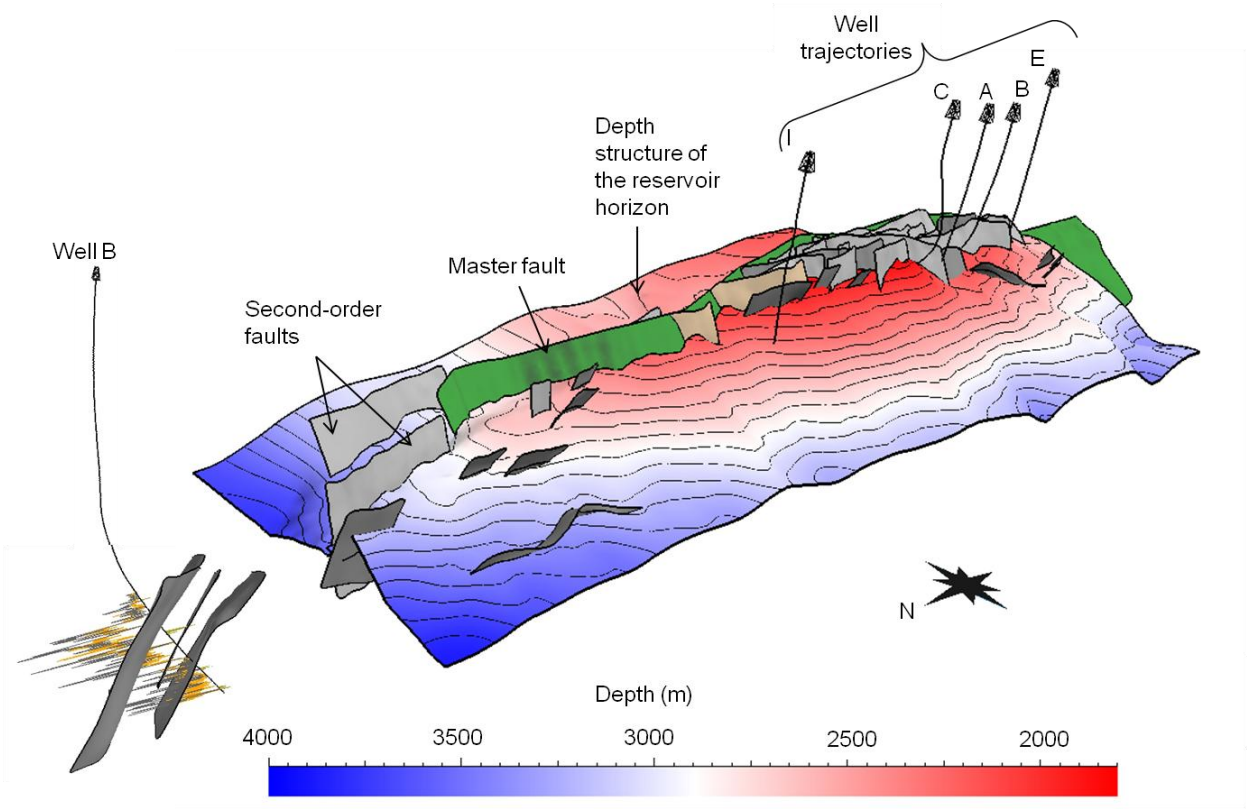

Figure 4.2: Three dimensional structural model of CPE gas field. The model shows the master fault (first order fault), second order faults, well bore trajectories and the depth structure of the reservoir horizon. The figure also shows well B intersecting three second-order faults.

4.6 DFN Model Development

In this study, a portion of the CPE gas field around well B is modeled. The reason behind this choice is that the only flow data available is a 76- hour-long flow after flow well test data performed on well B. It is expected that the flow characteristics in well B would primarily be governed by the regional reservoir characteristics, at least in the earlier stages that impact the well test (which is eventually used to calibrate the model). The FracMan software package is used for modeling the discrete fracture network (DFN) and upscaling the model. Eclipse simulator is used to perform flow simulations on the upscaled model in a dual porosity framework. A 1000 m × 1000 m × 540 m reservoir domain (540 meters is the thickness of the reservoir) which contains three second-order fault damage zones (Figure 4.3) is considered. Well B intersects all three second-order faults in this region. The strike length of the faults is 600 meters while the dip length is 2000 meters. The model domain is populated with fractures

comprising the damage zones and background fractures (regional fracture population outside the damage zone).

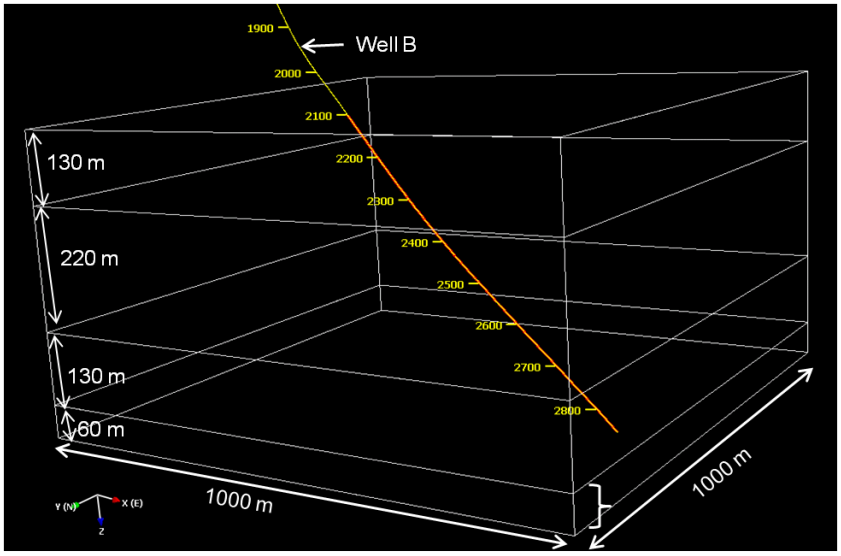

Figure 4.3: Model domain showing the reservoir comprising of four units with different fracture characteristics and the borehole trajectory.

4.6.1 Introduction of damage zones into the model

The spatial location of second-order faults is obtained from seismic images. The workflow for predicting damage zones around second-order faults (discussed in chapter 3) only provides information on the spatial variability and distribution of fracture density around the fault. It does not provide any information of fracture size. In order to constrain the fracture size, the following methodology is adopted. Consider a transect perpendicular to the fault along which the fracture density is known at every 1 meter distance from the fault (Figure 4.4). For example, if the fracture density at 21 meters from the fault is 1 fracture/m, one through-going 21-meter-long fracture is introduced. This fracture suffices for the fracture density 20 meters from the fault (which is also 1 fracture per meter). Now, if the fracture density 6 meters from the fault is 3 fractures per meter, we introduce two six-meter-long fractures from the fault, making the total fracture population three fractures at this point. In this manner, a fracture population that honors the spatial fracture density variability along a single transect is obtained. This exercise is repeated along each transect spaced 1 meter apart along the dipping length of the fault. The fractures are assumed to be square in shape, and the second dimension of the fracture is assumed to be in the plane of the fault. This method may suggest that the fractures are constrained to be

oriented perpendicular to the fault. However, this exercise is only used to constrain the fracture size and location in an attempt to honor the spatial heterogeneity in fracture density predicted from damage zone modeling (chapter 3). Fracture orientations are assigned stochastically using a distribution of fracture orientations identified from image logs. Distribution of fracture orientations in different regions of the reservoir is discussed in section 4.6.2 and shown in Figure 4.7.

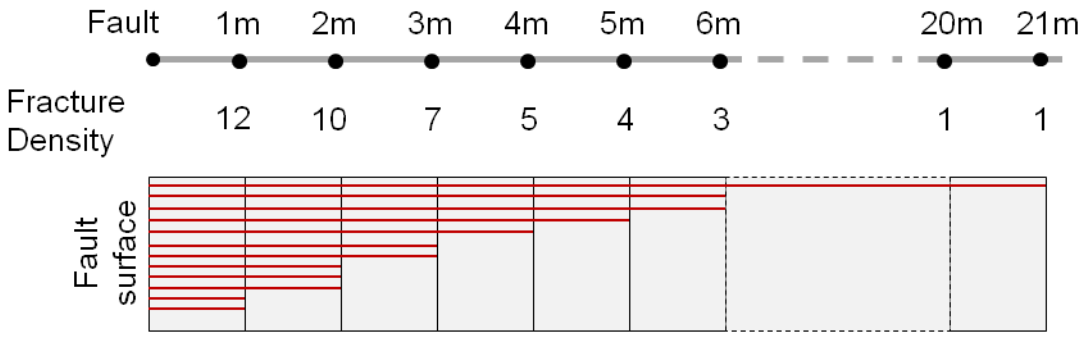

Figure 4.4: Assignment of lengths to fractures inside the damage zone. Fracture density (number of fractures per meter) is known at every one meter distance from the fault up to the width of the damage zone, which along this specific transect is 21 meters. The red lines represent the fracture population which is consistent with the above spatial fracture density distribution.

Figure 4.5 (a) shows the trajectory of the well B intersecting the trhee second-order faults (whose positions are constrained from 3D seismic images). Figure 4.5 (b) shows the model domain populated by the three damage zones (associated with second order faults) through which the wellbore traverses. The high concentration of fractures inside the damage zone creates a high permeability region. Since well B intersects the damage zones, it is hydraulically connected with these high permeability zones through which gas can be produced at considerably larger rates.

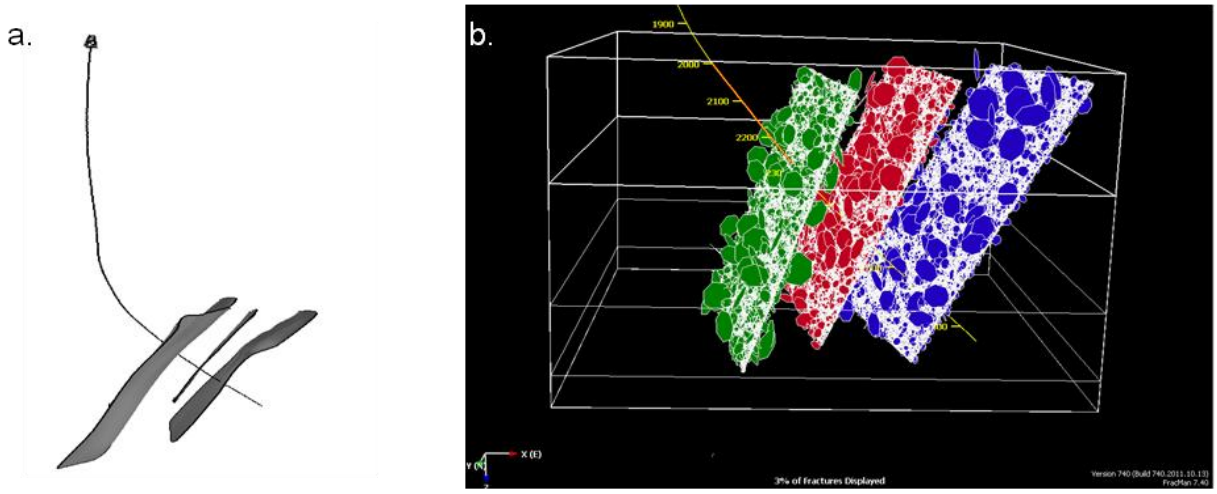

Figure 4.5: (a) Trajectory of well B showing the well intersecting three second-order faults whose positions are constrained from 3D seismic images. (b) A Discrete Fracture Network model domain showing fractures in the 3 damage zones associated with the 3 second-order reservoir scale faults that the well intersects (as seen in Figure 4.5(a)).

4.6.2 Introduction of background fractures into the model

Background fractures in the model domain are stochastically generated in FracMan. The parameters required for stochastic generation of fractures are the fracture intensity, distribution of fracture orientations, and distribution of fracture sizes. Figure 4.6 (a) shows the histogram of fractures identified in the image log in well B along with the positions where the well intersects the second-order faults. Figure 4.6 (b) shows the cumulative density plot of those fractures. The slope of the cumulative density plot is representative of the fracture density (P10 - number of fractures per unit length). Four regions of varying P10 (marked intervals 1-4) along the wellbore can be identified. Fracture intensity in intervals 1-4 is 0.8, 2.58, 0.8 and 2.04 fractures/m, respectively.

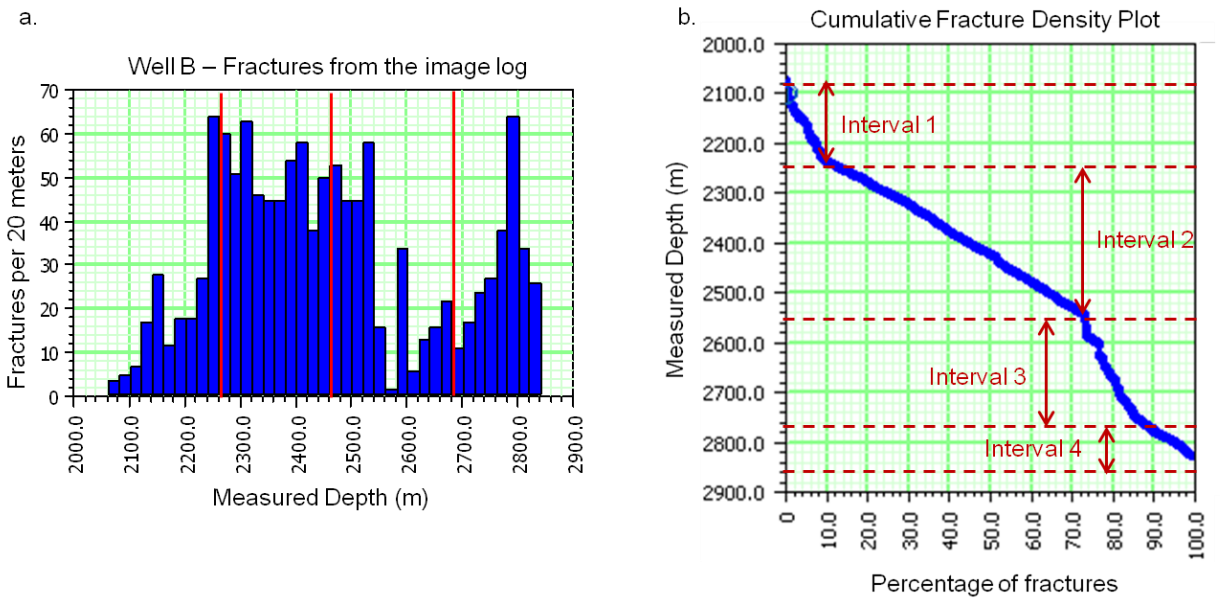

Figure 4.6: (a) Histogram showing fractures identified in the image log of well B. Red lines represent the points where the borehole intersects the reservoir-scale second-order faults. (b) Cumulative fracture density plot showing four intervals of differing fracture intensities along the borehole trajectory.

Next, statistical analysis is performed to identify various fracture sets in the fracture data obtained from the image log using the ISIS (Interactive Set Identification System) feature of FracMan. ISIS defines fracture sets from field data using an adaptive probabilistic pattern recognition algorithm. The distribution of the orientations of fractures assigned to each set is calculated, and then fractures are reassigned to sets according to probabilistic weights proportional to their similarity to other fractures in that set. The orientations of the fracture sets are then recalculated and this process is repeated until the fracture set assignment is optimized. Essentially, the statistical properties of each set are derived from the statistical properties of the fractures assigned to that set, and then fractures with a low probability of belonging to that set are removed and reassigned to another set. This ensures that the fractures are divided into groups being geologically and hydrologically similar. A complete description of the theory behind the pattern recognition algorithm can be found in the FracMan manual (2011). Figure 4.7 shows the contoured stereoplots of the major fracture sets present in the four intervals previously described. Intervals 1, 2, and 4 appear to have one major fracture set while interval 3 has three major fracture sets. We assume Fisher distribution to describe the distribution of fracture orientations in various intervals, and then calculate the Fisher distribution parameters that describe the data (mean, standard deviation) along with the statistical measures of the wellness of data fit. The

fracture orientation distribution parameters along with the fracture density (P10) of each set in each interval are provided in Table 4.1. Once the fracture orientation distribution parameters in each interval are obtained, these intervals are stochastically populated with fractures belonging to the sets present in that interval until the target fracture density P10 along the section of the borehole within that interval is reached.

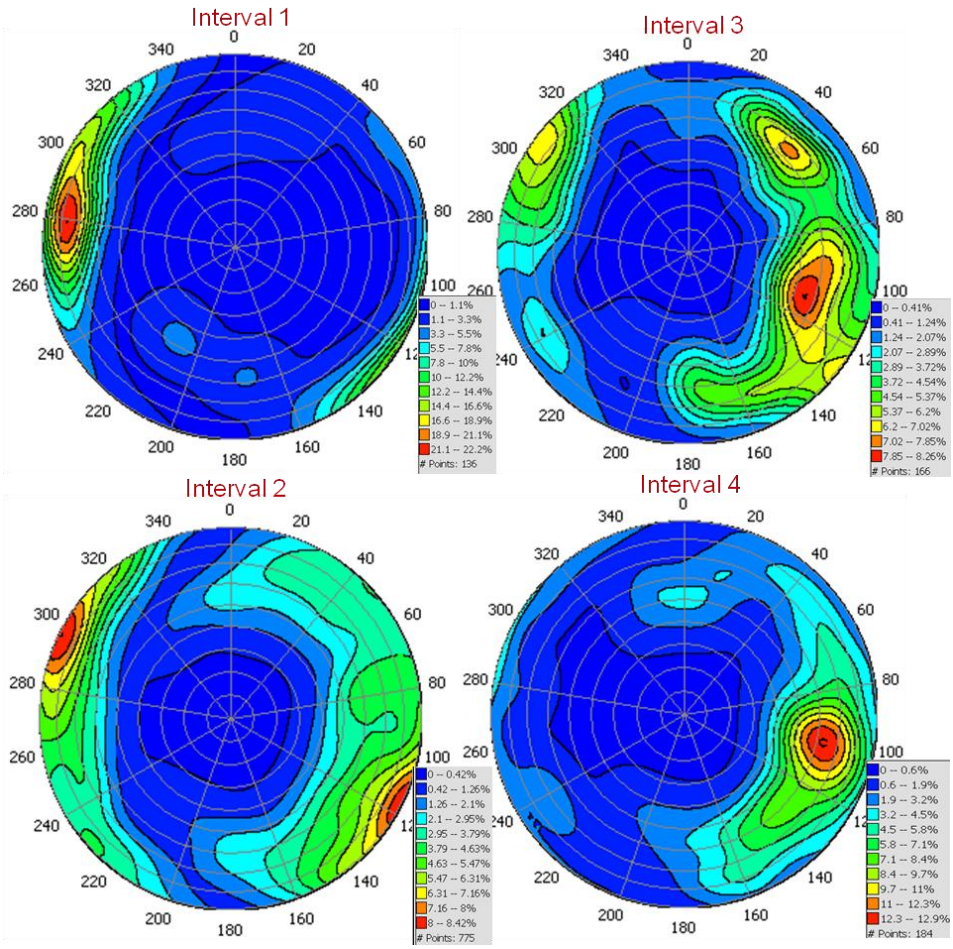

Figure 4.7: Contoured stereonets of fracture poles in various depth intervals along the borehole

Interval #	Measured Depth Interval (m)	Mean Pole Orientation (Plunge, Plunge dir)	Dispersion (K)	P10
1	2070-2240	289, 10	5.45	0.8
2	2240-2540	132, 1.5	4.25	2.58
3	2540-2750	120, 30 307, 2 44, 20	8.1 8.9 10.5	0.32 0.28 0.20
4	2750-2840	104, 28	3.7	2.04

Table 4.1: Tabulation of fracture density in the four intervals along the borehole, along with fracture orientation distribution (Fisher) parameters.

The next step is to assign a size and shape to these fractures. It is largely believed that power law models describe the length distribution of fractures. A large number of studies have been devoted to analyzing length distribution of fractures (Segall and Pollard, 1983; Gudmunsson, 1987; Villemin and Sunwoo, 1987; Childs et al., 1990; Scholz and Cowie, 1990; Davy, 1993; Odling, 1997; Main et al., 1999) in order to test the power law scaling model. However, despite numerous analyses and efforts, the statistical relevance of power law models is not established amongst the scientific community, primarily due to difficulties in obtaining a robust statistical analysis on severely limited data sets (Pickering et al., 1995; Bonnet et al., 2001). Odling et al. (1999) reported that the fracture lengths appear to follow a power law distribution ($N(l) = L_{min} l^{-n}$) with a decay rate n of ~2.1 over up to 4-5 orders of magnitude. In this study, we assume that fracture lengths honor such a power law distribution and constrain the minimum fracture length L_{min} to be 1 meter. The upper limit of the fractures is limited by the size of the model domain. Since it is difficult to put constraints on the aspect ratio of fractures, we assume fractures to be square-shaped in this study. The geometrical properties of background fractures and those comprising the damage zones are hence fixed. Figure 4.8 shows the DFN model comprising all fractures present in the model domain. Only one of the second-order fault damage zones is visible since the other two are embedded within the background fracture population.

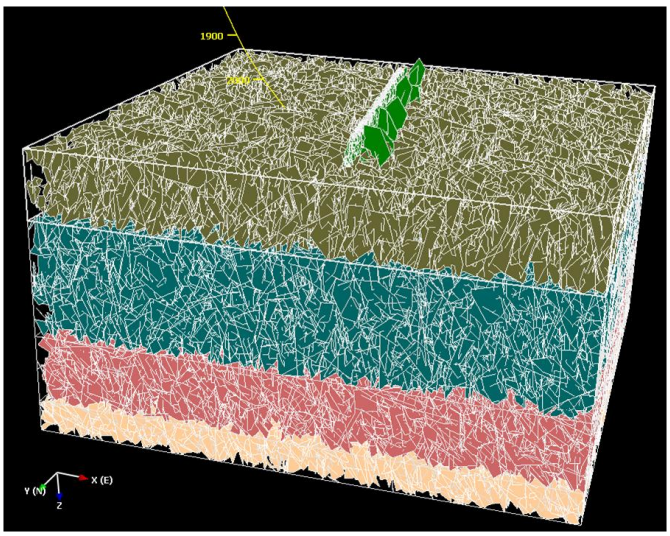

Figure 4.8: Discrete fracture network model showing fractures in various layers along with the damage zones. Only the top of one of the damage zones is visible since the others are concealed within the model background fractures.

4.6.3 Assignment of flow properties to the fracture population

Once the fracture population is established, fractures are assigned flow properties, namely aperture (mechanical and hydraulic), and permeability. Morphological analyses of fracture surfaces show prominent surface undulations (Giacomini, 2008). This leads to a spatially heterogeneous aperture distribution over the fracture surface. Studies also suggest that the fracture surface aperture distribution could be approximated by a normal distribution (Hakami, (1995) for the case of natural fractures, Esaki et al. (1999) for artificially created tensile fractures, and Lee and Cho, (2002) for tensile fractures in granite). Therefore, in the absence of a unique fracture aperture value, the definitions of aperture usually pertain to equivalent apertures. In the context of flow, it is important to distinguish between mechanical aperture and hydraulic aperture. Mechanical aperture is a measure of void spaces existing between fractures surfaces and is defined as the fracture volume (total volume of voids within the fracture) per unit area of the fracture surface. It is measured by methods such as using gas to measure fracture volume (Chen et al. 2000). Hydraulic aperture is representative of the equivalent area inside the fracture through which fluid actually flows. This is usually lesser than the mechanical aperture since a part of the total void volume that constitutes the mechanical aperture may not be connected to the interconnected void network through which flow actually occurs. Hydraulic aperture is usually calculated experimentally by calculating the fracture permeability k from flow experiments and using the parallel plate model to invert for hydraulic aperture a_h ($k = a_h^2/12$) (Chen et al., 2000).

In this study, both mechanical and hydraulic aperture values are assigned to fractures. Mechanical aperture determines the storage of the fracture (volume of hydrocarbon stored in the fracture) while hydraulic aperture determines the fracture permeability. Several studies show that fracture apertures are sensitive to the amount of normal stress acting on the fracture and the shear displacement across the fracture (Esaki et al., 1999; Chen et al., 2000; Lee and Cho, 2002). Willis-Richards et al. (1995) provide an expression for calculating the 'in contact' mechanical aperture.

$$a_m = \frac{a_0}{1+9\sigma'/\sigma_{nref}} + a_s + a_{res} \tag{4.8}$$

where a_0 is the initial total compliant aperture of the fracture, $\sigma'$is the effective normal stress acting on the fracture, σ_{nref} is the effective normal stress applied to cause 90% reduction in the compliant aperture, a_{res} is the residual aperture at high effective stress is usually considered negligible and ignored, and a_s is the change in aperture due to accumulated shear and can be expressed as equation 4.9 (Willis-Richards et al., 1995)

$$a_s = \frac{U\tan(\phi_{dil})}{1+\frac{9\sigma'}{\sigma_{nref}}} \tag{4.9}$$

U is the shear displacement across the fracture while ϕ_{dil} is the shear dilation angle resulting from shear displacement at low effective normal stress. Mechanical aperture can, therefore, be represented in the form shown in equation 4.10 (Tezuka et al. 2005).

$$a = \frac{a_0+U\tan(\phi_{dil})}{1+9\sigma'/\sigma_{nref}} = \frac{a_0(1+U\tan(\phi_{dil})/a_0)}{1+9\sigma'/\sigma_{nref}} = \frac{A.a_0}{1+9\sigma'/\sigma_{nref}} \tag{4.10}$$

where $A = (1 + U\tan(\phi_{dil})/a_0)$. Clearly (in accordance with experimental observations), the aperture scales directly with shear slip and inversely with normal stress acting on the fracture. The value of ϕ_{dil} used in this study is 10º (Chen et al. (2000) have reported a dilation angle of 10º and joint roughness coefficient (JRC will be used later) of 15 for one of the granitic samples studied). The amount of slip accumulated on a stimulated fracture is assumed to be ~0.5 mm. σ_{nref} accounts for the fracture stiffness. The effect of normal stress on reducing the fracture aperture of a stiffer fracture is less, therefore, aperture is directly proportional to σ_{nref}. The value of σ_{nref} used in this study are 10 and 40 MPa for un-stimulated (those not active in the current

stress state) and stimulated fractures respectively (partially following Moos and Barton (2008)). Moos and Barton have assumed σ_{nref} to be 100 MPa, but such an assumption leads to very high fracture permeability (~2-3 orders larger than those reported experimentally for fractures having undergone slip (Chen et al., 2000)). Fractures which have accumulated slip are stiffer due to the mismatch in asperities of the opposite faces. Fractures that are active in the current stress state can be identified by calculating the shear traction (τ) and effective normal traction (σ') acting on the fracture. Fractures that satisfy the condition $\tau \geq \mu\sigma'$ where μ is the coefficient of sliding friction (~0.6) are active in the given stress state (for details, see 2.10.5). a_0, the initial total compliant aperture of the fracture is largely unconstrained and is used to calibrate the flow properties of this model (section 4.8).

Hydraulic aperture is calculated from the mechanical aperture using Barton's equation (4.11) (Barton et al., 1985). Chen et al. (2000) show that Barton's model fits some of their experimental data reasonably well, though it does not completely account for the combined effects of surface roughness, waviness and contact area to address the apparent difference between mechanical and hydraulic aperture. However, in the absence of an alternative relationship between the two, Barton's model (4.11) is used to obtain the hydraulic fracture apertures.

$$a_h = a^2/JRC^{2.5} \tag{4.11}$$

JRC is the joint roughness coefficient which lies between 0 and 15. We use a value of 15 for JRC (Chen et al. (2000)). Fracture permeability is obtained from the hydraulic aperture assuming parallel plate model (Zimmerman and Bodvarsson, 1995; Bradley, 1987).

$$k = a_h^2/12 \tag{4.12}$$

The above formulation of apertures and permeability also honors the critically-stressed hypothesis according to which the fractures that are critically stressed in the current stress state have significantly larger permeability than the non-critically stressed fractures (Barton and Zoback, 1995; Zoback, 2007).

4.7 Fracture Upscaling

Accounting for all fractures comprising the DFN model discretely to model fluid flow is computationally impractical. Flow through discrete fractures is usually computed using finite element analysis (which involves meshing). The number of nodes in a model increases rapidly with increasing number of fractures in the model. If the fracture density is very high (for example inside the damage zone), the number of fracture intersections, and hence the number of nodes increases dramatically leading to problems with meshing, especially close to the borehole. Therefore, the DFN model is upscaled to a grid. To start with, the DFN is upscaled to a coarse grid. The grid is gradually refined until grid refinement stops impacting flow simulation results (flow solution converges). In this manner, a grid with uniformly-sized grid blocks of dimensions $12.5\ \text{m} \times 12.5\ \text{m} \times 12.5\ \text{m}$ turns out to be an appropriate grid block size. Fractures are upscaled to obtain the following equivalent grid properties - porosity, permeability tensor and shape factor for each grid block. The porosity in each grid block is obtained by a simple volume balance by computing the total fracture volume in each grid block. Effective directional grid block permeability tensor is computed using Oda's method (section 4.2.1) while the shape factor is computed using the methodology provided in section 4.4.2. For illustration, Figure 4.9 shows the upscaled grid block porosities and traces of long fractures on the DFN model boundaries.

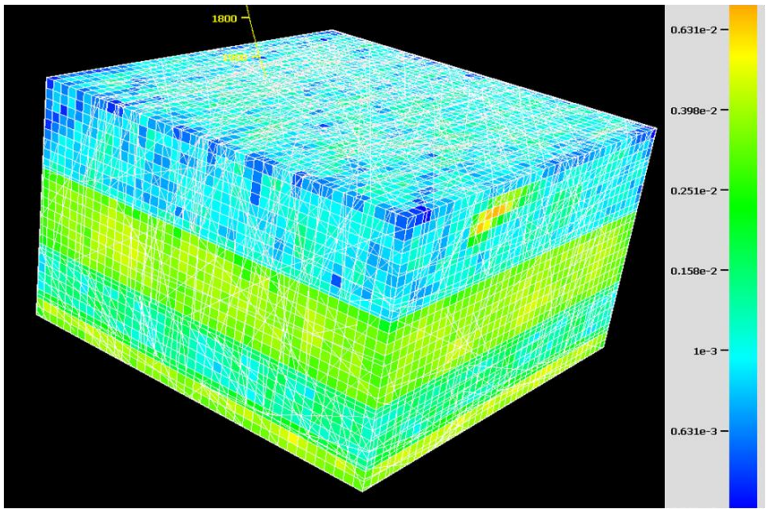

Figure 4.9: The DFN model showing the upscaled grid porosities and traces of the larger fractures on the domain boundaries

Well B encounters the Cenozoic basement at a depth of 2140 m. We assume the porosity of the basement to be 1.5%. All the basement permeability comes from fractures at all scales.

Stratigraphic unit CPE2 lies above 2140 m depth. The porosity of CPE2 ranges from 8-14% and matrix permeability is 0-8 md (pc, ConocoPhillips). In this model, we consider CPE2 to have a constant matrix porosity of 10% and matrix permeability of 4 md.

4.8 Model Calibration

The upscaled model is calibrated using a flow after flow well test. Flow during a well test is simulated through the upscaled reservoir model, and matched with the field well test data. The objective of well test simulation is to calibrate the flow properties of fractures by performing well test simulations on the upscaled DFN model and comparing the results with the actual field well test. Flow properties of fractures are adjusted using the a_0 value discussed in section 4.6.3.

4.8.1 Field Gas Well Test and Rate-Dependent Skin

A flow after flow well test was performed on well B. The well test was performed at flow rates of approximately 100, 150 and 200 million standard cubic feet per day (MMSCF/day) and the bottom-hole well pressure (BHP) was recorded (Figure 4.10). The duration for which the well was produced at these rates was ~ 28, 24 and 24 hours respectively.

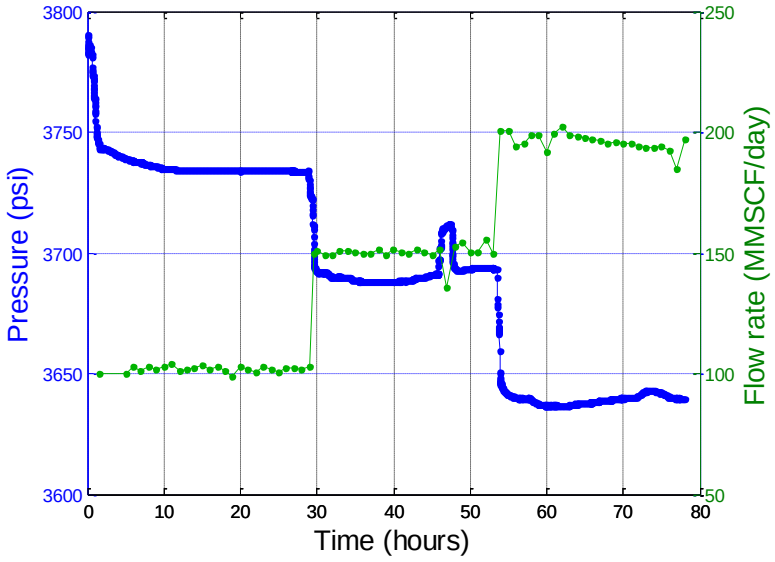

Figure 4.10: Flow after flow well test performed on well B. The test is performed at rates of 100, 150 and 200 MMSCF/day

An important consideration in the analysis of well tests performed on gas wells is the rate dependent skin effect which is an important feature of gas well tests and appears as a pressure

drop (could be positive or negative). Skin is the region around the wellbore of altered permeability caused due to invasion by mud filtrate or cement during drilling or completion of the well. This causes a relatively higher pressure drop during flow close to the borehole. Pressure drop due to the skin is the difference in the well pressure while flowing and the pressure that the well would have seen if the region around the well were undamaged. The skin factor is used to quantify the magnitude of the skin effect. The skin factor is usually a constant value when the fluids flowing are low compressibility liquids characterized by laminar flow for which Darcy's law is valid. (Skin factor is negative in cases where the region surrounding the borehole is fractured, for example during hydraulic stimulation operations). A difficulty that arises in gas well test interpretations is the nonlinearity of boundary conditions. This essentially is a result of non-Darcy effects close to the borehole. Darcy's law is valid only when flow is laminar which occurs at relatively low fluid velocities. Due to low gas viscosity, gas flow is usually non-laminar (though not strictly turbulent). Non-Darcy flow effects close to the borehole appear as a rate dependent skin (Muskat, 1946; Katz et al., 1959; Wattenbarger and Ramney, 1968). The total skin can be written as

$$\mathrm{s} = \mathrm{s}' + \mathrm{Dq}_{\mathrm{sc}} \tag{4.13}$$

where s' is the constant part, q_{sc} is the rate of gas flow while D is the rate of increase of skin with flow rate. The constant part of the total skin s' is due to damage around the borehole while the flow dependent part of the skin Dq_{sc} is due to varying flow rates. The two different skin effects can be evaluated individually using a flow after flow test (Rawlings and Schellhardt, 1936). Rate dependent skin factor D can be found using nonlinear regression. Well test analysis is performed to evaluate the skin effect using the Saphir software package. Detailed calculations evaluating the rate-dependent skin are provided in Appendix 4A. The values of s' and D obtained from well test analysis are 0.492 and 0.000042 respectively, where flow rate q_{sc} is in MSCF/day (thousand standard cubic feet per day). Therefore, the skin factors at flow rates of 100, 150 and 200 MMSCF/day are 4.69, 6.79 and 8.89 respectively. These values of skin factors result in pressure drops of 18.6, 40.6 and 70.6 psi.

4.8.2 Model Calibration and Validation

In this study, a small region of the reservoir around well B is modeled. In the absence of any other producing well in the vicinity (which is true during the duration of the well test), the surrounding region of the reservoir provides lateral pore pressure support to the region modeled. This is accounted for by providing constant pressure boundary condition on the sides of the model domain. Well test simulation is performed on the upscaled DFN model at a flow rate of 100 MMSCF/day and compared with the first phase of the field flow after flow well test to calibrate the model by tuning the slip a_0 parameter (discussed in section 4.6.3). The value of a_0 for which we get a reasonably good match is 1.33 mm. Figure 4.11 shows the actual pressure drawdown (in blue) and simulated drawdown curves (in red). It appears that the pressure sharply decreases as the production starts and then stabilizes at a reduced pressure. This probably represents aquifer support or lateral support from the surrounding reservoir (please note that we are only modeling a small part of the reservoir around well B which passes through 3 seismically identified second-order faults and their damage zones). The initial pressure decay in the simulated drawdown curve is sharper than that in the actual drawdown curve. A possible explanation could be borehole storage effects which we have not considered in this study. However, the match in the pressure at which the drawdown stabilizes is reasonably good. Using values of aperture and permeability obtained by a_0 value of 1.33, well tests are simulated at 150 and 200 MMSCF/day. Pressure drawdown curves at these rates are also shown in Figure 4.11. The pressure drop matches reasonably well. However, anomalously there is a gentle rise in pressure with time at both the flow rate, besides the sudden bump of 20 psi at 47 hours into the well test. The gradual rise in pressure can be explained by the fact that the flow rate is not held perfectly constant during the well test (Figure 4.10). The sudden bump of 20 psi coincides with the sudden fall in flow rate by approximately 13 MMSCF/day. However, since flow through reservoirs is a diffusive process, changes in pressure can only be gradual (solution to the diffusion equation only allows gradual changes of the diffusing entity). Therefore, the sudden change (rise and fall) of ~20 psi could be due to some unaccounted activity during the well test.

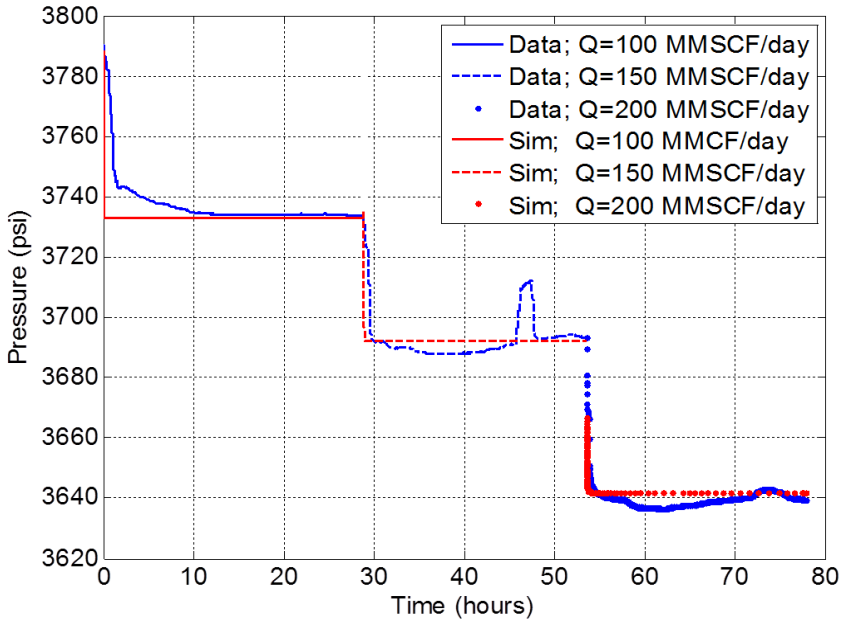

Figure 4.11: Pressure drawdown during a flow after flow test performed at 100, 150 and 200 MMSCF/day. Blue represents actual well test while red represents simulated values

4.9 Calibrated flow properties of fractures and the upscaled grid

This section shows the distribution of relevant flow properties of fractures comprising the DFN and cells of the upscaled grid. Figure 4.12 shows the distribution of the mechanical apertures of stimulated and unstimulated (critically stressed and non-critically stressed) fractures and faults comprising the DFN. The mechanical aperture of critically-stressed fractures ranges from ~ 180 – 340 µm while that of non-critically stressed fractures is considerably lesser, ranging from 30 – 120 µm. These values are in good agreement with those reported by Chen et al. (2000). They report mechanical apertures ranging from ~20 µm – 200 µm at a confining pressure of 35 MPa (representative of the average reservoir depth). In their experiments, aperture increases from 20-200 µm as shear displacement across the fracture increases from 0 to 1 mm. Therefore, the lower values are representative of non-critically stressed fractures/faults while the higher values are representative of critically stressed fractures/faults.

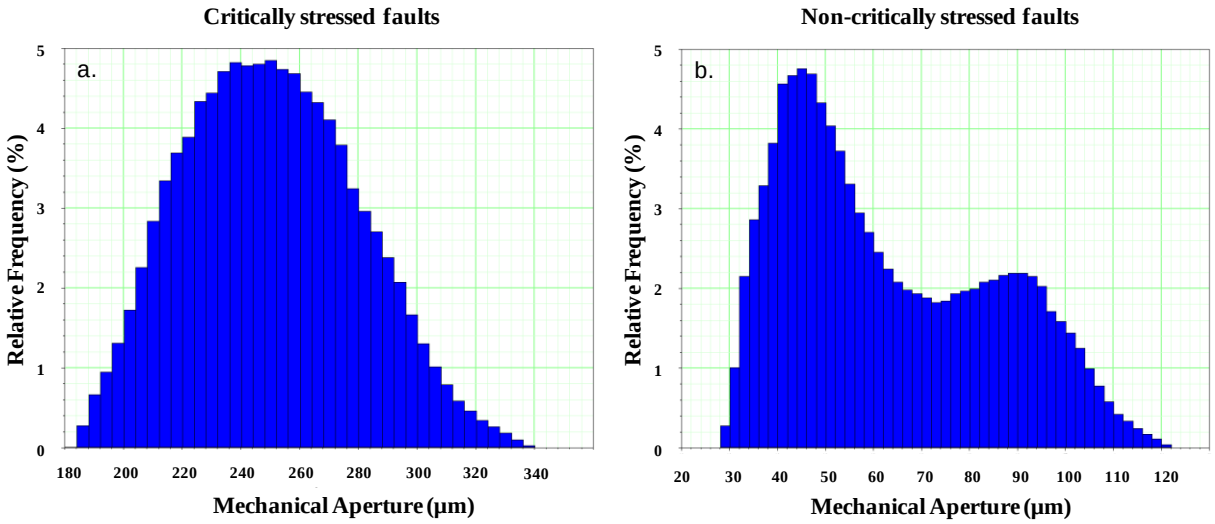

Figure 4.12: Distribution of the mechanical aperture of (a) stimulated and (b) unstimulated fractures and faults

Figure 4.13 shows the distribution of the hydraulic apertures of critically stressed and non-critically stressed fractures and faults derived from the mechanical aperture using Barton's model (4.11). These values (40-120 µm for critically stressed and 1-14 µm for non-critically stressed faults) are considerably lesser than the mechanical aperture and are of the same order as those reported experimentally by Chen et al. (2000).

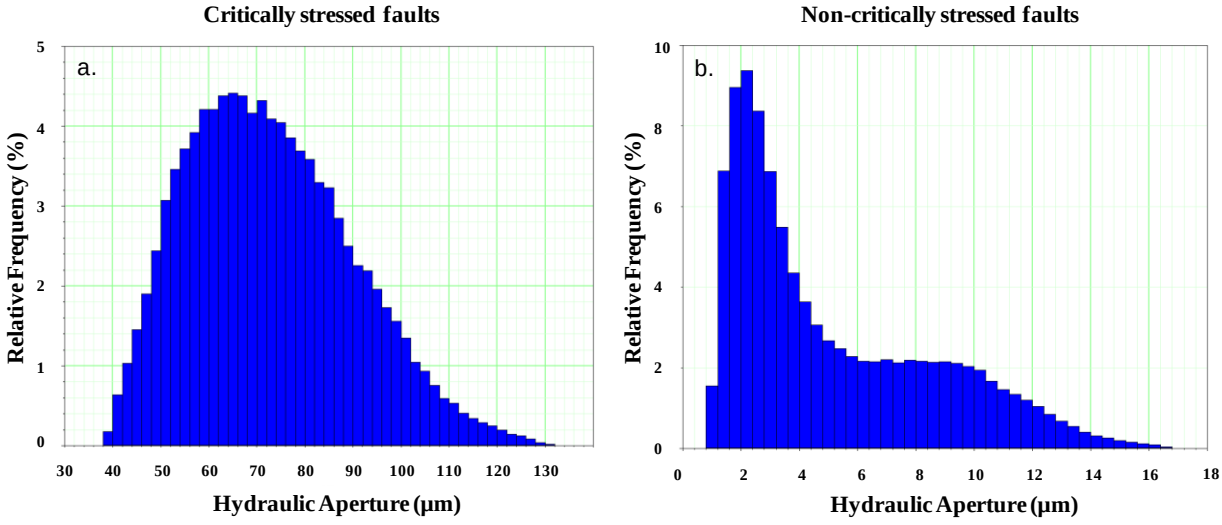

Figure 4.13: Distribution of the hydraulic aperture of (a) stimulated and (b) unstimulated fractures and faults

Figure 4.14 shows the distribution of fracture permeability that is derived from the hydraulic aperture using the parallel plate model. Permeability of most critically stressed

fractures/faults is ~ 200-600 Darcy which is almost 2 orders larger than that of non critically-stressed fractures/faults (~ 0.1-3 Darcy). These values are also in good agreement with those reported by Chen et al. (2000).

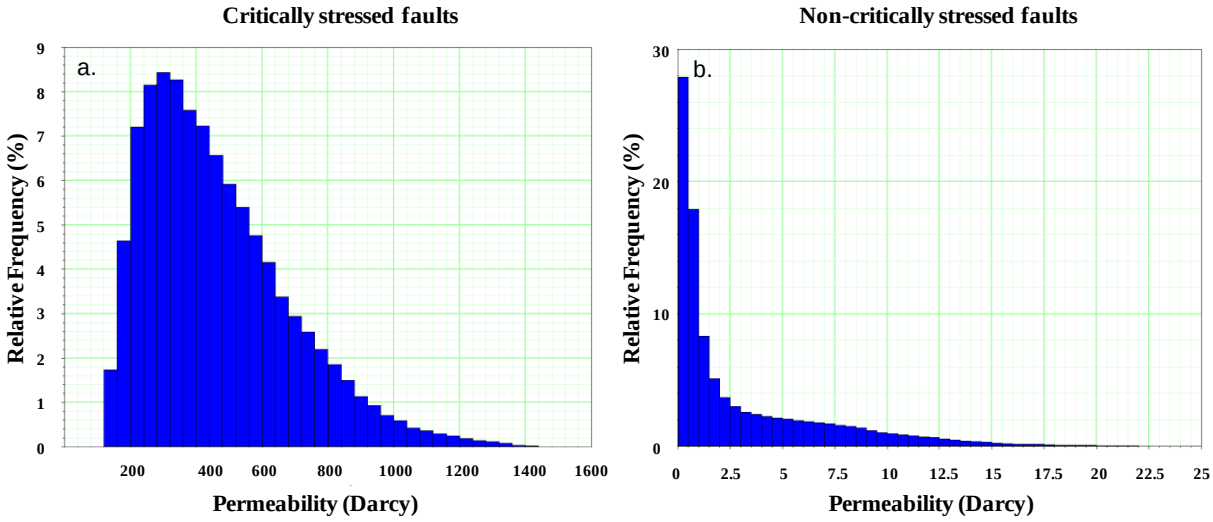

Figure 4.14: Distribution of the permeability of (a) stimulated and (b) unstimulated fractures and faults

Figure 4.15 shows the distribution of the permeability tensor components (Kxx, Kyy and Kzz) along with the equivalent grid porosity due to fracture volume. In most cells, Kxx ranges from 100-800 md, Kyy ranges from 400-2000 md, and Kzz ranges from 400-3000 md. The component of the permeability tensor in the Y and Z direction is significantly larger than in the X direction because most fractures and faults dip steeply and strike around N-S. The fracture permeability is large along the fracture plane, i.e. in the plane of the strike and dip. In the DFN model in this study, the Y axis is oriented along the north direction and the Z axis is directed vertically downwards. This leads to higher permeability along the plane containing lines in the N-S direction and in the vertically downwards direction, leading to larger Kyy and Kzz compared to Kxx.

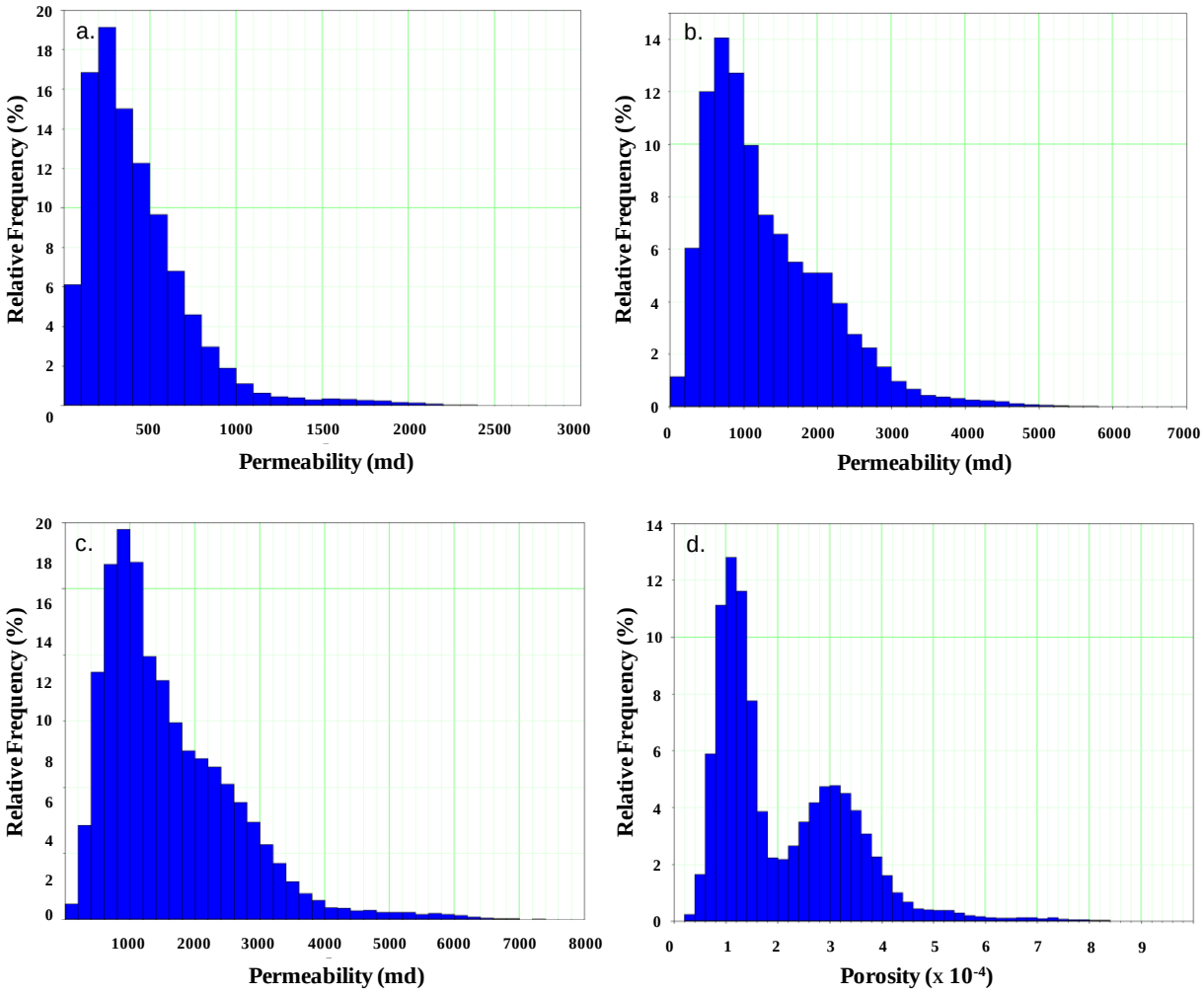

Figure 4.15: Distribution of the (a) K_{xx} (b) K_{yy} (c) K_{zz} components of the permeability tensor and (d) equivalent porosity of the cells in the upscaled grid

Figure 4.16 shows the distribution of shape factors (discussed in 4.4.2) in grid cells. The two plots show the difference in distribution due to the presence of damage zones. Figure 4.16 (a) represents the shape factor σ distribution in a grid obtained by upscaling the DFN containing background fractures alone (Bkg model), while Figure 4.16 (b) represents the distribution in a grid obtained by upscaling the DFN containing both, background fractures and damage zones (DZ model). The main difference is in the larges values of σ (larger than 200 in Figure 4.16(b)). Damage zones are characterized by a high fracture density which reduces the average spacing between fractures leading to high σ values. Large σ enables more rapid fluid exchange between the matrix and fractures which impacts the flow characteristics of the reservoir as discussed in the next section.

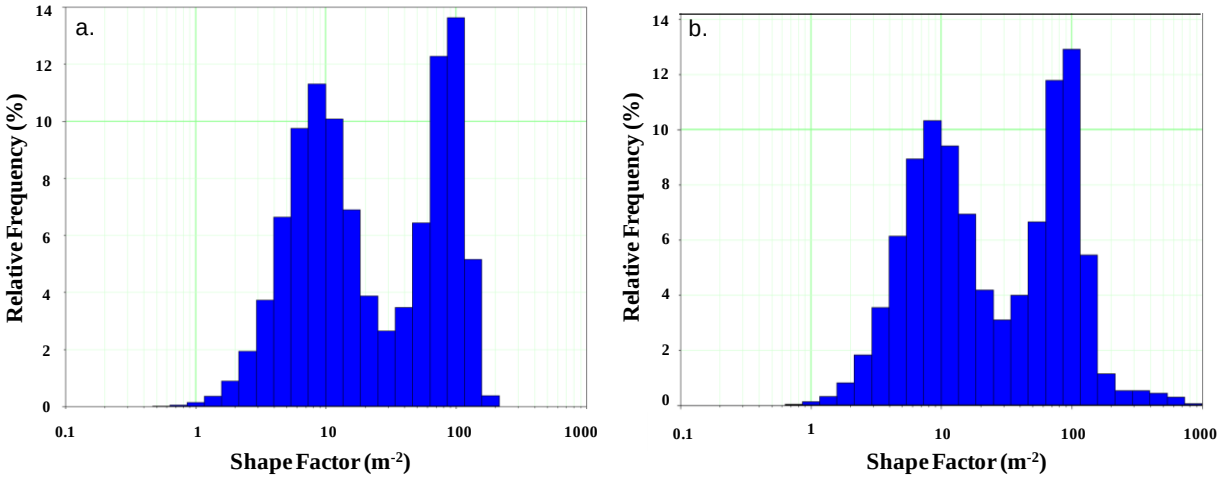

Figure 4.16: Distribution of the grid cell shape factors in the grid upscaled from the DFN model containing (a) background (region) fracture population only (b) containing background fractures and damage zones

4.10 Flow simulation in a dual porosity framework

Gas flow is simulated through the calibrated, upscaled reservoir model. Since relevant data such as PVT characteristics of the reservoir, production schedule, well pattern, production data etc. is not available, this study does not seek to predict reservoir performance. Rather, the focus of this study is to highlight the impact of damage zones on flow, and how ignoring damage zones while modeling flow through reservoirs may lead to erroneous conclusions. In order to demonstrate the impact of damage zones, flow is simulated through two models, one that is obtained from upscaling a DFN comprising of only the background fracture population (Bkg model), while the other is obtained by upscaling a DFN containing both, the background fracture population and damage zones (DZ model). The well produces dry gas at a constant rate of 30 MMSCF/day for a period of 300 days. The well is uncased, and produces all along the length through which it contacts the reservoir. A no-flow boundary condition is applied on the sides of the reservoir model. Figure 4.17 compares the decay in the bottom hole pressure (BHP) over the 300 days of production. The initial reservoir pressure is 3790 psi. As production commences, the BHP rapidly falls to ~ 3000 psi and 2400 psi in the DZ model and Bkg model respectively, after which it decays almost linearly at a constant rate for the next 300 days. The difference in the BHP in the two models at any instant is almost 600 psi. The BHP decay in the DZ model is less because the highly permeable damage zones channelize flow from the surrounding reservoir

towards the well. Since the gas can flow more easily towards the well, it prevents as large a pressure drop as is seen in the Bkg model. High permeability in damage zones is not the only reason for larger flow rates. The shape factor σ plays an important role in reservoirs that demonstrate dual porosity characteristics (as in the current study). Shape factor (which is representative of fracture density) governs the ease with which the matrix fluids interact with the fracture network. Fractures provide a highly permeable flow path, but the matrix provides fluid storage. High flow rates cannot be maintained with a high permeability fracture network alone. It is equally important for the matrix to feed fluids into the adjacent fractures at a rapid rate. In low matrix permeability reservoirs (as in dual porosity systems), a rapid exchange of fluids from the matrix to the adjacent fractures can only be achieved by a dense fracture network (so that the fluid in the matrix can quickly diffuse into the adjacent fractures). Damage zones provide both, the highly permeable fracture network and large fracture density (high σ as seen in Figure 4.16) that facilitates matrix-fracture interaction.

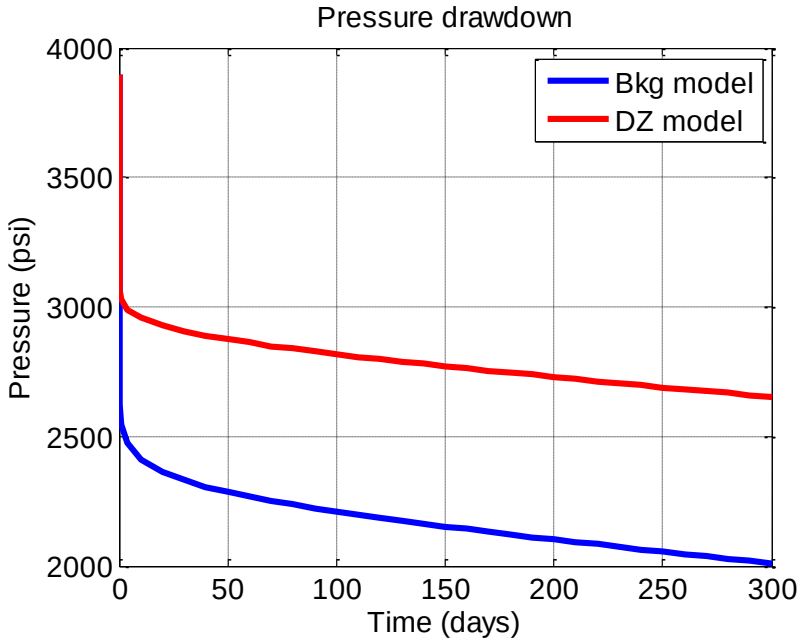

Figure 4.17: Pressure (BHP) drawdown in response to production of dry gas at a constant rate of 30 MMSCF/day. Blue curve represents the drawdown in a model obtained by upscaling the DFN containing only the background fracture population, while the red curve represents the drawdown in a model obtained by upscaling the DFN containing both background fractures and damage zones. Impact of damage zones on flow is clearly evident by the considerable difference in pressure drawdowns from the two models.

Next, we study the effect of various drilling strategies in fractured reservoirs. Three cases of the DZ model are considered (i.e. the reservoir grid obtained on upscaling the DFN model

containing damage zones is held fixed for the three cases). The only difference is in the well trajectories. In the first case, a deviated well is drilled so that it intersects all the 3 fault damage zones. In the second case, a deviated well is drilled such that it does not intersect any fault damage zone. In the third case, a vertical well is drilled without intersecting any damage zone. The pressure response on producing the well at 30 MMSCF/day for a period of 300 days for the three cases is shown in Figure 4.18. Comparing cases 1 and 2 clearly shows that the flow rates are larger when the well intersects damage zones as opposed to when it fails to intersect them. Therefore, in order to maximize flow rates and take full advantage of damage zones, it is important to course the wellbore trajectory through damage zones. Pressure decay in case 3 is significantly lower than cases 1 and 2. This may be due to three reasons. First, it is a vertical well, so the reservoir-well contact length is significantly lesser than for a deviated well. Second, due to the steeply dipping orientation of most fractures, the permeability in the vertical direction Kzz is larger than that in the horizontal directions. Therefore, flow rates are larger in the vertical direction. Since the projection of a deviated well in the vertical direction is larger than that of a vertical well, flow rates will be larger in the deviated well. Third, the well does not intersect any damage zones which provide highly permeable conduits between the well and the reservoir.

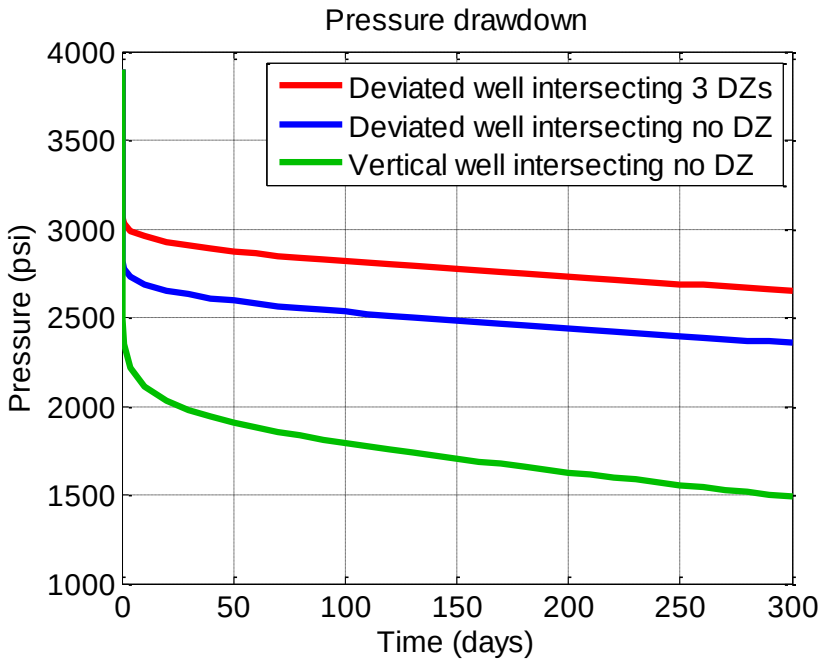

Figure 4.18: The three curves represent the pressure (BHP) drawdown in response to production of dry gas at a constant rate of 30 MMSCF/day for three different drilling scenarios.

These simulations suggest that in order to maximize flow rates into the well, well trajectories should be designed to intersect damage zones, they should be as perpendicular to the major fracture sets as possible so that the well presents a large projection in the direction of maximum flow (anisotropy), and the contact length of the well with the reservoir should be maximized. Of course, it may not be possible to design a wellbore trajectory which satisfies all three criteria. Besides, there may be borehole stability issues related to drilling in certain orientations depending on the in-situ stress state and surrounding rock properties (Zoback, 2007). This, therefore, turns into an optimization problem which is not discussed in this study. In this particular case, however, the deviated trajectory of well B intersects three fault damage zones, being deviated, traverses a large distance within the reservoir, and presents a large projection in the direction of maximum flow. As it turns out, well B, in fact, is the most productive well in the CPE gas field.

4.11 Summary

This work presents a methodology for generating reservoir models incorporating fault damage zones in a DFN framework. A 1000 m × 1000 m × 540 m region containing fault damage zones around well B in the CPE gas field is modeled. Dynamic rupture simulations are

used to model damage zones that populate the DFN. Information derived from image logs is used to generate the regional (background) fracture population stochastically. Aki-Richards' formulation and Barton's model are used to assign flow properties (aperture and permeability) to fractures. A large population of densely populated fractures with several intersections prevents the use of finite element methods for modeling flow discretely through the fracture network. However, a low matrix permeability and large fracture density allows us to idealize the reservoir as a dual porosity system. The DFN is upscaled to obtain an equivalent reservoir grid using Oda's method. In this study, we have converted the plastic strain field in the damage zone into a fracture population. This fracture population is later upscaled to obtain the permeability tensor using Oda's method. An alternate method that would avoid having to convert the plastic strains into a fracture population and subsequent upscaling is to obtain a permeability tensor from the plastic strain tensor. Dynamic rupture modeling provides the plastic strain tensor from which equivalent plastic strain (scalar measure of the plastic strain tensor) is obtained. Potentially, it may be possible to find a transformation function that converts the dilatant plastic strain tensor into an equivalent grid block permeability tensor. However, since we do not model the background fracture population numerically (in fact we generate them stochastically), we will still be required to upscale the background fracture population.

The model is calibrated using a flow after flow well test. Flow simulations (dry gas single phase flow) are performed with the objective of highlighting the impact of damage zones on flow, and not with the objective of predicting production since relevant data (PVT and production data, well pattern and production schedule etc.) is not available. Simulations are performed on the Bkg model (containing only background fractures) and the DZ model (containing fractures and damage zones). The well is produced at a constant rate of 30MMSCF/day for 300 days. Simulations show a difference of ~ 600 psi in the decay of BHP as a result of production, which can be attributed to the 3 fault damage zones that the well intersects. Three well drilling scenarios are also studied. These involve drilling a deviated well through damage zones, deviated well not intersecting damage zones and a vertical well not intersecting damage zones. Pressure decay in the case of the deviated well not intersecting damage zones is ~ 300 psi larger than when the wellbore intersects the three damage zones. Pressure decay in case of a vertical well not intersecting any damage zones is ~ 1150 psi greater than that in a deviated well that intersects the three damage zones.

4.12 Conclusion

Results from this study show that damage zones have a considerable effect on flow characteristics of fractured, low matrix permeability reservoirs (that exhibit dual-porosity characteristics). This highlights the need to incorporate damage zones while generating reservoir models to simulate flow and predict production. The large fracture density in damage zones facilitates flow by creating a spatially large high-permeability region into which fluid from the surrounding reservoir drains and gets channelized if the producing/perforation interval of the well intersects the damage zone.

Simulations also suggest that higher flow rates in the reservoir and better well performance can be achieved by coursing the well through damage zones, increasing the reservoir-wellbore contact length and providing a larger projection of the well in the direction of maximum flow (flow rates are different in different directions due to permeability anisotropy introduced by major fracture sets along their planes).

4.13 References

Barber, A. J., and M. J. Crow. 2005. Pre-Tertiary stratigraphy, in A. J. Barber, M. J. Crow, and J. S. Milsom, eds., Sumatra geology, resources and tectonic evolution. Geological Society (London) Memoir 31, 290

Barenblatt, G. I., and I. P. Zheltov. 1960. Fundamental equations of filtration of homogeneous liquids in fissured rocks. Sov Dokl Akad Nauk, 132(3), 545–8.

Barenblatt, G. I., I. P. Zheltov, and I. N. Kochina. 1960. Basic concepts in the theory of seepage of homogeneous liquids in fissured rocks. PMM (Society of Applied Mathematics and Mechanics), 24(5), 852–64.

Barton N., and V. Choubey. 1977. The shear strength of rock joints in theory and practice. Rock Mechanics and Rock Engineering, 10 (1-2), 1-54. doi: 10.1007/BF01261801

Barton, N., S. Bandis, and K. Bakhtar. 1985. Strength, deformation and conductivity coupling of rock joints. International Journal of Rock Mechanics and Mining Sciences & Geomechanics Abstracts, 22 (3), 121-140. doi: 10.1016/0148-9062(85)93227-9

Barton C. A., M. D. Zoback, and D. Moos. 1995. Fluid flow along potentially active faults in crystalline rock. Geology, 23, 683-686. doi: 10.1130/0091-7613(1995)023<0683:FFAPAF>2.3.CO;2

Berkowitz, B. 2002. Characterizing flow and transport in fractured geological media: A review. Advances in Water Resources, 25 (8-12), 861-884. doi: 10.1016/S0309-1708(02)00042-8

Bonnet, E., O. Bour, N. E. Odling, P. Davy, I. Main, P. Cowie, and B. Berkowitz. 2001. Scaling of geological systems in geological media. Reviews of Geophysics, 39 (3), 347-383. doi: 10.1029/1999RG000074

Bourbiaux, B., S. Granet, P. Landereau, B. Noetinger, S. Sarda, and J. C. Sabathier. 1999. Scaling up matrix fracture transfers in dual porosity models: theory and application. Society of Petroleum Engineers, document Id 56557-MS. doi: 10.2118/56557-MS

Bourne S. J., F. Brauckmann, L. Rijkels, B. J. Stephenson, A. Weber, and E. J. M. Willemse. 2000. Society of Petroleum Engineers. doi: 10.2118/87253-MS

Bourne S. J., and E. J. M. Willemse. 2001. Elastic stress control on the pattern of tensile fracturing around a small fault network at Nash Point, U.K. Journal of Structural Geology, 23 (11), 1753-1770. doi: 10.1016/S0191-8141(01)00027-X

Brown S. R., and R. L. Bruhn. 1998. Fluid permeability of deformable fracture networks. Journal of Geophysical Research, 103 (B2), 2489-2500. doi: 10.1029/97JB03113

Cacas, M.C., E. Ledoux, G. de Marsily, A. Barbreau, P. Calmels, B. Gaillard, and R. Margritta. 1990 (a). Modeling fracture flow with a stochastic discrete fracture network: Calibration and validation: 1. The flow model. Water Resources Research, 26(3), 479-489. doi: 10.1029/WR026i003p00491

Cacas, M.C., E. Ledoux, G. de Marsily, A. Barbreau, P. Calmels, B. Gaillard, and R. Margritta. 1990 (b). Modeling fracture flow with a stochastic discrete fracture network: Calibration and validation: 1. The transport model. Water Resources Research, 26(3), 491-500

Chen H. Y., and L. W. Teufel. 2000. Coupling Fluid-Flow and Geomechanics in Dual-Porosity Modeling of Naturally Fractured Reservoirs - Model Description and Comparison. Society of Petroleum Engineers, document Id 59043-MS. doi: 10.2118/59043-MS

Chen, Z., S. P. Narayan, Z. Yang, and S. S. Rahman (2000). An experimental investigation of hydraulic behaviour of fractures and joints in granitic rock. International Journal of Rock Mechanics and Mining Sciences, 37(7), 1061-1071. doi:10.1016/S1365-1609(00)00039-3

Childs, C., J.J. Walsh, J. Watterson. 1990. A method for estimation of the density of fault displacements below the limit of seismic resolution in reservoir formations, North Sea Oil and Gas Reservoirs II. The Norwegian Institute of Technology, Graham and Trotman, London, 309–318

Coats, K. H. 1989. Implicit compositional simulation of single-porosity and dual-porosity reservoirs. Society of Petroleum Engineers, document Id 18427-MS. doi: 10.2118/18427-MS

Couples G. D., H. Lewis, M. A. Reynolds, G. E. Pickup, and J. Ma. 2003. Upscaling fluid-flow and geomechanical properties in coupled matrix+ fractures + fluid systems. Society of Petroleum Engineers, document ID 79696-MS. doi: 10.2118/79696-MS

Dagan, G., and S. P. Neuman. 1997. Subsurface flow and transport: a stochastic approach. New York: Cambridge University Press.

Davy, P. 1993. On the frequency-length distribution of the San Andreas Fault. Journal of Geophysical Research, 98 (B7), 12141-12151.

Dershowitz, B., P. LaPointe, T. Eiben, and L. Wei. 2000. Integration of discrete fracture network methods with conventional simulator approaches. Society of Petroleum Engineers, Document ID 62498-PA. doi: 10.2118/62498-PA

De Smet, M. E. M., and A. J. Barber. 2005. Tertiary stratigraphy, in A. J. Barber, M. J. Crow, and J. S. Milsom, eds., Sumatra: Geology, resources and tectonic evolution. Geological Society (London) Memoir 31, 86–97

Durlofsky, L. J. 2003. Upscaling of geocellular models for reservoir flow simulation: A review of recent progress, paper presented at 7th International Forum on Reservoir Simulation.

Esaki, T., S. Du, Y. Mitani, K. Ikusada, and L. Jing (1999). Development of a shear-flow test apparatus and determination of coupled properties for a single rock joint. International Journal of Rock Mechanics and Mining Sciences, 36(5), 641-650. doi:10.1016/S0148-9062(99)00044-3

Firoozabadi, A., and L. Kent. 1990. Sixth SPE comparative solution project: dual porosity simulators. Journal of Petroleum Technology, 42 (6), 710 – 715, 762 – 763. doi: 10.2118/18741-PA

FracMan7. 2011. User's Manual. Golder Associates, Seattle.

FracMan7. 2009. FracMan workshop. Golder Associates, Seattle.

Giacomini, A., O. Buzzi, A. Ferrero, M. Migliazza, and G. Giani (2007). Numerical study of flow anisotropy within a single natural rock joint. International Journal of Rock Mechanics and Mining Sciences, 45(1), 47-58. doi:10.1016/j.ijrmms.2007.04.007

Gringarten E. 1996. 3-D geometric description of fractured reservoirs. Mathematical Geology, 28 (7). doi: 10.1007/BF02066006

Gudmundsson, A. 1987. Geometry, formation and development of tectonic fractures on the Reykjanes Peninsula, southwest Iceland. Tectonophysics, 139, 3-4, 295-308. doi: 10.1016/0040-1951(87)90103-X

Hakami, E. (1995). Aperture distribution of rock apertures. Ph.D. dissertation, Royal Institute of Technology, Stockholm, Sweden.

Hennings, P., P. Allwardt, P. Paul, C. Zahm, and R. Reid. 2012. Relationship between fractures, fault zones, stress and reservoir productivity in the Suban gas field, Sumatra, Indonesia. AAPG Bulletin, 96(4), 753-772. doi: 10.1306/08161109084

Katz, D. L., D. Cornell, R. Kobayashi, F. H. Poettmann, J. A. Vary, J. R. Elenbaas, and C. F. Weinaug. 1959. Handbook of natural gas engineering, McGraw-Hill Book Co. Inc., New York.

Kazemi H., M. S. Seth, and G. W. Thomas. 1969. The interpretation of interference tests in naturally fractured reservoirs with uniform fracture distribution. Society of Petroleum Engineers Journal, 9 (4). doi: 10.2118/2156-PA

Kazemi, H., and J. R. Gilman. 1993. Multiphase flows in fractured petroleum reservoirs. In: Bear J, Tsang CF, de Marsily G, editors. Flow and contaminant transport in fractured rocks. New York: Academic Press.

Lee, H. S., and T. F. Cho (2002). Hydraulic Characteristics of Rough Fractures in Linear Flow under Normal and Shear Load. Rock Mechanics and Rock Engineering, 35(4), 299-318. doi:10.1007/s00603-002-0028-y

Lee, S. H., M. F. Lough, and C. L. Jensen. 2001. Hierarchial modeling of flow in naturally fractured formations with multiple length scales. Water Resources Research, 37 (3), 443. doi: 10.1029/2000WR900340

Lim K. T., and K. Aziz. 1995. Matrix-fracture transfer shape factors for dual-porosity simulators. Journal of Petroleum Science and Engineering, 13 (3-4), 169-178. doi: 10.1016/0920-4105(95)00010-F

Long Jane C. S., and D. M. Billaux. 1987. From field data to fracture network modeling: An example incorporating spatial structure. Water Resources Research, 23 (7), 1201. doi: 10.1029/WR023i007p01201

Main, I. G., T. Leonard, O. Papasouliotis, C. G. Hatton, and P. G. Meredith. 1999. One slope or two? Detecting statistically significant breaks of slope in geophysical data, with application to fracture scaling relationships. Geophysical Research Letters, 26 (18), 2801-2804.

Margolin G., B. Berkowitz, and H. Scher. 1998. Structure, flow and generalized conductivity scaling in fracture networks. Water Resources Research, 34 (9), 2103-2121

Martel, S. J., and J. E. Peterson. 1991. Interdisciplinary characterization of fracture systems at the US/BK site, Grimsel laboratory, Switzerland. International Journal of Rock Mechanics, 28 (4), 295-323. doi: 10.1016/0148-9062(91)90596-E

Matthäi, S. K., S. Geiger, S. G. Roberts, A. Paluszny, M. Belayneh, A. Burri, A. Mezentsev, H. Lu, D. Coumou, T. Driesner, and C. A. Heinrich. 2007. Numerical simulation of multi-phase fluid flow in structurally complex reservoirs. Geological Society, London. Special Publications, 292, 405-429. doi: 10.1144/SP292.22

McCarthy, A. J., and C. F. Elders. 1997. Cenozoic deformation in Sumatra: Oblique subduction and the development of the Sumatran fault system, in A. J. Fraser, S. J. Matthews, and R. W. Murphy, eds., Petroleum geology of Southeast Asia. Geological Society (London) Special Publication 126, 355–363

Milsom, J. S. 2005. Seismology and neotectonics, in A. J. Barber, M. J. Crow, and J. S. Milsom, eds., Sumatra: Geology, resources and tectonic evolution. Geological Society (London) Memoir 31, 8–15

Moos, D., and C. A. Barton. 2008. Modeling uncertainty in the permeability of stress-sensitive fractures. American Rock Mechanics Association, document Id 08-312.

Muskat, M. 1946. The flow of homogeneous fluids. J. E. Edwards Inc., Ann Arbor, Michigan.

Narasimhan T. N., K. Pruess. 1987. MINC: An approach for analyzing transport in strongly heterogeneous systems. In: Proc NATO Adv Res Workshop on Advances in Analytical and Numerical Groundwater Flow and Quality Modeling, Lisbon, 2–6 June, 1987. Dordrecht: Martinus Nijhoff.

Niretnieks, I., T. Eriksen, and P. Tahtinen. 1983. Tracer movement in a single fissure in granitic rock: Some experimental results and their interpretation. Water Resources Journal, 18 (4), 849. doi: 10.1029/WR018i004p00849

Niretnieks, I. 1993. Solute transport in fractured rock – Applications to radionuclide waste repositories. In: Bear J, Tsang CF. de Marsily G, editors. Flow and contaminant transport in fractured rock. San diego: Academic press, Inc, 39-127.

Oda, M. 1985. Permeability tensor for discontinuous rock masses. Geotechnique, 35 (4).

Oda, M. 1986. An equivalent continuum model for coupled stress and fluid flow analysis in jointed rock masses. Water Resources Research, 22 (13), 1845. doi: 10.1029/WR022i013p01845

Odling, N. E. 1997. Scaling and connectivity of joint systems in sandstones from western Norway. 1997. Journal of Structural Geology, 19 (10), 1257-1271. doi: 10.1016/S0191-8141(97)00041-2

Odling, N. E., P. A. Gillespie, B. Bourgine, C. Castaing, J.P. Chiles, N. P. Christiansen, M. Eeles, E. Fillion, A. Genter, L. Madsen, C. Olsen, R. Trice, J. J. Walsh, and J. Watterson. 1999. Variations in fracture system geometry and their implications for fluid flow in fractured hydrocarbon reservoirs. Petroleum Geoscience, 5, 373-384. doi: 10.1144/petgeo.5.4.373

Paul, P., M. D. Zoback, and P. Hennings. 2009. Fluid flow in a fractured reservoir using a geomechanically constrained fault zone damage model for reservoir simulation. Society of Petroleum Engineers, 12(4), 562-575. doi: 10.2118/110542-PA

Pickering, G., J. M. Bull, and D. J. Sanderson. 1995. Sampling power-law distributions. Tectonophysics, 248 (1-2), 1-20. doi: 10.1016/0040-1951(95)00030-Q

Rawlins, E. S., and M. A. Schellhardt. 1936. Backpressure data on natural gas wells and their application to production practices. U. S. Bureau of Mines, Monograph, 7.

Scholz, C. H., and P. A. Cowie. 1990. Determination of total strain from faulting using slip measurements. Nature, 346, 837-839. doi: 10.1038/346837a0

Segall, P., and D. D. Pollard. 1983. Joint formation in granitic rock of the Sierra Nevada. Geological Society of America Bulletin, 94 (5), 563-575. doi: 10.1130/0016-7606(1983)

Šimůnek, J., D. Jacques, J.W. Hopmans, M. Inoue, M. Flury, and M.H . van Genuchten. 2002. Solute transport during variably saturated flow inverse methods. p. 1435–1449. In J.H. Dane and G.C. Topp (ed.) Methods of soil analysis. Part 4. Physical methods. SSSA Book Ser. 5. SSSA, Madison, WI.

Smart, B. G. D., J. M. Somerville, K. Edlman, and C. Jones. 2001. Stress sensitivity of fractured reservoirs. Journal of Petroleum Science and Engineering, 29 (1), 29-37

Tezuka, K., T. Tamagawa, and K. Watanabe. 2005. Numerical simulation of hydraulic shearing in fractured reservoir. Proceedings World Geothermal Congress 2005, Antalya, Turkey.

Thomas L. K., T. N. Dixon, and R. G. Pierson. 1983. Fractured reservoir simulation. Society of Petroleum Engineers, 23 (1), 42 – 54. doi: 10.2118/9305-PA

Ueda, Y., S. Murata, Y. Watanabe, and K. Funatsu. 1989. Investigation of the shape factor used in the dual-porosity reservoir simulator. Society of Petroleum Engineers, document Id 19469-MS. doi: 10.2118/19469-MS

Van Genuchten, M. Th., and P. J. Wierenga. 1976. Mess transfer studies in sorbing porous media I. Analytical solutions. Soil Science Society of American Journal, 40 (4), 473-480.

Villemin, T., and C. Sunwoo. 1987. Distribution logarithmique self-similaire des rejêts et longueurs de failles: exemple du Bassin Houiller Lorrain. C. r. Acad. Sci. Paris, 305, 1309−1312

Warren J. E.., and P. J. Root. 1963. The behavior of naturally fractured reservoirs. Society of Petroleum Engineers Journal, 3 (3). doi: 10.2118/426-PA

Wattenbarger, R. A., and H. J. Ramey Jr. 1968. Gas well testing with turbulence, damage and wellbore storage. Journal of Petroleum Technology, 20 (8), 877-887. doi: 10.2118/1835-PA

Willis-Richards, J., K. Watanabe, and H. Takahashi. 1996. Progress toward a stochastic rock mechanics model of engineered geothermal systems. Journal of Geophysical Research, 101 (B8), 481-17, 496. doi: 10.1029/96JB00882

Yamamoto, R. H., J. B. Padgett, W. T. Ford, and A. Boubeguira. 1971. Compositional reservoir simulator for fissured systems – the single block model. Society of Petroleum Engineers, document Id 2666-PA. doi: 10.2118/2666-PA

Zimmerman, R. W., and G. S. Bodvarsson. 1996. Hydraulic conductivity of rock fractures. Transport in porous media, 23, 1-30. doi: 10.1007/BF00145263

Zoback M. D. 2007. Reservoir Geomechanics. Cambridge University Press, Cambridge, 341

Appendix 4A – Evaluation of Rate-dependent Skin

Well test analysis is performed to evaluate the flow rate dependent skin effect using the Saphir software package. Figure 4A-1 shows the three individual flow periods plotted on a rate-normalized plot. The increasing skin factor with increasing flow rate is clearly evident from the non-alignment of the straight lines (shown in red) in semi-log plot for various flow rates. If the skin factors were same at all flow rates, the semi-log straight lines would be aligned with each other. The values of s' and D obtained from the well test analysis are 0.492 and 0.000042 respectively where flow rate q_{sc} is in MSCF/day (thousand standard cubic feet per day). The values of skin factor at 100, 150 and 200 MMSCF/day, therefore, are 4.69, 6.79 and 8.89, respectively.

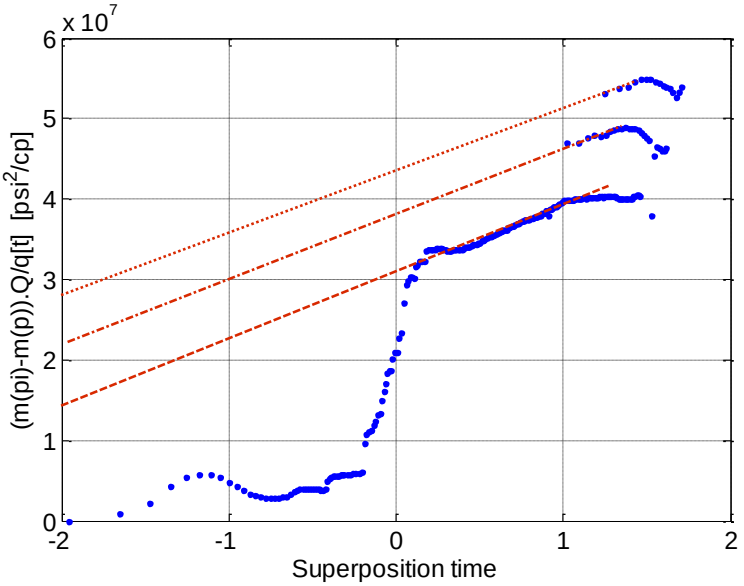

Figure 4A-1: Rate normalized semi-log plot of the flow after flow well test. The non-alignment of the three red lines at different flow rates is indicative of flow rate-dependent skin effect.

As mentioned previously, the skin effect results in a pressure drop. Pressure drop due to the skin effect is given by:

$$\Delta P_s = \frac{141.2 q B \mu s}{kh} \tag{4.14}$$

where ΔP_s is the pressure drop in psi, q is the flow rate in RB/day(reservoir barrels per day), B is the formation volume factor in RB/STB (reservoir barrels per stock tank barrel), μ is the viscosity in centipoise (cP), s is the skin factor, k is the permeability in millidarcy (md), and h is the reservoir thickness in feet. It is important to note that the units of qB are in RB/day. However, the formation factor for gas B_g is calculated in cu.ft./SCF while flow rate q_g is in MSCF/day. To assist in conversion, qB in RB/day is equivalent to ~ $178 q_g B_g$ in gas units. Reservoir thickness h is ~2500 feet, viscosity of methane μ at 3790 psi (reservoir pressure) and 90ºC (reservoir temperature assuming geothermal gradient) is ~0.02 cP. The value of formation factor for gas B_g is calculated as follows:

For methane, gas gravity $\gamma_g = 0.5537$

Reservoir temperature $T = 90℃ \approx 654°R$ (temperature in Rankine)

Pseudocritical pressure P_{pc} and temperatureT_{pc} (assuming California gases)

$$P_{pc} = 677 + 15\gamma_g - 37.5\gamma_g^2 = 673 \text{ psia}$$

$$T_{pc} = 168 + 325\gamma_g - 12.5\gamma_g^2 = 344°R$$

Reduced pressure P_r and temperature T_r

$$P_r = \frac{P}{P_{pc}} = \frac{3790}{673} = 5.6247$$

$$T_r = \frac{T}{T_{pc}} = \frac{654}{344} = 1.9005$$

Reduced density is calculated iteratively using the following scheme:

$$\rho_{k+1} = \rho_k - \frac{f(\rho_k)}{f\prime(\rho_k)}$$

where:

$$f(\rho) = a\rho^6 + b\rho^3 + c\rho^2 + d\rho + e\rho^3(1 + f\rho^2)\exp(-f\rho^2) - g$$

$$f'(\rho) = 6a\rho^5 + 3b\rho^2 + 2c\rho + d + e\rho^2[3 + f\rho^2(3 - 2f\rho^2)]\exp(-f\rho^2)$$

where:

$$a = 0.06423$$

$$b = 0.5353T_r - 0.6123$$

$$c = 0.3151T_r - 1.0467 - 0.5783/T_r^2$$

$$d = T_r$$

$$e = 0.6816/T_r^2$$

$$f = 0.6845$$

$$g = 0.27P_r$$

$$\rho_0 = 0.27P_r/T_r$$

The value of reduced density ρ comes out to be 0.8338

The z-factor is given by $z = \frac{\rho_0}{\rho} = \frac{0.27P_r}{\rho T_r}$ =0.9584

Formation factor in ft3/SCF $B_g = 0.02829zT/P = 0.0047 ft^3/SCF$

Using equation 4.14, the pressure drop due to skin at 100, 150 and 200 MMSCF/day flow rates, therefore, are 18.6, 40.6 and 70.6 psi.

Chapter 5

SLIP-INDUCED DAMAGE AROUND SMALL NATURAL FRACTURES AND FAULTS DURING HYDRAULIC STIMULATION OPERATIONS

5.1 Abstract

Two-dimensional plane-strain dynamic rupture models featuring a strongly rate-weakening friction and off-fault Drucker-Prager plasticity are used to model damage caused due to slip induced on small natural fractures and faults in the vicinity of hydraulic fractures during slick-water hydraulic fracturing operations. The area of study is the Barnett gas field in Texas. The objective is to investigate whether co-seismic slip on natural fractures induced by increase in pore pressure during hydraulic fracture operations is the primary deformation mechanism leading to increase in matrix permeability. Modeling is performed in the framework of continuum plasticity. Modeling slip on a single one meter long fault surrounded by damaged rock (zero cohesion) suggests that the inelastic deformation produced is not substantial enough to create additional porosity and permeability that would warrant the large increase in flow rates observed as a consequence of hydraulic fracturing operations. However, slip on mis-oriented faults (angle between the fault plane and direction of maximum principal stress lying between ~ 5 and 25˚)

leads to the creation of strain localization features at fault tips, which suggest the formation of new fractures. The new fractures increase the percolation zone (and hence the flow rate) by firstly, providing a larger cumulative area of fractures hydraulically connected to the well (and therefore, a larger area for gas to diffuse out of the formation form), and secondly, increasing the connectivity of the pre-existing fracture network (leading to greater reservoir penetration). The magnitude of increase in the percolation zone and hence the amount of stimulation appears to be correlated to the initial fracture population. Regions poorly fractured are not substantially stimulated even if strongly hydraulically fractured, as opposed to the well fractured regions which are substantially stimulated. Therefore, reservoir fracture characterization along with prediction of the pre-existing fracture network and the regional stress state could help predict the effectiveness and spatial variability of reservoir stimulation, and help improve the efficiency of hydraulic fracturing operations.

5.2 Introduction

Multi-stage slick-water hydraulic fracturing is a commonly deployed technology for stimulating organic-rich shale gas reservoirs in order to produce commercial quantities of natural gas. However, the physical mechanism responsible for stimulating the formation is poorly understood. The common understanding is that water diffuses from the created hydraulic fracture into the surrounding natural fractures and faults (Figure 5.1). Increase in pore pressure on the surface of these fractures reduces the effective normal stress resolved on the fractures and induces slip. This shear slip increases the fracture permeability. Slip on a large number of natural fractures and faults creates a network of relatively permeable flow paths hydraulically connected to the hydraulic fracture and hence the well. Microseismic events recorded during hydraulic fracturing operations provide evidence of this shear slip. Even though a hydraulically conductive fracture network is established as a result of shear slip, the outstanding question is how the gas diffuses from the rock matrix into the hydraulically conductive fracture network. Since the permeability of these shale reservoirs is of the order of nanodarcies, gas would not be able to diffuse through the rock matrix into the hydraulically connected fracture network at the commercial rates observed post hydraulic fracturing operations unless either the fracture density is very high or the permeability of the matrix itself gets enhanced. In this study, we model the effect of a co-seismic slip across a small natural fault on the porosity and permeability of the

matrix surrounding the fracture. We expect that as the rupture propagates on the fault, the stress concentrations associated with the propagating rupture creates inelastic shear and dilatant deformations around the fracture leading to an increase in matrix porosity and permeability.

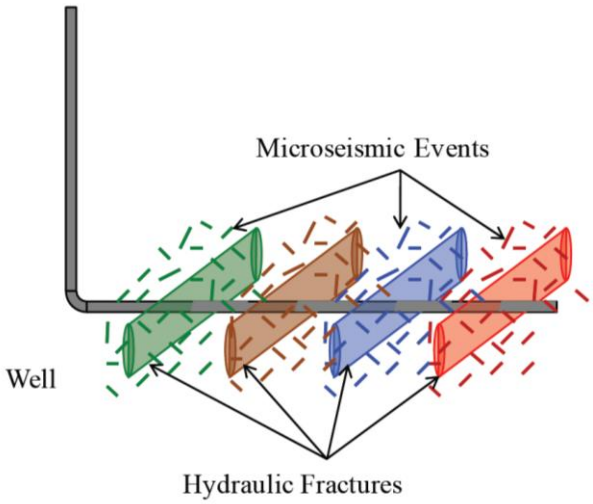

Figure 5.1: Schematic showing Microseismic events due to slip induced on natural fractures during hydraulic fracturing operations

5.3 Current Study

In this study, principles of dynamic rupture propagation are used to numerically model volumetric strains and damage created due to slip on a fault plane (the methodology adopted is similar to the one discussed in chapter 3, except that the model scale in chapter 3 was of the order of kilometers, while in this study, the scale is of the order of 1-3 meters). As the rupture propagates, stress perturbations are induced around the rupture tip, leading to failure. Rupture propagation is studied using two-dimensional plain-strain models. The off-fault material is described by a Drucker-Prager elastic-plastic rheology. A similar assumption has also been made in other published studies on dynamic rupture propagation (Andrews, 2005; Ben-Zion and Shi, 2005; Duan and Day, 2008; Ma, 2009; Templeton and Rice, 2008; Viesca et al., 2008). Two cases have been considered in this study, one in which rock strength (and cohesion) has been neglected, and the other in which it has been accounted for. The coefficient of friction obeys a rate-and-state law that features the direct effect and evolution (over slip L which evolves over a characteristic distance R_0) towards a strongly velocity-weakening steady state friction coefficient. A complete description of the friction law and plasticity formulation is provided in

section 3.4.3 and also in Dunham et al., (2011a). The model parameters chosen to describe the friction law and the off-fault material rheology are mentioned in Appendix 5A.

This approach is used to model dilatant plastic strains generated in the surrounding rock due to slip across small natural fractures and faults as a consequence of increased pore pressure arising from slick-water hydraulic fracturing operations. The spatial extent of inelastic deformations from the fault surface and the magnitude of plastic strains are used to assess whether or not co-seismic slip on fractures/faults significantly stimulates the reservoir.

5.4 Model Development and Initial Conditions

5.4.1 Model set-up

A 1 meter long fault buried in a homogeneous half space is considered (Figure 5.2). This length is larger than the critical nucleation length (minimum fault length required for a rupture to nucleate), which is approximately 0.1 meters, but small enough to host microearthquakes of the order of magnitudes observed in microseismicity monitoring programs (magnitudes -1 to -3). The fracture is located at a depth of 8500 feet (2590 meters). A range of fault orientations with respect to the in-situ stress state is considered.

An absorbing boundary condition is applied to all the four sides of the model domain. The fault is assumed to be oriented along the X axis with the origin lying at the center of the fault. For the purpose of modeling, it is assumed that the fluid from the hydraulic fracture seeps into the surrounding formation and enters the fault from the left tip. The pore pressure, therefore, starts building up gradually around the left tip and induces slip on the fault when the effective normal stress has been sufficiently reduced over some critical rupture nucleation region. Hence, the slip nucleates towards the left tip of the fault and propagates along the positive X direction.

5.4.2 Background stresses

Next, the model described above is loaded with a normal faulting stress state. The vertical stress and the minimum horizontal stress are assumed to be the maximum and minimum principal stresses, while the maximum horizontal stress lies in the plane of the fault. The regional stress state was constrained by frictional strength using information of wellbore breakouts and

drilling induced tensile fractures identified in image logs, and rock strength and coefficient of internal friction obtained from triaxial experiments (Sone, 2012). The vertical stress is obtained by integrating the density log and is 1.1 psi/ft. The minimum horizontal stress obtained from the measured fracture gradient is 0.65 psi/ft while the maximum horizontal stress constrained is 0.73 psi/ft. The fault is assumed to be located at a depth of 2.2 km. This results in the maximum (S_v), intermediate (S_{hmax}) and minimum (S_{hmin}) principal stresses being 54.78 MPa, 36 MPa and 28.2 MPa respectively. Pore pressure is hydrostatic (0.45 psi/ft) while the UCS is 150 MPa (Sone, 2012).

Four cases have been considered where the angle ψ between the fracture plane and the direction of the maximum principal stress (vertical direction) is 10˚, 20˚, 30˚ and 40˚. The value of τ/σ_n for the four cases is 0.43, 0.67, 0.70 and 0.63. As mentioned previously in chapter 3, the mode of rupture propagation depends on the value of τ/σ_n. Ruptures for all of the above 4 cases propagate as cracks. Although substantial evidence suggests that ruptures on large faults propagate as self-healing pulses (since the slip modeled by only pulse-like propagation scales with observed values), nothing definitive could be said about co-seismic slip on faults of length on the order of a meter.

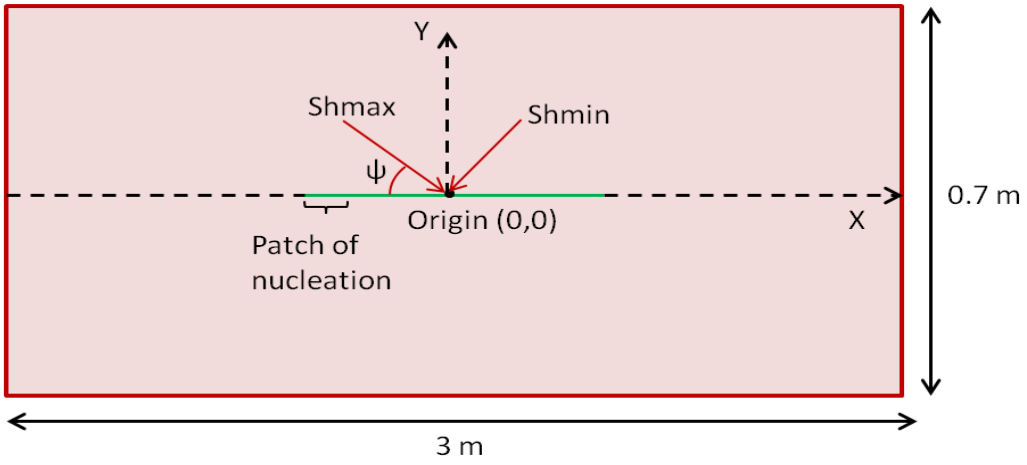

Figure 5.2: Two-dimensional idealization to model slip on a vertically dipping buried natural fault. The green line represents the fault surface. X axis is aligned along the fracture.

5.4.3 Simulation details and input parameters

A 2D finite-difference method is used to model dynamic rupture propagation. This is done in the framework of continuum plasticity. The governing equations form a system of first-order

partial differential equations with an algebraic constraint. The structured mesh discretizes the medium keeping the grid spacing 2.5 mm and 5 mm in the X and Y directions respectively. All components of velocity and stress are defined at each grid point. Spatial derivatives are approximated using a summation-by-parts finite difference method (Kreiss and Scherer, 1974, 1977; Strand, 1994; Mattsson and Nordström, 2004). The boundary conditions are weakly enforced using the simultaneous approximation term technique (Carpenter et al., 1994). This scheme is high-order accurate (Kozdon et al., 2009). For more details on the numerical method and simulation process, please refer to Dunham et al., (2011a) and Kozdon et al., (2011). Table 1 in Appendix A-1 lists the values of various model parameters used in the simulations. The parameters of the friction law are similar to those used by Noda et al., (2009) who selected them from a compilation of laboratory studies. The time step is 0.2 μs.

5.4.4 Arresting a propagating rupture

Ruptures propagating on small natural fractures and faults as a result of induced slip probably arrest due to limited fault length. As discussed in section 3.6.5, arresting the rupture abruptly generates large plastic strains. This is an artifact of the sudden stoppage of the rupture that creates large stress perturbations. Seismic inversions suggest that the rupture arrest process is gradual. However, in case of slip induced on small natural faults, ruptures probably arrest over much smaller distances as compared to those on large faults. The rupture arrest process is mimicked in these simulations by ramping up the value of the direct effect parameter a to values larger than the evolution effect parameter b gradually over a small spatial distance of ~ 5 centimeters. Ramping up the a value over a relatively smaller spatial distance creates relatively large stress perturbations and plastic strains at the fault tips (discussed later in section 5.5).

5.5 Results

Figure 5.3 shows the profiles of the slip induced on the fracture at every 0.4 micro seconds. As previously mentioned, it is assumed that the fluid slowly diffuses into the fault from the left tip via a hydraulically conductive fracture network and then creates conditions feasible for rupture nucleation by sufficiently reducing the effective normal stress over a 25 cm long patch (close to the left fracture tip). Post nucleation, the rupture propagates till it reaches the right tip. Figure 5.3 shows slip profiles for a single case when the angle ψ between the fracture surface

and the direction of the maximum horizontal stress is 30º. The maximum slip is approximately 0.15 mm. Assuming a square 1 m × 1 m fault, the scalar seismic moment is approximately

$$M_0 = \mu A d = (30 \times 10^9) N/m^2 \times 1 m^2 \times 0.00015 m = 45 \times 10^6 \text{ Nm}$$

where μ is the shear modulus (~ 30 GPa), A is the area of cross-section of the fault and d is the average slip. The magnitude of this micro earthquake is

$$M_w = (2/3 \log M_0 - 6.03) = -0.97$$

This is one of the larger magnitude earthquakes since most of the micro-earthquakes recorded are approximately -2 to -3 in magnitude.

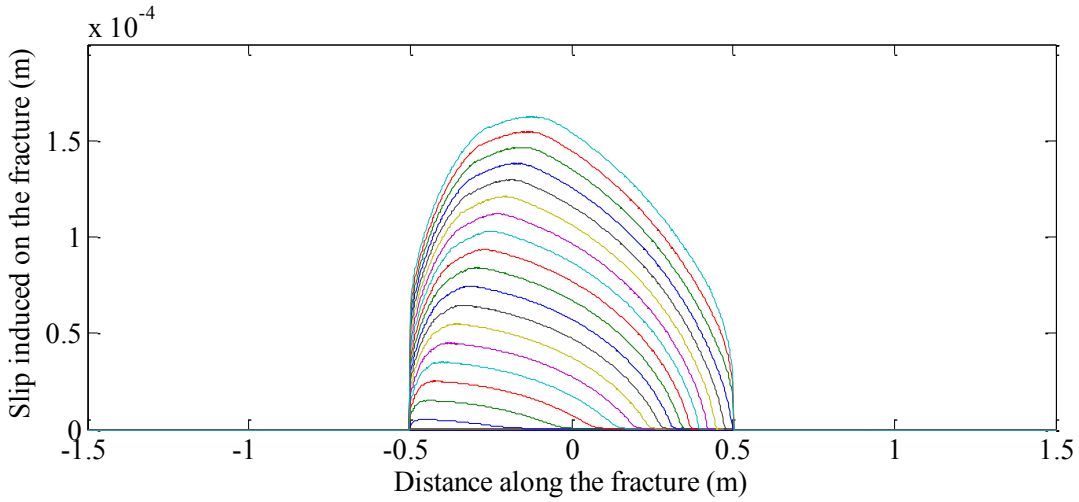

Figure 5.3: Plot showing the profile of slip induced on a natural fracture during hydraulic fracturing. Various lines represent slip profile at every 0.4 micro-seconds of rupture propagation on the fault.

Figure 5.4 shows the plastic strain field generated due to slip induced on faults which are oriented such that the angle ψ between the fracture and the direction of maximum principal stress (in the vertical direction) is 10˚, 20˚, 30˚ and 40˚ (the fault planes have been rotated to be horizontal to facilitate representation). In these simulations, the rock is assumed to be cohesion-less. We notice that the distribution of plastic strains are in accordance with Templeton and Rice (2008), who have shown that the region undergoing inelastic deformation around a propagating crack tip depends on the angle ψ between the fault plane and the direction of maximum principal stress. For ψ less than 20º, the inelastic deformation occurs primarily in the compressional quadrants while for ψ larger than 45º, the inelastic deformation occurs exclusively in the

extensional quadrants. In Figure 5.4(a) where ψ is 10º, plastic strains are primarily restricted to the compressional quadrant (with respect to the direction of rupture propagation), and the plastic strain lobe transitions to the extensional quadrant as angle ψ increases (Figures 5.4(b) and (c)) until it is completely in the extensional quadrant when ψ is 40º (Figure 5.4 (d)). We also notice that the spatial region experiencing plastic strains is larger for larger values of ψ. From Figure 5.4 (a) and (b), however, we notice the formation of strain localization features at the tips of the slipping fault. Strain localization features could suggest the formation of new fractures. The size of fractures formed is very similar to (same order of magnitude) the size of the slipping fault. The implications of the formation of strain localization features are discussed in section 5.6.

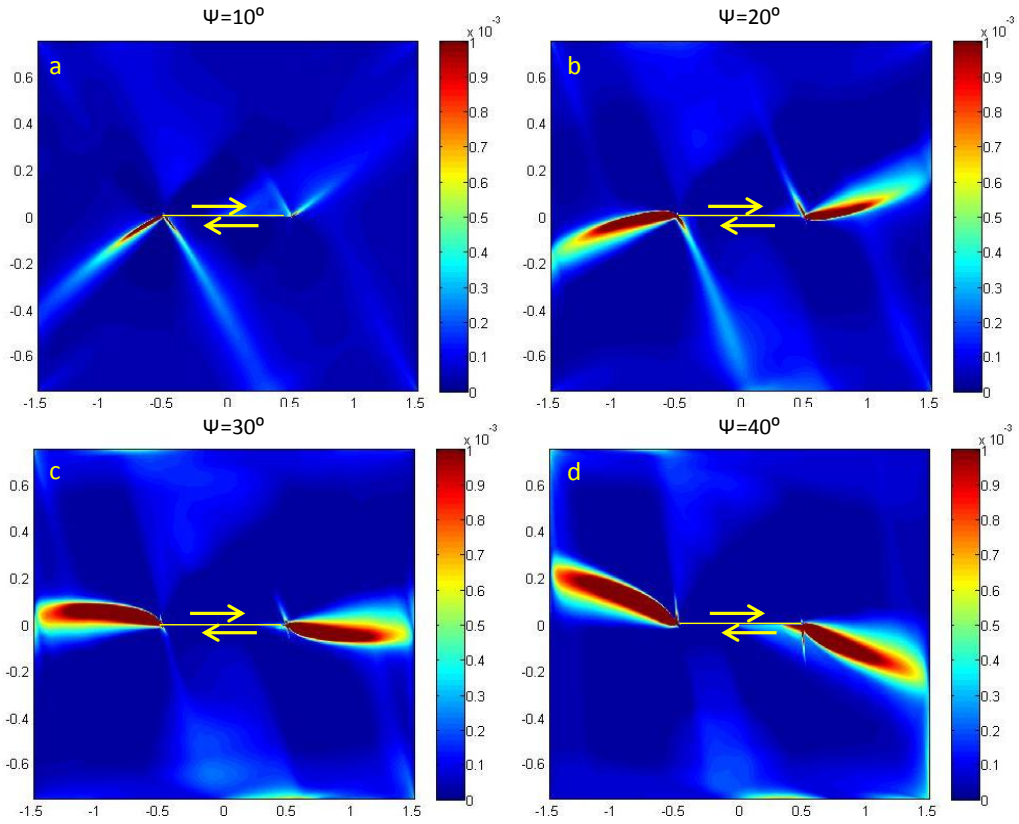

Figure 5.4: Equivalent plastic shear strain field generated due to slip induced on a fault during hydraulic fracturing. All dimensions are in meters. The angle ψ between the fracture plane and the vertical stress is (a) 10º (b) 20º (c) 30º (d) 40º. Plastic strains are generated primarily in the compressional quadrant at low angles of ψ and in the extensional quadrant at larger angles. The region experiencing plastic strains increases as the angle ψ increases. The colors represent plastic shear strains. Dilatant plastic strains are a product of shear plastic strains and dilatancy.

It is clear that despite our assumption of cohesion-less rock, the region experiencing inelastic deformation is very limited. Besides, the magnitude of plastic strains is modest, the

maximum being approximately 0.001. On performing a simple volume balance, if we consider a volume V having porosity $\emptyset$, the volume created by dilatant plastic strain within this element of volume V is $\beta\gamma^p V$ where β is the dilatancy and γ^p is the shear plastic strain. The new porosity, therefore, is approximately $\frac{\emptyset V+\beta\gamma^p V}{V+\beta\gamma^p V} = \frac{\emptyset+\beta\gamma^p}{1+\beta\gamma^p} \sim (\emptyset + \beta\gamma^p)$. The porosity of Barnett shale is approximately 2-9 % (Sone, 2012). Assuming a dilatancy of 0.28 and maximum shear plastic strain of 0.001, the increase in porosity is 0.00028. This is a negligible increase in the 0.02-0.09 porosity of shale, and probably has a negligible impact on permeability.

The above simulations were performed assuming cohesion-less rock surrounding the fault. However, triaxial experiments suggest a UCS of 150 MPa (Sone et al., 2012). The plastic strain field obtained due to slip induced on a fault assuming rock strength of 150 MPa is shown in Figure 5.5. The angle ψ chosen is 30º. It is clear that almost no plastic strains are generated except very close to the fault tips. The results are similar when other values of ψ are chosen. That said, a question that needs careful thought is what really is an appropriate rock strength representative of the rock mass around a fault? The rock mass around a fault may have small fractures and flaws, unlike the intact core samples on which triaxial tests are performed. Therefore, the average strength of the rock mass surrounding the fault would definitely be lesser than the rock strength of a small intact rock core sample. However, it is difficult to quantize this loss in rock strength due to fractures and flaws in the rock.

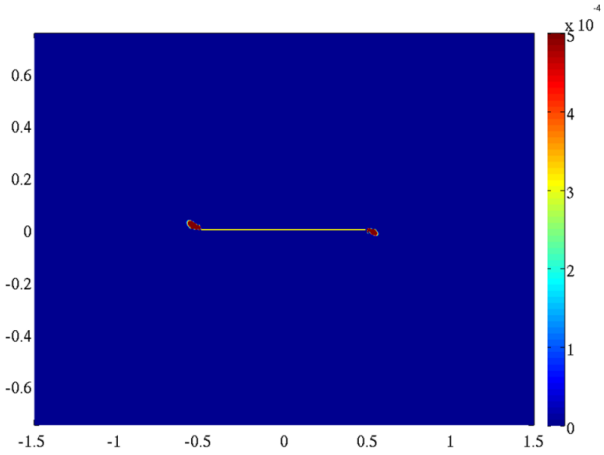

Figure 5.5: Equivalent plastic shear strain field generated due to slip induced on a natural fracture during hydraulic fracturing assuming that the UCS of the surrounding rock is 150 MPa (reported from triaxial experiments). The angle ψ between the fracture plane and direction of the maximum principal stress is 30º.

In order to avoid using a fixed value of cohesion (or UCS), we instead calculate the amount of cohesion that is required to prevent inelastic deformations at different points around the fracture. Larger values of cohesion would be required at points which experience large stress perturbations and vice-versa. Figure 5.6 shows the cohesion required at various points around the natural fault to prevent the rock from deforming inelastically. The figures represent 4 different values of angle ψ. It is clear from Figure 5.6 that large cohesion values are required to prevent inelastic deformations close to the fault tip, but beyond distances as less as 10 centimeters, even modest values of cohesion (~ 10 MPa) are sufficient to prevent the rock from deforming inelastically. In general, it could be fair to assume that the value of cohesion representative of the rock mass around a natural fault would at least be ~ 10 MPa. In such a scenario, damage and hence extra porosity and permeability created in the rock mass surrounding a fault due to coseiemic slip induced on it during hydraulic fracturing is almost negligible.

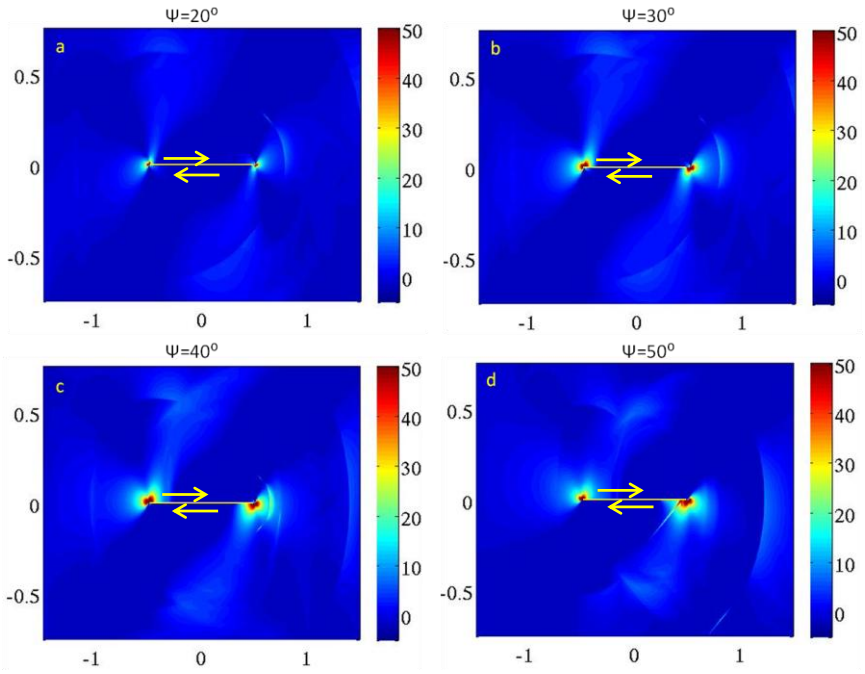

Figure 5.6: Cohesion required at various points around a natural fracture to prevent the formation of inelastic strains due to slip induced on a natural fracture oriented at (a) 20º (b) 30º (c) 40º and (d) 50º with respect to the direction of the maximum horizontal stress.

5.6 Formation of new fractures and increase in the percolation zone

Although slip on small natural faults does not significantly affect the porosity and permeability of the surrounding rock matrix, slip on poorly oriented faults (angle between the

fault surface and direction of maximum principal stress is 5-25˚), does produce strain localization features at fault tips which could suggest the formation of a new fractures. Although strain localization features are only noticed when we ignore rock cohesion, a case could be made that the rock strength measured on core samples is not representative of the entire rock mass on a larger scale due to the presence of small-scale heterogeneities and flaws. The new fracture (strain localization feature) may form along a locally 'flawed' region. Figure 5.4(a) suggests that two fractures form at approximately 30˚ and 120˚ with respect to the plane of the slipping fault (in the compressional quadrant) when ψ is 10˚ while Figure 5.4 (b) suggests the formation of one strain localization feature (fracture) at an angle of 120˚ from the fault tip in the compressional quadrant when ψ is 20˚. The formation of new fractures can potentially increase the fracture network connectivity within the reservoir and the percolation zone (we define percolation zone as the cumulative area of fractures hydraulically connected to the well). The flow rate depends on the total surface area of fractures through which flow can occur, i.e. the total area of fractures hydraulically connected (via a continuous network of hydraulically active fractures) to the well, and hence the percolation zone ($q = k_f A_f$ where q is the flow rate and A_f is the percolation zone).

Since the matrix permeability of Barnett is on the order of nanodarcies, it is almost certain that most of the gas flow occurs through fractures. We hypothesize, however, that most flow in the Barnett, in fact, occurs only through critically-stressed fractures since the mechanically active state of critically stressed fractures enhances their permeability (2.3.1). However, there may be several isolated critically-stressed fractures that are not hydraulically connected to the producing well. Therefore, it is only those critically stressed fractures that are hydraulically connected to the producing well that contribute to fluid flow. The sum of areas of critically stressed fractures that are hydraulically connected to the producing well the percolation zone. During hydraulic fracturing, water from the created hydraulic fractures seeps into the surrounding formation and increases the pore pressure. Pore pressures may rise to as large as 0.9 times the minimum principal stress. Elevated pore pressures cause several natural fractures and faults in the surrounding formation to slip. Induced slip not only increases the population of the critically stressed faults (and hence the percolation zone), but it may also create new fractures (as shown by numerical modeling in this study) that increase the fracture connectivity within the reservoir.

We show this increase in the percolation zone by modeling a fracture network in the following section.

5.6.1 Model Development

Fracture connectivity and increase in the percolation zone as a result of hydraulic stimulation is studied in the framework of discrete fracture networks (similar to that in chapter 4). The FracMan software package is used for modeling the DFN. The area of study is the Barnett reservoir. A 1200 ft × 600 ft × 2250 ft reservoir domain (along a 2250 ft long segment of a horizontal well that was perforated and fractured) is modeled (Figure 5.7). The hydraulic fractures are modeled as hexagonal planes with an effective radius of 200 feet (effective radius of a polygon is the radius of a circle whose area is equal to the area of the polygon). The spacing between the created hydraulic fractures is assumed to be ~ 310 feet.

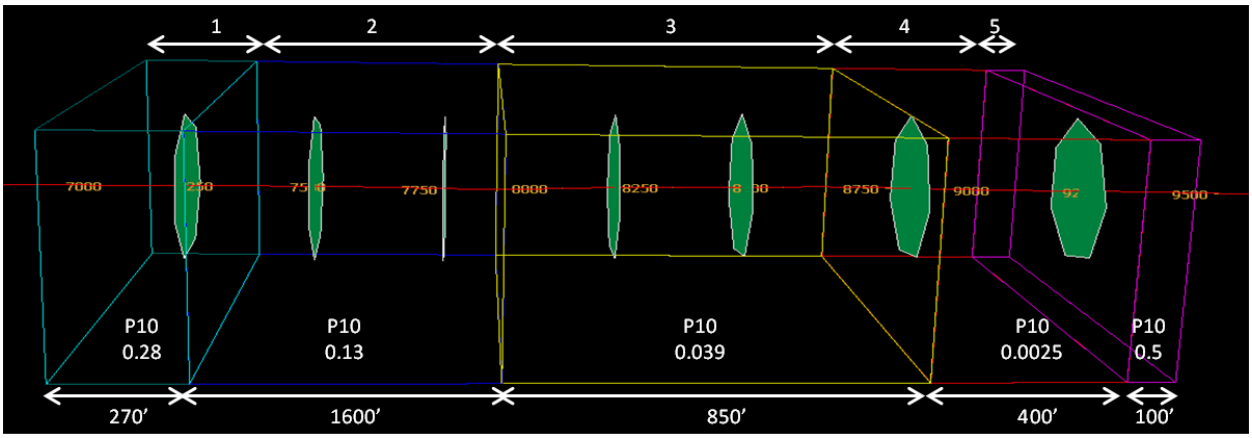

Figure 5.7: Model domain showing the modeled portion of the reservoir along a 2250 feet long segment of a horizontal well. The green surfaces represent the created hydraulic fractures. The five regions (numbered 1-5) outlined in different colors represent regions of different P10 (fracture density per unit distance) observed in image logs. The red line represents the well trajectory. All dimensions are in feet.

5.6.2 Generation of the Discrete Fracture Network

Background fractures in the model domain are stochastically generated using the FracMan software suite. The parameters required for stochastic generation of fractures are the fracture intensity, distribution of fracture orientations, and distribution of fracture sizes. Figure 5.8 shows the cumulative density plot of fractures identified in the wellbore image log. The slope of the cumulative density plot is representative of the fracture density (P10 - number of fractures per unit length). Five regions of varying P10 (marked intervals 1-5) along the wellbore can be

identified. Fracture intensity in intervals 1-5 are 0.28, 0.13, 0.039, 0.0025 and 0.5 fractures /m respectively.

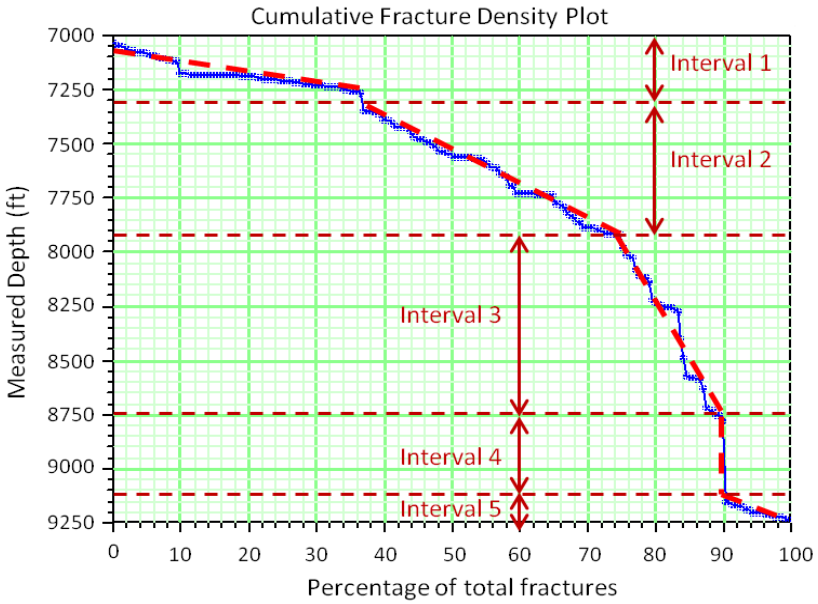

Figure 5.8: Cumulative fracture density plot of fractures identified in the image log. Slope of the line represents the fracture density. The five intervals represent regions having distinctly different fracture densities.

Next, statistical analysis is performed to identify various fracture sets in the fracture data obtained from the image log using the ISIS (Interactive Set Identification System) feature of FracMan (see section 4.6.2 for details). Figure 5.9 shows the schematic of the strike of fractures identified in the image log and intersecting the well along with contoured stereoplots of the major fracture sets present in the fracture population. There appear to be two major fracture sets. A Fisher distribution is assumed to describe the distribution of fracture orientations in the two sets. The mean orientation of poles in the first fracture set is approximately a trend of 10° and a plunge of 4° with a dispersion of 50, while that in the second fracture set is a trend of 320°, plunge of 8° with a dispersion of 20. The larger the dispersion, the more concentrated are the fractures oriented about the mean orientation. 75% of the total fracture population belongs to the first set while 25% belong to the second set. Similar to the assumption in chapter 4 (4.6.2), the fracture size is assumed to be described by a power law $N(l) = L_{min} l^{-n}$ with a decay rate n of ~2.1 and L_{min} of 5 feet. The distribution of fracture lengths is shown in Figure 5.10. Once the fracture intensity, size, and orientation distribution parameters in each interval are obtained,

these intervals are stochastically populated with fractures belonging to the sets present in that interval until the target fracture density P10 along the section of the borehole is reached.

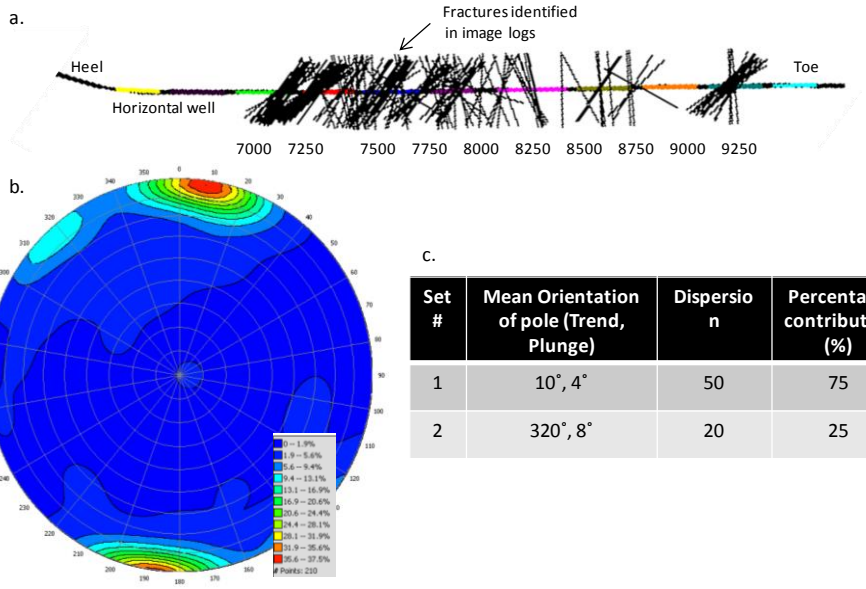

c.

Set #	Mean Orientation of pole (Trend, Plunge)	Dispersion	Percentage contribution (%)
1	10˚, 4˚	50	75
2	320˚, 8˚	20	25

Figure 5.9: (a) Schematic of the well along with fractures identified in the image log. Dimensions are in feet (b) Contoured stereonet of the poles of these fractures (c) Fisher distribution parameters of fracture sets

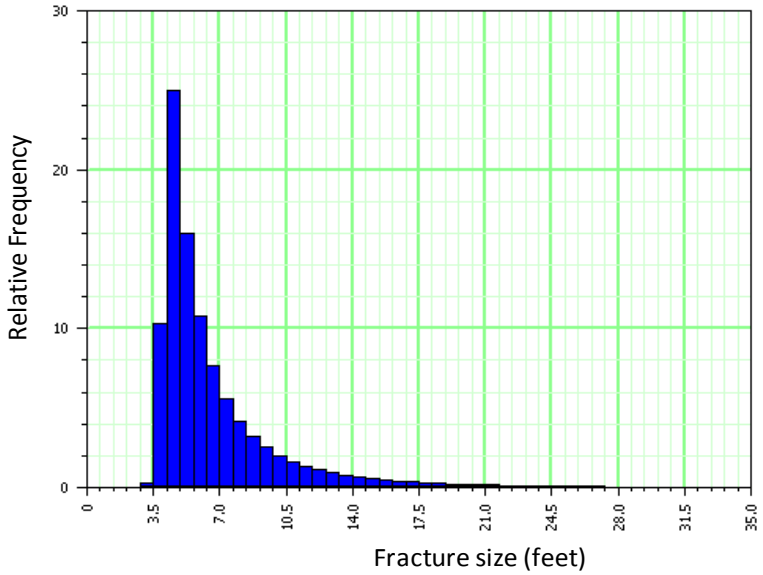

Figure 5.10: Histogram of length of fractures assuming a power law distribution.

5.6.3 Fracture connectivity analysis and percolation zone

Figure 5.11(b) shows the DFN model comprising all fractures present in the model domain. None of the fractures are critically stressed in the present day stress state (section 5.4.2)

(hydrostatic pore pressure conditions). This results in extremely low hydraulic connectivity of fractures with the well and almost negligible flow rates. Hydraulic stimulation creates hydraulic fractures and pressurizes the formation leading to an increase in pore pressure. Pore pressure in the formation surrounding hydraulic fractures can reach up to 0.9 times the minimum principal stress. Increase in pore pressure hydraulically activates several natural fractures and faults by inducing slip. This dramatically increases the network of hydraulically conductive (critically stressed) fractures that is hydraulically connected to the well (Figure 5.11(c)). The network of fractures hydraulically connected to the well is the percolation zone. Modeling of slip across natural faults (section 5.5) suggests the formation of fractures around poorly-oriented faults. We identify the poorly-oriented faults and fractures ($\psi \in 5 - 25°$) in the percolation zone, and introduce new fractures at their tips (two fractures when ψ lies between 5° and 15°, and one fracture when ψ lies between 15° and 25°, as mentioned earlier). Figure 5.11(d) shows the network of new fractures. The new critically stressed fractures not only contribute to flow themselves, but they also increase the connectivity of the pre-existing fracture network, and therefore, increase the percolation zone. Figure 5.11(e) shows the updated percolation zone, i.e. the new population of critically-stressed fractures and faults that are hydraulically connected to the producing well (comprising of both the pre-existing and newly formed fractures).

The initial percolation zone prior to reservoir stimulation is almost negligible with no critically stressed faults. Reservoir stimulation creates the hydraulic fractures and the increase in pore pressure induces slip on the surrounding pre-existing natural fractures and faults. This leads to an increase in the percolation zone, and hence the rate of flow. There are essentially three contributors enhancing the percolation zone. First is the contribution from the area created by the main hydraulic fractures themselves. Second is the set of pre-existing fractures and faults that are activated as a consequence of increase in pore pressure, and are also hydraulically connected to the well. The third contributor is the set of new critically stressed fractures hydraulically connected to the well, i.e. the newly percolating fractures. In the model described above, contribution from the hydraulic fractures is 8.79×10^5 sq. ft. Percolation zone obtained by considering the hydraulic fractures and the critically stressed fractures and faults in the pre-existing fracture population is 8.38×10^7 sq. ft (Figure 5.11 (c) – increase of ~ 95 times), while the percolation zone obtained by considering the total fracture population, including those newly

created due to slip on pre-existing faults is 15.47×10^7 sq. ft (Figure 5.11 (e) - ~176 times increase). Clearly, the contribution from the surface area of the hydraulic fractures is insignificant compared to contributions from the hydraulically connected fractures and faults in enhancing the percolation zone, and hence the flow rates. This shows that stimulating the pre-existing fracture network is key to stimulation, not only the creation of hydraulic fractures. The relevant statistics, i.e. number of all and critically stressed fractures along with the percolation zone before and after reservoir stimulation is provided in Appendix 5A-2.

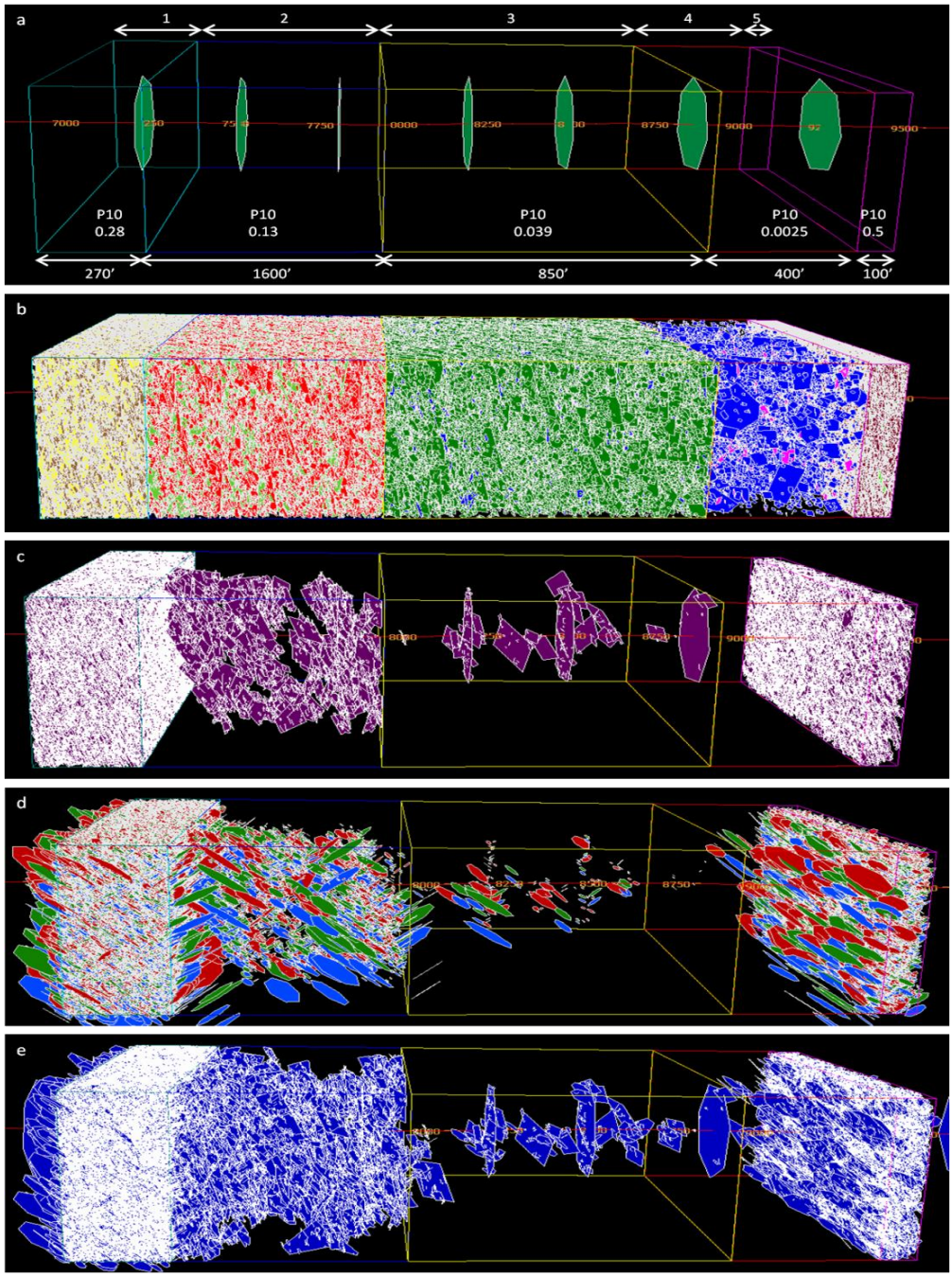

Figure 5.11: (a) Model set-up showing the various intervals, horizontal well and hydraulic fractures (b) DFN showing the pre-existing fracture population (c) Critically-stressed fracture network hydraulically connected to the well i.e. percolation zone post stimulation considering only the initial fracture population (d) New fractures created due to slip induced on poorly-oriented fractures (e) Critically-stressed fracture network hydraulically connected to the well i.e. percolation zone post stimulation considering both, the preexisting and newly formed fractures.

We also consider a case with a larger number of hydraulic fractures, assuming the inter spacing between hydraulic fractures to be 50 feet (as opposed to 310 feet earlier). Figure 5.12 (a)

shows the model domain with 45 hydraulic fractures with a spacing of 50 feet. By considering a larger number of hydraulic fractures, we expect greater fracture connectivity, and hence a larger percolation zone. Figure 5.12 (b) shows the percolation zone (critically stressed fractures hydraulically connected to the well) considering only the pre-existing fractures while Figure 5.12 (c) shows the percolation zone considering both, the pre-existing fracture population and the newly formed fractures. The percolation zones in Figures 5.12 (b) and (c) are 9.08×10^7 sq. ft. and 16.07×10^7 sq. ft. respectively, while the contribution from the area of the hydraulic fractures alone is only 5.66×10^6 sq. ft. Clearly, the contribution from natural fractures and faults is significantly larger than that from hydraulic fractures alone. The relevant statistics, i.e. number of all and critically stressed fractures along with the percolation zone before and after reservoir stimulation is provided in Appendix 5A-2.

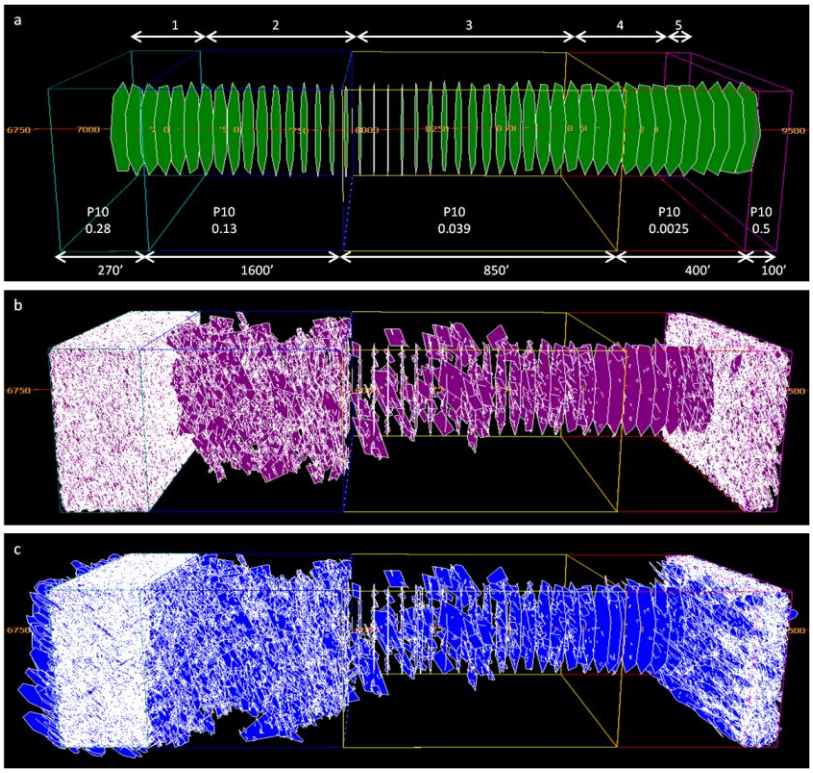

Figure 5.12: (a) Model set-up showing the various intervals, horizontal well and hydraulic fractures with an interspacing of 50 feet (c) Critically-stressed fracture network hydraulically connected to the well i.e. percolation zone post stimulation considering only the initial fracture population (c) Critically-stressed fracture network hydraulically connected to the well i.e. percolation zone post stimulation considering both, the preexisting and newly formed fractures.

Figure 5.13 shows the contributions towards the percolation zone from the three contributors previously discussed, for both, an inter hydraulic-fracture spacing of 310 feet (in

blue) and 50 feet (in red). Clearly, the contribution from natural fractures and faults is significantly larger than that from hydraulic fractures alone. It is also clear that although the percolation zone obtained with a larger number of hydraulic fractures is larger than that obtained with fewer hydraulic fractures, the difference is only subtle (~3-8 %), most of that difference being due to a larger area of hydraulic fractures created and not due to the difference in the surrounding percolation zone. This clearly suggests that it is not the number of hydraulic fractures, but the pre-existing fracture network that determines the potential of the reservoir to be stimulated. If the formation is poorly fractured, the creation of a hydraulic fracture will activate very few fractures, in which case the percolation zone will primarily comprise of the area of hydraulic fractures created. We can, therefore, hypothesize that for a successful stimulation program, the pre-existing fracture density should be larger than some critical/threshold fracture density such that they can be stimulated during hydraulic fracturing operations in order to create a pervasive, hydraulically connected fracture network that penetrates deep into the formation, maximizing the contact area of the hydraulically connected fracture network with the reservoir and the percolation zone.

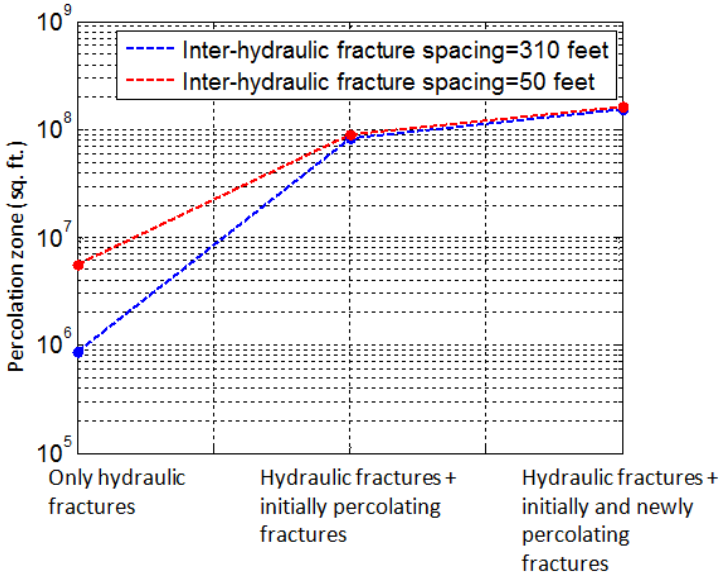

Figure 5.13: Contributions from the three primary contributors – hydraulic fractures, pre-existing percolating fractures and newly created percolating fractures, towards the percolation zone. Red line represents the case when the spacing between hydraulic fractures is 30 feet while blue line represents the case when the inter-spacing between hydraulic fractures is 310 feet.

Next, we discuss the variability in stimulation during various stages of hydraulic fracturing, considering the case with an inter-hydraulic spacing of 310 feet. The bar chart in

Figure 5.14 shows the percolation zone created during various stages of hydraulic fracturing (each of the seven hydraulic fractures each formed in a different stage, assuming one perforation per stage), along with the contributions to the total percolation zone by the hydraulic fractures, pre-existing percolating fractures and the newly-created percolating fractures. To ease visualization of relative contributions, Figure 5.14 (a) shows the percolation zone on a logarithmic scale while Figure 5.14 (b) shows the percolation zone on a linear scale. It is clearly seen that the contribution from hydraulic fractures is almost insignificant (Figure 5.14 (a)). Contributions from pre-existing and newly formed percolating fractures seem to be on the same order of magnitude (Figure 5.14 (b)). Figure 5.14 (c) shows the percolating zone associated with each of the stages, each stage represented by a different color. Stage 7 (close to the heel of the horizontal well) appears to be the most prolific stage with maximum stimulation followed by stage 1 (close to the well toe). Stages 5 and 6 produce moderate reservoir stimulation, while stages 2, 3 and 4 result in insignificant stimulation. This is due to the scarce population of natural fractures around the location of these stages to start with, suggesting that a substantial fracture population is critical to stimulating a reservoir. Regions of the reservoir with a greater population appear to have a higher potential for stimulation. The above analysis, therefore, suggests that maximum flow rates would be observed after stage 7, followed by stages 1, 5 and 6. Stages 2, 3, and 4 would have minimal flow rates. This, therefore, explains the variability in the effectiveness of reservoir stimulation, and hence production in different regions of the reservoir.

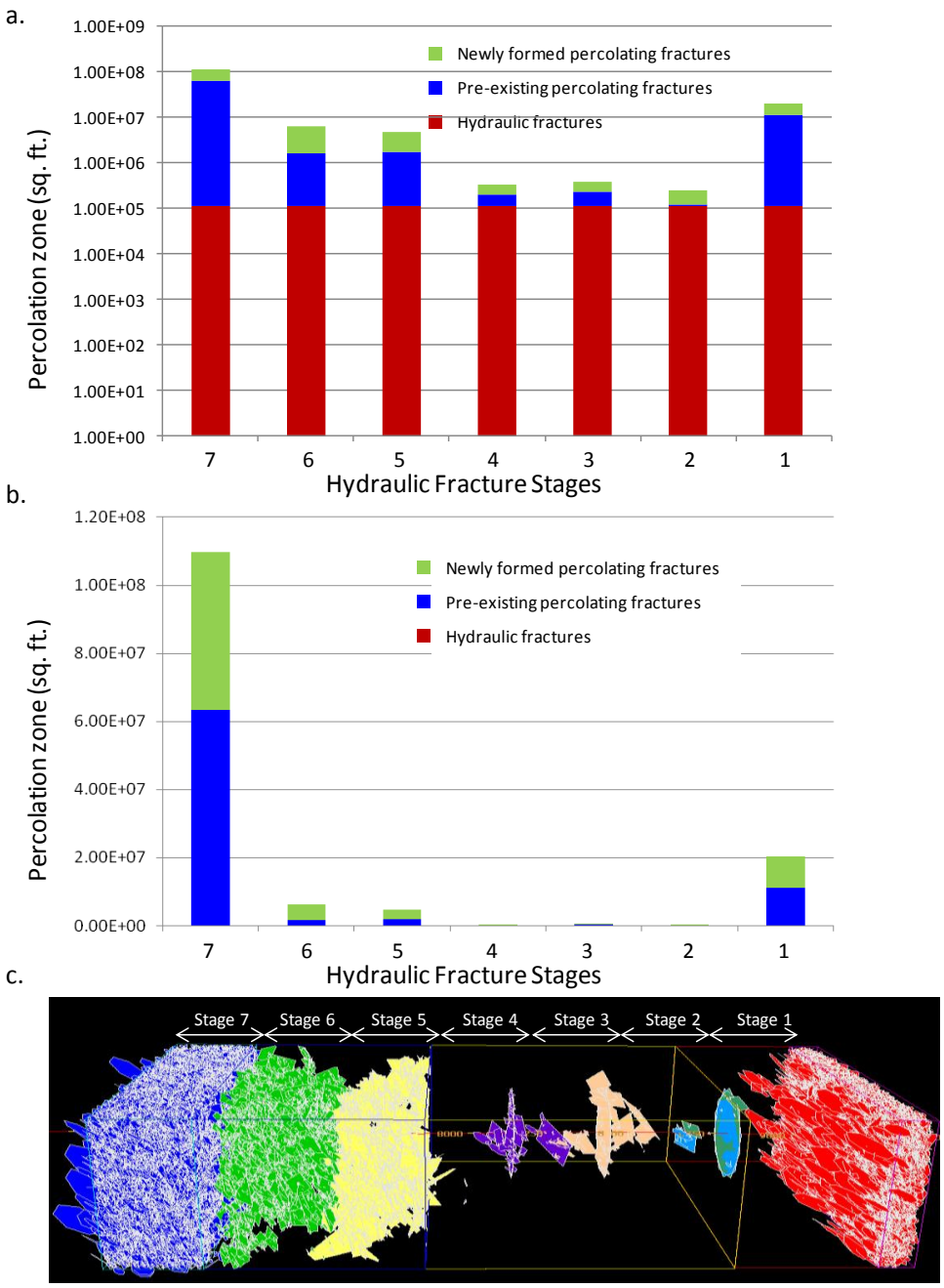

Figure 5.14: Percolation zone resulting from various stages of hydraulic fracturing performed along a horizontal well, along with relative contributions from the hydraulic fracture, pre-existing percolating fractures, and newly formed percolating fractures. Percolation zone shown on a (a) logarithmic and (b) linear scale (c) Fracture network comprising the percolation zone associated with various stages

5.7 Discussion

The primary deformation mechanism responsible for increased flow rates post hydraulic stimulation operations is still an outstanding question. Modeling co-seismic slip on small faults

suggests that co-seismic slip on natural fractures and faults does not enhance the permeability and porosity of the surrounding rock to the extent as to warrant the dramatic increase in flow rates observed post hydraulic stimulation. A simple mass balance calculation illustrates that the cumulative deformation associated with microseismic events can account for only a small fraction of the production.

Moreover, several studies report experimentally observed values of fracture permeability under various stress conditions (Esaki et al., 1999; Chen et al., 2000; Lee and Cho, 2002). Lee and Cho (2000) show that fracture permeability decreases with increase in normal stress on the fracture. Permeability also depends on shear displacement across the fracture. However, two contradicting factors influence the hydraulic behavior of fractures during shearing: dilation and gouge production from asperity degradation. Fracture permeability initially increases with shear displacement due to dilation; however, with further slip, formation of gouge material obstructs flow through the fracture and decreases the effective permeability. They have shown that a minimum of 3 mm slip is required to enhance the fracture permeability by one or two orders of magnitude. The magnitude of slip during a -1 magnitude event is 0.15 mm. Most micro-earthquakes are approximately -2 to -3 in magnitude, which involve even lesser slips. Therefore, it seems that co-seismic slip not only fails to enhance the surrounding matrix porosity and permeability, it most likely does not significantly increase fracture permeability as well. This is in conflict with the prevalent paradigm that co-seismic slip creates a network of relatively permeable flow paths that increases gas flow rates and production. However, these experiments were performed on granite samples. Experiments on shale samples performed by Kassis and Sondergald (2010) show that permeability can increase by up to 3 orders for ~ 0.15 mm of slip. This slip is of the same order as that which occurs during earthquakes ~ -1 in magnitude. Moreover, numerical modeling in this study suggests that formation of new fractures as a result of slip induced on poorly-oriented fractures and faults. This increases the percolation zone by not only creating new fractures, but also increasing the hydraulic connectivity of the original fracture network. This increased penetration into the reservoir could potentially be one of the mechanisms that could explain increased flow rates post reservoir stimulation.

Zoback et al., (2012) argue that slow slip, and not co-seismic slip on pre-existing fractures and faults is the dominant deformation mechanism contributing to reservoir stimulation during

hydraulic fracturing of low permeability gas shales. They show that faults in shales with clay content greater than 30% are expected to slip 'slowly' as compared to those where clay content is less than 30% in which case the slip is unstable or co-seismic. This is a consequence of the transition of fault frictional behavior from velocity strengthening to velocity weakening with decreasing clay content. They also illustrate through modeling that slip on poorly oriented faults is slow, principally because slip cannot travel faster than the speed of fluid pressure propagation along the fault plane. Since slow slip does not generate high frequency seismic waves, these events are not routinely detected in conventional microseismic monitoring programs. They argue that the spatial extent of microseismic events only portrays a generalized picture of regions in the reservoir which are getting pressurized during the stimulation operation and has nothing to do with actual reservoir stimulation. This explains the poor correlation between micro seismicity and relative productivity. These slow slip events seem to appear as long period long duration seismic events (Das and Zoback, 2011). Modeling in this study, however, suggests that although co-seismic slip events may not directly be deforming the surrounding rock enough so as to significantly enhance rock flow properties, they could potentially create new fractures that increase the percolation zone by firstly, providing a larger cumulative fracture surface area (and therefore a larger region for the gas to diffuse from), and secondly, increasing fracture network connectivity (and therefore increasing reservoir penetration). Primary deformation mechanisms responsible for increased flow rates post reservoir stimulation pose an outstanding question, but slow slip events that potentially enhance fracture permeability, along with coseismic slip that possibly increases the percolation zone could potentially be two important mechanisms responsible for reservoir stimulation.

5.8 Conclusion

This study shows that co-seismic slip induced on natural fractures and faults as a result of increase in pore pressure during hydraulic fracture operations does not produce significant plastic strains that could potentially create porosity and enhance the matrix permeability of the rock surrounding the faults. However, slip on poorly-oriented faults (angle between the fault and the direction of the maximum principal stress lying approximately between 5 and 25˚) leads to the formation of fractures at the fault tips. Creation of new fractures increases the percolation zone and reservoir penetration not only by increasing the cumulative area of the fracture network

hydraulically connected to the well (percolation zone) but also increasing the connectivity of the pre-existing fracture network. Increase in the percolation zone appears to depend more critically on the characteristics of the initial fracture population than the number of hydraulic fractures created. Areas where the initial fracture density is low do not experience a large increase in percolation zone post stimulation even if the formation is severely hydraulically fractured, suggesting that reservoir stimulation is directly correlated with the initial fracture population. This could explain the great variability in the productivity of shale gas wells, and reservoir stimulation response in a given area. This work also makes the case that fractures created due to slip induced on pre-existing fractures and faults could be effective in stimulating production from the extremely low permeability shale gas reservoirs. If this is true, shale gas development could be approached from a predictive perspective by developing modeling techniques that facilitate reservoir fracture characterization (representative fracture size, intensity and orientation distributions), an understanding of the stress state and its impact on reservoir stimulation, along with predicting appropriate pore pressures that could optimize reservoir stimulation.

5.9 References

Andrews, D. J. (2005). Rupture dynamics with energy loss outside the slip zone. Journal of Geophysical Research, 110(B1), 1-14. doi:10.1029/2004JB003191

Ben-Zion, Y., and Shi, Z. (2005). Dynamic rupture on a material interface with spontaneous generation of plastic strain in the bulk. Earth and Planetary Science Letters, 236(1-2), 486-496. doi:10.1016/j.epsl.2005.03.025

Carpenter, M. H., Gottlieb, D., and Abarbanel, S. (1994). Time-Stable Boundary Conditions for Finite-Difference Schemes Solving Hyperbolic Systems: Methodology and Application to HIgh-Order Compact Schemes. Journal of Computational Physics, 111(2), 220-236. doi:10.1006/jcph.1994.1057

Chen, Z., Narayan, S. P., Yang, Z., and Rahman, S. S. (2000). An experimental investigation of hydraulic behaviour of fractures and joints in granitic rock. International Journal of Rock Mechanics and Mining Sciences, 37(7), 1061-1071. doi:10.1016/S1365-1609(00)00039-3

Das, I., and Zoback, M. D. (2011). Long-period, Long-duration Seismic Events During Hydraulic Fracturing Stimulation of a Shale Gas Reservoir, The Leading Edge, July, 2011.

Duan, B., and Day, S. M. (2008). Inelastic strain distribution and seismic radiation from rupture of a fault kink. Journal of Geophysical Research, 113(B12), 1-19. doi:10.1029/2008JB005847

Dunham, E. M., Belanger, D., Cong, L., and Kozdon, J. E. (2011). Earthquake Ruptures with Strongly Rate-Weakening Friction and Off-Fault Plasticity, Part 1: Planar Faults. Bulletin of the Seismological Society of America, 101(5), 2296-2307. doi:10.1785/0120100075

Esaki, T., Du, S., Mitani, Y., Ikusada, K., and Jing, L. (1999). Development of a shear-flow test apparatus and determination of coupled properties for a single rock joint. International Journal of Rock Mechanics and Mining Sciences, 36(5), 641-650. doi:10.1016/S0148-9062(99)00044-3

Kassis, S., and C. H. Sondergald (2012). Fracture permeability of gas shales: Effects of roughness, fracture offset, proppant and effective stress. Society of Petroleum Engineers, 131376.

Kreiss, H.-O., and G. Scherer (1974). Mathematical Aspects of Finite Elements in Partial Differential Equations, edited by C. de Boor, Academic Press, New York, 195–212.

Kozdon, J. E., E. M. Dunham, and J. Nordström (2009). High-order treatment of fault boundary conditions using summation-by-parts finite difference methods, Eos Trans. AGU 90, no. 52, Fall Meet. Suppl.,Abstract S31A-1697.

Kozdon, J. E., Dunham, E. M., and Nordström, J. (2011). Interaction of Waves with Frictional Interfaces Using Summation-by-Parts Difference Operators: Weak Enforcement of Nonlinear Boundary Conditions. Journal of Scientific Computing, 50(2), 341-367. doi:10.1007/s10915-011-9485-3

Lee, H. S., and Cho, T. F. (2002). Hydraulic Characteristics of Rough Fractures in Linear Flow under Normal and Shear Load. Rock Mechanics and Rock Engineering, 35(4), 299-318. doi:10.1007/s00603-002-0028-y

Ma, S. (2009). Distinct asymmetry in rupture-induced inelastic strain across dipping faults: An off-fault yielding model. Geophysical Research Letters, 36(20), 1-5. doi:10.1029/2009GL040666

Mattsson, K., and Nordström, J. (2004). Summation by parts operators for finite difference approximations of second derivatives. Journal of Computational Physics, 199(2), 503-540. doi:10.1016/j.jcp.2004.03.001

Noda, H., Dunham, E. M., and Rice, J. R. (2009). Earthquake ruptures with thermal weakening and the operation of major faults at low overall stress levels. Journal of Geophysical Research, 114(B7). doi:10.1029/2008JB006143

Sone, H. (2012). Mechanical Properties of Shale Gas Reservoir Rocks and its Relation to the In-situ Stress Variation Observed in Shale Gas Reservoirs. Ph.D. dissertation, Stanford University, California, USA.

Strand, B. (1994). Summation by Parts for Finite Difference Approximations for d/dx. Journal of Computational Physics.

Templeton, E. L., and Rice, J. R. (2008). Off-fault plasticity and earthquake rupture dynamics: 1. Dry materials or neglect of fluid pressure changes. Journal of Geophysical Research, 113(B9), 1-19. doi:10.1029/2007JB005529

Viesca, R. C., Templeton, E. L., and Rice, J. R. (2008). Off-fault plasticity and earthquake rupture dynamics: 2. Effects of fluid saturation. Journal of Geophysical Research, 113(B9), 1-13. doi:10.1029/2007JB005530

Zoback, M. D., Kohli, A., Das, I., and McClure, M. (2012). The Importance of Slow Slip on Faults During Hydraulic Fracturing Stimulation of Gas Shale Reservoirs. SPE-155476 Americas Unconventional Resources Conference, Pittsburg, Pennsylvania, USA, 5-7 June, 2012.

Appendix 5A-1

Table 5A-1 below lists the values of various model parameters used in the simulations. The details of choosing these parameters are mentioned in section 3.4.3.

Material Properties		
Shear Modulus	G	32.04 GPa
Shear Wave Speed	Cs	3.464 km/s
Poisson's Ratio	υ	0.25
Drucker-Prager internal friction parameter	μ	0.5735
Drucker-Prager plastic dilatancy parameter	β	μ/2=0.2867
Friction Law Parameter		
Direct effect parameter	a	0.016
Evolution effect parameter	b	0.02
Reference slip velocity	v_o	1 μm/s
Steady state friction coefficient at Vo	f_o	0.75
State evolution distance	L	1.34 μm
Weakening slip velocity	V_w	0.17 m/s
Fully weakened friction coefficient	f_w	0.13
Initial Conditions		
Vertical (intermediate principal) stress	S_v	65 MPa
Maximum horizontal (principal) stress	S_{hmax}	85 MPa
Minimum horizontal (principal) stress	S_{hmin}	45 MPa
Pore Pressure	P_p	30.5 MPa
Initial state variable	Θ	0.68
Other		
Characteristic extent of state-evolution distance	R_o	0.5 m

Table 5A-1: Model parameters used in dynamic rupture simulations

Appendix 5A-2

Tables 5A-2 and 5A-3 list the number of all and critically stressed fractures present before and after reservoir stimulation when the interspacing between the created hydraulic fractures is 310 feet and 50 feet respectively. They also list the number of fractures hydraulically connected to the well and the percolation zone. Since the process of generating the DFN is stochastic, it is not very helpful to analyze the results in terms of numbers of fractures, since each realization of

populating the model with fractures could produce a different number of fractures. It is more helpful to analyze in relative terms, such as relative increase in the fracture population, or relative number of all fractures that are critically stressed etc. Analysis in terms of the percolation zone can also be a quantitative measure of stimulation, since it represents the total area through which the gas can diffuse out into the hydraulically connected fracture network into the well. The percolation zone prior to stimulation is negligible, but increases very significantly on stimulating the reservoir and increasing the pore pressure from 0.45 to 0.58 psi/ft. On further considering the effect of newly formed fractures on enhancing the connectivity of the pre-existing fracture network and contributing to flow themselves, the percolation zone further almost doubles.

	Before stimulation	After stimulation			
		Hydraulic Fracture	Only pre-existing fracture population	Newly created fractures	Pre-existing and newly created fractures
Total fractures (#)	2,179,305	7	2,179,305	324,620	2,503,925
Critically stressed fractures (#)	0 (0%)	NA	381,735 (18% of all fractures)	245,730 (75% of all created fractures)	627,465 (25% of all fractures)
Critically stressed fractures hydraulically connected to the well (#)	0	NA	269,983 (12% of all fractures)	NA	539,001 (21.5% of all fractures)
Percolation zone (sq. ft.)	0	$8.79*10^5$	$8.38*10^7$	NA	$15.45*10^7$

Table 5A-2: Statistics showing the number of all and critically stressed fractures before and after stimulation, along with the percolation zone – Interspacing between hydraulic fractures is 310 feet.

	Before stimulation	After stimulation			
		Hydraulic Fracture	Only pre-existing fracture population	Newly created fractures	Pre-existing and newly created fractures
Total fractures (#)	2,179,305	45	2,179,305	324,620	2,503,925
Critically stressed fractures (#)	0 (0%)	NA	381,735 (18% of all fractures)	245,730 (75% of all created fractures)	627,465 (25% of all fractures)
Critically stressed fractures hydraulically connected to the well (#)	0	NA	272,541(12.5% of all fractures)	NA	541,474 (21.6% of all fractures)
Percolation zone (sq. ft.)	0	$5.66*10^6$	$9.08*10^7$	NA	$16.07*10^7$

Table 5A-3: Statistics showing the number of all and critically stressed fractures before and after stimulation, along with the percolation zone – Interspacing between hydraulic fractures is 50 feet.